PROFILING THE HETEROGENEITY OF INTRACELLULAR RECYCLING IN AGING SKELETAL MUSCLE AT THE INDIVIDUAL CELL AND ORGANELLE LEVELS

A DISSERTATION
SUBMITTED TO THE FACULTY OF THE
UNIVERSITY OF MINNESOTA
BY

Heather M. Grundhofer Brown

IN PARTIAL FULFILLMENT OF THE REQUIREMENTS
FOR THE DEGREE OF
DOCTOR OF PHILOSOPHY

Edgar A. Arriaga, Advisor

March 2019

Acknowledgements

I could not have done this work without the encouragement, mentoring and support of a wonderful network of mentors, colleagues, family, and friends.
I must first thank Dr. Edgar Arriaga for his guidance and unyielding positivity. I am a better scientist for having worked with you.

I would also like to thank a number of faculty at the University of Minnesota who supported various projects through the years: Dr. Valérie Pierre, Dr. Michael Kyba, Dr. Dawn Lowe, Dr. Gengyun “Coco” Le, Dr. Sunny Chan, Dr. David Bernlohr, Dr. Michael Bowser, Dr. Mark Distefano; your support, insight and advice was invaluable.

To my graduate student colleagues from the Arriaga lab at the University of Minnesota, in particular Michelle Kuhns, Katherine Muratore & Marzieh Ramezani; I couldn’t have asked for a better set of friends with whom to share this experience.
And finally, thank you to my husband Rob, who always gave me his unyielding love and support, whether or not science was “working”.

Dedication

This thesis is dedicated to my husband, Rob, and my parents: Marlys & Mark Andersen, and Timothy Luger.

Abstract

Autophagy is a degradative intracellular process induced in response to various intrinsic and extrinsic stresses to prevent cell damage and promote cell survival. Dysregulated autophagy has been implicated in a wide range of age-related dysfunction and disease, therefore methods are needed to for the quantification of autophagy flux. In this thesis, techniques are described for the measurement of autophagy flux at the individual cell level during myogenesis and in phenotypically separated cell subsets from young and geriatric murine skeletal muscle using mass cytometry. In addition, multiplexed measurements of individual autophagy-related organelles are discussed. These techniques provide insight to the heterogeneity of autophagy flux at the individual cell and organelle level, which could inform the fundamental understanding of the necessity of autophagy for the maintenance of skeletal muscle mass and function in aging tissues.

A method was developed to measure autophagy flux in whole cells by mass cytometry. This method provides accurate quantification of autophagy-related cellular targets in whole cells via *post-hoc* non-specific binding correction and total antibody loading normalization and was able to detect small changes in autophagy flux induced via pharmacological treatment. Application of this method to heterogeneous cultures of differentiating myoblasts suggest that autophagy flux is increased during myoblast fusion, while specific degradation of mitochondria via mitophagy is increased during myoblast proliferation, expanding current knowledge of the regulation of autophagy flux during myoblast differentiation.

Satellite cells, pro- and anti-inflammatory macrophages and fibroadipogenic progenitor (FAP) cells are key players in maintaining the regenerative potential of skeletal muscle. Using the method developed for monitoring autophagy flux in myogenesis above, the contribution of each cell type to the overall decrease of autophagy flux described in the literature was determined. This analysis provides insight into the specific cell types demonstrating decreased autophagy flux with

age in skeletal muscle and revealed potential differences in the need for general or selective degradation of cargo via autophagy.

Individual autophagy-related organelle heterogeneity was quantified using mass cytometry. Autophagy-related organelles from murine skeletal muscle, brain, and liver were labeled with a lipid membrane stain, DDD-Tb, which enabled detection of individual organelles via mass cytometry. Analysis of specific organelle types revealed organelle associations which can be used to understand the progression of autophagy.

In the future, these methods can be expanded and applied to biological models of aging to gain high-resolution insight into the organelle types most directly associated with age-related dysfunction and disease.

Table of Contents

List of Tables

Chapter 4

Chapter 7

Appendix A

Appendix B

Appendix C

List of Figures

Chapter 2

Chapter 3

Chapter 4

Chapter 5

Chapter 7

Appendix A

Appendix B

Appendix C

Appendix D

List of Schemes

Chapter 7

List of Abbreviations

ABP	activity based probe
ATGs	autophagy-related protein/gene
ATP	adenosine triphosphate
Bec1	beclin 1
BSA	bovine serum albumin
CCR2	chemokin-CC-motif receptor 2
CE-LIF	capillary electrophoresis with laser-induced fluorescence
CSM	cell staining media
cyclen	1,4,7,10-tetraazacyclododecane
CyTOF	cytometry by time of flight
DAPI	4′,6-diamidino-2-phenylindole
DC	dual count
DDD-Tb	didodecyl-DTPA-Tb
DMEM	Dulbecco's modified eagle medium
DMSO	dimethyl sulfoxide
DOTA	1,4,7,10-tetraazacyclododecane-1,4,7,10-tetraacetic acid
DTPA	diethylenetriaminepentaacetic acid
EGTA	ethylene-bis(oxyethylenenitrilo tetraacetic acid
ESI-MS	electrospray ionization - mass spectrometry
FACS	fluorescence-activated cell sorting
FAPs	fibroadipogenic progenitor cells
FBS	fetal bovine serum
FWHM	full width at half max
GAPDH	glyceraldehyde 3-phosphate dehydrogenase
HEPES	hydroxyethyl piperazineethanesulfonic acid
HS	horse serum
ICP-MS	inductively coupled plasma-mass spectrometry
K_d	dissociation constant
KO	knock-out
LAMP2	lysosomal-associated membrane protein 2
LC3	microtubule-associated protein 1A/1B-light chain 3
MCP	metal-chelating polymers
Mfn1/Mfn2	mitofusin 1 / mitofusin 2
MHC	myosin heavy chain
MOPS	3-(N-morpholino) propanesulfonic acid
mTORC1	mammalian target of rapamycin complex 1

MyoG	myogenin
NaN_3	sodium azide
NMR	nuclear magnetic resonance
OPA1	optic atrophy 1
OXPHOS	oxidative phosphorylation
p62	nucleoporin p62
PAX7	paired box protein 7
PBS	phosphate-buffered saline
PCA	principle component analysis
PCR	polymerase chain reaction
PDGRFα	platelet-derived growth factor receptor-alpha
PEG	polyethylene glycol
PICs	$PW1^+/Pax7^-$ interstitial cells
Pink1	PTEN-induced kinase 1
PTFE	polytetrafluoroethylene
PVDF	polyvinylidene difluoride
PW1	Paternally expressed gene 3
ROS	reactive oxygen species
SDS-PAGE	sodium dodecyl sulfate - polyacrylamide gel electrophoresis
SEC	size exclusion chromatography
SELEX	selective evolution of ligands by exponential enrichment
siRNA	silencing RNA
SNE	stochastic neighbor embedding
SPAAC	strain-promoted copper-free azide-alkyne [3+2] cycloaddition chemistry
SPADE	spanning-tree progression of density normalized events
t-SNE	Barnes-Hut implemented T-distributed stochastic neighbor embedding algorithm
TBS	tris-buffered saline
TBS/T	tris-buffered saline + 0.1% tween-20
TCEP	tris(2-carboxyethyl) phosphine hydrochloride
TEM	transmission electron microscopy
TFA	trifluoroacetic acid
TOF	time-of-flight
TOMM22	translocase of outer membrane 22
TPP	triphenylphosphonium
Tris-HCl	tris(hydroxymethyl)aminomethane hydrochloride
WT	wild type
αCHCA	α-cyano-4-hydroxycinnamic acid

Chapter 1

Introduction

The global population of individuals over 60 years is expanding in parallel with increased life expectancy and is set to double by 2050.[1-2] However, preservation of human health is not always sustained with increased life expectancy. Of the 1.5 million individuals over the at of 65 admitted to long-term care facilities each year in the United States, 33% are institutionalized solely due to their inability to perform activities of daily living often precipitated by a gradual but persistent decline in skeletal muscle mass and function, termed sarcopenia.[3] Undoubtedly, the study of this age-related decline is vital to ensuring the health and happiness of our aging population.

Macroautophagy (herein referred to as autophagy) is a catabolic intracellular recycling process by which long-lived proteins and organelles are degraded. In short, autophagy encompasses the recognition, sequestration, delivery, and degradation of cytosolic cargoes and is constitutively active in nearly all eukaryotic cells.[4] Autophagy is a predominately cytoprotective process that enables the adaption of individual cells or organs to changing conditions.[5] Reduced autophagy has long been studied for its potential contribution to age-related dysfunction and disease.[6] Indeed, the unifying theme in age-related autophagy studies is the maintenance of quality control mechanisms and their gradual loss with age[7] Considering this model, it is not hard to imagine that accumulation of damage over a relatively long period of time as quality control functions wane results in age-related dysfunction. The mechanism by which autophagy flux decreases with age is unclear, but given its complex regulation and the prolonged, stochastic process of aging, it is likely complicated and heterogeneous.

A major challenge in characterizing the contribution of decreased autophagy flux to aging-related pathologies is the heterogeneous nature of higher-order biological models of aging. In vitro cellular studies of autophagy have exponentially increased our current understanding of autophagy progression and regulation, but the complexity of higher-order biological models such as mice and humans confound analyses of autophagy flux via currently available methods[8]. Often, within a single tissue such as skeletal muscle many phenotypically and functionally

diverse cell types coexist and work together to maintain tissue health.[9-11] Due to the diverse function of each cell type present in a given tissue, autophagy regulation and flux may differ in each cell type, thus bulk analyses of tissue may obscure the unique regulation of autophagy in each type. Similarly, individual cell analysis can confound the intricate inter-organelle type associations occurring inside individual cells.[12] Cells contain many autophagy-related organelles at any time, and co-detection of all autophagy-related organelles in a single cell can lead to ambiguous interpretations of autophagy organelle trafficking and function.

Better methods for the simultaneous characterization of heterogeneous cell or organelle populations and their unique autophagic function are required for a conclusive understanding of the contribution of decreased autophagy flux to age-related dysfunction and disease in complex tissues. This thesis describes new methods for quantifying autophagy flux in heterogeneous whole cell populations and the detection of heterogeneous individual autophagy-related organelles isolated from specific tissues.

Chapter 2 describes background information related to individual cell and organelle analysis and introduces the techniques used in this work. The current understanding of autophagy and its dysfunction in aged skeletal muscle is also discussed.

Chapter 3 describes the development of a method for the relative quantification of autophagy flux in whole cells via mass cytometry. *Post-hoc* correction of individual cell data for non-specific antibody probe binding and normalization for total antibody probe loading into each cell resulted in accurate per cell antibody counts. Titration of antibody probes using this method identified optimal antibody staining concentrations for subsequent experiments. Differentiating myoblasts were analysed using the optimized antibody staining concentrations identified for the analysis of autophagy flux. We found that autophagy flux is increased specifically during myoblast fusion and quickly decreases in fully formed myotubes, but specific degradation of mitochondria is increased earlier during differentiation and is maintained in formed myotubes.

Chapter 4 describes the quantification of autophagy flux in the heterogeneous interstitial cell populations in young and aged skeletal muscle. The method allows for the analysis of individual cell subsets of interest including tissue resident stem cells (satellite cells), pro- and anti-inflammatory macrophages, and fibroadipogenic progenitor cells which were recently shown to have myogenic potential. The method revealed decreased autophagy flux in both satellite cells and fibroadipogenic progenitor cells with age, but not anti-inflammatory macrophages, providing a more detailed view of the contribution of decreased autophagy flux to decreased muscle mass and function observed with age.

Chapter 5 describes a method to measure the heterogeneity of individual autophagy-related organelles from murine skeletal muscle, liver, and brain using mass cytometry. This method was used to identify unique organelle types involved in autophagy and profile their intra-organelle type heterogeneity and inter-population associations. This method allows for the analysis of associations between organelles, providing insight into the progression of autophagy in each of the analysed tissues.

Chapter 6 summarizes the conclusions and significance of this work. Specifically, we have developed methods to monitor the heterogeneity of autophagy progression at the whole cell and individual organelle levels. These methods may be valuable in the elucidation of the contribution of autophagy to decreased muscle mass and function with age.

Chapter 7 describes possible improvements to currently available mass cytometry reagents described in Chapter 2, as well as the development of novel reagents for the detection of unique organelles. Individual organelles contain relatively few targets for antibody probe binding, thus the synthesis of a metal-chelating dendrimer which could increase technique sensitivity nearly ten-fold is discussed in Chapter 7. Not all organelles of interest are easily identified using commercially available antibodies, thus Chapter 7 also describes the development of aptamers for the identification of unique autophagy-related organelles. and cationic, lipophilic reagents for the identification of intact mitochondria. It is well

known that cellular protein abundance does not necessarily report on activity. Chapter 7 also discusses application of activity-based probes for the detection of enzyme activity via mass cytometry.

Overall, the work described in this thesis represents a contribution of new methods for studying the heterogeneity of autophagy in whole cells and individual organelles via mass cytometry, which will advance the fundamental understanding of decreased autophagic flux in age-related declines in skeletal muscle mass and function. Elucidation of the role of decreased autophagy flux may contribute to the discovery of treatments to extend the healthy lifespan of our aging population.

Chapter 2

Background

2.1 Potential impact of single-cell or single-organelle analysis

Robert Hooke first observed heterogeneous cell types in plants and animals in 1665. For the last three and a half centuries, scientists have tried to catalog and understand the diverse functions of different cell types. How does cellular diversity arise? How do separate cell types in a single tissue work together? The advancements have been vast, but these same questions captivate us even now.

The advent of single-cell analyses techniques at the genomic, transcriptomic, and proteomic levels represent a turning point in cell biology research. The observation and analysis of single cells in the fields of genomics, metabolomics, and transcriptomics have revealed that multiple cell types or functionally distinct subpopulations often coexist in biological systems. These variations at the single cell level are thought to be biologically meaningful, producing varying outcomes at the organism level. Similarly, heterogeneity exists at the sub-cellular organelle level.[13] Organelles are adaptive to intrinsic and extrinsic stresses and subject to dysfunction with damage; therefore, organelle heterogeneity exists in regard to differences at the spatial, temporal, and functional levels.[12]

Before single cell or organelle analyses were methodologically possible, population-level analyses were used for decades, contributing to monumental advances in human health such as the discovery of penicillin,[14] statins,[15] and the function of mitochondria as energy centers of cells.[16] Population-level measurements capture population state and the associated change with perturbation. When making population-level measurements, it is assumed that the measured average state represents the dominant biological affect in single cells. In reality a population averaged measurement may not represent the true state of any single cell or organelle, confounding our understanding of complex biological systems. Simpson's paradox describes the phenomena whereby the relationship between a pair of variables reverses when considering a third variable.[17] Partitioning data based on the third variable results in sign reversal of the observed relationship in aggregated data (Figure 2.1). Thus, failing to compartmentalize data

by a distinguishing variable can lead to qualitatively incorrect interpretation of population-level data.

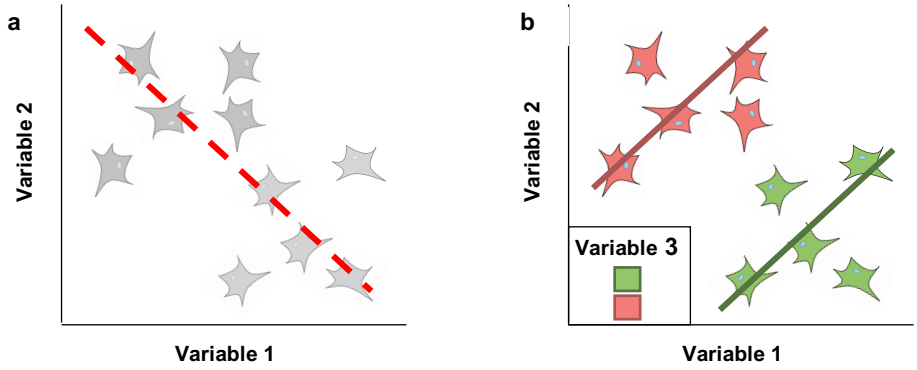

Figure 2.1. Single cell measurements preserve information lost via population-level analyses. Simpson's paradox describes the misleading effect of averaging population-level data (a), when failing to consider other distinguishing variables (b).

Single cell or organelle analyses are methodologically challenging given the high sensitivity necessary to detect material in a single bio-particle, the high throughput necessary to assess heterogeneity, and the desire for multiplexed single bio-particle analysis to probe complex interactions. Techniques for single cell analysis continue to emerge with notable contributions in the fields of microfluidic devices, capillary electrophoresis, and cytometry. Microfluidic analyses of single cell and organelle proteomes have been realized through cell arrays[18-20]and single cell barcode chips.[21-26] Capillary electrophoresis with laser-induced fluorescence has been employed for assessing the heterogeneity of organelle electrophoretic mobility and function.[27-33] Multi-parameter fluorescence flow cytometry is perhaps the most well-known technique for multiple target detection and analysis in single cells.[34] Developments of this technology have allowed for simultaneous analysis of up to 18 parameters,[35] though more common analyses include far fewer parameters to eliminate the need for complicated deconvolution of fluorescence signals, which is inherent due to the similarity of excitation and emission spectra of fluorescent labels used in such studies.

2.2 Mass cytometry for multiplexed individual bio-particle analysis

A related technique to fluorescence flow cytometry is mass cytometry. This technique uses inductively coupled plasma-mass spectrometry (ICP-MS) to detect and quantify lanthanide ions that report on the abundance of cellular targets in single cells. Due to the low abundance of lanthanides in biological particles such as cells and organelles, and the phenomenal sensitivity of ICP-MS for elemental analysis, mass cytometry has adequate sensitivity to measure a small number of proteins per cell. The mass resolution of time-of-flight mass spectrometry makes this technique adequate to detect a high number of pure isotopic elements (upwards of 50), surpassing the number of possible parameters detected by flow cytometry. Mass cytometry is similar to flow cytometry in that antibodies are used as specific target affinity reagents labeled with reporters, but whereas conventional flow cytometry uses fluorescent reporters, mass cytometry uses polymers chelating isotopically pure lanthanide ions.

A unique feature of mass cytometry is the use of an ICP that fully ionizes all components in a sample, which then allows for detection of a wide range of lanthanide ions from the antibodies used to labeling cellular targets in single cells. Before the introduction of mass cytometry, ICP-MS had been used to detect metal tagged antibodies specific to cellular markers in cell lysates, but these findings could not be related back to specific cell types in a heterogeneous cell population.[36] Other relevant prior work includes the ICP-MS analysis of single cells from suspensions that had been labeled with lanthanides and analyzed using conventional instrumentation.[37-42] The work in single cells, led to the advancement of elemental analysis of individual, antibody-labeled cells, establishing mass cytometry as a new technique.[43] The report of successfully using an ICP-MS for individual cell analysis was revolutionary in that it provided high resolution and unprecedented multiplexing capabilities necessary for thorough analysis of complex biological systems. The first commercialized CyTOF (Cytometry by Time Of Flight) instrument was available in 2009, and featured an analytical m/z range of 103-193, maximum throughput of ~1,000 events/second and had a dynamic range covering 4 orders of magnitude. Subsequent models named CyTOF2 (second generation instrumentation) and Helios (third generation) further improved these and other parameters, including the number of parameters that can be measured per cell (upwards

of 50), peak sample introduction rates (2,000 cells per second), improved dynamic ranges (4.5 orders of magnitude). These figures of merit far surpass the abilities of currently available flow cytometers. Every method described in this work harness the multiplexed capabilities and wide dynamic range of the CyTOF2 instrument to profile cellular target abundance.

2.2.1 Instrument description

Mass cytometers contain three modules including: sample introduction microfluidics, ion optics, and a time-of-flight (TOF) mass spectrometer. The sample introduction system includes a port through which cells are flowed into the instrument followed by a series of specialized glassware to encapsulate cells in individual liquid droplets from which cells are vaporized, atomized and ionized (Figure 2.2, box 2). The ion optics system selects all ions of interest and guides them towards the mass spectrometer (Figure 2.2, box 2). The third module is a TOF mass spectrometer, used to identify and quantify the abundance of each ion of interest (Figure 2.2, box 3). These modules and their function are described in detail below.

Sample Introduction and Ionization (Figure 2.2, box 1)

The introduction of cell samples into the mass cytometer has evolved with each new version of CyTOF instrumentation. Introduction of cell samples into the first or second-generation mass cytometer is accomplished using a syringe pump and one or two-sample loop microfluidic system. Via a syringe, an aliquot of the cell suspension is manually pushed into a sample loop. Then, a flow injection valve rotates so that flow from a syringe pump displaces the loop contents to deliver them to the nebulizer via a sample introduction capillary. The newest generation of mass cytometer, Helios, has a pneumatic sample introduction system that uses argon gas to force cell suspensions into the sample uptake probe and onward to the nebulizer.

As cells from the cell suspension are introduced into the nebulizer via the sample introduction capillary, a fine spray of droplets containing individual cells is produced by the pressure exerted on the suspension from the argon gas exiting the tip of the concentric nebulizer (Figure 2.2, box 1). This aerosol is directly injected into a heated spray chamber (~200˚C) supplied with argon makeup gas where the cell-containing droplets are partially desolvated.[43] The partially-desolvated droplets then travel through an ICP torch producing a high temperature argon plasma (5500-7000 K) where they are vaporized, atomized, and

ionized.[43-44] For each cell being ionized, the process results in a cloud of ions with a diameter of ~ 2 mm. The expansion of the ion cloud for each cell is diffusion-limited, meaning these clouds are roughly the same size, no matter the size of the cell introduced.[44] Thus, the analysis of single cells in samples with cells of multiple sizes is not biased after ionization.

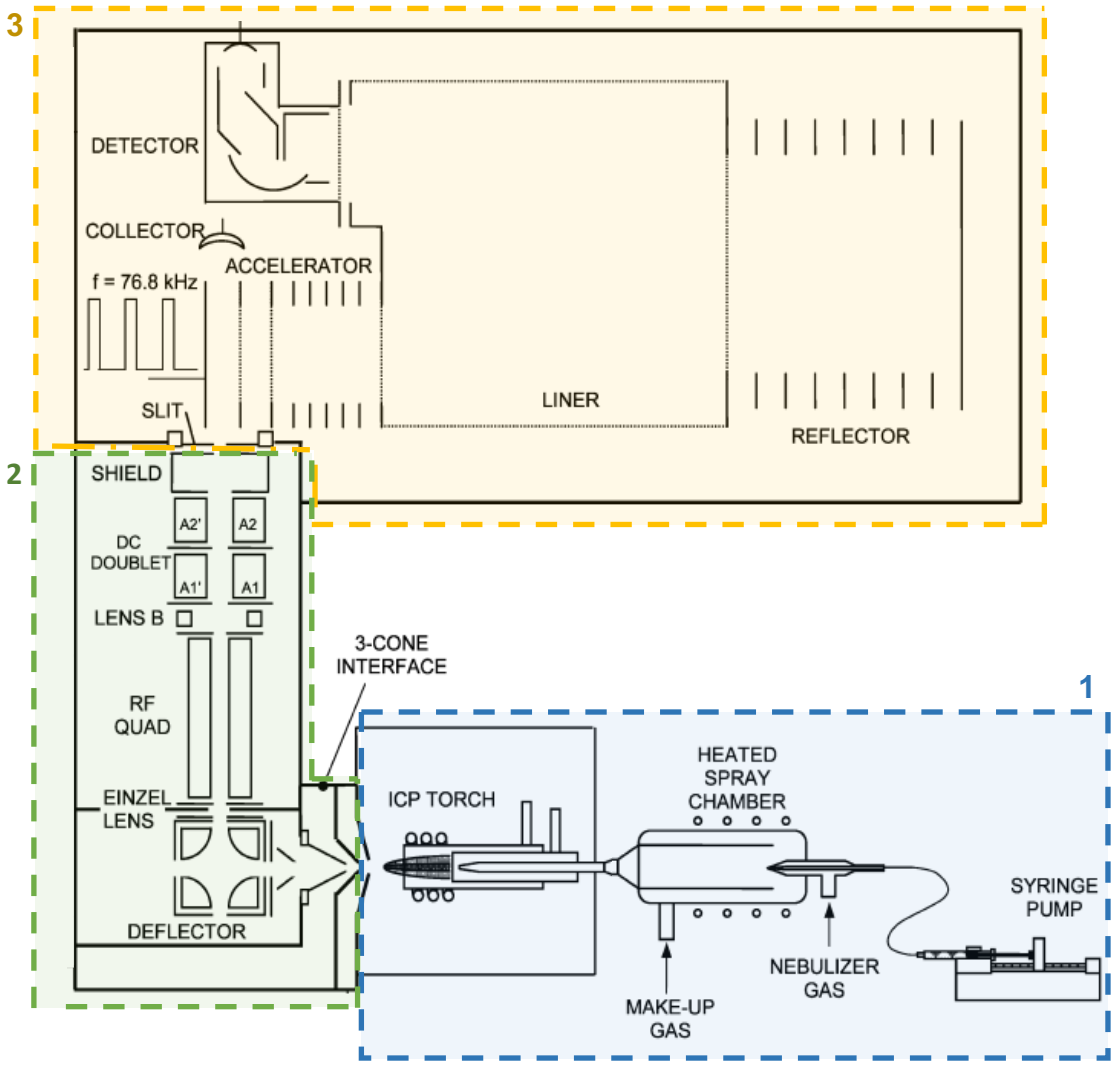

Figure 2.2. General overview of CyTOF hardware. After samples are introduced to the instrument, they are aerosolized via the nebulizer, desolvated in the spray chamber, and sequentially vaporized, atomized, and ionized as they exit the ICP torch (box 1). The resulting ion cloud is filtered, focused, and guided toward the detector via the RF quadrupole shown in box 2. Separation and detection of relevant metal ions takes place in the time-of-flight (TOF) detector in box 3. Figure modified from Bandura.[43]

This allows for the technique to be truly quantitative as the number of metal ions detected is directly related to the number of ions introduced.[44] However, despite the chemical similarity of the lanthanide series of metals, ion transmission through the instrument is not identical for each isotope. In fact, the transmission efficiency profile across the relevant mass range is unique to each mass cytometer. As has been reported,[45-46] we observe an asymmetrical bell curve shape centered around the middle of the mass range. We also observe a nearly 3-fold change in transmission efficiency across the mass range for the CyTOF 2 at the University of Minnesota (Figure 2.3). Post-hoc correction for variation in transmission efficiency for quantitative comparisons between mass channels is described in Chapters 3 through 5 of this work.

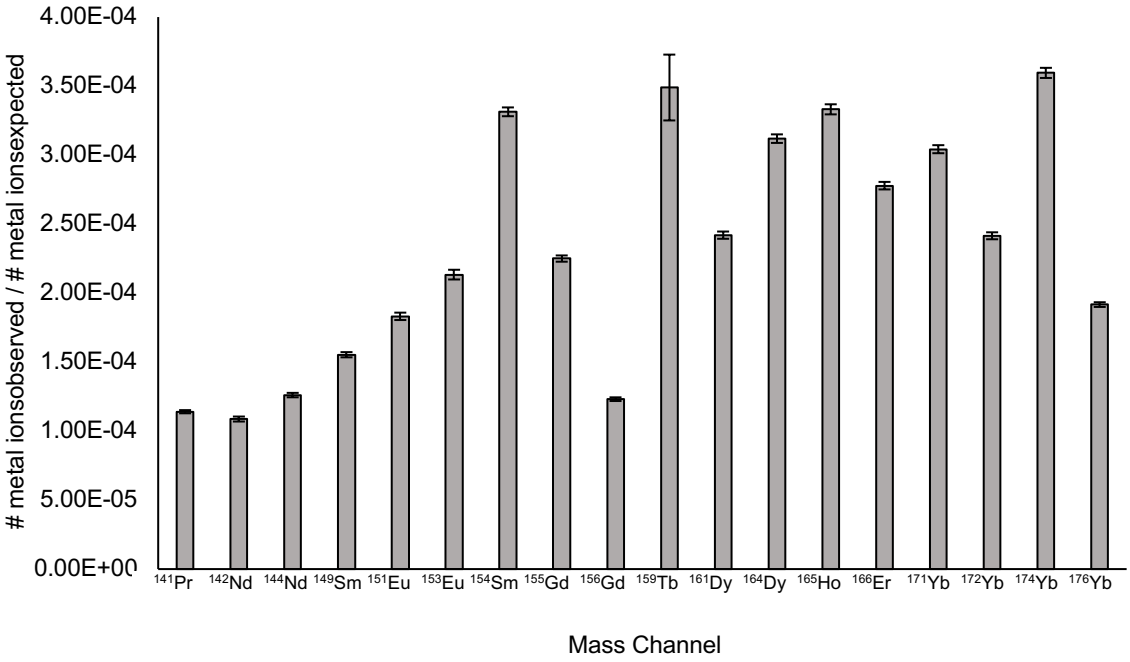

Figure 2.3. Transmission Efficiency on CyTOF2 at the University of Minnesota. We observe an asymmetrical bell-shaped curve centered over the middle of the mass range for CyTOF2. We also observe a nearly 3-fold change in transmission efficiency across the mass range which has implications for the mass channel comparisons made in Chapters 3 through 5.

Ion Optics (Figure 2.2, box 2)

Ions produced at the ICP torch are sampled through a three-cone interface, which serves as a low-pressure, controlled entrance into the low vacuum ion optics chamber. Sampler, skimmer and reducing cones reduce the pressure while cooling

and focusing the ion cloud. A quadrupole ion deflector then filters out neutral atoms that will interfere with downstream analysis. Positively charged ions are directed perpendicularly out of the ion deflector toward downstream ion optics for eventual mass analysis, while neutral atoms follow an uninterrupted path toward a turbomolecular pump. Another quadrupole (RF QUAD in Figure 2.2, box 2) serves to filter out low mass ions (H^+, C^+, O^+, N^+, OH^+, CO^+, O_2^+, Ar^+, ArH^+, ArO^+) that predominate in the ion cloud after ionization. Thus, ions leave the quadrupole in packets with a specific mass range, each packet corresponding to an ion cloud, which in turn corresponds to an individual cell. The filtered ion packets leaving the RF QUAD then pass through a DC quadrupole doublet (DC DOUBLET in Figure 2.2, box 2) which flattens the ion stream to allow for injection into the TOF mass spectrometer.

Time of Flight Mass Spectrometer (Figure 2.2, box 3)

Ion packets are introduced through a vacuum interface (SLIT in Figure 2.2, box 3) to an accelerator where ions experience sequential voltage pulses at a frequency of 76.8 kHz. The result is a portion of ions from each packet are sampled (pushed) into the TOF mass spectrometer every 13 µs, accelerated by the pulsed electric field which impinges a constant kinetic energy regardless of the ion mass to charge ratio (m/z). In total, the ion packet from each cell is sampled 20 – 75 times.

The kinetic energy acquired by all ions through acceleration translates into a unique time of flight (t) corresponding to each m/z from the accelerator plate, via the reflector, to the detector. Using two empirically derived constants, t_0 and A, the relationship between (t) and (m/z) is

$$t = t_0 + A\sqrt{\frac{m}{z}} \qquad \text{Equation 2.1}$$

As deduced from equation 1, the ions with smallest m/z value reach the detector first. Ions will continue to arrive according to increasing m/z order. Typically, isotopes with masses differing by 1 amu have ions arriving at the detector 20-25 ns apart. Because the detector response is faster than 20 ns, the

detector has a resolution better than 1 amu, which is sufficient to detect the various lanthanide isotopes used to labels antibodies.

2.2.2 Signal integration

A dynode electron multiplier detects ions as they arrive at the end of the TOF mass spectrometer drift tube. Depending on the number of ions with a given m/z reaching the detector during the 13 μs duration of a packet of ions, the detector operates in a pulse counting mode (for low number of ions) or an integration mode (for high number of ions). When the ion density approaching the detector increases, particles will simultaneously arrive resulting in an underestimate of counts. Thus, integration of the analog signal is a more useful quantification method in this case. The relevant concentration range at which CyTOF operates requires that dual data be collected, meaning both counting and integration modes are applied to each m/z value of interest (channel). A user-defined threshold defines when integrated intensity and pulse counting are selected for processing the signal. When the integrated intensity is used, outputs are converted to ion counts using the equation below, where the Dual Count Coefficient is a constant determined experimentally for each mass channel.

$$\text{Count} = (\text{Dual Count Coefficient}) \times \text{Intensity} \qquad \text{Equation 2.2}$$

Individual mass spectra containing counts for each m/z value (channel) are written into integrated mass data files (*.imd). To obtain meaningful data, the instrument user must set criteria to identify signals (events) corresponding to single cells. These criteria are minimal signal intensity and duration of the event, typically 20-50 spectra. Signals for each m/z value (channel) are integrated across all mass spectra collected for individual events (20-50 spectra / event) and written into text (*.txt) and/or flow cytometry standard (*.fcs) files which include metadata such as instrument conditions and channel annotations.[44] Events with an abnormally long, bi-modal signal correspond to overlapping events, and must be removed post-acquisition.[44] The frequency of analyzed

events can be visualized during data acquisition in the form of a rain plot consisting of stacked mass spectra shown in Figure 2.4. Visualization of individual organelles on rain plots in Chapter 5 provided evidence of particle detection.

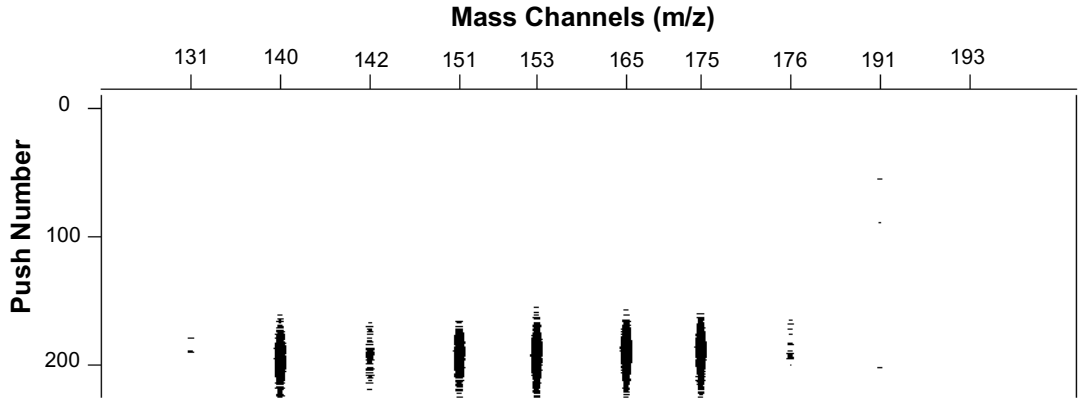

Figure 2.4. Representative rain plot from CyTOF2. Consecutive mass spectra showing integrated signal for a single detected event. Each "push" is recorded as a separate mass spectrum. The y-axis identifies the spectra (in sequence) over which detected organelle event signals are integrated. The x-axis shows the relevant m/z channels. Dark lines in the plot area indicate detected ions.

2.2.3 Data normalization

The most common instrument data output is the *.fcs file type, which has standard content guidelines.[47] Commonly, mass cytometry *.fcs files are normalized to correct for instrument response drift. Factors that contribute to response drift include: i) build-up of cellular debris and subsequent decrease in detection sensitivity, which is relevant after multiple hours of data collection,[48] and ii) differences due to cleaning and daily calibration.[49]

Correction for drifting is based on normalization of signal intensities relative to those of dedicated isotopes embedded in polystyrene beads.[49] When detected in the mass cytometer, bead events are uniquely identifiable by the combination of isotopes present (^{140}Ce, ^{142}Ce ^{151}Eu, ^{153}Eu,^{165}Ho, ^{175}Lu, ^{176}Lu). Because drift equally affects the signals from lanthanide ions originating from polystyrene beads and those attributed to other labeling reagents, the lanthanide ion signal from beads is used to define normalization factors for all other lanthanide ions in cell samples.

Two approaches are available for signal intensity normalization. The first approach normalizes data to a global standard determined for each lot of lanthanide isotope

embedded polystyrene beads provided by the manufacturer, allowing for inter-and intra-experiment normalization, including normalization across instruments. Specifically, it is an algorithm embedded within the mass cytometer operating software (version 6.0.626 and above). This data normalization algorithm was used in Chapters 3 through 5 to normalize mass cytometry data collected over long periods of time. The correction factor is defined as the ratio of the predetermined signal value (provided by the manufacturer) and the measured median value for each mass included in the bead standards. The algorithm linearly interpolates between measured mass channel intensities to apply the normalization factors to detected experimental mass channels. The second method normalizes data using the same lanthanide isotope embedded polystyrene beads, but median intensity values are normalized within a given experimental file instead of normalization to a predetermined standard. In this method, a moving median for the signal of each isotope mass included in the beads is calculated as a function of time to determine a “fitted slope value”, as shown in Figure 2.5. This “fitted slope value” is used as a correction factor that is applied to all cell events.[48]

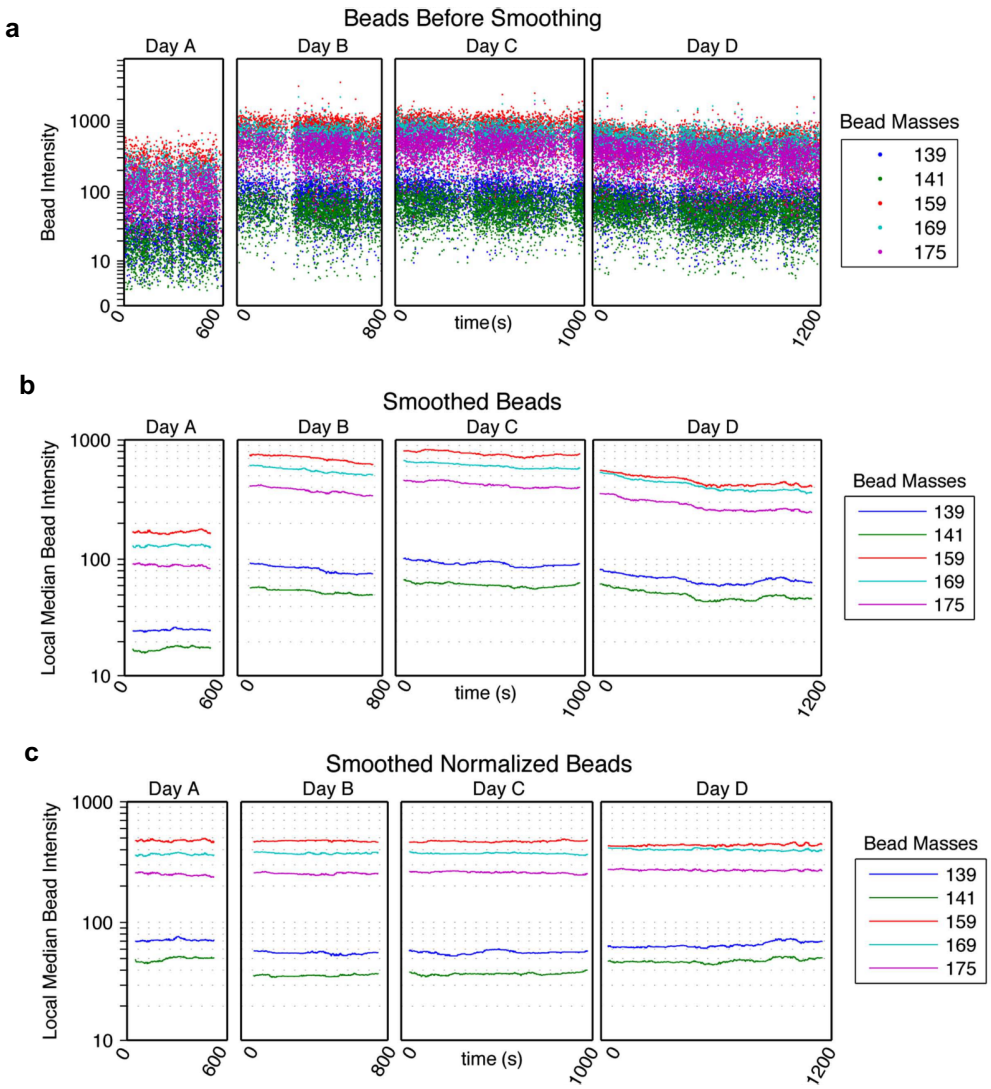

Figure 2.5. Normalization of mass cytometry data via calibration beads. The median signal intensity measured from calibration beads can be used to normalize data that would otherwise vary due to instrumental differences at the time of data acquisition. (a) Raw intensities from beads collected on four different days were plotted vs acquisition time. (b) Smoothed data results from the calculation of a moving median of each bead channel across 500 beads. Visible declines in intensity over acquisition time are apparent in each bead channel. (c) Normalization involves multiplying individual raw bead intensities by a correction factor, resulting in corrected intensities for all analyzed events. Figure reprinted with permission from Finck et al.[48]

2.2.4 Available reagents

A number of cell labeling reagents exist to identify specific cellular targets during mass cytometry analysis. Most often, antibodies covalently bound to metal chelating polymers (MCPs) are used to detect cellular targets of interest. In addition, cell identifying reagents are often used to label double-stranded nucleic acids or cellular debris. MCPs, described in detail below, are commonly used in mass cytometry analyses and were used in Chapters 3 through 5 of this work.

Whole cell analyses in Chapters 3 and 4 also employed the metallointercalators and live/dead stains described below.

Metal Chelating Polymers

For the purpose of mass cytometry MCPs are loaded with a pure lanthanide isotope and conjugated to an antibody. The same MCP molecule can be used for labeling all antibodies, but each unique antibody clone is assigned a unique lanthanide isotope. Great similarity in chemical properties of the lanthanide series of metals makes it possible to use a wide range of isotopes with the same MCP chemistry. Furthermore, lanthanides have low natural abundance and are commercially availability as purified isotopes.[50-52] Loading capacity (lanthanide ion/polymer chain) of each MCP is dictated by the molecular structure of MCPs. In general, the structure of MCPs includes three linked scaffolds with separate functions (Figure 2.6) including a polymer backbone, metal chelating ligand, and a linker.

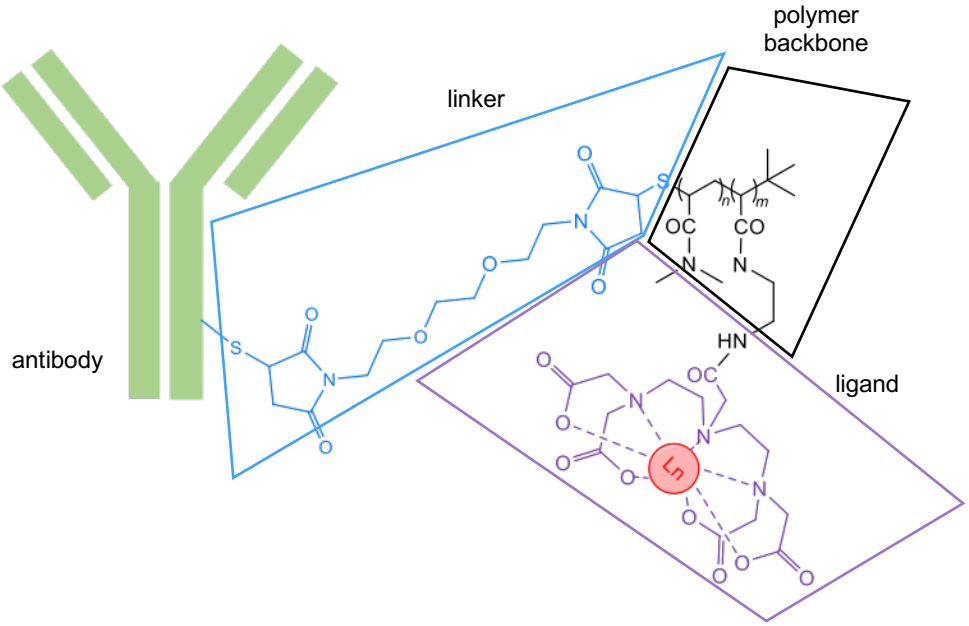

Figure 2.6. General structure of metal chelating polymer (MCP) for labeling antibodies. MCPs contain three main components. These include: i) a polymer backbone ("polymer backbone"), ii) metal chelating ligands ("ligand"), and iii) a linking moiety ("linker") that connects the polymer backbone to an antibody ("antibody"). Metal chelating ligands, usually DTPA or DOTA, are covalently attached to the polymer backbone at periodic intervals. The polymer is connected to the antibody through a maleimide linkage that reacts with free sulfhydryl moieties in a partially reduced antibody. Together with the number of lanthanide ions ("Ln") associated with each polymer, the number of polymers attached to each antibody determines the overall number of metal ions that are associated with each antibody.

The most common metal chelating ligands are multidentate polyaminocarboxylates, such as diethylenetriaminepentaacetic acid (DTPA) and 1,4,7,10-tetraazacyclododecane-1,4,7,10-tetraacetic acid (DOTA), because they coordinate lanthanide ions with low dissociation constants.[53] The most commonly used linker relies on the reaction of maleimide with sulfhydryl groups produced by reducing disulfide bonds within the Fc portion of an antibody. Although chemistries that would covalently bind the polymer to lysine residues in the antibody are also feasible, there exists a general concern that random lysine modifications could result in a loss of antibody specificity.

Because sensitivity of mass cytometry and other ICP-MS techniques is expected to increase linearly with lanthanide content, developments in MCPs have attempted to chelate more lanthanide ions per polymer. The first report by Lou and coworkers described 33 DOTA ligands per polymer chain,[50] representing the maximum number of lanthanide ions loaded onto a polymer. Later MCPs described by Majonis and coworkers were able to attach 68 ± 7 lanthanide-chelating ligands per polymer. They also determined that on average a conjugated antibody displayed, 2.4 ± 0.3 polymers, giving a total of 161 ± 4 lanthanide ions per antibody.[51] To increase the utility of lanthanide-chelating polymer conjugated antibodies, dual-labeled antibodies have been reported,[54-56] which contain both fluorophore and lanthanides as reporters to facilitate cross-platform validation of antibody localization or cell-subpopulation enrichment prior to mass cytometry analysis.

Metallointercalators

The ability to identify signals originating from intact cells is critical for accurate analysis of single cell suspensions. Ornatsky and coworkers describe the use of the well characterized polypyridyl metal complexes (metallointercalators) for this purpose.[42] These reagents can help identify single cells among cellular debris, identify cell cycle phases, and normalize signal intensities across cell populations. Similar to the MCPs above, metallointercalators usually contain a transition metal, such as Rh, Ru, or Ir, whose abundance within individual cells is an indirect

measurement of DNA content. In original reports, three ligands of the metallointercalator bind to the transition metal[57-59] (Figure 2.7).

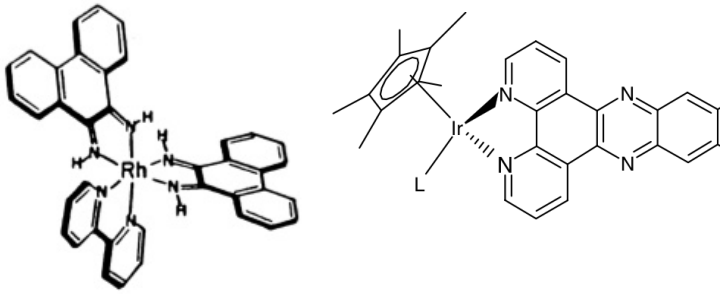

Figure 2.7 DNA metallointercalator. usually contain three ligands bound to a transition element. Insertion of a planar aromatic ligand between double stranded DNA base-pairs have strong associated electrostatic interactions resulting in low dissociation constants a stable interaction monitored via mass cytometry. Reprinted with permission from Pyle[60] and Schäfer[57].

The strong interactions between DNA and the metallointercalator are dominated by electrostatic forces and insertion of planar aromatic ligand between nucleotide base pairs.[59] This interaction has a low dissociation constant ($K_d < 10^{-8}$ M), which allows for use of metallointercalators for accurate determination of DNA content within a cell.

For proper use in mass cytometric analysis, the signal of a metallointercalator must increase linearly with its incubation concentration and not be affected by the presence of other labeling reagents. For instance, increasing incubation concentrations of iridium intercalator in cells resulted in a linear increase in measured signal (Figure 2.8). Importantly, signal originating from metal-labeled antibodies was not affected by increasing concentrations of iridium intercalator.[42] This behavior is also observed in commercially available metallointercalators used in mass cytometry experiments to identify nucleated cells.

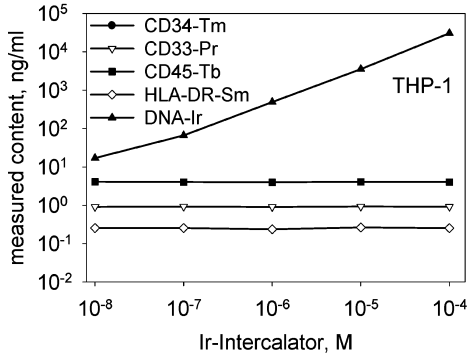

Figure 2.8. Expected DNA metallointercalator response. An essential characteristic of DNA intercalators is that they not interfere with the labeling of other cellular targets with antibodies. Ornatsky and coworkers showed that even with increasing concentrations of DNA intercalator (DNA-Ir), the measured signal from antibodies incubated at constant concentrations is unchanging. CD34-Tm, CD33-PR, CD45-Tb HLA-DR-Sm, are all metal labeled antibodies specific to surface proteins on immune cells. Reprinted with permission from Ornatsky.[42]

Metallointercalator content is often used to trigger mass spectra integration thereby collecting detected events, and to and identify cells. To trigger mass spectra integration the distribution of the ion reporters (e.g. ^{191}Ir and ^{193}Ir) must be Gaussian over the spectra which define the event, and the full width at half max (FWHM) must be at least 200 μs. To identify a collected event as an intact cell, the number of integrated mass spectra and metallointercalator content are compared and must meet expected thresholds.[42] Following mass spectra integration, collected single cell events are examined for abundance of other molecular markers reported by their respective antibody-MCP conjugates.

Live/Dead Stains

High throughput single cell analyses require identification and exclusion of non-viable cells in subsequent data analysis. In fluorescence flow cytometry, such cells can be identified by the accumulation of fluorescent dyes that do not cross intact plasma membranes. In mass cytometry, the chemotherapy drug cisplatin acts as a live-cell impermeable stain, which enters cells with compromised plasma membranes more quickly than cells with intact plasma membranes.[61] Once inside the cells, it reacts with protein nucleophiles such as R-SH or R-S-CH_3[62-63] to form covalent Pt-S bonds. This covalent modification is stable through subsequent fixation, permeabilization and antibody staining procedures, making it an ideal viability dye for mass cytometry. The accumulation of cisplatin in non-viable cells is observed as a signal in the ^{195}Pt channel with overall intensity dependent on cisplatin incubation concentration and duration. The optimal concentration of cisplatin should provide a consistent distribution of viable/non-viable cells as reported by other methods (Figure 2.9) [61].

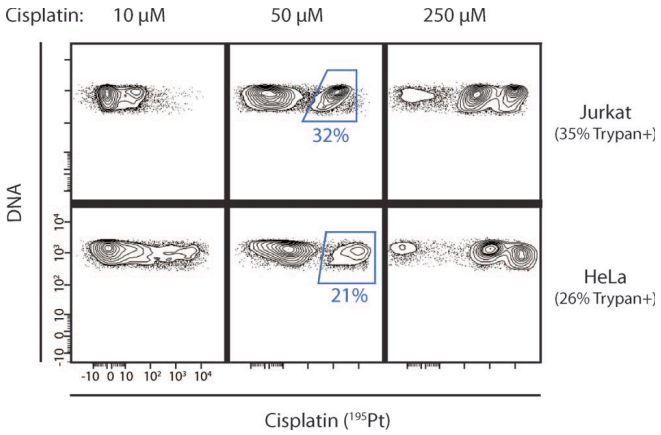

Figure 2.9. Determination of cell viability via cisplatin content. Three incubation concentrations were titrated in both suspended (Jurkat) and adherent (HeLa) cell lines. A known percentage (determined via Trypan blue exclusion) of heat killed cells of the same type were added to viable suspensions of each cell line to assess the accuracy of each incubation concentration. They conclude that the dead cell population identified using the middle concentration of cisplatin (50 µM) correlates well with their trypan blue exclusion assay results. Reprinted with permission from Fienberg.[61]

2.2.5 Data Analysis Strategies

After normalization (see section 2.2.4), data are gated to select single-cell events and eliminate non-viable cells (see section 2.2.5) and then processed using algorithms such as those described below.

Dimensionality Reduction (Highlighting: PCA & viSNE)

While the highly-dimensional data produced via mass cytometry can be highly informative, visualization of the data in a manageable number of dimensions is critical to successful inference of biological meaning. The challenge of dimensionality reduction is accomplished through the projection of multi-dimensional data in 2D or 3D space using surrogate dimensions, while maintaining relationships. Approaches to dimensionality reduction can be grouped into two separate categories: linear and non-linear, with principle component analysis (PCA) and stochastic neighbor embedding (SNE) being an example of each applied to mass cytometry data. In Chapter 5, inter-organelle type heterogeneity was visualized using a variation of SNE.

Linear dimensionality reduction as implemented via PCA condenses multi-dimensional data into two or three principle components that can reproduce the major sources of variance. Data can be plotted against these principle component axes, with separation of single-cell populations along a given axis indicating large variance in a specific principle component. While PCA has been applied to mass cytometry[64] data, a limitation of PCA is its inability to distinguish between geodesic and Euclidean space when analyzing biological data which has many non-linear relationships.

Non-linear dimensionality reduction overcomes the limitations of its linear counterpart through maintaining the geodesic distance between points when projected to

two or three dimensions. For mass cytometry, a variation of SNE called t-SNE is commonly used, in the form of viSNE. The viSNE algorithm represents data in as a highly dimensional point cloud where the number of dimensions (*n*), is defined by the number of measured parameters. Within viSNE, an optimization algorithm finds a projection of the points from highly-dimensional space into two, or three-dimensional space so that pair-wise distances between points are conserved, effectively conserving both the local and global geometry of the entire cloud.[65] The resulting plot looks similar to a biaxial dot plot, but the positions of the cells are related to their position in high-dimensional space[66] (Figure 2.10).

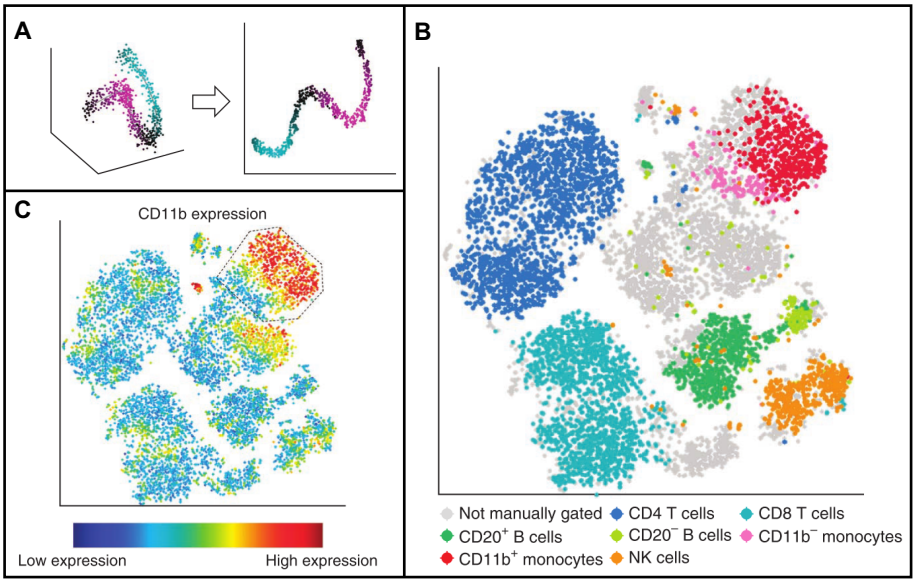

Figure 2.10. viSNE algorithm. (A) viSNE projects multi-dimensional data into two dimensions with high fidelity of spatial arrangement. This is confirmed by identification of cell subpopulations that are similar to one another by both manual gating and viSNE analysis (B, colored and gray clouds, respectively). (C) Signal intensity of cell populations is added back to viSNE maps for a given marker. Single cell resolution is retained, so that each dot in a viSNE map is representative of a single cell event. Modified and reprinted with permission from Amir.[66]

The algorithm is sensitive to small subsets of cells and takes into account pairwise comparisons between all cells included in the analysis, giving confidence to cell positioning within the viSNE map. There are some inherent limitations to this algorithm, such as the domination of the viSNE map by highly abundant or intense structures, making small features difficult to resolve without prior sub-setting, and ii) the computational demand which limits the number of cells that can be mapped. However, its single cell resolution offers powerful advantages. For instance, viSNE has been used for detection

of small subpopulations of phenotypically aberrant cells that have a “different - from - normal” phenotype (Figure 2.11).

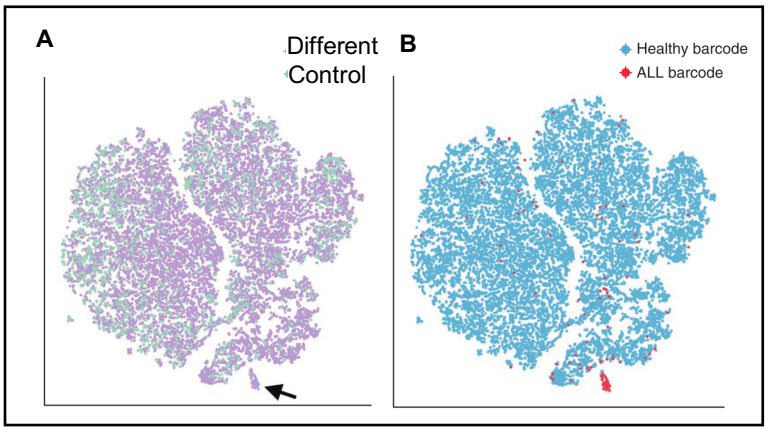

Figure 2.11. viSNE can be used to detect “different – from – normal phenotypes”. Amir and coworkers show the ability of viSNE to detect these small subpopulations of cells by creating a “synthetic” sample with barcoded cells of a specific phenotype spiked into a sample with a different phenotypic profile at a concentration of 0.25%. They blind the viSNE algorithm to the channel indicating the phenotypic group of each cell, but the algorithm is still able to correctly identify the subpopulation of spiked cells that are different vs the control (A, arrow). When the analysis is repeated to include the barcoding channel indicating the phenotype (different or control), the algorithm shows that the subpopulation indicated in A is made from the “different” sample only. Modified and reprinted with permission from Amir.[66]

Clustering (Highlighting: SPADE & X-shift)

The existence of many phenotypically distinct cell types in a biological system, despite containing identical genomes, highlights the usefulness of high-dimensional single-cell analysis. Mass cytometry lends itself to studying these heterogeneous cell populations because of its unique ability to monitor many parameters per cell across thousands of cells. Clustering algorithms work to group cells that are similar to one another making the visualization and biological analysis of the resulting data more manageable. Similar to some dimensionality reduction algorithms, the first step in most clustering algorithms is to project the single cell data into an n dimensional point cloud. Where the mechanism of these algorithms tends to diverge is in the method of identifying and clustering cells that are similar to one another. Approaches have included agglomerative and k-nearest neighbor based clustering, implemented by the SPADE (spanning-tree progression of density normalized events) and X-shift algorithms, respectively.

SPADE was the first reported algorithm used to successfully partition separate cell subtypes based on a curated set of phenotypic cell targets in mass cytometry data.[46, 67] The algorithm was designed to preserve rare cell sub-populations through density dependent down-sampling, which works to provide more equal representation of highly abundant and rare cell sub-populations. Following down-sampling cells undergo hierarchical, agglomerative clustering, an iterative process in which individual cells are merged into phenotypically similar clusters until a user-specified number of clusters has formed. Clusters are connected to their most phenotypically similar clusters via a minimum total edge length, forming a minimum spanning tree to enable an approximate 2D visualization of the point cloud geometry (Figure 2.12). Two major limitations of the original SPADE algorithm are the agglomerative clustering method, and the stochastic process of density-dependent down-sampling. The use of an agglomerative approach inherently reduces the resolution of single-cell data impeding down-stream high-resolution analysis of individual cells. The stochastic down-sampling process used to preserve rare cell sub-populations and increase computational efficiency often provides inconsistent SPADE analyses for identical datasets.

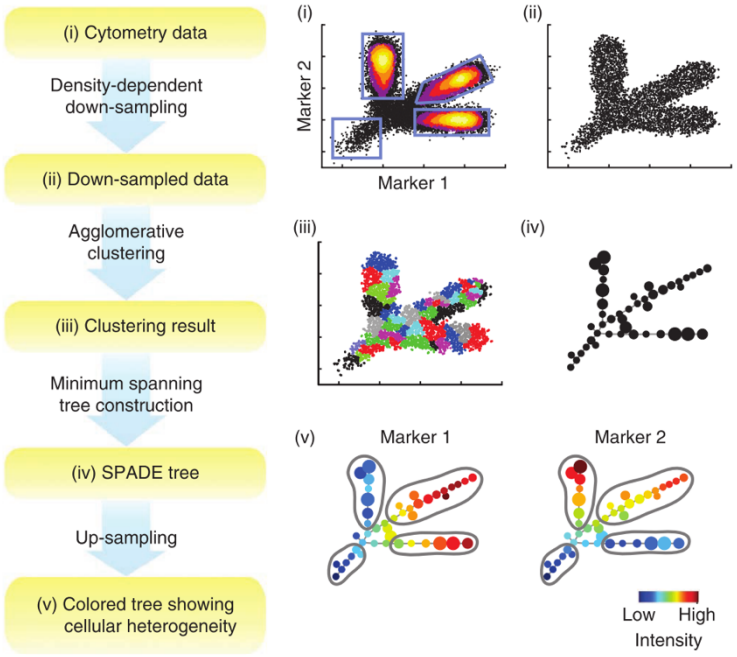

Figure 2.12. Analysis of multi-dimensional cytometry data using the SPADE algorithm. Cytometry data is visualized on a biaxial dot plot (i), and down-sampled to normalize event density (ii). Agglomerative clustering defines sub-populations of cells with similar staining across all channels (iii). These clusters are visualized in a minimum-spanning tree (iv), where each node is a single cluster whose size is representative of the number of cells included. The data is then up-sampled and colored to represent the intensity of a given marker across the entire cell population. Reprinted with permission from Qiu.[67]

Many algorithms have been developed in recent years, some of which have overcome these issues. When comparing clustering algorithm performance, researchers can use a parameter called an F-measure statistic, which can compare the ability of clustering algorithms to reproduce clusters that match expertly gated cytometry data.[68] A recently reported clustering algorithm, X-shift,[69] produced the highest F-measure statistic (16.59) when tested against a number of algorithms including SPADE (14.86) and Phenograph[70] (14.63), indicating it was capable of the most precise and accurate clustering. The X-shift algorithm clusters similar cells through searching for density maxima in k-nearest neighbor classified data, which become cluster centroids. Cells not originally captured in these clusters are assigned to existing or new clusters via an ascending or descending density estimation. Clusters are then tested for density separation, and where deemed appropriate, merged. This algorithm was demonstrated on phenotypically labeled samples of bone-marrow where X-shift was able not only phenotypically identify canonical hematopoietic cell sub-populations, but also identified previously undescribed populations that could aid in the further understanding of the hematopoietic lineage and its development.[69] While clustering algorithms have improved the preservation of rare subsets since the original report of SPADE,[67] this work will focus on the use of SNE dimensionality reduction algorithms to preserve single cell or organelle resolution.

Trajectory Progression (Highlighting: Wanderlust)

Most complex organisms have a continuum of transitional cell subsets from progenitor to mature cell populations. A number of algorithms have been designed to align single cells to an approximated trajectory describing their most likely developmental path *de novo*.[71-73] Using the ergodic hypothesis that a snapshot of a cell ensemble can inform the behavior of an individuals over time, these algorithms accurately infer a temporal relationship between cells that would otherwise be hidden in conventional multi-parametric data analysis (Figure 2.13).

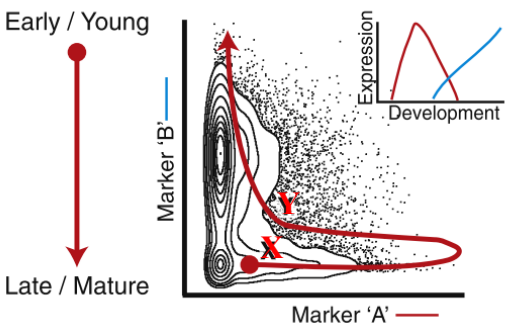

Figure 2.13. Pseudotime projection of cells to predict developmental trajectory progression. Cells of vastly different developmental stages can be close to one another in Euclidean space, masking the non-linearity in their pathway to maturity. The points X and Y in the developmental pathway are developmentally distant, but spatially close. The wanderlust algorithm has been shown to correctly identify the developmental pathway of a specific cell types that are not obvious. Reprinted from Bendall.[71]

The first implementation was called Wanderlust, which calculates a trajectory score for each cell, identifying its location across a developmental path based on distance from a user-identified "early" cell. Initially, a random set of cells are chosen as waypoint cells whose use as "intermediates" help to refine the position of neighboring cells. After waypoint cells are chosen, the data are transformed into an ensemble of randomly generated graphs, where each cell is represented as a node, and is connected to its k nearest neighbors (cells most similar to it) via edges whose weight are based on the similarity of the two cells. The goal is to minimize the path length between similar cells, so that the developmental order of cells can be determined. The two steps of this algorithm, i) initiation and ii) trajectory calculation, are performed iteratively until the location of each individual cell converge. The position of each cell in the ensemble of graphs is then averaged to provide a temporal output map (Figure 2.14).

The algorithm has been used to predict the developmental path of hematopoietic stem cells to naïve B cells. In Chapter 3, the algorithm was used to predict the expression of myogenic transcription factors during myoblast differentiation. Further iterations of this type of predictive trajectory progression algorithm have included branching over the pseudo-time axis to more closely represent trajectories expected in biological systems.[72]

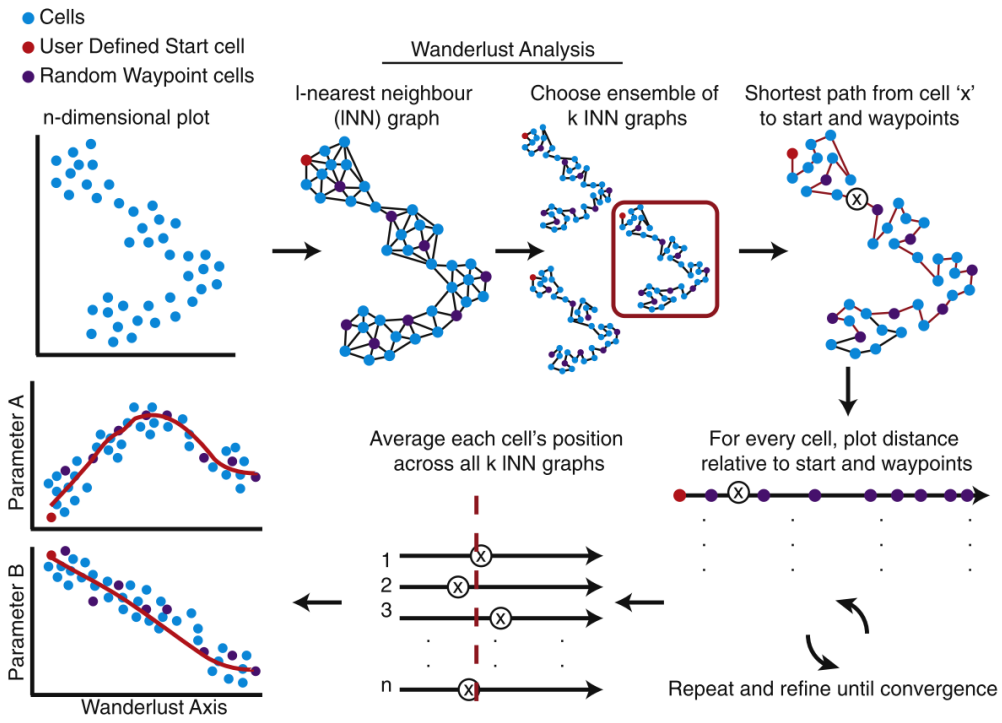

Figure 2.14. Trajectory prediction by Wanderlust. The wanderlust algorithm plots cells in n dimensional space where n is the number of user defined, phenotypic parameters. The user defines a "Start" cell, and the algorithm randomly chooses "Waypoint" cells whose positions are used as reference points when calculating the minimum distances between all cells in k-nearest neighbor graphs. An ensemble of k graphs is assembled and the shortest path from every cell to the "Start" and "Waypoint" cells is iteratively calculated for each graph. These values are averaged to give the final trajectory. Trends by parameter can be visualized on the wanderlust axis, showing increasing or decreasing expression over developmental time. Reprinted with permission from Bendall.[71]

2.3 Autophagy in skeletal muscle

The global population of individuals over 60 years is expanding in parallel with increased life expectancy and is set to double by 2050.[1-2] However, preservation of human health is not always sustained with increased life expectancy. Of the 1.5 million individuals over the at of 65 admitted to long-term care facilities each year in the United States, 33% are institutionalized solely due to their inability to perform activities of daily living.[3] Skeletal muscle provides the contractile force necessary for motion and is the largest metabolic organ in the human body. Loss of skeletal muscle mass and function, termed sarcopenia, significantly contributes to the frailty and decreased mobility of our aging population. Understanding the molecular basis for age-related decline in muscle

mass, function and regeneration is an unmet, urgent topic for translational bio-medical research to identify possible areas for intervention which might increase the healthspan of our aging population.

The cause of the observed loss of total mass and decline in function and regeneration in skeletal muscle with age is unknown, but most likely results as a combination of many disrupted cellular mechanisms, including macroautophagy.[74-77] Macroautophagy (hereafter referred to as autophagy) is normally responsible for the recycling of unnecessary or damaged proteins and organelles, such as mitochondria. In response to stress (e.g. nutritional deficiency, organellar damage) the proteins responsible for this intracellular recycling process either increase or decrease in abundance to maintain cellular homeostasis. When autophagy does not respond to these stresses, proteins and organelles within cells incur damage, but fail to be cleared, from the cytosol, resulting in cellular dysfunction and death. In general, current research points to autophagy as a critical molecular pathway for understanding the decline in mass, functionality and regenerative potential in skeletal muscle, though it is unclear whether the rate of autophagy flux is increased or decreased.[78-79] Chapters 3 and 4 describe methods for direct measurement of autophagy flux in several unique cell subsets across biological models of myogenesis and aging, respectively.

A confounding factor in the analysis of autophagy in skeletal muscle is the presence of many cell types with diverse functions[80-81] (Figure 2.15). Those which participate in muscle function, repair, and maintenance include: i) muscle fibers, ii) macrophages, iii) satellite cells, iv) fibro-adipogenic progenitors (FAPs), v) $PW1^{+}/Pax7^{-}$ interstitial cells (PICs), and vi) vessel-associated stem cells. In Chapter 4, autophagy flux is quantified in satellite cells, macrophages and FAPs as the main mononuclear cell subsets responsible for skeletal muscle regeneration.

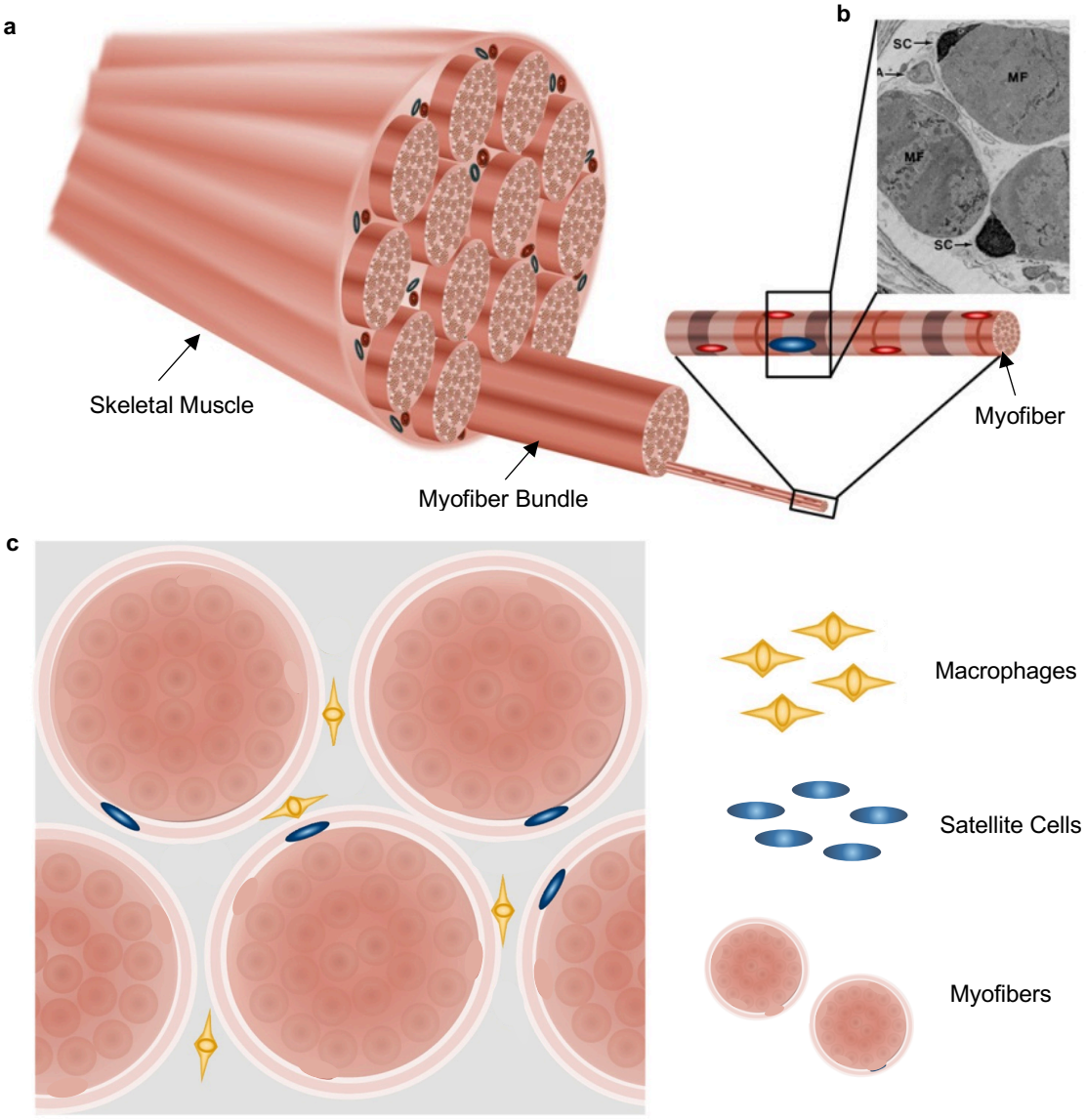

Figure 2.15. Skeletal muscle tissue is a highly heterogeneous tissue. (a) Whole skeletal muscle tissue is made up of bundles of myofibers. Myofibers are long, cylindrical multi-nucleated cells responsible for generation of contractile force. (b) Each myofiber is supported by repair and regenerative cell types such as satellite cells (SC). (c) Cross sectional view of a myofiber bundle shows the sub-sarcolemmal position of satellite cells on myofibers. Macrophages mediate the inflammatory response in muscle repair and operate between in the interstitial space.

Muscle fibers are long cylindrical multi-nucleated cells whose main function is to contract and relax, giving rise to gross motor function in mammals. Increases in intracellular recycling, without equal or greater increases in total protein synthesis in this cell type would result in a loss of individual muscle fiber mass, consistent with the observed decline of muscle mass in aged muscles. Macrophages, part of the human immune system, are required for efficient repair

of muscle tissue after injury[82] indicating that decreased functionality mediated though decreased autophagy flux may be responsible for the reduced regenerative potential of aged muscle. Injured muscle also requires a set of regenerative stem-like cells, termed satellite cells, for muscle tissue repair. These cells proliferate, differentiate and fuse to other differentiating cells, or pre-existing myofibers to restore functionality and mass after injury. Current studies have shown that the number of satellite cells is reduced in aged muscles, which may be due, in part, to decreased autophagy flux.[83] Each of these cell types may show a different degree and direction of dysfunctional autophagy, complicating analysis of bulk tissue. Because bulk tissue analyses average responses across many cells, no detail on individual cell type regulation of autophagy can be gained. Chapter 4 describes the relative autophagy flux in young and geriatric satellite cells, macrophages, and FAP cells. The analysis overcomes the hurdle of confounding results from bulk analyses and grows our knowledge of the contribution of autophagy flux from other cell types involved in skeletal muscle maintenance.

2.3.1 Function and Regulation of Autophagy

Autophagy was first observed in 1963 by Christian de Duve, who observed how cells broke down their sub-cellular contents inside a specific vacuole he called a lysosome. The original discovery of autophagy-related proteins (ATGs) that were essential for cargo delivery to hydrolytic vacuoles in yeast occurred more 30 years ago via genetic screens. Since these initial observations, the field has exploded and the fundamental importance of autophagy to living cells has been observed.

Autophagy is an intracellular degradative process that clears long-lived or damaged proteins and organelles from the cellular milieu through a set of unique sub-cellular organelles (Figure 2.16). Sequestration of cargoes marked for degradation by phagophore membranes produce mature autophagosomes. These double-walled organelles fuse with lysosomes containing hydrolyases which work to degrade autophagosome cargo in the autolysosome. Flux through this pathway is increased in times of cellular stress to break down existing, but damaged or unnecessary intracellular components resulting in the production of constituent

nucleic or amino acids. Thus, cells reduce accumulating waste and produce the building blocks necessary to respond to stress.

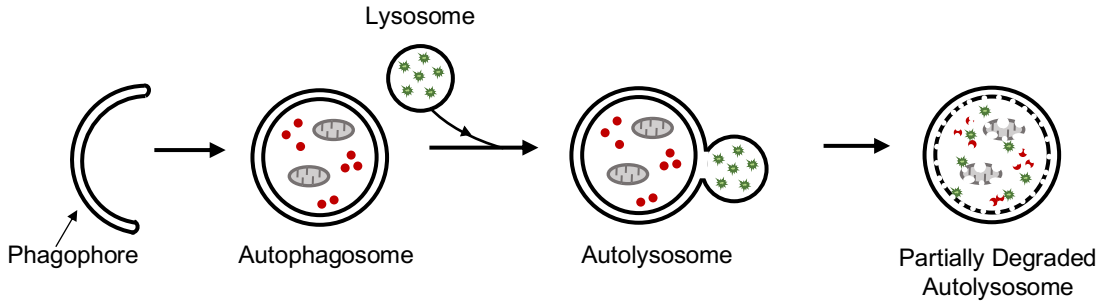

Figure 2.16. Autophagy proceeds through a unique set of sub-cellular organelles. A double-walled phagophore membrane encapsulates long-lived proteins and/or organelles. Fully-formed autophagosomes fuse with lysosomes containing hydrolases to form an autolysosome. The hydrolases present in the autolysosome degrade its contents, producing nucleic and amino acid building blocks.

The process is carried out though coordinated interaction of many ATGs as well as other proteins known to participate in cellular homeostasis. The regulation of the autophagy process can be broken down into four sequential sections: i) initiation and phagophore nucleation, ii) phagophore expansion, iii) cargo sequestration and membrane sealing, iv) autophagosome maturation and fusion with lysosomes. Because autophagy is constitutively active, these processes occur sequentially, but constantly within individual cells. Precise mechanisms driving autophagy flux can be monitored through concurrent measurement of the autophagy machinery. For example, the protein microtubule-associated protein 1A/1B-light chain 3 (LC3) is ubiquitous in mammalian cells, though it exists in two isoforms, LC3-I and LC3-II. LC3-I is a cytosolic protein that is processed by various ATGs to produce the LC3-II isoform which is conjugated to phosphotidylethanolamine (Figure 2.17). The LC3-II isoform is recruited to autophagosomal membranes in support of membrane elongation and closure. Metal-labelled antibodies specific to LC3 (cytosolic or membrane bound) are used throughout this work to monitor autophagy flux. In Chapters 3 and 4, total LC3 (including LC3-I and LC3-II is quantified in whole cells. Chapter 5 reports the detection of LC3-II bound to organelle membranes.

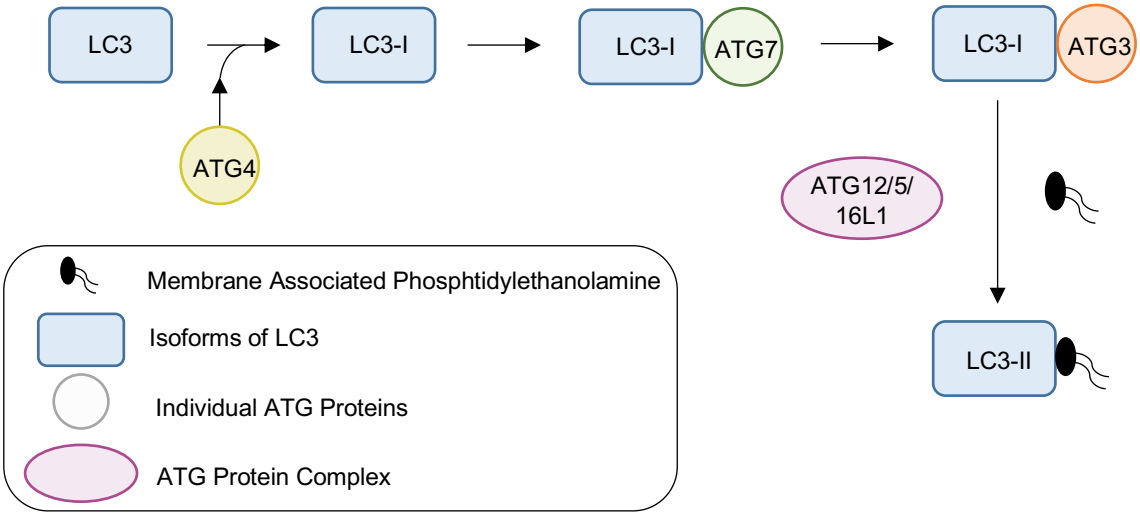

Figure 2.17. Mechanism of LC3 protein lipidation. LC3 protein is processed by ATG4 to reveal a C-terminus glycine (LC3-I). ATG7 activates LC3-I and subsequently transfers it to ATG3. The ATG12/5/16L1 complex facilitates the conjugation of LC3-I to phosphotidylethanolamine (LC3-II), which associates with the elongating phagophore.

Modulation of autophagy flux using genetic or pharmacological manipulation induces functional changes that can be monitored to determine their role in autophagy flux. Modulating the expression or function of ATGs that participate in the initial stages of autophagy block the formation of mature autophagy-related organelles. For example, genetic ablation or of ATG5 required for LC3-II lipidation results in the absence processed LC3-II and formation of mature autophagosomes (Figure 2.18). Genetic ablation of ATG7 is used in Chapter 3 to confirm accurate quantification of autophagy flux via mass cytometry in myoblasts.

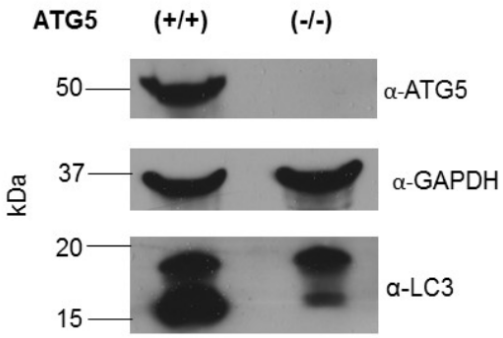

Figure 2.18. Effect of ATG5 ablation on autophagy flux. Genetic manipulation of ATGs participating in organelle formation results in a lack of mature autophagy-related organelles. Protein expression analysis of ATG5 deficient mouse embryonic fibroblasts via western blot show the absence of ATG5, and the lack of formation of LC3-II isoform indicating a lack of mature autophagy-related organelles. Reprinted with permission from Muratore.[30]

Conversely, modulation of expression or function of ATGs that participate later in the autophagy process block the degradation of formed autophagy-related organelles. For example, the treatment of cells with bafilomycin A1 a V-ATPase inhibitor modulates lysosomal pH to prevent degradation of mature autophagy-related organelles (Figure 2.19).

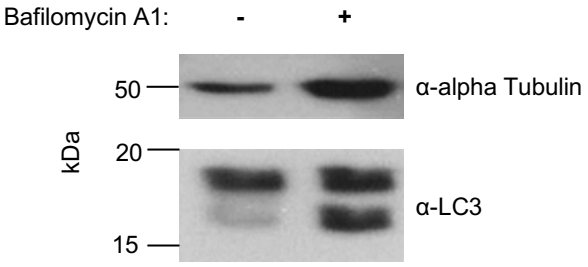

Figure 2.19. Effect of V-ATPase inhibitor bafilomycin A1 on degradation of autophagy-related organelles. Late stage inhibition of autophagy-related organelles results in the accumulation of LC3-II, and overall accumulation of total LC3. Primary fibroblasts from rat were treated with 200 μM Bafilomycin A1 in culture for 4 hrs. prior to harvest and western blot analysis. Modified and used with permission from Kogot-Levin.[84]

Autophagy is often described as a general lysosomal degradative pathway however, it can also show incredible specificity. While general autophagy flux is increased during cellular stress such as nutrient deprivation, selective autophagy often functions in cell maintenance and homeostasis.[85] An example of selective autophagy is the degradation of mitochondria (i.e. mitophagy) which proceeds via specific signalling mediated by PINK1 and ubiquitin[86] (Figure 2.20). Mitochondria play an essential role in energy production in cells through oxidative phosphorylation (OXPHOS). A by-product of aberrant OXPHOS are reactive oxygen species (ROS), which can cause intracellular damage; thus, mitochondrial fidelity is critically important to cellular function. If damage due to ROS accumulate, mitophagy flux will increase to degrade the damaged organelles. In Chapter 3, the method described for the relative quantification of autophagy flux can also quantify detection selective autophagy flux, including mitophagy.

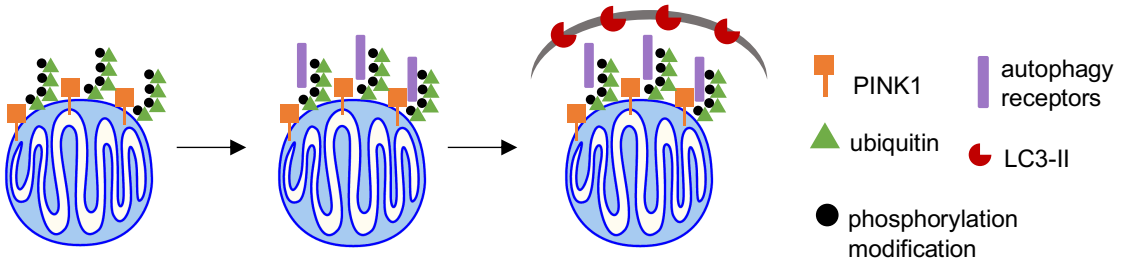

Figure 2.20. Selective degradation of mitochondria via mitophagy. Selective degradation of mitochondria proceeds by the formation and phosphorylation of chains of ubiquitin at the outer mitochondrial membrane by PINK1. Phosphorylated ubiquitin chains recruit and bind autophagy receptors, which in turn recruit LC3-II decorated phagophore membranes.

2.3.2 Function of autophagy in myogenesis and muscle homeostasis

Skeletal muscle has a remarkable regenerative capacity mediated by the presence of muscle stem cells, termed satellite cells. These tissue-resident stem cells remain mitotically and metabolically quiescent until the need for muscle repair or remodelling arises. In response to myofiber damage, quiescent satellite cells are activated and re-enter the cell cycle. They undergo asymmetrical division to produce progeny capable of differentiation and fusion, as well as an uncommitted stem cell population to serve as a reserve population for future proliferation.[87] Myoblasts produced through satellite cell proliferation activate a differentiation program which allows them to fuse with each other or existing myofibers.[88]

Recent studies have shown that autophagy is a critical process in myogenesis, participating in both satellite cell proliferation[83] and myoblast differentiation and fusion.[89] Garcia-Prat and co-workers show that satellite cells from geriatric mice (>28 mo.) enter a non-proliferative senescent state, which results in fewer and non-functional satellite cells. Importantly, geriatric satellite cells display reduced autophagic flux compared to young (<3 mo.) control cells, indicating a decline in the cytoprotective effect of autophagy as a constitutively active “clean-up” process. Thus, autophagy is a necessary process for maintaining satellite cell stemness through the prevention of a senescent cell state.

Proliferating satellite cells produce myoblasts capable of differentiation and fusion to repair myofibers (Figure 2.21). Differentiating myoblasts require active autophagy for successful formation of myofibers. Sin and co-workers show that the progression from differentiating myoblast to myofiber induces a metabolic shift

from primarily glycolytic state to reliance on OXPHOS for the production of adenosine triphosphate, to support the increased energetic demand of myofibers. A highly developed network of mitochondria is required for OXPHOS, resulting in increased rates of mitochondrial degradation via mitophagy and biogenesis during differentiation. Autophagy is required for this dramatic intracellular remodelling.

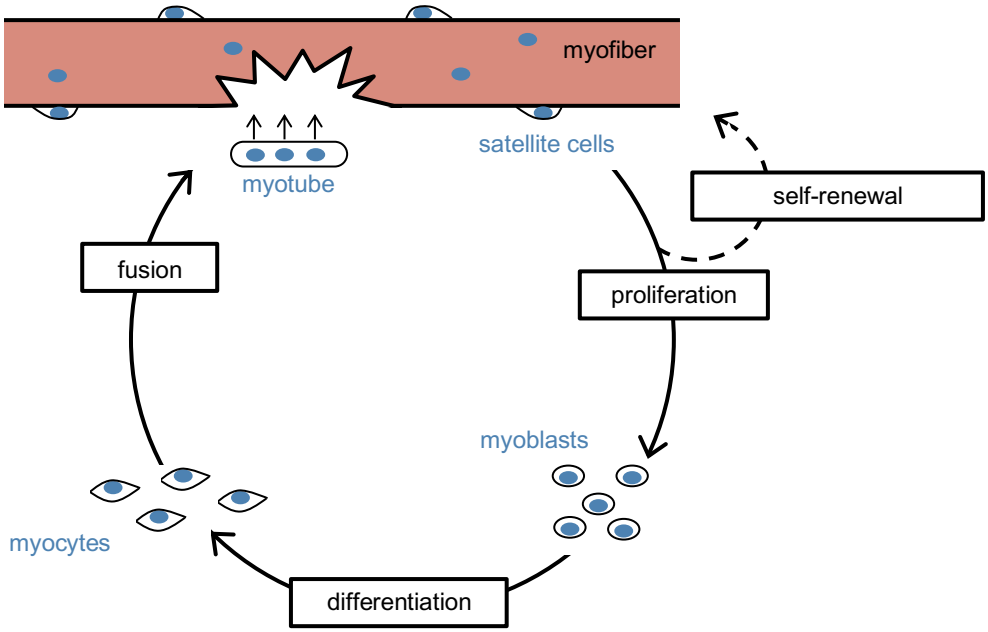

Figure 2.21. Process of myogenesis. After an insult to muscle tissue satellite cells are activated and proliferate asymmetrically to form myoblasts and repopulate the satellite cell niche. Myoblasts undergo differentiation to form myocytes capable of fusion to form myotubes. Myotubes fuse to myofibers to repair damage. Modified and adapted from Pichavant.[90]

As in myogenesis, autophagy is required for maintenance of mature myofibers. Abnormal organelles can be observed in age-related atrophy in skeletal muscle, and muscle fibers harbouring these organelles display sectional atrophy, splitting, and increased levels of oxidative damage.[91-92] In agreement with these observations in aged skeletal muscle, Masiero and coworkers show that autophagy-related gene 7 (ATG7) knockout specifically in skeletal muscle of adult mice results in muscle atrophy, loss of force production, and morphological hallmarks of myopathies. Interestingly, the muscle-specific suppression of autophagy exacerbates muscle loss due to denervation and fasting.[74] A similar

phenotype has been reported with muscle-specific knock-out of ATG5, with a significant reduction of muscle mass, and accumulation of excessive protein.[93]

Similarly, recent studies have shown that the skeletal muscle resident immune compartment contributes to the maintenance of skeletal muscle mass and function. Macrophages maintain stem cell populations in numerous tissues including skin and bone marrow,[94-97] and have been shown to give stem cells "license" to execute their differentiation program.[98] Conversely, hyperactivity of this compartment has been observed with age.[99] The term "Inflamm-ageing" was coined to describe the systemic, chronic inflammation[100] characterized by this imbalance between pro- and anti-inflammatory immune function. Dysfunctional autophagy, resulting in the accumulation of damaged proteins and organelles is thought to be a main driver of the shift towards a pro-inflammatory state with age.[101-102]

Taken together these studies illustrate the complex and tightly regulated flux of autophagy during myogenesis and skeletal muscle maintenance. While informative, these reports lack the single-cell resolution or multiplexed analysis necessary to unravel the mechanism driving autophagy flux dysregulation, and its contribution to decreased myogenesis. Chapters 3 and 4 of this work describe methods for the single cell or organelle analysis of autophagy flux in myogenesis and aging, increasing our fundamental understanding of dysregulated autophagy in these biological processes.

Chapter 3

Single-Cell Analysis of Autophagy during Myogenesis in Murine Myoblasts via Mass Cytometry

All data collection and analyses were done by H.M.G. Brown. Michelle Kuhns advised on experimental design and method development.

Skeletal muscle is able to regenerate after insult, a property conferred by tissue resident stem-like satellite cells. Satellite cells are activated, proliferate, and differentiate to maintain skeletal muscle. Dysfunctional autophagy has been implicated in the muscle number and functional declines observed in satellite cells with age, though the mechanism by which this occurs has not been investigated. Due to the phenotypic diversity of myoblasts during myogenesis, and the complex regulation of autophagy function, a multi-dimensional, individual cell analysis of autophagy flux during myogenesis is required. Here we describe the first individual cell analysis of autophagy in differentiating myoblasts using mass cytometry. Myoblasts were phenotypically identified by their position in the myogenic lineage, followed by the quantification of autophagic flux in each identified subset. We found that autophagy is upregulated specifically during myoblast fusion and declines in myotubes. However, the specific degradation of mitochondria via mitophagy is upregulated much earlier in the myogenic lineage and is maintained though myotube formation. This observation is in line with the changing energetic needs of myoblasts as they shift from a glycolysis to oxidative phosphorylation. We report the development of a novel method for the multiplexed analysis of differentiating myoblasts used to probe the timing and expression of autophagy-related targets throughout the myogenic lineage. This work expands the current understanding of autophagy regulation in regenerating skeletal muscle.

3.1 Introduction

Skeletal muscle is a highly heterogeneous tissue with a remarkable capacity for regeneration. This ability for self-renewal is conferred by myoblast progenitors termed satellite cells which follow a trajectory of activation and proliferation to expand the myoblast compartment. After expansion, myoblasts begin a myogenic differentiation program in which they fuse to other differentiating myoblasts or pre-existing myotubes. This process proceeds in a highly heterogeneous manner, where not all myoblasts will express the transcription factors necessary to commit to myogenic differentiation[103-104] providing a set of ‘reserve cells’ capable of differentiation. Dysfunctional autophagy has been implicated in the numerical

decline in satellite cell populations,[83] though the mechanism for decreased autophagy flux in aged satellite cells is unclear.

Autophagy is a constitutively active biological process whose flux can be increased in times of changing cellular needs. For example, autophagic flux has been shown to be increased during cellular remodelling,[105-106] such as is observed in the myogenic differentiation program.[83, 107-108] Importantly, these reports do not specify the stage of myoblast differentiation in which autophagy flux is increased. We hypothesize that the reported changes in autophagy flux occur at a specific point in the myogenic lineage, in response to changing metabolic needs and intracellular remodelling. Due to the phenotypic diversity of myoblasts during myogenesis, and the complex regulation of autophagy function, a multi-dimensional, individual cell analysis of autophagy flux during myogenesis is required.

Mass cytometry is an emerging technique for multi-dimensional individual cell analysis using a single-particle inductively-coupled plasma mass spectrometer (ICP-MS).[43] This technique detects and quantifies upwards of 45 separate cellular targets on the surface or within individual cells, expanding the multi-dimensional capabilities of individual cell analysis beyond what is currently possible with comparable techniques such as flow cytometry. Mass cytometry was recently used to further illuminate phenotypically unique satellite cell transition states in muscle regeneration.[109] In this work we will focus on differentiating myoblasts, a later time point in the myogenic lineage. Differentiating myoblasts were phenotyped based on their expression of canonical myogenic markers such as MyoD, myogenin (MyoG), and myosin heavy-chain (MHC).[88] These myogenic markers and other autophagy-related targets will be indirectly detected via antibodies covalently labelled with a polymer chelating isotopically pure lanthanide ions. Unique lanthanide isotopes are assigned to each antibody and are detected in individual cells at a specific m/z ratio in a time-of-flight mass spectrometer after ionization in the ICP.

The use of antibodies for detection of specific cellular targets has been widely applied in spite of the known pitfalls of promiscuous off-target binding and lot-to-lot variability, sometimes producing questionable published research findings.[110] In individual cell analysis via immuno-labeling, as has been used to profile phenotypic variation of immune and myoblast progenitor cells,[46, 109] the wide variety of distinct cell types present in a single sample provides inherent negative controls for estimations of non-specific antibody binding, negating the need for a genetically manipulated negative control animal or cell line. The individual cell analysis of autophagy is unique in that there are no known, genetically unaltered mammalian cell types that do not express autophagy-related proteins. Thus, the current limitation to quantifying autophagic activity using individual cell immuno-labelling techniques, such as mass cytometry, lies in the need to create genetically modified knock-out biological models to estimate off-target antibody binding for each antibody used. Creating and characterizing genetic knock-out systems for the upwards of 45 cellular targets that can be measured using mass cytometry, exponentially increases the difficulty, time and resources of the investigation. To overcome the need for creating an excessive number of genetically knocked-out biological models to assess non-specific antibody interactions, we developed a signal correction and normalization method that reveals accurate antibody binding using isotype and total antibody loading controls. Specifically, off-target antibody binding is estimated by isotype control antibodies which lack a specific cellular target. Variation in cell size and permeability is assessed by quantifying a highly abundant and constitutively expressed protein such as glyceraldehyde 3-phosphate dehydrogenase (GAPDH).

First, we validated the use of the correction and normalization method by titrating the autophagy-related antibodies in both genetically knocked out and pharmacologically reduced models of autophagy flux in myoblasts to identify antibody exposure concentrations producing accurate measurements of autophagy flux. Then, we identified phenotypically unique cell subsets across the myogenic lineage via a predicted development trajectory using Wanderlust.[71] We

then quantified autophagy flux across the myogenic lineage and found it to be upregulated specifically during myoblast fusion, while mitophagy flux increases much earlier and persists through myotube formation.

3.2 Materials and Methods

3.2.1 Materials, Reagents, Buffers, and Solutions.

Phosphate buffered saline (10x, 0.2 M KH_2PO4, 1.5 M NaCl, pH 7.2) was obtained from Rockland Immunochemicals (Limerick, PA). Methanol, Triton X-100, sucrose, Tris(hydroxymethyl)aminomethane hydrochloride (Tris-HCl), Bovine serum albumin (BSA), bafilomycin A1, rapamycin, sodium azide (NaN_3), nitric acid, and hydrochloric acid and dimethyl sulfoxide (DMSO) was obtained from Sigma Aldrich (St. Louis, MO). Fetal bovine serum (FBS), horse serum (HS), Dulbecco's Modified Eagle Medium (DMEM), Penicillin-Streptomycin (10,000 U/mL), trypsin-EDTA (5% v/v), Prolong anti-fade mountant with DAPI, and AlexaFluor 594-Phalloidin were obtained from Thermo Fischer Scientific (Waltham, MA). Maxpar X8 Multimetal Labeling Kit, Maxpar Fix & Perm Buffer, Nuclear Antigen Staining Buffer Set, Cell-ID Intercalator, cell-ID cisplatin, and 10× EQ Four Element Calibration Beads were obtained from Fluidigm (San Francisco, CA). Tween-20 and Tris-buffered saline (TBS) were obtained from Bio-Rad (Hercules, CA). Water was purified with a Millipore Synergy UV system (18.2mΩ/cm, Bedford, MA). Phosphate-buffered saline (PBS) was diluted 1:10 in purified water. Cell staining buffer consisted of 1x PBS, 2% (w/v) BSA, and 0.02% NaN_3.

3.2.2 Antibody panel design and characterization.

Specific antibodies were chosen after a preliminary screen using fluorescence microscopy and western blots to assess specificity and signal strength against an appropriate isotype control antibody. Where required, carrier protein was removed from purchased antibody formulations using buffer exchange and IgG purification kits (Thermo Scientific, Waltham, MA). Where suitable specific antibodies were not available, a hybridoma cell line (MHC; clone BF35) developed by Lucas and Schiaffino, were obtained from the Developmental Studies Hybridoma bank, created by the NICHD of the NIH and maintained at The

University of Iowa, Department of Biology, Iowa City, IA 52242. Hybridomas were sub-cultured at The University of Minnesota – Twin Cities, and sent to ProMab Biotechnologies (Richmond, CA) for large-scale antibody production and purification.

Selected antibodies were metal-labeled using the Maxpar metal-labeling kit (Fluidigm, San Francisco, CA), per manufacturer instructions. Protein concentrations after metal-loaded polymer conjugation was calculated from measured A_{280} values (Jasco, Oklahoma City, OK). The average number of lanthanide atoms per antibody was calculated by quantifying the number of lanthanide ions and antibody molecules per unit volume. The number of lanthanide ions were quantified by comparison to a standard solution of lanthanide ions of known concentration. Briefly, metal-labeled antibodies were diluted 1:1,000 from their stock concentrations into 2% HCl, followed by two subsequent 1:1,000 dilutions into 2% HNO_3 for a total dilution factor of 1:10,000. Lanthanide standard solutions were prepared in 2% HNO_3 to a final concentration of 50pM. Solutions were sequentially flowed into the CyTOF2 mass cytometer and data was acquired for all metal channels simultaneously in “solution mode” using the following parameters: step value = 1, settling time = 20 s, pushes / reading = 76,800. The steady signal resulting from the lanthanide standard was used to calculate the lanthanide atom concentration in the diluted antibody sample (see Appendix A, Table A1).

3.2.3 Cell Culture Conditions

C2C12 and L6 myoblasts (ATCC, Manassas, VA) were maintained at 37°C, 5% CO_2 in DMEM supplemented with 10% FBS containing 1000 units penicillin, and 10 µg/mL streptomycin. Cells were propagated at a ratio of approximately 1:30 (v/v) every 48-72 hours, using 0.5% trypsin-EDTA in PBS. Differentiation of C2C12 myoblasts took place over 120 hours in DMEM supplemented with 2% HS containing 1000 units penicillin, and 10 µg/mL streptomycin The ATG7 KO L6 myoblasts were produced using CRISPR/Cas9 technology by the Genome Engineering Shared Resource at The University of Minnesota (Minneapolis, MN).

3.2.4 Western Blot

Cells were harvested into 250 mM sucrose, 10mM Tris-HCl buffer containing protease inhibitors (Pierce, Waltham, MA). Cells were lysed via sonication and total protein quantification of whole cell lysates was measured using a detergent compatible version of the Lowry assay (Bio-Rad, Hercules, CA). Whole cell lysates were separated via SDS-PAGE. Proteins were transferred to nitrocellulose (0.45 μm) or PVDF (0.2 μm) membranes. Membranes were blocked in a solution of 4% milk in tris-buffered saline containing 0.1% Tween-20 (TBS/T). Membranes were probed overnight with anti-LC3, anti-GAPDH, anti-p62, and anti-ATG7 antibodies in 4% milk solutions in TBS/T. Membranes were subsequently probed with an anti-rabbit HRP conjugated secondary antibody in TBS/T. All washes between antibody and substrate incubations were done in TBS/T. Completed blots were visualized on an X-ray film using chemiluminescent substrate. Films were digitized using a scanner.

3.2.5 Fluorescence Microscopy

C2C12 cells were differentiated in 4-well Lab-Tek chamber slides. At each differentiation time point (0, 24, 48, 72, 96, 120 hrs.) cells were stained with AlexaFluor 594 Phalloidin per manufacturer protocol to visualize actin. Briefly, cells were fixed in 3.7% MeOH-free formaldehyde for 10 min. at room temperature. Following fixation, cells were permeabilized with 0.1% Triton X-100 in PBS for 5 minutes. Each chamber was washed twice with PBS and incubated in 165 nM AlexaFluor 594 Phalloidin in 1% BSA in PBS for 20 minutes at room temperature. Cells were washed twice with PBS, followed by preservation in ProLong Gold Antifade Mountant with DAPI to stain nucleic acids.

Images were acquired on an Olympus IX81 inverted microscope equipped with a Hamamatsu C-9100 EM-CCD camera and operated using HCImage.

3.2.6 Mass Cytometry Sample Preparation and Data Acquisition

Two days prior to harvest, cells were expanded into four 75 cm flasks per condition (WT, KO, drug-treatment). At the time of harvest, cells from all four flasks of a given condition were collected into a single tube and counted. These large cell

samples were stained with Cell-ID cisplatin (5 μM) and quenched using cell staining buffer. Cells were aliquoted to ~600,000 cells / sample, fixed, and permeabilized. Permeabilized cells were incubated in serially diluted cocktails of antibodies described in Table A1, washed using cell staining buffer, and incubated at 4°C overnight in Cell-ID Intercalator-Ir (diluted to 62.5nM final concentration in Maxpar Fix & Perm buffer). Prior to analysis on the CyTOF2 mass cytometer (Fluidigm, San Francisco, CA), cells were washed with cell staining buffer and purified H_2O (18.2 MΩ, Millipore, Bedford, MA). Data was acquired using the following instrument parameters: noise reduction, cell length = 10-150, lower convolution threshold = 0.2. Samples were then diluted to 5×10^5 in a solution of 1× EQ Four Element Calibration Beads in ultrapure water to attain an event detection rate of approximately 150-200 events / second.

3.2.7 Data Analysis

After acquisition data were normalized via instrument software (Helios software, version 6.7) and EQ normalization beads. Using equation 3.1 the number of unique ions associated with each event (# $ions_{Ab}$) was calculated using the equation below, where DC_{Ab} represents the dual count signal of a single antibody chelating a unique metal isotope *m* from an individual organelle and the TE_m is the empirically determined transmission efficiency of *m*. This was done on an individual cell basis for all isotopes monitored.

$$\#\ ions_{Ab} = \frac{DC_{Ab}}{TE_m} \qquad \text{Equation 3.1}$$

Following quantification of each unique isotope per cell, we calculated the number of all antibodies represented per cell using equation 3.2, where correction factor represents the average number of metal ions chelated by a single antibody protein.

$$\#\ Ab\ per\ cell = \frac{\#\ ions_{Ab}}{correction\ factor} \qquad \text{Equation 3.2}$$

These calculations allow for the quantitative comparison of the number of each type of antibody in an individual event. Using these calculated values, the

correction for non-specific binding and total antibody loading was performed using the equation below.

$$\text{corrected and normalized \# Ab per cell} = \frac{\text{\# specific Ab - \# isotype Ab}}{\text{\# GAPDH Ab - \# rabbit isotype Ab}} \qquad \text{Equation 3.3}$$

After calculation of the corrected and normalized # antibodies per cell, data were subjected to a quality control check where cells containing equal or larger numbers of isotype than specific antibodies were removed from subsequent analyses (see Appendix A, Figure A1 and Table A2). This was done for all specific antibodies, including GAPDH.

Mass cytometry data processing, plots, and histograms were made using software available at www.dvssciences.com, www.cytobank.org, www.flowjo.com, and custom R scripts. Densitometric analyses of western blot images were performed using ImageJ 2.0.0–rc-43/.1.51j (rsb.info.nih.gov/ij/). Background subtraction and scaling of epifluorescence microscopy images was done using HCImage.

3.3 Results and Discussion

3.3.1 Non-specific Antibody Binding is Quantified Through Correction and Normalization

We hypothesized that accurate signal arising from specific antibody binding can be calculated by correcting for promiscuous antibody-cell interactions and normalizing variation in per cell total antibody loading. This was accomplished through individual cell measurements of a host- and type-matched isotype control antibody and a housekeeping protein antibody, such as the commonly used GAPDH protein, followed by a mathematical correction and normalization to these two parameters in individual cells. This required a quantitative comparison between individual signals in a single cell event. Importantly, it has been established that lanthanide ion transmission efficiency varies across the relevant mass range of the CyTOF2 leading to unequal detection sensitivities.[45] As discussed in Chapter 2, the pattern of transmission efficiency is unique to each CyTOF instrument (Figure 2.3), thus to facilitate the direct comparison between individual isotope signal in a single cell event the empirical characterization and

subsequent correction of isotope transmission efficiency in individual cell data is required (see Equation 3.1).

To test our correction and normalization method, we assembled and characterized a panel of antibodies relevant to autophagy (see Appendix A, Table A1) including the relevant isotype and GAPDH antibody controls. This information, in conjunction with isotope transmission efficiency characteristics allow for the calculation and comparison of the number of antibodies bound per cell. We titrated the panel of antibodies in an autophagy-related protein 7 (ATG7) knock-out L6 rat myoblast cell line. ATG7 is an essential autophagy-related gene responsible for autophagy-organelle membrane formation. Elimination of this gene results in the accumulation of cytosolic LC3 (LC3-I) rather than the membrane bound isoform (LC3-II) as shown in Figure 3.1.

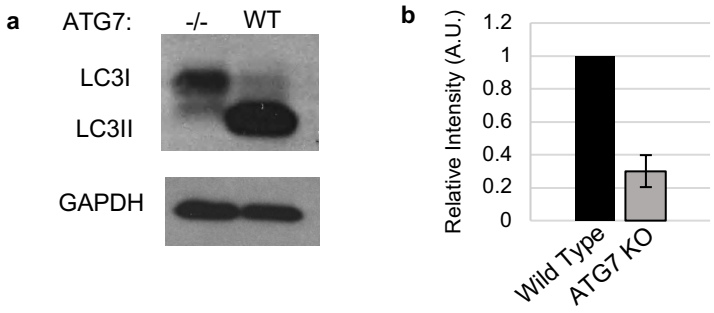

Figure 3.1 Representative western blot for ATG7 KO L6 myoblasts. (a) ATG7 KO prevents the lipidation of LC3-I to form LC3-II. (b) Densiometric analysis of the western blot in (a), showing a 70% reduction of total LC3 content in the ATG7 KO vs wild type. Error bar represents one standard deviation of two biological replicates. See Appendix A, Figure A2 for western blot analysis of p62 and Atg7 in this cell line.

Titrations are useful to identify antibody probe staining concentrations that maximize signal resulting from specific epitope-paratope interactions and minimize signal resulting from non-specific interactions. Incorrect antibody probe incubation can significantly influence antigen quantification and confound biological interpretation. To visualize the resulting titration data, the matrices of measured single cell data were processed to calculate the number of antibodies bound to each cell using equations (3.1) and (3.2) (see Appendix A, Figure A3 for

representative histogram visualizations of each autophagy marker before and after correction and normalization).

As expected for an accurate antibody titration, as antibody incubation concentration increases the corrected and normalized number of anti-LC3 antibodies bound per cell increases. As shown in Figure 3.2a, the median number of antibodies per cell begins to plateau at 2 µg/mL antibody concentration. The plateau starting at 2 µg/mL antibody staining concentration in the corrected and normalized titration curve (Figure 3.2a) indicates that antibody staining concentrations in excess of this value will show an increase in signal mainly due to non-specific or excessive antibody loading.

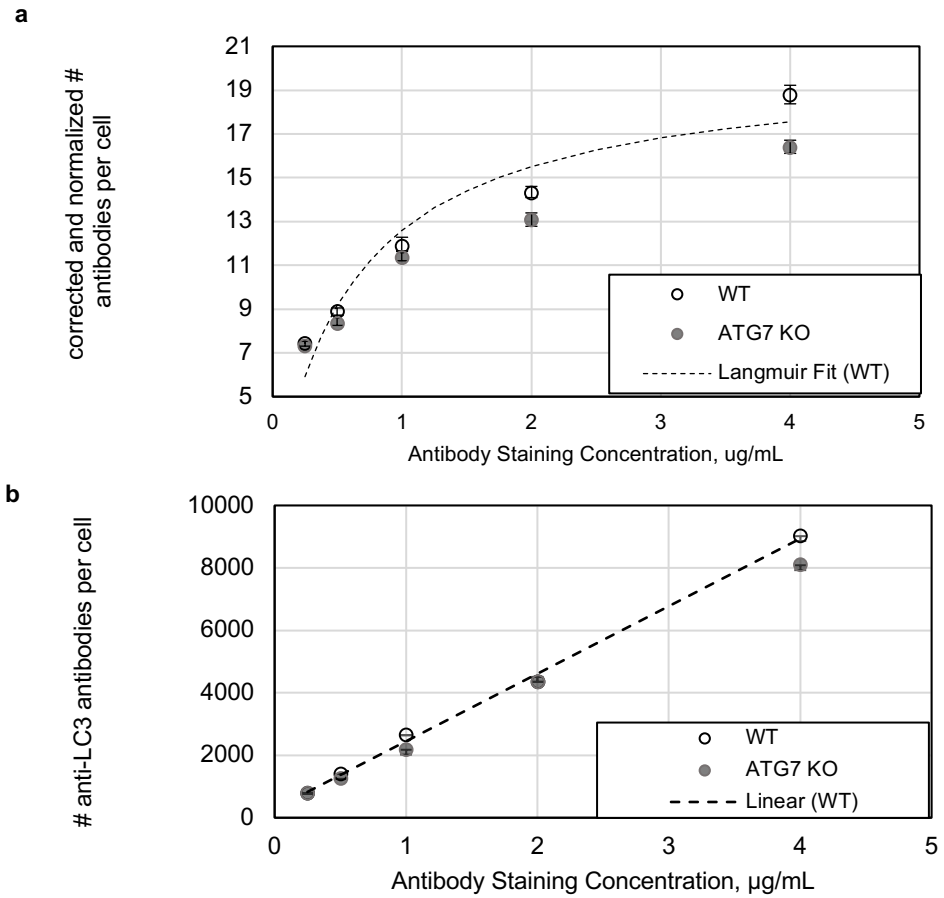

Figure 3.2. Correction and normalization of specific antibody probe signal reveals expected trend for affinity reagent titration. (a) corrected and normalized titration curve for total detected LC3. The corrected and normalized data can be fitted using a Langmuir isotherm of mono-layer adsorption (Ag_o = 20.20 (µg/mL),

K = 1.66 (mL/µg), $K_d = 4.01\times10^{-9}$ M^{-1}, p = 0.0457), using equation 3.4. See Appendix A, Figure A4 for corrected and normalized titration curves of other autophagy-related targets. (b) unaltered titration curves show a linear trend of increasing signal with antibody staining concentration. The goodness of the linear fit (x variable = 2163.1, y-intercept = 285.01, R^2 = 0.997), indicates the influence of non-specific antibody probe binding on the number of antibodies bound per cell. Error bars represent a 95% confidence interval about the population median.

The corrected and normalized titration plots can be fitted to a Langmuir isotherm for mono-layer adsorption using equation 3.4.[111]

$$[B] = \frac{K[Ag_o][Ab]}{(1 + K \times [Ab])} \qquad \text{Equation 3.4}$$

In equation 3.4, [B] is total concentration of bound antibody probe (µg/mL), *K* represents the equilibrium association constant assuming a single-step homogenous binding regime (mL/µg), [112] is the concentration of free antibody (µg/mL), and $[Ag_o]$ represents the number of binding sites (µg/mL). The dashed line in Figure 3.2a, shows the fitted Langmuir isotherm for the corrected and normalized WT titration curve indicating that it is an acceptable estimate of true antibody binding (Ag_o = 20.20 (µg/mL), K = 1.66 (mL/µg), $K_d = 4.01\times10^{-9}$ M^{-1}, p = 0.0457).

The same data without correction and normalization show a linear trend in signal intensity with increasing antibody staining concentration (Fig. 3.2b, see Appendix A, Figure A5 for unaltered titration curves of other autophagy-related targets). Taken together, these data suggest the correction and normalization protocol works to quantify non-specific antibody labeling in individual cells.

3.3.2 Small Changes in Autophagy Flux can be Measured after Data Normalization

Functionally ablated cell lines are useful for mechanistic understandings of cellular function, but do not always mirror the potential for gradual decline in function of *in vivo* systems. To assess the sensitivity of the correction and normalization method, we titrated the developed autophagy-related antibody probe panel in a C2C12 mouse myoblast cell line which had been treated with pharmacological agents to both induce autophagic flux and halt autophagic

organelle degradation. Cells were treated with rapamycin (100 nM, 3 h), to inhibit the kinase-activity of mTORC1, which in turn increases autophagic activity. One hour later, cells were treated with bafilomycin A1 (100 nM, 2 h), to halt degradation of autolysosomes through the inactivation of lysosomal hydrolases. This pharmacological treatment induced a small but consistent accumulation of total LC3, of about 1.3 times that of the control (Figure 3.3). This same pharmacological treatment was used to prepare C2C12 cells for mass cytometry analysis, where treated and control cells were used to titrate antibodies against all autophagy-related targets of interest.

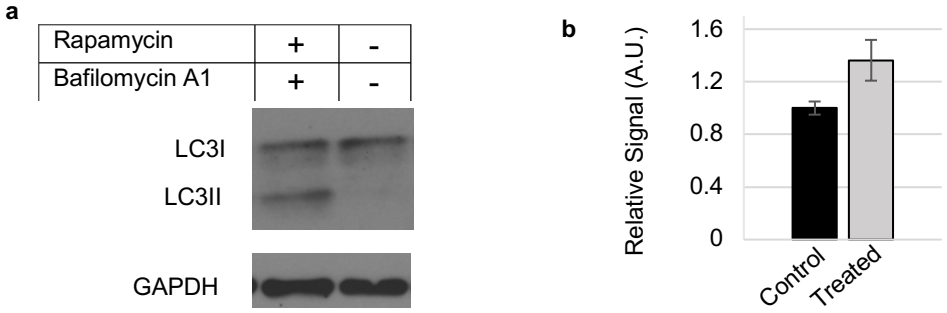

Figure 3.3. Induction of small changes in autophagy flux using rapamycin and bafilomycin A1. (a) representative western blot showing magnitude of change in autophagy in C2C12 myoblasts treated with rapamycin and bafilomycin A1. (b) densitometric analysis of biological triplicates shown in A. Error bars represent standard deviation of three independent measurements.

The resulting matrices of single-cell data were corrected and normalized using the method described above (Equations 3.1-3). The resulting titration curve for the anti-LC3 antibody probe shows both pharmacologically treated and control titration curves behave as expected with a sharp rise in signal with increasing antibody probe incubation conditions. A distinct plateau is observed at 2 µg/mL antibody staining concentration for the control series indicating the optimal antibody staining concentration for this condition (Figure 3.4a, see Appendix A, Figure A6 for corrected and normalized titration curves of other autophagy-related targets). No distinct plateau is observed for the treated cells though the rate of increase slows between the 2 and 4 ug/mL interval relative to the 1 to 2 ug/mL interval. Remarkably, the relative increase in total LC3 content found via western blot (1.3 ± 0.1, Figure 3.3) between treated and control samples is recapitulated in

at the 2 µg/mL antibody staining concentration in the mass cytometry titration (1.25 ± 0.01, Figure 3.4a, dash box). Interestingly, a similar ratio for treated versus control cells is observed in the non-corrected and normalized mass cytometry data (1.20 ± 0.01, Figure 3.4b, solid box). This shows the ability of this method to remove signal attributable to non-specific antibody interactions and total antibody loading while preserving biologically relevant data allowing users to choose accurate antibody incubation concentrations for all future analyses. Taken together, these data show that the normalization and correction method maintain biologically relevant information while eliminating signal from non-specific antibody probe binding. We also assessed the robustness of the correction and normalization method using different isotype antibody clones and sample preparations and observed comparable results (see Appendix A, Figures A8-9).

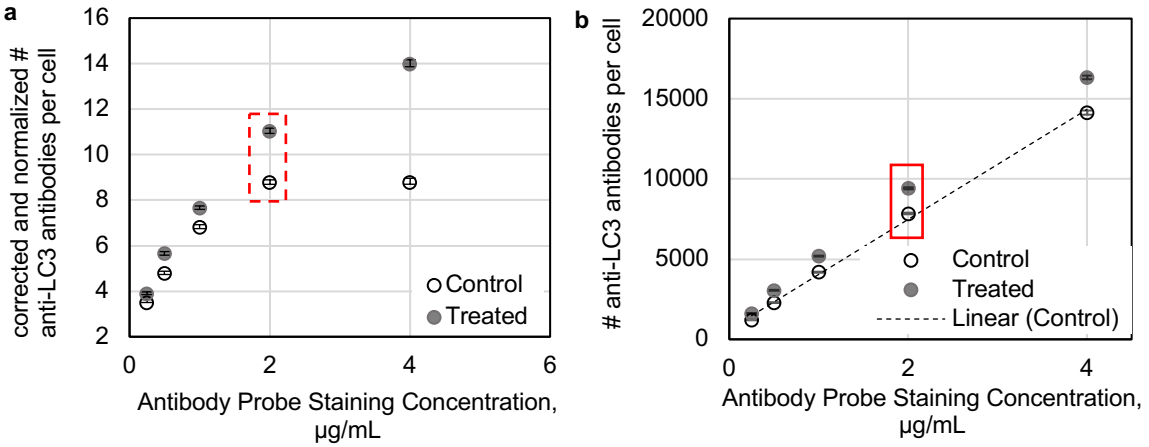

Figure 3.4. The correction and normalization is sensitive to small changes in protein abundance. (a) corrected and normalized titration curve for total LC3. In the control series, the median # of anti-LC3 antibodies per cell rise rapidly, then plateau at 2 µg/mL indicating the appropriate antibody staining concentration for future experiments. (b) unaltered titration curve for total LC3 content, showing a linear trend (R^2 = 0.996). See Appendix A, Figure A7 for unaltered titration curves of other autophagy-related targets. Error bars are 95% confidence interval of the population median.

3.3.3 Progression of Myoblast Differentiation Induces Autophagic Flux

Myogenesis is a heterogeneous biological process in which myoblasts differentiate and fuse to other differentiating myoblasts or pre-existing myofibers. This process is driven by the timed expression of four myogenic regulatory factors: MyoD, Myf-5, MyoG, and MRF4. Because these regulatory factors control temporally distinct aspects of the myogenic lineage, functionally distinct

populations of differentiating myoblasts can be phenotypically identified through the expression of these myogenic regulatory factors.[113] MyoD is a transcription factor known to regulate contractile protein synthesis and mitochondrial biogenesis.[114] Expression of MyoD increases during myoblast proliferation and decreases as myocytes and myotubes are formed. MyoG primarily regulates expression of terminal differentiation genes needed for cell fusion.[113] Thus, expression of MyoG is increased later in the myogenic program. Myosin heavy chain protein (MHC) isoform expression is increased in contractile myotubes relative to myoblasts and its relatively increased expression is used in this study as a marker for terminally differentiated myotubes.[115] Antibodies specific for MyoD, myogenin and MHC isoforms were metal-labeled and used to phenotypically identify unique subsets of differentiating myoblasts based on the expression of these proteins.

A powerful aspect of single-cell analysis is the ability to trace cell lineage. Myogenesis is hallmarked by the progression of cells from immature to mature states, conventionally represented as distinct cell subsets as described above. Using antibodies specific to the myogenic markers mentioned above (MyoD, MyoG, and MHC), C2C12 myoblasts were differentiated for 0, 24, 48, 72, 96 or 120 hours (Figure 3.5), lifted using trypsin (see Appendix A, Figure A10), and analyzed using mass cytometry.

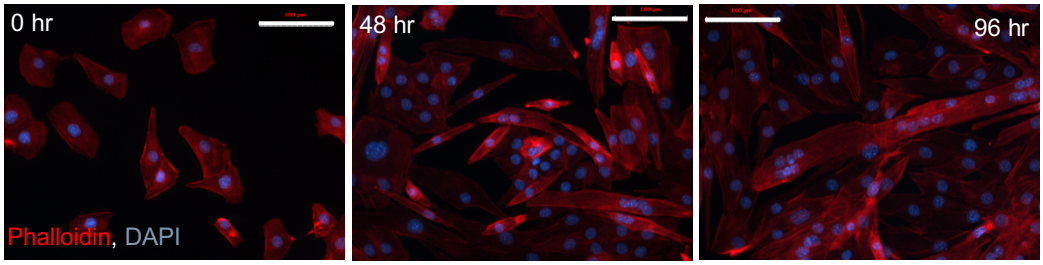

Figure 3.5. Representative images of differentiating C2C12 murine myoblasts. At 0 hrs. of differentiation (left) only mononuclear cells are observed, in an irregular, round shape. After 48 hrs. of differentiation (center), myoblasts are elongated, some have fused to become multi-nucleated myotubes. After 96 hrs. of differentiation, many myotubes are observed, with numerous nuclei per myotube. Scale bar is 100 μm. Phalloidin 546 and DAPI were used to stain the cytoskeleton and nuclei, respectively.

Rather than manually sub-setting individual cells based on their expected MyoD, MyoG, and MHC expression we employed the Wanderlust algorithm to

predict the progression of cell differentiation *de novo* by aligning cells from a given lineage to a unified trajectory.[71] As was expected, Wanderlust analysis of a heterogeneous population of differentiating myoblasts and myotubes predicted that of the three phenotypic markers described above, MyoD expression increases first, followed by MyoG; MHC increases last, as MyoD expression declines (Figure 3.6a). Manual gating of cell subsets was subsequently performed, adhering to the predicted phenotypic expression profile (see Appendix A, Figure A11). The proportion of cells in each subsequent cell subset in the myogenic lineage (Figure 3.6a), increases with increased time in differentiation conditions (Figure 3.6b). Cells not exposed to differentiation conditions express MyoD, though two distinct populations $MyoD^{hi}$ and $MyoD^{lo}$ are apparent (see Appendix A, Figure A11). As reported previously, this set of $MyoD^{lo}$ cells are likely capable of differentiation but instead stay in the quiescent state as 'reserve cells'.[116] Notably, at 120 hours of differentiation the population of quiescent $MyoD^{lo}$ cells increases, presumably as the myoblast compartment is regenerated.

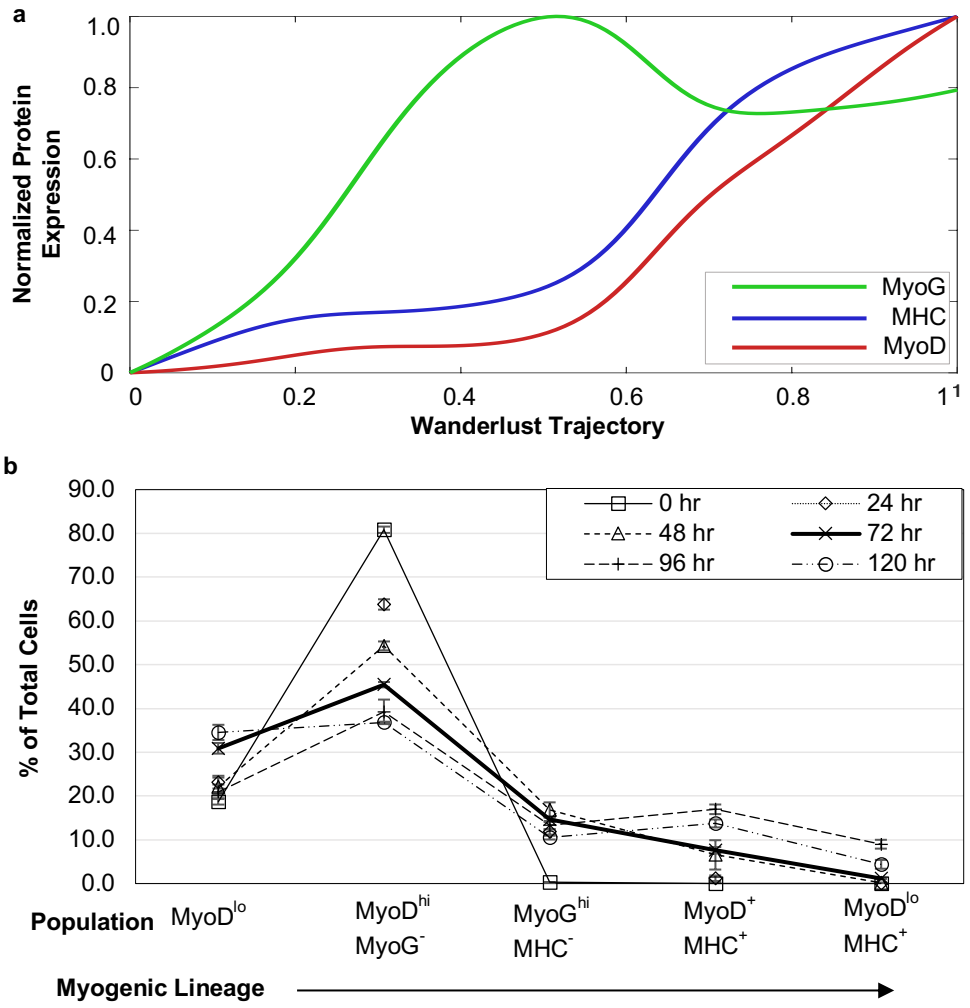

Figure 3.6. Prediction and characterization of unique phenotypic cell subsets. (a) We employed the Wanderlust algorithm to predict myogenic regulatory factor expression along the myogenic lineage. As expected, MyoD was expressed first, followed by MyoG and MHC. All subsequent manual gating followed the predicted pattern. (b) The proportion of cells in each unique cell subset in the myogenic lineage change with time spend in differentiation media, indicated in chart legend.

It has been reported that autophagy flux is increased during myogenesis, though a single-cell analysis of autophagy flux during myogenesis has not been reported. We prepared a panel of metal-labeled autophagy-related antibodies to accurately assess autophagy flux during differentiation in the cell subsets identified above. Antibody staining concentrations were chosen through the analysis of titration curves constructed for each antibody included in the panel (Figure 3.4a, Figure A6). Myoblasts exposed to differentiation conditions for 0, 24, 48, 72, 96 or

120 hours were exposed to Bafilomycin A1 for 2 hours prior to harvest to halt the degradation of autophagy-related organelles, which would result in accumulation of these organelles and their markers. Such accumulation is a surrogate for autophagy flux, thus providing a read of the rate of autophagy flux in each unique cell subset. As was expected, autophagy flux was increased during myogenesis (Figure 3.7).

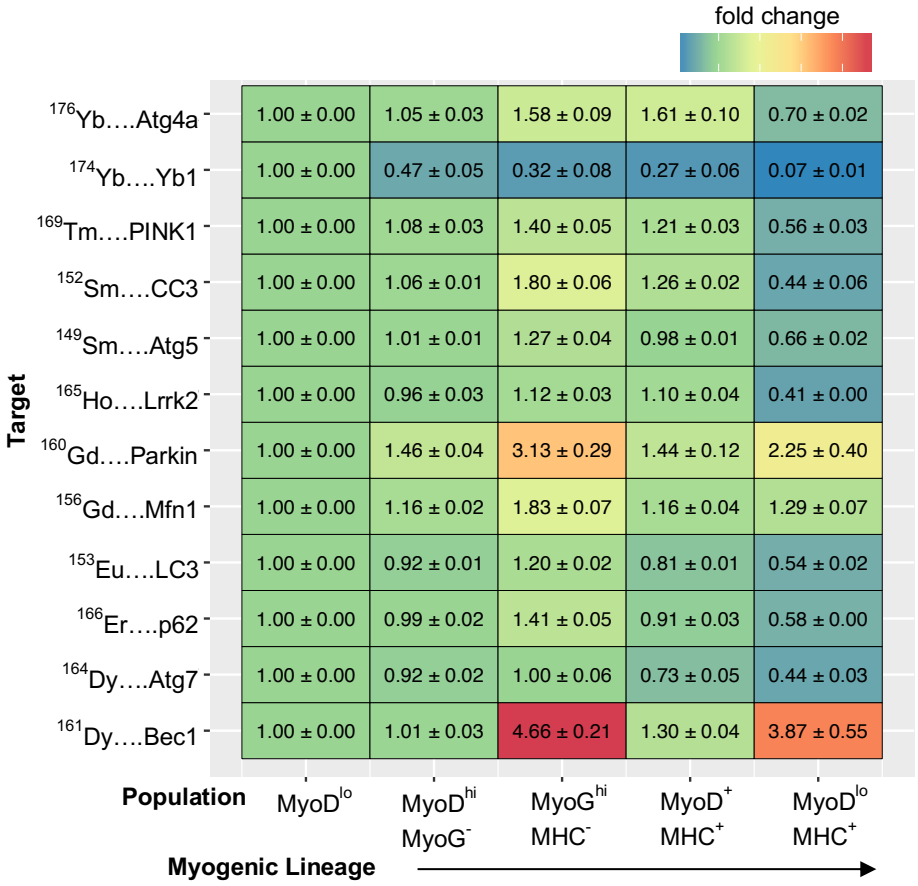

Figure 3.7. Measurement of autophagy flux along the trajectory of the myogenic lineage. MyoD^{lo} cells (column 1) represent the beginning of the myogenic lineage as proliferating but not differentiating myoblasts. The median signal intensity for each autophagy target (rows) in subsequent populations has been normalized back to its non-differentiating (MyoD^{lo}) control. The number in each cell represents the fold change from the MyoD^{lo} population for each autophagy target. Interestingly, general autophagy markers (Atg4a, Lrrk2, LC3, p62, Atg5, Bec1) peak during myoblast fusion (MyoG^{hi}, MHC^{-}), falling off abruptly after MHC is expressed. Conversely, expression of some mitophagy specific markers (Mfn1, Parkin) starts earlier in the myogenic program, and persists through myotube formation. Fold change is represented as mean of three biological replicates ± standard deviation.

Notably, most general autophagy markers such as Atg5, LC3, and p62 do not significantly increase in relative abundance until cells express myogenin and MHC,

markers of mid-to-late differentiation of myoblasts. As differentiating myoblasts cease to express, myogenin autophagy flux is significantly decreased, indicating the lack of autophagy flux needed to maintain differentiated myotubes. Conversely, proteins specifically marking mitochondria for autophagic degradation (i.e. mitophagy) such as Pink1, Mfn1, Parkin, and Bec1 (a known binding partner of Pink1[117]) show a gradual increase in relative abundance that peaks as cells express both MyoG and MHC. The abundance of these proteins is largely maintained even as MyoG expression decreases. Taken together, these data suggest that while autophagy flux is increased in myogenesis the increase occurs almost exclusively in cells at mid-to-late time points in the myogenic lineage and decreases significantly in formed myotubes (Figure 3.7, $MyoD^{lo}$, MHC^{+}). However, mitophagy flux increases gradually throughout differentiation and is maintained in myotubes, likely due to the changing metabolic requirements of this cell type.[89]

3.4 Discussion

This report describes the single cell analysis of autophagy flux in differentiating murine myoblasts, made possible through the development of a *post-hoc* data correction and normalization method for the accurate assessment of non-specific antibody binding in mass cytometry experiments. We found that non-specific antibody probe binding could be quantified and corrected using lanthanide-ion chelating isotype antibodies, and antibody loading into individual cells can be estimated using a lanthanide-ion chelating anti-GAPDH antibody as an individual cell internal standard analogous to loading controls used in bulk protein analyses (i.e. Western blots). The *post-hoc* data correction method described above shows that non-specific antibody binding and antibody loading can be corrected to reveal true, and biologically relevant signal. This method was used to choose appropriate antibody staining concentrations for the quantitative analysis of *in vitro* myogenesis.

The asynchronous progression of myogenesis has thus far prevented a detailed analysis of autophagy flux. Differentiating myoblasts can fuse to one

another, or pre-existing myotubes to regenerate damaged tissue. While bulk analyses of this process have provided the insight that autophagy flux is increased during myogenesis, the timing and magnitude of this increase in the frame of the myogenic lineage was largely unknown. We found that the order of myogenic regulatory factor expression could be predicted de novo from a heterogeneous population of cells representing a snapshot of continuous myogenic lineage. This analysis provided phenotypically unique cell subsets representing discrete points along the myogenic lineage for further study. Specifically, we found that a large portion of myoblasts will not express the myogenic regulatory factors required for differentiation despite increasing time spent in conditions known to induce differentiation. These cells are likely 'reserve cells' described in the literature that maintain quiescence despite the environmental stimuli inducing differentiation.[103] We also found that as myotube formation increased, the proportion of quiescent cells also increased, indicating replenishment of the myoblast compartment, likely in preparation for further differentiation.[116] As expected, myoblasts left to differentiate for increasingly longer times, will contain proportionally increasing cell subsets expressing the myogenic regulatory factors MyoD and MyoG, and the terminal differentiation marker MHC.

Autophagy flux is required for myogenesis[108] and decreased autophagy flux has been implicated in the decreased number and function of regenerative satellite cells with age.[83] However, the distinct point at which autophagy flux is impaired is unknown. We found that in an *in vitro* model of myoblast differentiation, accumulation of autophagy-related organelles indicative of autophagy flux increase during myoblast fusion and is significantly decreased in myotubes. Conversely, mitophagy-specific proteins (i.e. Pink1, Mfn1, Parkin, and Bec1) gradually increase in abundance throughout MyoG, peaking during myoblast fusion and is largely maintained in myotubes. These measures of autophagy and mitophagy flux show that while the autophagy machinery is indeed required for myogenesis, perhaps the more pertinent effect is the remodeling of the

mitochondrial network. This agrees with the increased energetic requirements and shifting metabolism observed in myotubes versus myoblasts.[89]

3.5 Conclusions

In conclusion, this study reports a method for the analysis of accurate antibody probe binding in multi-parameter mass cytometry experiments without the need for excessive genetically modified or pharmacologically biological models. This strategy is universally applicable to mass cytometry experiments where genetically knocked-out biological models are unavailable or impractical. Using accurate antibody incubation concentrations, we probed the rate of autophagy flux in distinct cell subsets present in asynchronous cultures of differentiating myoblasts, finding that autophagy flux spikes during myoblast fusion while mitophagy-specific protein expression gradually increases, likely due to changing energy and metabolism demands.

Chapter 4

Multiplexed Analysis of Autophagy Flux in the Mononuclear Fraction of Young and Geriatric Murine Skeletal Muscle

All data collection and analyses were done by H.M.G. Brown. Drs. Michael Kyba, Dawn Lowe, Sunny Chan, Cavan Riley, and Gengyun “Coco” Le advised on experimental design and method development.

Skeletal muscle is a highly complex tissue capable of repair or regeneration in response to damage or stress. Aging muscle undergoes a loss of its myogenic potential, which may reflect a reduction in the number of satellite cells that are necessary for myogenesis, as well as a reduction in the myogenic capacity of tissue-resident stem cells. Due to the highly heterogenous nature of skeletal muscle, decreased autophagic flux cannot be assigned to any single cell type, confounding the biological interpretation of bulk analyses. We hypothesized that harnessing the multiparameter capabilities of mass cytometry, would allow for the phenotypic identification of satellite cells, M2 macrophages and FAPs and simultaneous profiling of autophagy flux in each cell type to understand the potential for each cell population to uniquely contribute to the observed overall decrease in autophagy flux with age in skeletal muscle. We observed a significant decline in the satellite cell subset in geriatric muscle compared to young. We also observed decreased autophagy flux in satellite and FAP cells, but not M2 macrophages. These findings support the current perspective in the field that autophagy flux decreases with age in satellite cells, but also identifies decreased autophagy flux in FAP cells with age in skeletal muscle.

4.1 Introduction

Skeletal muscle is a highly complex tissue capable of repair or regeneration in response to damage or stress. The ability to self-renew is mainly driven by the myogenic potential of tissue resident stem cells, termed satellite cells. Following muscle damage, satellite cells are activated by cytokines and growth factors.[118] Activated satellite cells asymmetrically proliferate to both expand the myoblast compartment and reproduce a mitotically quiescent subset of cells for later proliferation.[87, 116] Myoblasts will differentiate and fuse to each other or existing myofibers to regenerate muscle mass and function. Beyond satellite cells, a wide variety of resident mononuclear cells also contribute to the satellite cell niche and participate in tissue homeostasis, such as macrophages and fibroadipogentic progenitor cells. Classically, macrophages promote phagocytosis through pro-inflammatory signalling, though some evidence suggests alternate activation of

macrophages to an anti-inflammatory phenotype in muscle following damage fosters an environment where satellite cells can act to repair damaged myofibers.[119] Fibroadipogenic progenitor (FAP) cells are characterized by their expression of platelet-derived growth factor receptor-alpha (PDGRFα). Upregulation of PDGRFα is observed in acute and chronic models of skeletal muscle damage, which contributes to the formation of excess fibrous connective tissue during repair.[120] Thus, proper regulation of satellite cell, macrophage, and FAP populations contributes to overall skeletal muscle homeostasis and regenerative capacity.

Aging muscle undergoes a loss in its myogenic potential,[74] which may reflect a reduction in the number of satellite cells that are necessary for myogenesis,[121] as well as a reduction in the myogenic capacity of aged satellite cells.[83] Whether this observed decline occurs via extrinsic factors derived from the satellite cell niche, including macrophage or FAP signalling, or via cell-intrinsic regulation of the myogenic program is unclear.[122] Whole tissue analyses of aged and young tissue via western blot implicate decreased autophagy flux as a contributing factor to reduced myogenic capacity.[108] Autophagy is a constitutively active, catabolic intra-cellular process by which long-lived or damaged proteins and organelles are degraded. The decline of autophagic flux results in the accumulation of damaged proteins and organelles and eventually, apoptosis.[4] Due to the highly heterogenous nature of skeletal muscle, decreased autophagic flux cannot be assigned to any single cell type, confounding the biological interpretation of these bulk analyses.

Mass cytometry is an emerging technique for multi-dimensional individual cell analysis using a single-particle inductively-coupled plasma mass spectrometer (ICP-MS)[43 43]. This technique detects and quantifies upwards of 45 separate cellular targets on the surface or within individual cells, expanding the multi-dimensional capabilities of individual cell analysis beyond what is currently possible with comparable techniques such as flow cytometry. The technique relies the quantification of isotopically pure lanthanide ions in individual cells which are

chelated to unique antibodies specific to cellular targets of interest. We hypothesized that harnessing the multiparameter capabilities of mass cytometry, would allow for the phenotypic identification of satellite cells, M2 macrophages and FAPs and simultaneous profiling of autophagy flux in each cell type to understand the potential for each cell population to uniquely contribute to the observed overall decrease in autophagy flux with age in skeletal muscle. We observed a significant decline in the satellite cell subset in geriatric muscle compared to young. We also observed decreased autophagy flux in satellite and FAP cells, but not M2 macrophages. These findings support the current perspective in the field that autophagy flux decreases with age in satellite cells, but also identifies decreased autophagy flux in FAP cells with age in skeletal muscle.

4.2 Materials and Methods

4.2.1 Reagents and Materials

Ham's F-10 media, horse serum, fetal bovine serum, HEPES buffer, Penicillin-Streptomycin (10,000 U/mL), collagenase II, Tris(2-carboxyethyl) phosphine hydrochloride (TCEP), and dispase II were obtained from Thermo Fischer Scientific (Waltham, MA). Dulbecco's Modified Eagle Medium was obtained from GE Healthcare Life Sciences (Marlborough, MA). Phosphate buffered saline (10x, 0.2 M KH_2PO_4, 1.5 M NaCl, pH 7.2) was obtained from Rockland Immunochemicals (Limerick, PA). Bovine serum albumin (BSA), vinblastine, rapamycin, sodium azide (NaN_3), and dimethyl sulfoxide (DMSO) was obtained from Sigma Aldrich (St. Louis, MO). Maxpar X8 Multimetal Labeling Kit, Maxpar Fix & Perm Buffer, Nuclear Antigen Staining Buffer Set, Cell-ID Intercalator, cell-ID cisplatin, and 10× EQ Four Element Calibration Beads were obtained from Fluidigm (San Francisco, CA). Cell strainers (40 μm), needles (16- and 18-gauge) and syringes (10 mL) were obtained from BD biosciences (Franklin Lakes, NJ). Debris removal kit was obtained from Miltenyi Biotec (Bergisch Gladbach, Germany). Water was purified with a Millipore Synergy UV system (18.2mΩ/cm, Bedford, MA). Rinsing buffer consisted of Ham's F-10 media, 10% horse serum, 10mM HEPES, Penicillin-Streptomycin (100 U/mL). Digestion

solution 1 consisted of DMEM, 0.2% (w/v) collagenase II, Penicillin-streptomycin (100 U/mL). Digestion solution 2 consisted of Ham's F-10 media, 0.2% (w/v) collagenase II, 0.2% (w/v) dispase II. PBS was diluted 1:10 in purified water. Cell staining buffer consisted of 1x PBS, 2% (w/v) BSA, and 0.02% NaN_3.

4.2.2 Animal Care and Sample Preparation

Female C57BL/6 mice were obtained from Jackson Laboratory or the National Institute on Aging. It has been reported that muscle mass and functional loss is noticeable in old mice (20-24 mo.) and is highly prevalent in geriatric mice (28-32 mo.).[123] To minimize the number of mice needed for these pilot studies we choose only one small range of ages to investigate in this study (25-28 mo.). Young mice (3-5 mo.) were used as relative controls for autophagy flux and cell enumeration studies. Young mice (<2 mo., n = 15), were obtained from Jackson Laboratory (Bar Harbor, ME) and housed four animals per cage for at least 1 week at the University of Minnesota prior to harvest. Geriatric mice were obtained from the National Institute on Aging at 21 mo. of age (n = 20). They were housed at the University of Minnesota (four animals / cage) for an additional four months prior to harvest. All mice were exposed to a 12-hour light/dark cycle and were provided food and water ad libitum. A power analysis from preliminary phenotyping experiments indicated a need for 14-17 animals for acceptable statistical power (0.8 to 0.9). Whole hind limb skeletal muscle was harvested over from all surviving mice over a two-month period. On each day of harvest two geriatric (>24 mo.) and one young (< 4 mo.) were euthanized with pentobarbital sodium (200 mg/kg body mass, ip) followed by tissue dissection. All tissues were stored on ice or at 4°C throughout sample preparation unless otherwise noted. All protocols were approved by the Institutional Animal Care and Use Committee at the University of Minnesota (protocol # 1602-33497A).

4.2.3 Antibody Panel Design and Characterization

Antibodies specific for autophagy-related targets were chosen after a preliminary screen using fluorescence microscopy and western blots to assess specificity and signal strength against an appropriate isotype control antibody (data

not shown). Phenotypic antibodies were chosen based on literature precedence and validated for their ability to identify specific cellular subpopulations. Where suitable specific antibodies were not available, a hybridoma cell line (α-MHC, clone: BF35) developed by Lucas and Schiaffino, was obtained from the Developmental Studies Hybridoma bank, created by the NICHD of the NIH and maintained at The University of Iowa, Department of Biology, Iowa City, IA 52242. Hybridomas were sub-cultured at The University of Minnesota – Twin Cities, and sent to ProMab Biotechnologies (Richmond, CA) for large-scale antibody production and purification.

Where available, pre-metal-labeled antibodies were purchased from Fluidigm (San Francisco, CA). When appropriate metal-labeled clones were unavailable antibodies were metal-labeled using the Maxpar metal-labeling kit (Fluidigm, San Francisco, CA), per manufacturer instructions. Protein concentrations after metal-loaded polymer conjugation was calculated from measured A_{280} values (Jasco, Oklahoma City, OK). The average number of metal atoms per antibody was calculated using the lanthanide concentration and the measured stock antibody concentration. Briefly, metal-labeled antibodies were diluted 1:10,000 from their stock concentrations into 2% HNO_3. Lanthanide standards (Fluidigm, San Francisco, CA) were prepared in 2% HNO_3 to a final concentration of 50pM. Solutions were sequentially injected into the CyTOF2 mass cytometer and data was acquired for all m/z ratios simultaneously in “solution mode” using the following parameters: step value = 1, settling time = 20 s, pushes / reading = 76,800. The signal resulting from the lanthanide standard was used to calculate the lanthanide atom concentration in the diluted antibody sample. This value was divided by the number of antibody molecules present in the diluted antibody sample. See Appendix B, Table B1 for antibody panel characterization.

4.2.4 Mass Cytometry Sample Preparation and Data Acquisition

Satellite cell isolation protocol was adapted from Brack.[124] Briefly, all hindlimb muscle was dissected and visible tendons, connective tissue and fat were trimmed. Resulting tissue was minced using a flat razor blade on a petri dish to produce

myofiber fragments. Myofiber fragments were subjected to digestion in digestion solution 1 for 90 minutes at 37°C. The resulting suspension was washed twice with rinsing buffer. Satellite cells were further released from myofiber segments via mechanical disruption through trituration though a jagged Pasteur pipette, followed by a wash to remove large pieces of adipose tissue. The resulting pellet was resuspended in digestion solution 2 and incubated at 37°C for 30 minutes. The digested suspension was further mechanically disrupted via tituration through 16- and 18-gauge needs, then filtered through 40 µm cell strainers. The resulting suspension was then titurated through an 18-gauge needle a second time and washed twice with rinsing buffer.

Each sample was subjected to a debris removal protocol to remove remaining small particulate. Briefly, cell suspensions were resuspended in 6.2 mL of ice-cold PBS in a 15-mL conical tube. Debris removal solution was added to 8 mL total volume and the solution was mixed. Each sample was overlaid with 4 mL of ice-cold PBS and centrifuged at 3,000 × g for 10 minutes at 4°C. Three phases were formed, the top two were aspirated and discarded. Ice-cold PBS was added to a total volume of 15-mL, inverted three times, and centrifuged at 1,000 × g for 10 minutes at 4°C. The supernatant was aspirated to produce a reduced-debris pellet.

Cells were resuspended in rinsing buffer and incubated in 110 nM rapamycin and 100 nM bafilomycin A1, or DMSO vehicle control (contralateral control) for 4 hrs at 37°C, 5% CO_2. Cells were collected, washed once with washing buffer and frozen in FBS containing 10% DMSO for storage.

Cells were thawed and resuspended in a 1:10,000 dilution of benzonase in DMEM to digest free DNA. Cell samples were stained with cisplatin (5 µM, Fluidigm) in PBS, and quenched with cell staining buffer. After two washes in cell staining buffer, cells were incubated in a cocktail of extracellular antibodies (see Appendix B, Table B1) in cell staining buffer for 1 hour at room temperature. Following two washes in cell staining buffer, cells were fixed, permeabilized using the Nuclear Antigen Staining Buffer Set, and incubated in a cocktail of intracellular antibodies (see Appendix B, Table B1) for 1 hour at room temperature. Cells were

washed twice more with cell staining buffer and incubated at 4°C overnight in Cell-ID Intercalator-Ir (diluted to 62.5nM final concentration in Maxpar Fix & Perm buffer). Prior to analysis on the CyTOF2 mass cytometer, cells were washed with cell staining buffer and purified H_2O.

4.2.5 Mass Cytometry Data Analysis

Data was acquired on a CyTOF2 mass cytometer (Fluidigm, San Francisco, CA). Samples were diluted 1:10^6 in a solution of 1× EQ Four Element Calibration Beads in ultrapure water to attain an event detection rate of approximately 300 events / second. Data was acquired using the following instrument parameters: noise reduction, cell length = 10-150, lower convolution threshold = 0.2. Flow cytometry standard (.fcs) files were bead normalized (Helios software, version 6.7, Fluidigm), and then converted to plain text (.txt) files for further analysis in R. The number of ions associated with each cell event (# $ions_{Ab}$) was calculated using the equation below, where DC_{Ab} represents the dual count signal of the antibody chelating a unique lanthanide isotope, defined as *m*. TE_m is the empirically determined transmission efficiency of unique lanthanide isotope *m* for the CyTOF2 at the University of Minnesota.

$$\#\ ions_{Ab} = \frac{DC_{Ab}}{TE_m} \qquad \text{Equation 4.1}$$

Then, the number of each unique antibody present per cell (# Ab per cell) was calculated using a correction factor via the following equation.

$$\#\ Ab\ per\ cell = \frac{\#\ ions_{Ab}}{correction\ factor} \qquad \text{Equation 4.2}$$

The correction factor describes the number of lanthanide ions chelated to each antibody (see Appendix B, Table B1). This calculation was carried out for all antibodies, regardless of specificity.

Cells were stained with host-matched, isotype control antibodies, each chelating a unique lanthanide isotope, to estimate the non-specific binding properties of each specific marker antibody. To obtain specific marker signal (corrected # specific Ab), the number of isotype antibodies per organelle (# isotype

Ab) was subtracted from the number of specific antibodies per cell event (# specific Ab), using the following expression.

$$\text{corrected \# specific Ab} = \text{\# specific Ab} - \text{\# isotype Ab} \quad \text{Equation 4.3}$$

4.3 Results and Discussion

4.3.1 Phenotypic Identification of the Mononuclear Fraction of Murine Skeletal Muscle

It has long been hypothesized that the reduced regenerative capacity of aged skeletal muscle is due, in part, to a reduced pool of satellite cells.[125-126] We hypothesized that the decline in the satellite cell compartment of aged skeletal muscle may also be accompanied by an increase in the population of mature, pro-inflammatory macrophages, and a concurrent decline in anti-inflammatory macrophages. In addition, we expected an increase in the number of pro-fibrotic FAP cells. To investigate this hypothesis, we developed a panel of eight antibodies (see Appendix B, Table B1) to phenotypically identify satellite cells, pro- and anti-inflammatory macrophages, and FAPs (see Appendix B, Figure B1 for gating scheme) in young (3-4 mo.) and geriatric (25-28 mo.) murine skeletal muscle.

As expected, the muscle mass of young and aged mice varied with young mice maintaining approximately 1.6 times the muscle mass (reported as % of total body weight) as geriatric mice (Figure 4.1), indicating a functional loss of muscle maintenance in our aged skeletal muscle model.

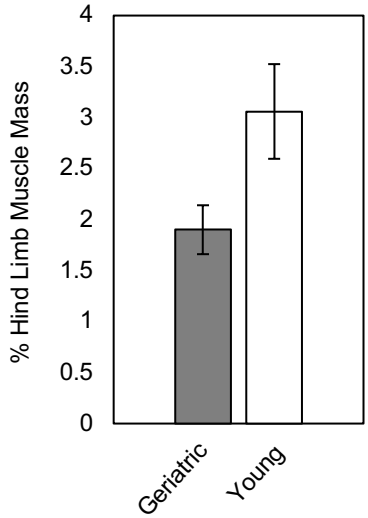

Figure 4.1. Percent muscle mass of young and geriatric C56BL/6 mice. The observed muscle mass of young and geriatric mice varied as expected with young mice maintaining approximately 1.6 times more tissue mass than geriatric mice (n = 6 for each age group). Student's t-Test reveals a statistically significant difference ($p = 0.00089$). Error bars represent one standard deviation of the mean.

As was shown by Lepper[127] and Sambasivan,[128] paired box 7 protein positive ($Pax7^+$) satellite cells are required for muscle repair following acute injury. Through phenotypic identification of satellite cells, we saw a significant decline in the number of identified satellite cells in geriatric skeletal muscle (94 % decrease of as a proportion of intact cells, $p = 0.043$, $n = 8$) compared to young controls (Table 4.1). Thus, the depleted $Pax7^+$ satellite cell pool we observed in aged skeletal muscle may significantly influence its myogenic capacity.

Table 4.1. Percent phenotypically identified cell populations of interest. The abundance of satellite cells is significantly reduced by 94% in geriatric versus young hind limb skeletal muscle (Student's t-Test, $p = 0.043$). No other cell type showed an age-correlated change in abundance.

	% population of detected cells			
	M1 Macrophages	**M2 Macrophages**	**Satellite Cells**	**FAP cells**
Young - 1	0.05	2.70	0.08	1.40
Young - 2	0.05	2.02	0.04	2.47
Young - 3	0.35	2.36	0.01	1.34
Geriatric - 1	0.27	3.09	0.70	13.10
Geriatric - 2	0.11	2.88	0.25	1.57
Geriatric - 3	0.01	0.91	0.81	23.30
Geriatric - 4	0.02	1.62	1.28	12.10

Recent studies have shown that the skeletal muscle resident immune compartment contributes to the myogenic potential of satellite cells after injury.[129-130] Macrophages maintain stem cell populations in numerous tissues including skin and bone marrow,[94-97] and have been shown to give stem cells "license" to execute their differentiation program.[98] For example, Sun and coworkers showed that when the macrophage-specific, critical inflammatory signaling receptor chemokine-CC-motif receptor 2 (CCR2) is genetically knocked out, innate M1 macrophage signaling is blocked and muscle repair is abrogated.[107] With this in mind, we hypothesized that a numerical decline of macrophages (either pro- or anti-inflammatory) may also contribute to the atrophy and reduced regenerative capacity observed in aged skeletal muscle. However, we observed heterogenous range of abundance of both anti- and pro-macrophage abundance in biological

replicates (Table 4.1). On average, we identified 0.2% and 0.1% of intact cells as pro-inflammatory M1 macrophages in geriatric and young skeletal muscle, respectively (%$RSD_{geriatric}$: 112%, n = 4, and %RSD_{young}: 114%, n = 4). Similarly, only 1.8% and 2.1% of intact cells were identified as anti-inflammatory M2 macrophages in geriatric and young skeletal muscle, respectively (%$RSD_{M2\ macrophages,\ geriatric}$: 62%, n = 4, and %$RSD_{M2\ macrophages,\ young}$: 49%, n = 4). These data suggest that resident M1 and M2 macrophage abundance in skeletal muscle is not a significant factor affecting myogenic potential of aged skeletal muscle, though they lack the statistical power to confirm this hypothesis. The distribution of phenotypic marker intensity for each animal differed, which could affect the %RSD reported above. These inconsistencies could have been a result of non-normalized cell counts per sample prior to antibody staining. Non-normalized cell counts may affect the degree to which non-specific antibody binding contributes to signal used to identify individual cell types. Future experiments with an increased number of replicates and normalized cell counts may provide sufficient statistical power to confirm the extreme heterogeneity we observed in this study. In addition, future experiments should include markers to compare the efficacy of innate immune system signalling in aged versus young skeletal muscle.

As noted above, $Pax7^+$ satellite cells are required for skeletal muscle maintenance. In the absence of efficient muscle repair via satellite cells, other non-myogenic mesenchymal progenitors, such as FAPs, can produce excessive fibrous or adipose tissue.[10, 131] The accumulation of ectopic tissues is deleterious to injured skeletal muscle and propagate weakness though further destruction of myofibers.[131] Enumeration of the FAP populations in young and geriatric skeletal muscle showed extreme heterogeneity in FAP abundance across age. Of detected intact cells, 1.2% and 12.2% were identified as FAP cells from geriatric and young mice, respectively (%$RSD_{\%\ FAP,\ geriatric}$: 77%, n = 4, and %$RSD_{\%\ FAP,\ young}$: 73%, n = 4). We also compared the relative abundance of each phenotypically identified population within the same sample, and across age-matched samples. We found no trend between relative abundance of any population.

4.3.2 Changes in Autophagy Flux across Macrophages, Satellite and Fibro-adiopogenic Precursor Cells in Young versus Geriatric Mice

In accordance with our original hypothesis, we sought to measure autophagy flux in each identified cell type to understand the potential for each to uniquely contribute to the observed overall decrease in autophagy flux with age in skeletal muscle. Previous work[83] had measured total LC3 content as a marker of autophagy flux in single satellite cells from geriatric and young mice. Though to our knowledge, autophagy flux has not been quantified in skeletal muscle resident M2 macrophages or FAP cells. Thus, we sought to provide a more thorough description of autophagy flux in aged skeletal muscle through the analysis of autophagy flux in satellite cells, M2 macrophages and FAP cells.

It has been shown that autophagy is required for satellite cells to maintain stemness[83] therefore, we expect to find decreased autophagic flux in satellite cells in our analysis. We hypothesize that the age-related chronic low grade inflammatory state known as “inflamm-ageing”,[132] may be related to decreased anti-inflammatory M2 macrophage function via insufficient autophagic flux. Additionally, recent reports suggest that interactions between FAP and satellite cells regulate satellite cell fate,[133] thus insufficient autophagy in FAP cells may contribute to dysregulated satellite cell activation in geriatric skeletal muscle.

Using the multiplexing capacity of mass cytometry, we simultaneously identified satellite cells, M2 macrophages and FAPs and measured the total LC3 content of each as a surrogate for autophagic flux (Figure 4.2a, see Appendix B, Figure B3 for additional autophagy markers). We found that after bafilomycin A1 treatment ex vivo, satellite and FAP cells from young skeletal muscle had increased levels of total LC3 over geriatric muscle, indicating higher rates of active autophagy flux. Conversely, M2 macrophages showed no change between geriatric and young skeletal muscle, though bafilomycin A1 treatment did cause a slight increase in total LC3 signal (ratio >1), indicating autophagy flux in M2 macrophages is active and does not differ in between young and geriatric skeletal muscle.

p62 is one of many adaptor proteins that facilitates selective autophagy via interactions between the inner membrane of a phagophore and polyubiquitinated cargoes labelled for degradation[134]. In the absence of selective autophagy, p62 is constantly turned over and therefore is often used as a marker for general autophagy flux. Concurrently with selective autophagy, p62 is post-translationally modified to induce its function as an autophagy adaptor, both through increased affinity for cargoes and ability to interact with LC3 at the phagophore inner membrane[135]. We measured total p62 content concurrently with LC3 above to confirm changes in autophagy flux in bafilomycin A1 treated satellite cells, M2 macrophages and FAP cells (Figure 4.2, right). As was expected, slight accumulation of p62 in both geriatric and young M2 macrophages indicates autophagy flux is active and occurring at similar rates in both groups. Similarly, differential accumulation of p62 in young FAP cells indicates autophagy flux is active. No accumulation of p62 was observed in geriatric FAP cells indicating attenuated autophagy flux in this cell subset.

Interestingly, we observed an accumulation of p62 in geriatric satellite cells treated with bafilomycin A1. This was unexpected based on the observation of decreased autophagic flux in geriatric satellite cells made above. Taken together, these data suggest that while autophagy flux is decreased in geriatric satellite cells, accumulation of p62 at selected cargoes still occurs. In Chapter 3, we showed that autophagy flux is increased during myoblast differentiation and fusion, and that mitophagy is specifically increased in these processes. Thus, signalling for selective degradation of cargoes maybe intact in geriatric satellite cells even though autophagic flux is decreased.

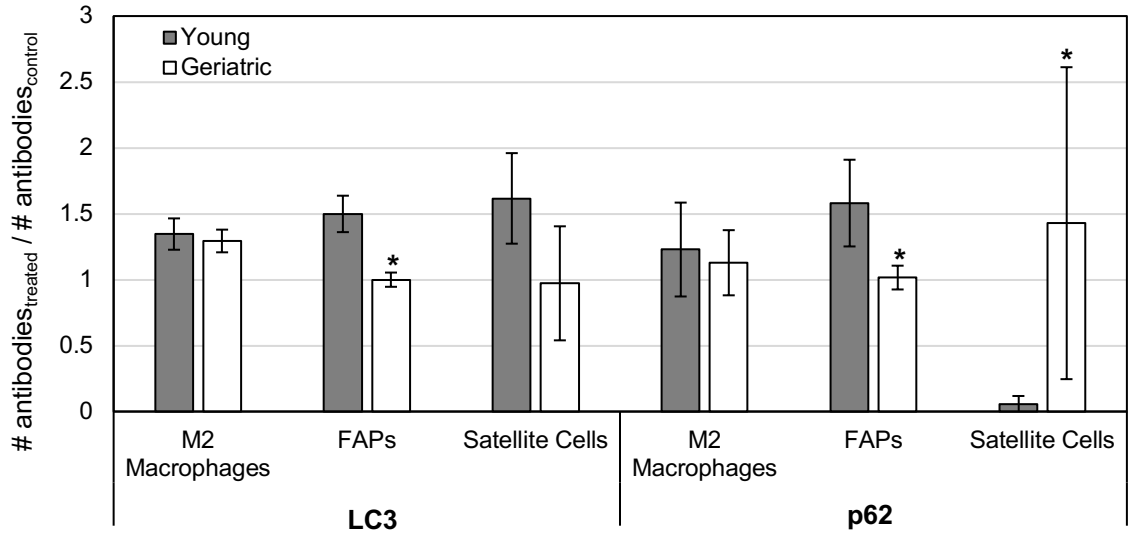

Figure 4.2. Ratio of the number of antibodies detected in bafilomycin A1 treated versus control cells. Mononuclear cells isolated from skeletal muscle of the whole hindlimb of geriatric and young mice were treated ex vivo with bafilomycin A1 (100 nM, 4h.) or a DMSO vehicle control. Analysis of the cells via mass cytometry allowed for the phenotypic separation of M2 macrophages, FAP cells, and satellite cells, and subsequent quantification of total LC3 and p62 in each. The ratio shown indicates the relative abundance of LC3 or p62 in the treated and control samples. Error bars represent 95% confidence intervals. These data represent four separate samples from two animals. * indicates $p<0.05$ between geriatric and young samples.

4.4 Conclusions

This work describes the first single cell analysis of phenotype and function in skeletal mononuclear cells. We found that satellite cells had significantly decreased abundance in geriatric skeletal muscle while there was no age-correlated change in abundance for either M2 macrophages or FAPs. We also evaluated the autophagic flux of each cell type via quantification of total LC3 and found that autophagy flux in M2 macrophages is not changed from young to geriatric skeletal muscle. Conversely, we found that autophagy flux is decreased in FAP and satellite cells from geriatric skeletal muscle. These results were confirmed via concurrent analysis of p62 in each cell type for each age group. Interestingly, accumulation of p62 in satellite cells from geriatric skeletal muscle indicates that while autophagy flux may be attenuated, selective autophagy signalling is intact.

This analysis used 21 of nearly 50 available lanthanide isotopes, so future analyses will expand both the phenotypic and functional analysis of the

mononuclear fraction of skeletal muscle. Ideally, additional interstitial cell types will be investigated including vessel-associated stem cells[136] and $PW1^{+}/Pax7^{-}$ interstitial cells (PICs).[137] In addition, expanding the breadth of autophagy-related markers monitored in each cell type will provide more detail on the role of decreased autophagy flux in FAP and satellite cells. Other functional aspects of each cell type could also be monitored to probe their contribution to the satellite cell niche. For example, while autophagy flux in M2 macrophages does not change with age, other functions such as cytokine signalling has yet to be investigated. Harnessing the multiplexing power of mass cytometry for the concurrent analysis cell phenotype and function in aged skeletal muscle will provide unprecedented insight into its decreased regeneration potential.

Chapter 5

Mass Cytometry for Monitoring Autophagy at the Individual Organelle Level

Reprinted (adapted) with permission from Brown, H.M.G.; Arriaga, E.A., Quantifying Heterogeneity of Individual Organelles in Mixed Populations via Mass Cytometry, *Anal. Chem.*, **2018**, *90* (22), 13315–13321.

Nick Livezey assisted in the metallation of the DDD-3Na^+ reagent and interpretation of ^{1}H-NMR spectra.

.

Macroautophagy is a complex degradative intracellular process by which long-lived proteins and damaged organelles are cleared. Common methods for the analysis of autophagy are bulk measurements which mask organelle heterogeneity and complicate the analysis of inter-organelle association and trafficking. Thus, methods for individual organelle quantification are needed to address these deficiencies. Current techniques for quantifying individual autophagy organelles are either low through-put or are dimensionally limited. We make use of the multiparametric capability of mass cytometry to investigate phenotypic heterogeneity in autophagy-related organelle types that have been isolated from murine brain, liver, and skeletal muscle. Detection and phenotypic classification of individual organelles were accomplished through the use of a lanthanide-chelating membrane stain and organelle-specific antibodies. Post-hoc sample matrix background correction and non-specific antibody binding corrections provide quantitative measures of inter-organelle associations and heterogeneity. This is the first demonstration of multiparametric individual organelle analysis via mass cytometry. The method described here illustrates the potential for further investigation of the inherently complex inter-organelle associations, trafficking and heterogeneity present most eukaryotic biological systems.

5.1 Introduction

A growing body of evidence demonstrates organelle of various types interact with each other to coordinate complex biological processes.[138] For example, bulk intra-cellular recycling (macroautophagy) degrades long-lived proteins and damaged organelles releasing biomolecules that are used as biological building blocks. Macroautophagy is constitutively active and proceeds through at least four phenotypically unique organelle types whose interactions are dynamically coordinated to respond to intra- and extra-cellular stimuli. Dysfunctional macroautophagy has been implicated in age-related health decline, including neurodegenerative diseases, sarcopenia, and liver pathologies,[6, 139]

where autophagy activity is generally decreased. Currently, the role of organelle heterogeneity in the development of these and other diseases hallmarked by dysfunctional organelle-related processes is unclear because bulk or whole-cell analyses (i.e. western blots, flow cytometry) cannot distinguish different organelle types. Previously reported methods for individual organelle analysis include: transmission electron microscopy,[140] capillary electrophoresis with laser-induced fluorescence detection,[27, 29-30] and flow cytometry.[141-142] These techniques are either low-throughput, lack sensitivity or are dimensionally-limited.

Here, we report a multi-dimensional analysis of individual organelles detected via mass cytometry to reveal organelle population heterogeneity in macro- and mitophagy across multiple tissues. Mass cytometry has been used to conduct multi-dimensional analyses of individual cells,[46] but has not been used for analyses of organelles. Mass cytometry relies on the use of antibodies, in which each unique antibody of the panel binds and identifies its specific molecular target. Each antibody is conjugated to a chelating polymer loaded with a different lanthanide isotope. Labeled particles are flowed through a micro-nebulizer to produce single-particle droplets which are vaporized, atomized and ionized via an inductively coupled plasma to produce ion clouds corresponding to individual particles. The temporally resolved ion clouds are analyzed via a time-of-flight mass spectrometer where the amount of lanthanide bound to each particle is quantified.[43]

Post-hoc correction for sample matrix background signal and non-specific antibody interactions were carried out on an individual organelle basis to reveal true signal for each reporter in each organelle. We confirm the analysis of individual particles rather than organelle aggregates through the analysis of filtered organelle suspensions, assessing the changing distribution of membrane stain intensity as a marker for aggregates. The corrected, individual organelle data are visualized using the Barnes-Hut implemented T-distributed stochastic neighbor embedding algorithm (t-SNE) to assess intra-population heterogeneity that is evident even within phenotypically similar organelle populations.

5.2 Materials and Methods

5.2.1 Materials, Reagents, Buffers, and Solutions.

Sucrose, hydroxyethyl piperazineethanesulfonic acid (HEPES), mannitol, ethylenediaminetetraacetic acid (EDTA), ethylene-bis(oxyethylenenitrilo) tetraacetic acid (EGTA), 3-(N-morpholino) propanesulfonic acid (MOPS), Tris(hydroxymethyl)aminomethane (Tris), Tris(hydroxymethyl)aminomethane hydrochloride (Tris-HCl), potassium chloride, sodium chloride, potassium phosphate monobasic (KH_2PO4), sodium azide, Methanol-free formaldehyde (16%), nitric acid, hydrochloric acid, sodium hydroxide, diethylenetriaminepentaacetic acid (DTPA), dodecan-1-amine, dimethylformamide, chloroform ($CHCl_3$), trifluoroacetic acid (TFA), and α-Cyano-4-hydroxycinnamic acid (αCHCA) were obtained from Sigma-Aldrich (St. Louis, MO). Tris(2-carboxyethyl) phosphine hydrochloride (TCEP), and terbium (III) chloride hexahydrate ($TbCl_3 \cdot 6H2O$) were obtained from Thermo Scientific (Waltham, MA). Phosphate buffered saline (PBS, 10× concentration, 1.37 M NaCl, 27 mM KCl, 80 mM Na_2HPO_4, and 20 mM KH_2PO_4, pH 7.4), and Tween-20 was obtained from Bio-Rad (Hercules, CA). Percoll density gradient media was obtained from GE Healthcare Life Sci-ences (Marlborough, MA). Maxpar X8 Multimetal Labeling Kit, Maxpar Fix & Perm Buffer, Cell-ID Intercalator, and 10× EQ Four Element Calibration Beads were obtained from Fluidigm (San Francisco, CA). Water was purified with a Millipore Synergy UV system (18.2mΩ/cm, Bedford, MA). Polytetrafluoroethylene (PTFE) syringe filters (0. 2 μm pore size) were obtained from Pall Industries (Port Washington, NY). Polycarbonate membranes were obtained from EMD Millipore (Burlington, MA). MSEGTA buffer consisted of 225 mM mannitol, 75 mM sucrose, 5 mM HEPES, 1 mM EGTA, pH 7.4. When necessary additives were included such as 3 μM bovine serum albumin (MSEGTA-BSA), or percoll density gradient media (12% or 24% Percoll-MSEGTA). Liver isolation buffer (IB_L) consisted of 13 mM Tris, 14 mM MOPS, 10 mM EGTA, 200 mM sucrose, pH 7.4. Muscle isolation buffer 1 (IB_{m1}) consisted of 67 mM sucrose, 50 mM Tris-HCl, 50 mM KCl, 10 mM EDTA, 3 μM BSA, pH 7.4. Muscle isolation

buffer 2 (IB_{m2}) consisted of 250 mM sucrose, 2 mM EGTA, 15 mM Tris-HCl, pH 7.4. Cell staining media (CSM) consisted of 20 mM KH_2PO_4, 150 mM NaCl, 7.5 µM bovine serum albumin, 800 µM NaN_3, pH 7.2.

5.2.2 Antibody Panel Design and Characterization.

Selected antibodies were metal-labeled using a Maxpar metal-labeling kit, per manufacturer instructions. Briefly, isotopically pure lanthanide (Ln) ions were loaded into linear Ln-chelating polymer (similar structure to those published by Lou[50]). IgG antibodies were reduced using TCEP, and then incubated with Ln-chelating polymers for 90 minutes. Conjugates were rinsed to remove unbound Ln-chelated polymer and resuspended at 0.5 mg/mL. The average number of lanthanide atoms per antibody was calculated by quantifying the number of lanthanide ions and anti-body molecules per unit volume. The number of lanthanide ions were quantified by comparison to a standard solution of lanthanide ions of known concentration. Briefly, metal-labeled antibodies were diluted 1:1,000 from their stock concentrations into 2% HCl, followed by two subsequent 1:1,000 dilutions into 2% HNO_3 for a total dilution factor of 1:10,000. Lanthanide standard solutions were prepared in 2% HNO_3 to a final concentration of 50pM. Solutions were sequentially flowed into the CyTOF2 mass cytometer and data was acquired for all metal channels simultaneously in “solution mode” using the following parameters: step value = 1, settling time = 20 s, pushes / reading = 76,800. The steady signal resulting from the lanthanide standard was used to calculate the lanthanide atom concentration in the diluted antibody sample (see Appendix C, Table C1).

5.2.3 Didodecyl-DTPA-Tb Synthesis and Metallation

DDD-Tb was synthesized as reported by Leipold and co-workers, using 99.9% pure terbium chloride (aq.) rather than the reported europium chloride (aq.).[143] Briefly, diethylenetriamine pentaacetic acid dianhydride (1.5 g, 4.2 mmol) was dissolved in DMF (75 mL) and maintained at 40ºC. Dodecan-1-amine (2.2 g, 11.7 mmol) was dissolved in $CHCl_3$ (70 mL), added-dropwise to the reaction, and

stirred overnight. The solid product was collected via filtration and resuspended in ultrapure H_2O (100 mL) containing minimal NaOH (1 M, 10 mL) to solubilize the solid. The resulting solution was lyophilized, then resuspended in $CHCl_3$ (70 mL) and filtered to remove excess NaOH. The solid was dried under reduced pressure to afford the tri-sodium didodecyl-DTPA salt (2.4 g, 301 μmol, 77 % yield). Matrix-assisted laser desorption / ionization – mass spectrometry (MALDI-MS, positive reflectron mode, αCHCA matrix with 0.1% TFA) (m/z): $[M+3Na-H]^+$ calculated for C38H73N5O8Na3, 797.00; found 796.62. Electrospray ionization – mass spectrometry (ESI-MS, negative mode) (m/z): [M+H]- calculated for $C_{38}H_{70}N_5O_8$, 725.0; found 724.9. ^1H NMR (400 MHz, D_2O): δ 3.7-2.9 (m, br, 18 H, CH_2), 1.22 (m, br, 44 H, CH_2), 0.79 (t, 6 H, J = 5.6 Hz, CH_3).

Didodecyl-DTPA-3Na ligand (200 mg, 252 μmol) was dissolved in 25 mM aqueous $TbCl_3$ (141 mg, 378 μmol) and left at room temperature for 15 minutes. The solution was lyophilized and excess $TbCl_3$ was removed using a $CHCl_3$ extraction resulting in the metallated DDD-Tb ligand (200 mg, 227 μmol, 90% yield). DDD-Tb was dissolved to 0.2 mM in aqueous 50 mM NaCl and filtered through a 0.2 μm PTFE filter.

5.2.4 Organelle Isolation and Immunolabeling

Female C57BL/6 mice were obtained from Jackson Laboratories or the National Institute on Aging. Mice were euthanized with sodium pentobarbital (200 mg/kg body mass, ip) followed by tissue dissection. All tissues were stored on ice or at 4°C throughout organelle sample preparation unless otherwise noted. All protocols were approved by the Institutional Animal Care and Use Committee at the University of Minnesota (protocol # 1602-33497A).

Organelles were isolated from tissues of interest (brain, hind limb skeletal muscle, and liver) using procedures adapted from Chinopoulos or Frezza.[144-145] Brain tissue was dissected and placed into MSEGTA-BSA buffer. The tissue was homogenized using a Potter-Elvehjem homogenizer (Wheaton, Millville, NJ) and stroked ten times at 1,600 r.p.m. The homogenate was transferred to clean microcentrifuge tubes and centrifuged for 5 minutes at 500 × g. The cloudy

supernatant was transferred to clean micro-centrifuge tubes as the post-nuclear fraction and centrifuged at 14,000 × g for 10 minutes. The pelleted organelle fraction is resuspended in 12% Percoll – MSEGTA buffer, layered over 24% Percoll – MSEGTA, and centrifuged for 16,100 × g for 25 minutes. The resulting sample had two opaque layers sandwiching a clear band. The top two portions of the sample were removed, and the opaque bottom layer was washed twice with MSEGTA buffer producing a visible organelle pellet after the final wash.

Dissected liver was transferred to IB_L. The tissue was rinsed with IB_L until free of blood, then minced in a petri dish with a flat razor blade. The minced tissue was homogenized using a Potter-Elvehjem homogenizer stroked four times at 1,600 r.p.m. The homogenate was transferred to clean microcentrifuge tubes and centrifuged at 600 × g for 10 minutes. The cloudy supernatant was transferred to clean microcentrifuge tubes as the post-nuclear fraction and centrifuged at 10,000 × g for 10 minutes. The resulting organelle pellet was washed once with IB_L producing a final organelle pellet.

Dissected hind limb skeletal muscle was transferred to PBS containing 10 mM EDTA. Visible tendons, connective tissue and fat were trimmed, and tissue was minced using a flat razor blade on a petri dish, then rinsed with PBS containing 10 mM EDTA. Minced muscle tissue was enzymatically digested (0.05% trypsin, 10 mM EDTA) for 30-45 minutes at 37°C. Following digestion, tissue was centrifuged at 200 × g for 5 minutes and resuspended in IB_{m1}. The tissue was homogenized using a Dounce homogenizer. Each sample was stroked 10 times with pestle A (clearance: 0.114 ± 0.025mm), followed by 10 strokes with pestle B (clearance: 0.05 ± 0.025mm). The homogenate was transferred to microcentrifuge tubes and centrifuged at 600 × g for 10 minutes. The resulting cloudy supernatant was transferred to clean microcentrifuge tubes as the post-nuclear fraction and centrifuged at 10,000 × g for 10 minutes. The resulting organelle pellet was resuspended in IB_{m2}, and centrifuged at 10,000 × g for 10 minutes, producing a final organelle pellet.

The organelle pellet for each tissue was resuspended in IB_L and aliquoted to obtain samples with similar opacity. Each sample was washed once with IB_L, then stained with antibodies in CSM for one hour at room temperature. Organelles were washed twice with CSM and resuspended in 4% formaldehyde for 30 minutes at room temperature. Fixed organelles were washed twice with PBS, then resuspended in 0.2 mg/mL DDD-Tb in 0.09% NaCl for 30 minutes at room temperature. Organelles were washed twice with PBS supplemented with 0.05% Tween-20 and resuspended in Maxpar Fix & Perm Buffer containing 63 nM Cell-ID Intercalator-Ir for 24 hours. Prior to data acquisition, organelles were washed twice with CSM, and twice with ultrapure water.

5.2.5 Mass Cytometry Data Acquisition and Pre-processing

Data was acquired on a CyTOF2 mass cytometer (Fluidigm, San Francisco, CA). Samples were diluted $1:10^6$ in a solution of 1× EQ Four Element Calibration Beads in ultrapure water to attain an event detection rate of approximately 300 events / second. Organelle event data was acquired using the following instrument parameters: noise reduction, cell length = 10-150, lower convolution threshold = 0.2. To define a blank for each sample, the $1:10^6$ diluted organelle suspension was filtered through a 0.2 µm polycarbonate filter to remove intact organelles. The resulting filtrate was analyzed in solution mode using the following parameters: step value = 1, settling time = 20 s, pushes / reading = 50. Intra-assay precision was assessed via technical replicates and showed detected event signal intensity was relatively stable in each monitored mass channel over thirteen hours of data acquisition (see Appendix C, Figure C1).

5.2.6 Mass Cytometry Data Analysis

Threshold values for signal above sample matrix noise for each monitored mass channel were calculated for each sample as the mean signal in a given channel plus three times the standard deviation (see Appendix C, Figure C2 and Table C2). Threshold values were used as the lower bound of gates when

identifying phenotypically distinct organelle populations (see Appendix C, Figure C3, red bars).

The number of ions associated with each organelle event (# $ions_{Ab}$) was calculated using the equation below, where DC_{Ab} represents the dual count signal of the antibody chelating a unique lanthanide isotope, defined as m. TE_m is the empirically determined transmission efficiency of unique lanthanide isotope *m* for the CyTOF2 at the University of Minnesota.

$$\frac{DC_{Ab}}{TE_m} = \#\ ions_{Ab} \qquad \text{Equation 5.1}$$

Then, the number of each unique antibody present per organelle (# Ab per organelle) was calculated using a correction factor via the following equation.

$$\frac{\#\ ions_{Ab}}{\text{correction factor}} = \#\ \text{Ab per organelle} \qquad \text{Equation 5.2}$$

The correction factor describes the number of lanthanide ions chelated to each antibody (listed in Table C1). This calculation was carried out for all antibodies, regardless of specificity. Organelle suspensions were stained with host-matched, isotype control antibodies, each chelating a unique lanthanide isotope, to estimate the non-specific binding proper-ties of each specific marker antibody. To obtain specific marker signal (corrected # specific Ab), the number of isotype antibodies per organelle (# isotype Ab) was subtracted from the number of specific antibodies per organelle (# specific Ab), using the following expression.

$$\#\ \text{specific antibodies} - \#\ \text{non-specific antibodies} = \text{corrected \# of specific antibodies}$$

Equation 5.3

Where appropriate, the corrected # of specific antibodies was normalized to the number of DDD-Tb molecules pre-sent in each organelle (corrected # specific Ab per organelle). This was done using the following equation, where $DC_{DDD\text{-}Tb}$ is the dual count signal measured for the DDD-Tb mass channel and TE_{159Tb} is the empirically derived trans-mission efficiency specific to the ^{159}Tb mass channel.

$$\frac{\text{corrected \# of specific Ab}}{\left(DC_{DDD\text{-}Tb} / TE_{159Tb}\right)} = \text{corrected \# specific Ab per organelle}$$

Equation 5.4

t-SNE analysis was done using the Rtsne package in the R statistical programming environment. The following parameters were used: perplexity = 20, Θ = 0.5, maximum iterations = 5,000, and eta = 10, resulting in a set of two-dimensional coordinates for each organelle used to plot clusters of individual organelles in two-dimensional space. Distributions for each relevant marker in a phenotypically identified population of organelles were binned into deciles. Coloring of the individual organelles in each t-SNE plot indicate the decile in which a given organelle falls.

5.3 Results and Discussion

5.3.1 Individual Organelle Detection via Didodecyl-DTPA-Tb Ligand

As discussed in Chapter 2, mass cytometry analysis of whole cells requires a diagnostic signal that distinguishes intact particles from debris and triggers mass spectra integration. In the case of whole cells, this is accomplished through the use of pentamethylcyclopentadienyl-Ir(III)-dipyridophenazine (Figure 5.1a). The generic identification of organelles by mass cytometry makes use of a didodecyl-diethylenetriaminepentaacetic acid (DTPA) ligand chelating $^{159}Tb^{3+}$ (DDD-Tb, Figure 5.1b). The long alkyl chains of DDD-Tb are incorporated into lipid bilayers,[146] making it an ideal reagent to label organelle membranes for mass cytometry analysis. A variation of the reagent was first described for use in mass cytometry by Leipold and who used it in the analysis of individual bacteria.[143]

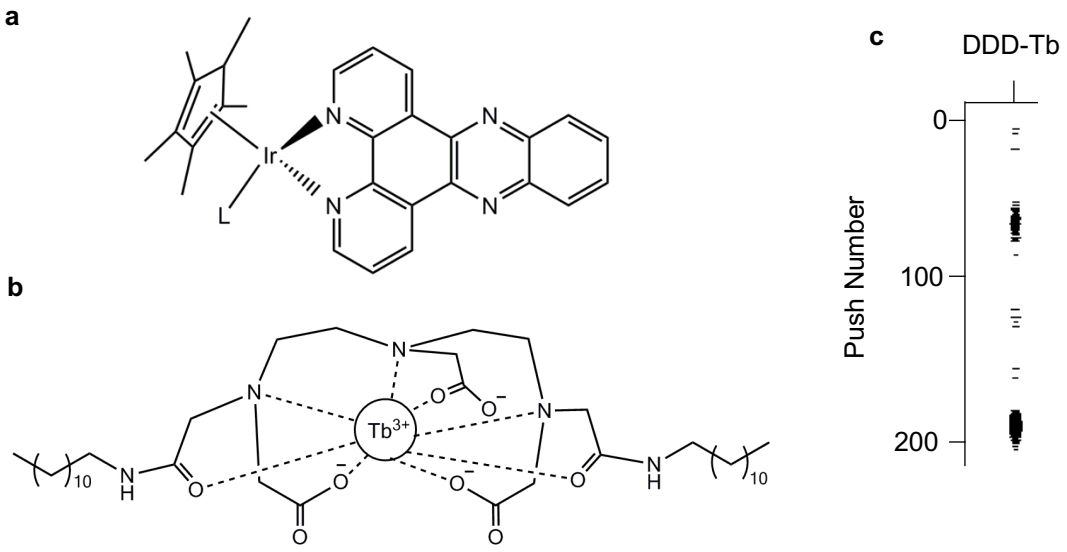

Figure 5.1 Structure and function of event identification ligands. (a) Structure of pentamethylcyclopentadienyl-Ir(III)-dipyridophenazine, a cell identification reagent commonly used in whole cell mass cytometry experiments. The planar aromatic portion of the ligand inserts into DNA base pairs with a low dissociation constant afforded through highly favorable electrostatic interactions, providing a stable measure of DNA per cell. Reprinted with permission from Schäfer.[57] (b) Structure of DDD-Tb, a general membrane stain used in this study to identify organelles. The long alkyl chains of DDD-Tb intercalate into lipid membranes providing an identifying signal for intact organelles. (c) Rain plot showing low background between two detected organelle events, n = 29,858 organelle events. The y-axis identifies the spectra (in sequence) over which detected organelle event signals are integrated. The x-axis shows the relevant m/z channel, ^{159}Tb. Dark lines in the plot area indicate detected $^{159}Tb^{3+}$ ions.

To define signals of organelle events a background signal was obtained by mass spectrometric analysis of filtrates resulting from filtering organelle suspensions through a 0.2-μm polycarbonate membrane (see Appendix C, Figure C2). Thus, the filtrate is devoid of organelles (>0.2-μm), the resulting signal plus 3 times the standard deviation was used as an organelle event identification threshold (see Appendix C, Table C2). We also sought to understand how organelle aggregates, detected as single events, would affect the results. Mass spectrometric analysis of filtrates of an organelle suspension filtered through 8.0- or 1.2-μm polycarbonate membranes, did not affect the modes of the DDD-Tb signal distributions (Figure 5.2a). Also, a QQ-plot comparison of the 8.0-μm filtered and unfiltered distribution show almost no variation (Figure 5.2b), indicating that detected organelle events in the unfiltered sample are <8.0-μm, and mostly

represent the detection of individual organelles. Autophagy-related organelles regularly fuse during the autophagy process, thus absolute autophagy-related organelle sizes will vary and likely be larger than that of the individual organelle alone.

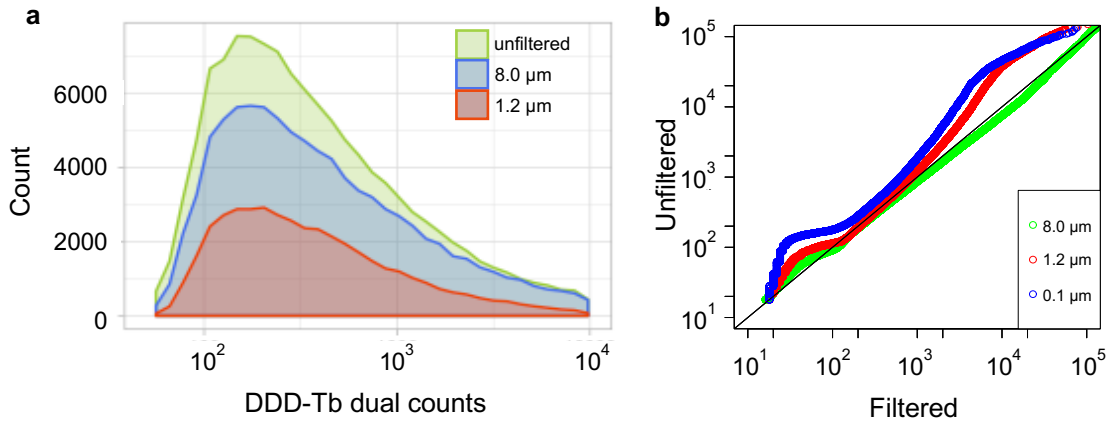

Figure 5.2 Individual Organelle Detection via Mass Cytometry. (a) Distributions of organelle frequency vs DDD-Tb dual count (DC) signal obtained after filtration through polycarbonate filters. The similarity in the mode of DC signal (unfiltered: 294 ± 2.5 dual counts, 8.0 µm: 323 ± 4 dual counts, 1.2 µm: 287 ± 4 dual counts), indicates that detected events represent are likely individual organelles rather than aggregated organelles. (b) QQ-plot comparing the DDD-Tb distributions of 0.1-, 1.2-, 8.0-µm filtered or unfiltered samples. The adherence of the 8.0-µm trace to an y = x line indicates the detection of organelles <8.0-µm as individual organelles.

5.3.2 Identification of Phenotypically Separate Organelle types via Antibodies in Multiple Tissues

Autophagy progression involves various organelle types. Here, these organelle types were identified by the unique pattern of antibodies bound to each organelle. Notably, autophagosomes and phagophores were detected through the binding of anti-LC3 antibodies and lysosomes were detected through the binding of anti-LAMP2 antibodies (see Appendix C, Figure C3). These organelle types made up 6% and 46% of the total number of phenotyped organelle events, from murine brain (Figure 5.3). That is, their relative number abundance was ~ 1:8. The only surrogate for comparisons of relative abundance of organelles found in the literature were cross-sections in TEM images of murine brain, which showed autophagosomal vacuoles and lysosomes, occupying 0.8 and 3.3% of the cytoplasmic cross-sectional area, respectively (relative abundance, ~ 1:4).[147-148]

While the relative abundance in this source and our data show the same trend, the remarkable feature of the mass cytometric results is the ability to deepen the classification of organelles detected, including autolysosomes (6%) and autolysosomes with mitochondrial association (4%), (Figure 5.3). Association between autolysosomes with their cargo (e.g. mitochondria) is critical to assess selective forms of autophagy (e.g. mitophagy) and to uncover their roles in biological systems.

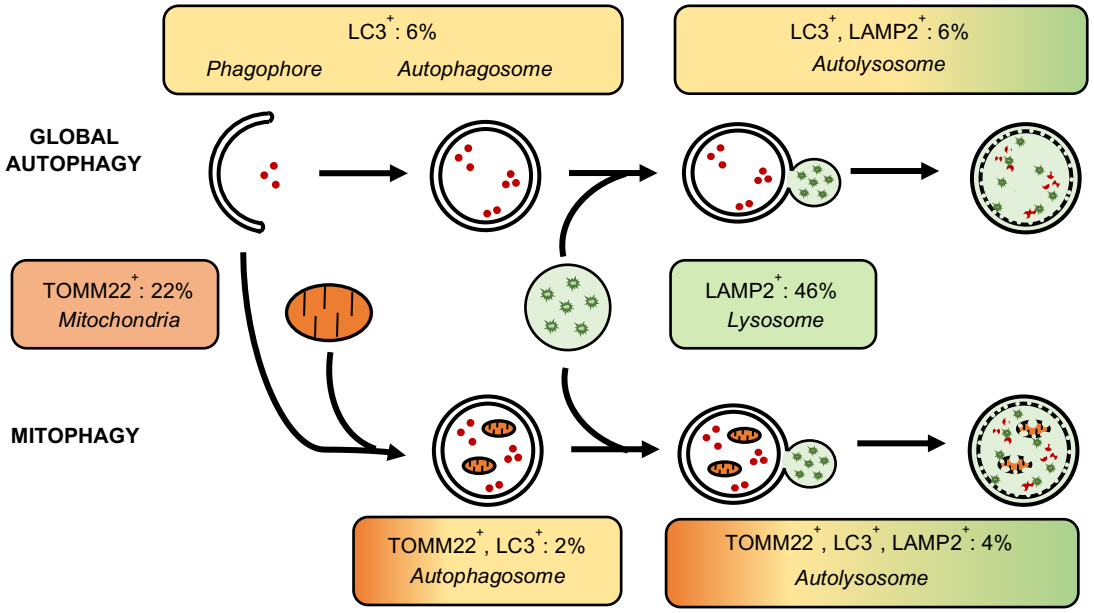

Figure 5.3 Phenotypically identified autophagy organelle populations via Mass Cytometry. Phenotypically identified organelles can be assigned to the unique organelles which make up the autophagy process. The percentage of each identified organelle type that participates in either macroautophagy or mitophagy in brain tissue is shown (see Appendix C, figure C4 for corresponding analysis of liver and skeletal muscle tissue).

Mass cytometry measurements allows for the calculation of the number of antibodies of each type bound to each organelle (equation 5.1-2 and Figure 5.4). Taking the number of DDD-Tb molecules per organelle as an indicator of relative total membrane volume, the number of antibodies of each type per organelle, normalized by membrane volume provide additional insight into autophagy progression. Whether monitoring the LAMP marker (lysosome → autolysosome, Figure 5.4a), TOM22 marker (mitochondria → mitochondria associated with the autophagosome → mitochondria associated with the autolysosome, Figure 5.4b),

or LC3 marker (autophagosome, phagophore → autolysosome, Figure 5.4c), the relative abundance of each marker decreases with autophagy progression, supporting a general increase of membrane content with a consistent number of markers per organelle. This decrease displays different rates for brain (B), liver (L), and muscle (M) (Figure 5.4), which may indicate custom responses to tissue-specific, autophagy-relevant stimuli such as nutrient availability. For $LAMP2^+$ organelles (lysosomes, Figure 5.4a), the number of normalized LAMP2 tags per event is lower for $LC3^+$-$LAMP2^+$ organelles representing autolysosomes (auto-lyso) and auto-lyso-mito events relative to lysosomes. This trend is less pronounced in organelles from liver. For $TOMM22^+$ organelles (mitochondria, Figure 5.4b), the number of normalized TOM22 tags per event was lower for dual-positive $LC3^+$-$TOMM22^+$ organelles representing autophagosomes associated with mitochondria (auto-mito), and even lower for triple positive $LC3^+$-$LAMP2^+$-$TOMM22^+$ organelles representing autolysosomes associated with mitochondria (auto-lyso-mito). This may be the result of an increase of lipid-rich membrane stained with DDD-Tb as multiple organelles associate, but the unchanging abundance of TOMM22 proteins per organelle. For $LC3^+$ organelles (phagophores, autophagosomes and autolysosomes, Figure 5.4c), the number of normalized LC3 tags is higher for autophagy organelles prior the association with lysosomes (auto-lyso), or mitochondria (auto-mito and auto-lyso-mito). It is worth noticing that the normalized abundance of LC3 tags is higher for auto-mito suggesting that a more extensive LC3-decorated membrane is required for processing mitochondria (mitophagy) than for other forms of autophagy. Thus, comparison of the number of specific markers between organelle types is a quantitative measure of autophagy progression in each tissue type (see Appendix C, Figure C5 for non-normalized antibody count per organelle).

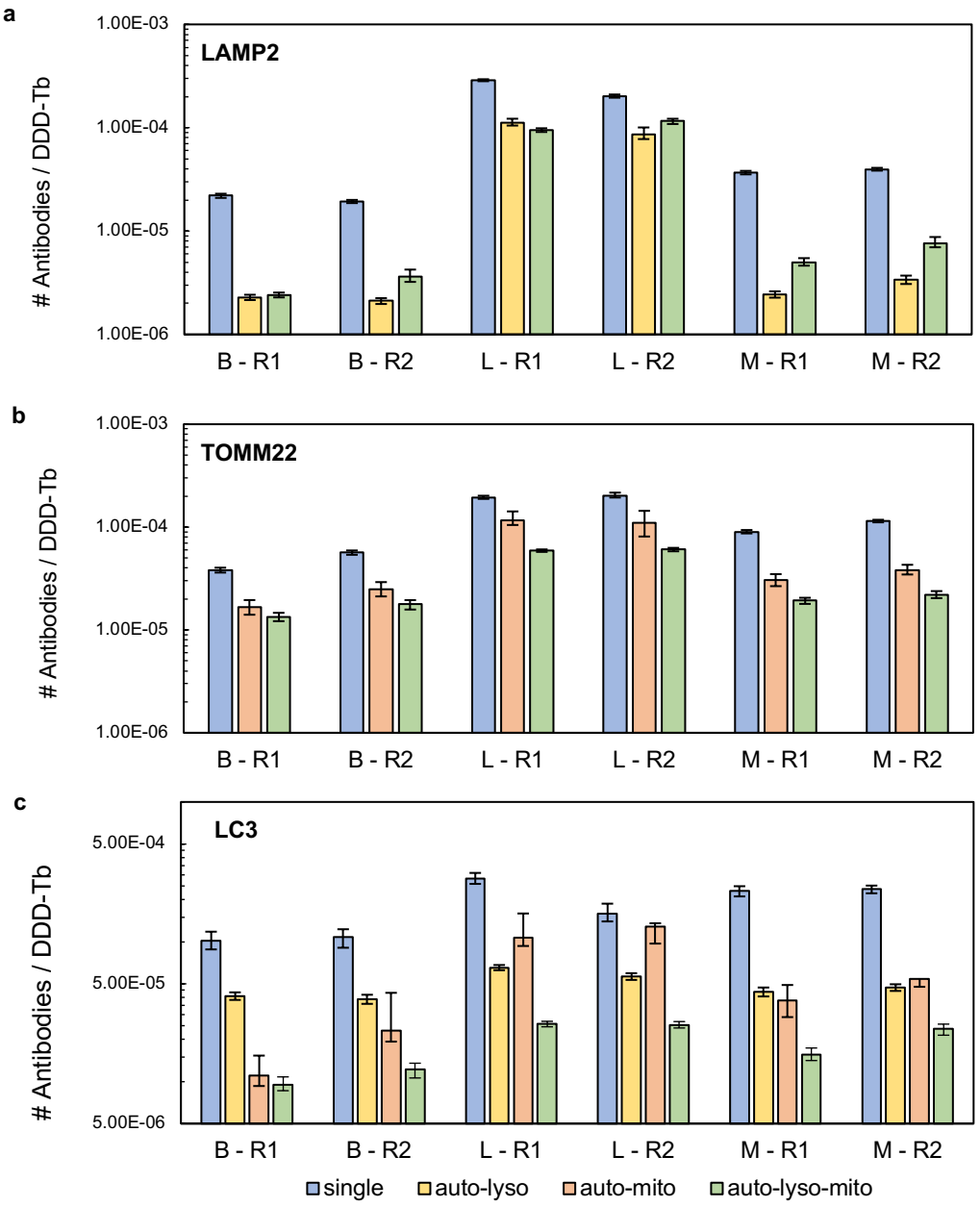

Figure 5.4 Normalized number of antibody tags per detected autophagy organelle. The number of specific marker antibodies per organelle was calculated and normalized by DDD-Tb abundance and then each marker was compared across phenotypically unique organelle populations from the same sample and across biological replicates. The number of specific antibodies varies across tissue but is consistent across biological replicates. See Appendix C, Figure C5 for non-normalized count of antibodies bound per organelle. Error represented as 95% confidence intervals of the median. B = brain, L = liver, M = skeletal muscle, R1 = biological replicate 1, R2 = biological replicate 2.

5.3.3 Multiplexed Analysis of Organelle Interactions

The true power of multi-parameter individual organelle analysis lies in the ability to detect heterogeneity in phenotypically identified organelle populations. Because organelles often traverse entire biochemical pathways, organelle heterogeneity may influence individual cell heterogeneity through significant changes in function. For example, heterogeneous changes in intracellular mitochondrial membrane potential have been associated with dysregulated gene expression of MFN1, MFN2 and OPA1 which normally facilitate mitochondrial fusion events. The dysregulation of these genes has been associated with a number of neurodegenerative diseases.[149-151] In order to assess inter-population organelle heterogeneity, organelles were clustered using the t-SNE algorithm,[152] such that organelles containing similar normalized levels of each antibody type, were close to one another in high-dimensional space. Based on relative cluster position, two dimensional coordinates are assigned to each organelle allowing for the two-dimensional projection of multi-dimensional data (Figure 5.5). Each column represents the two-dimensional projection of a given marker, while each row represents different combinations of organelle specific markers. Panels for triple positive organelles (Figure 5.5, first row) represent autolysosomes engaged in mitophagy. The second row of panels represent autophagosomes enveloping mitochondria, while the third row of panels represent autolysosomes *sans* mitochondria. The large variation in color (heat map) of each panel is indicative of inter-population heterogeneity. As expected, it is evident that even phenotypically similar organelles are not identical. Subpopulations of autolysosomes (Figure 5.5, third row) show fairly low heterogeneity as the decile classification for each marker is relatively similar (green dashed circles). This is not necessarily the case for the autophagosomes enveloping mitochondria (Figure 5, second row). The circled subpopulation indicates a relatively high abundance of the autophagosome marker LC3, but moderate abundance of TOMM22, a marker for mitochondria. The relative size of this subpopulation is very heterogeneous as indicated by the wide color variation in DDD-Tb signal. Taken together, we could speculate that this

particular subpopulation is a collection of autophagosomes at distinct points of closure around mitochondria. This same reasoning could be employed in the analysis of autophagosomes engaged in mitophagy (Figure 5.5, first row), in that the large variation in the circled subpopulation could represent different stages of degradation of mitochondria and release of LC3.

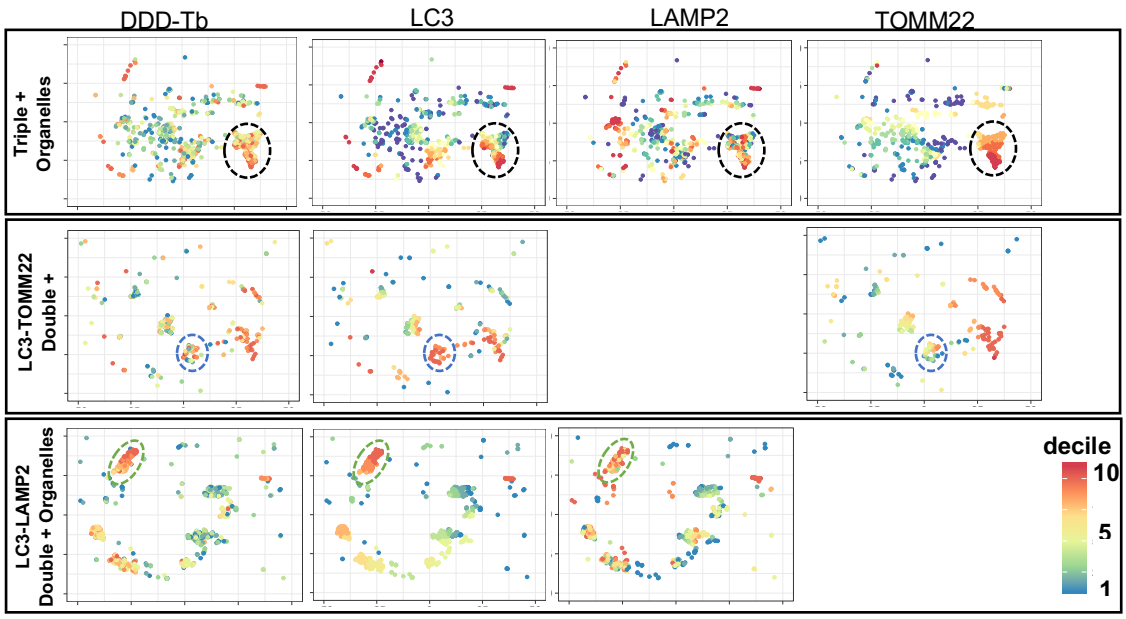

Figure 5.5 Two-dimensional cluster analysis of heterogeneous autophagy organelle sub-populations. t-SNE plots from brain tissue show phenotypically identified populations of organelles. Distributions of specific markers on individual organelles were binned into deciles and color-coded according to their assigned decile. Wide variation in color across specific markers in t-SNE plots indicate heterogeneous sub-populations (dashes), which may have significantly different function (see Appendix C, Figure C6 for analysis of liver and Figure C7 for analysis of skeletal muscle tissue).

5.4 Conclusions

Further analysis of these heterogeneous organelle populations will be possible using an expanded antibody panel to include other markers of macroautophagy and mitophagy such as the ubiquitous nucleoporin p62, PTEN-induced putative kinase 1, and Parkin. This type of high-dimensional individual organelle analysis could illuminate functional, morphological or phenotypic variation that drive disease development. This analysis used 6 of nearly 50 available mass channels, leaving room for many additional markers. We expect this multi-parameter technique to expand our understanding of sub-cellular

organelle variation in the progression of disease across many tissue and organelle types.

Chapter 6

Conclusions

The main outcomes of the work described in this thesis include the development of methods to i) correct for non-specific antibody binding in mass cytometry analyses enabling the measurement of autophagy flux in individual differentiating myoblasts, ii) measure autophagy flux in phenotypically identified cell subsets from skeletal muscle via mass cytometry, and iii) a method for the detection and characterization of individual autophagy-related organelles via mass cytometry.

In Chapter 3, we report a method for measuring autophagy flux in differentiating myoblasts made possible through identification of appropriate autophagy-related antibody staining concentrations. Optimization of autophagy-related antibody staining concentrations through *post-hoc* processing of titration data corrected for non-specific antibody binding and total antibody loading. Using the optimized antibody staining concentrations, we measured autophagy flux in an asynchronous culture of differentiating myoblasts. We found that autophagy is upregulated during mid-to-late differentiation as differentiating myoblasts fuse to one another or pre-existing myotubes and drops off as myotubes are formed. However, mitophagy flux increases earlier in the myogenic program, and persists past fusion through the formation of myotubes. This method is useful to identifying the point in myogenic lineage during which autophagy flux is required. One limitation of the method is the low cellular abundance of useful phenotypic and autophagy-related markers; improvements to the available mass cytometry reagent to address this limitation are described in Chapter 7.

In Chapter 4, we describe a method to measure autophagy flux in phenotypically identified mononuclear cells from murine skeletal muscle. We found that the satellite cell populations are significantly reduced in geriatric skeletal muscle, but no age-related correlation existed between the pro- or anti-inflammatory macrophages or fibroadipogenic progenitor cells. Autophagy flux was simultaneously quantified in each cell type. We found that autophagy flux is unaffected by age in anti-inflammatory macrophages. Conversely, we found that autophagy flux is decreased in both satellite cells and fibroadipogenic progenitors

from geriatric muscle. Interestingly, while autophagy flux was attenuated in both of these cell types, autophagy signalling (via p62) seemed to be intact in satellite cells. This work represents the first single cell analysis of autophagy flux fibroadipogenic progenitor cells and muscle-resident macrophages. Application of this method to additional biological replicates to validate our initial observations will provide insight into the observed decrease in autophagy flux reported at the bulk tissue level. One limitation of this method is the inability to relate cellular target abundance to function; one way to address this issue is to design mass cytometry compatible probes that report on function or specific protein activity as described in Chapter 7.

In Chapter 5, we describe a method for the detection and characterization of individual autophagy-related organelles from multiple tissue types via mass cytometry. This is made possible through the use of a lipid-intercalating, lanthanide chelating reagent and phenotypic antibodies. Due to the quantitative nature of mass cytometry detection, we were able to quantify the number of antibodies bound per organelle. We found extensive inter- and intra-population heterogeneity within and across tissue types. This tool will be useful in future studies characterizing organelle-organelle interactions. We recognized two limitations to this method. First, the low abundance of some cellular targets on individual organelles limits the range of possible biological questions that could be probed, though as mentioned above this is addressed in Chapter 7. Second, the availability of reliable antibodies against autophagy-related organelles is quite low. Chapter 7 describes a selection of aptamers specific to autophagosomes for their specific detection. In addition, Chapter 7 also describes the synthesis of a novel small molecule for the functional labelling of mitochondria for individual organelle analyses via mass cytometry.

Overall, the work described in this thesis represent the development of new methods for the measurement of autophagy flux via mass cytometry. Further development of these methods to include additional relevant autophagy-related markers or phenotypically unique cell subsets will deepen our current

understanding of the contribution dysregulated autophagy plays in the development of age-related muscle mass and functional decline. The insight gained may lead to new treatments for age-related musculoskeletal disorders.

Chapter 7

Future Work

Drs. Valerie Pierre and Evan Weitz assisted in developing the synthetic scheme for the dendrimer mass tag. Dr. Sylvie Pallioux assisted in the synthesis of the mitochondria-targeting functional reagent. Dr. Mark Distefano and Kiall Suazo provided the isoprenoid analog for prenylation measurements.

Current limitations to the comprehensive analysis of autophagy flux in skeletal muscle via mass cytometry include inadequate sensitivity for low abundance cellular targets and morphological constraints of cells. The sensitivity of mass cytometry analyses is limited by inherent design of biological reporters. Specifically, the relatively low number of lanthanide ions chelated per antibody limits analyses to cellular targets that are in high abundance in each cell, and the unavailability of reliable antibodies for each cellular target of interest limits the range of most studies involving autophagy. The analyses presented in each chapter of this work could be enhanced by the addition of other low abundance markers of selective autophagy processes. The method describing the analysis of individual organelles by mass cytometry (see Chapter 5) is also limited by the relatively low abundance of cellular targets per organelle but has the added conundrum of non-unique phenotypic cellular targets. For instance, detection of autophagy-related organelles via metal-labelled anti-LC3 antibodies will provide data encompassing all autophagy organelles labelled with LC3-II (i.e. phagophore, autophagosomes, autolysosomes), regardless of their unique function.

Morphological constraints on cells for mass cytometry analysis originate with the design of the instrument which affect the delivery of large and non-spherical cells to the ICP torch. While chapters 3 and 4 describe autophagy flux in a variety of cell types involved in myogenesis and the maintenance of skeletal muscle via mass cytometry, monitoring autophagy flux in other important cell types such as segments of muscle fibers is currently hindered by the unique morphology of these multi-nucleated, cylindrical cells. The future work described here will focus on both available labelling reagents to address the issues for quantifying autophagy flux using mass cytometry at the individual cell or organelle level and improvements to methodology for the analysis of morphologically unique cell types.

7.1 Improving Available Mass Cytometry Reagents

Available mass cytometry reagents can be categorized by function into two main categories, intact cell identification and biological reporters. Metallointercalators are an example of an intact cell identification reagent, which works towards identification of intact cells via intense, detectable signal in individual cells after intercalation into dsDNA. Antibodies labelled with MCPs are an example of a biological reporter, which report on the biological phenotype or function of a given cell or organelle. As described in Chapter 2, metal chelating polymers commonly used in mass cytometry are composed of a linear polymer backbone decorated with multidentate polyaminocarboxylates, such as diethylenetriaminepentaacetic acid (DTPA), which coordinate lanthanide ions with relatively low dissociation constants ($K_d = 10^{-16}$).[53] The polymer is covalently bound to an antibody though a maleimide linker which reacts with sulfhydryl groups produced by reducing disulfide bonds within the Fc portion of the antibody[50] (see Figure 2.5). Each antibody can bind four to five polymers each containing about 30 lanthanide atoms each, for an average of 120-160 reporter ions per antibody.[153]

A main limitation in quantifying autophagic flux is a lack of unique markers for each type organelle involved in the cellular process. With nearly 30 known ATG proteins, the variety of proteins expressed at each step of the autophagic process is astonishing, but with some organelles containing many of these proteins constitutively, it is difficult to unambiguously identify each organelle simultaneously.[154] Table 7.1 shows that some organelles uniquely express a target protein that can be detected using antibodies as a selective marker in quantitative

Table 7.1. Unique target proteins for autophagy organelles. A lack of unique target proteins for autophagy organelles complicates the analysis of autophagy flux.

Autophagy Organelle of Interest	Unique Target Protein
Phagophore	LC3-II
Autophagosome	LC3-II
Autolysosome	LAMP2, LC3-II
Lysosome	LAMP2
Mitochondria	TOMM22

assays. Conversely, autophagosomes and phagophores lack uniquely expressed proteins, making them difficult to specifically observe. As described in Chapter 2, LC3 detected in individual cells using commercially available antibodies can be attributed to either organelles (LC3-II) or unprocessed, cytosolic protein (LC3-I).

For these reasons, improvements to lanthanide chelating molecules and specificity conferring reagents would drastically improve the analyses of autophagy flux via mass cytometry.

7.1.1 Development of Dendrimers for Improving Technique Sensitivity

The main limitation of the currently available linear lanthanide loaded polymer is the possibility of false negatives for low abundance cellular targets such as the transcription factor Pax7 used in Chapter 3, and most targets found on individual organelles analysed in Chapter 5. Due to the relatively low number of lanthanide atoms associated with each antibody, low abundance cellular targets (< 5,000 copies/cell) may not be effectively sampled by the ICP-TOF-MS leading to a false negative result. This is due to the low number of ions that successfully navigate the three-aperture interface that serves to sample only the middle of the ion beam exiting the ICP torch.[42, 153] Two approaches to resolve this problem include: i) improve the limit of detection for the ICP-TOF-MS by major hardware improvements, or ii) chelate more lanthanide atoms per polymer. Improvements to lanthanide chelating polymers would need to increase the number of chelated lanthanide ions between 7-9 fold to achieve limits of detection similar to flow cytometry.[155]

Extending the length of the commonly used linear polymer[50] to add additional DTPA-containing monomers is a possibility, but other challenges arise when an extremely long tail-like polymer is able to wrap around the antibody and interfere with the specificity-conferring hypervariable region.[156] Lanthanide ion nanocrystals were recently reported[157-158] as mass tags for improved sensitivity in mass cytometry analyses. While lanthanide nanocrystals would exponentially increase

the number of lanthanide ions per antibody, improving sensitivity, the wide distribution in the number of lanthanide ions per nanocrystal is not suitable for analytical analysis of cellular target abundance. A more efficient and controlled method of increasing the number of lanthanide atoms chelated per antibody without interfering with cellular target binding is to synthesize a metallo-dendrimer with a globular macrostructure that can be tethered to the non-variable region via a relatively short carbon chain.

Synthetically derived dendrimers are generally described as containing a central core with radially stemming monomers, often creating large tree-like macrostructures.[159] The overall structure of a dendrimer can be described as having three separate regions: the core, the interior (branches), and the periphery (Figure 7.1).

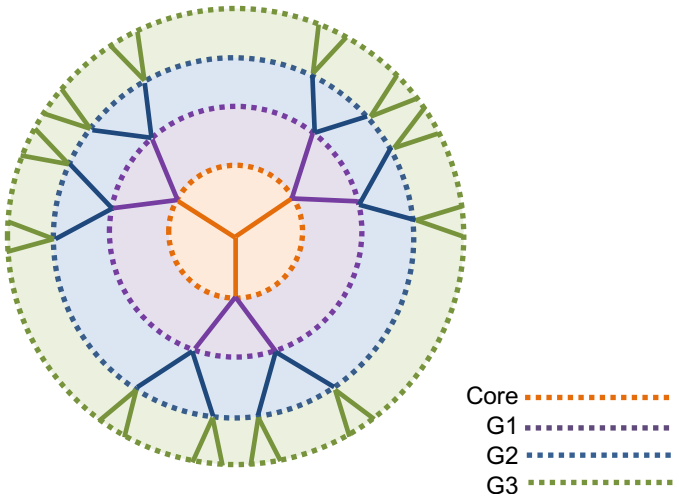

Figure 7.1. Schematic of G3 dendrimer scaffold. Each generation is shown in a different layer with dotted lines showing branch points. Figure modified with permission from Lee. [160]

The number of points at which the interior structure branches defines the generation (G1, G2, G3). The step-wise synthesis of dendrimers result in theoretically mono-disperse synthesis, as opposed to statistically controlled synthesis typically used for linear polymers. The final size of the dendrimer is ultimately governed by the lack of three-dimensional space available for further growth.[160] Metallo-dendrimers have been reported[161-162] with a number of different theoretical designs, including those with metals only at their core, only at the

periphery, scattered throughout the interior branches, or a combination of all three.[159] In order to increase the sensitivity of mass cytometry, a maximum number of lanthanide atoms would need to fit into each dendrimer.

In collaboration with Dr. Valerie Pierre and Dr. Evan Weitz, a lanthanide containing dendrimer we have designed a synthetic plan to produce a dendrimer capable of chelating 1,093 lanthanide reporter ions in six generations. The synthesis will be accomplished in four synthetic schemes. To date, attempts to complete this synthetic plan have produced products in low yield hindering progress. These issues are addressed in the "Improvements for synthetic schemes" sub-heading of this section (see page 99).

In short, this synthetic plan describes a divergent dendrimer synthesis. Three separate schemes will provide three unique macrocycles (CORE, MONOMER A, and MONOMER B) bearing four pendant arms in a 1:3 ratio. The core macrocycle will be used as a scaffold to which Monomers A and B will be added in a stepwise fashion to assemble the macrostructure. To minimize the number of synthetic steps needed to attach each subsequent shell of monomer, a two-step deprotection-reaction scheme will be used. The reaction is based on the original 1,3-Huisgen cycloaddition "click" chemistry, which consists of a Cu(I)-catalyzed alkyne azide [3 + 2] cycloaddition (CuAAC) to form a 1,4-disubstituted 1,2,3-triazole group.[163] There are many practical advantageous characteristics of the CuAAC reaction in the context of dendrimer construction, including quantitative yields, a broad set of compatible reaction conditions, and simplified work-up steps.[164]

General Considerations

In each scheme, a common synthetic method is used to install pendant arms on each nitrogen of 1,4,7,10-tetraazacyclododecane (cyclen). The common functional group at one end of each fully synthesized pendant arm is an α-

bromoacetamide, whose substitution on each of the nitrogens of cyclen forms an appropriate lanthanide chelating environment. Each pendant arm contains an alkyl chain terminated with a primary amine, which forms the α-bromoacetamide after reaction with bromoacetyl bromide. Another common theme in each monomer synthesis one unique arm and three identical others. Each monomer is first mono-substituted with one pendant arm[165] and then exhaustively alkylated to yield a fully-substituted DOTA-tetramide ligand. The second alkylation is accomplished by reacting one equivalent of the mono-substituted cyclen with an excess of the second pendant arm. As shown in the following sections, the monomer arm composition changes for each monomer, but all arm installations follow a common reaction pathway.

Dendrimer Core (Scheme 7.1)

The first pendant arm of the dendrimer core contains a 3400 MW polyethylene glycol (PEG) moiety that will serve as an attachment point when the completed dendrimer is conjugated to a specificity conferring reagent. This tether is attached to the core to take advantage of the selectivity afforded by a single attachment point. Specifically, a commercially available 3400 MW PEG, terminated with an Fmoc-protected amine on one side and carboxylic acid on the other side (**CORE-2**), will be coupled to UV-active 2-(9,10-dioxo)anthrylmethyl group to yield a an ester (**CORE-3**). The resulting pendant arm is UV-active to aid in detection of the compound throughout the synthesis. This protecting group

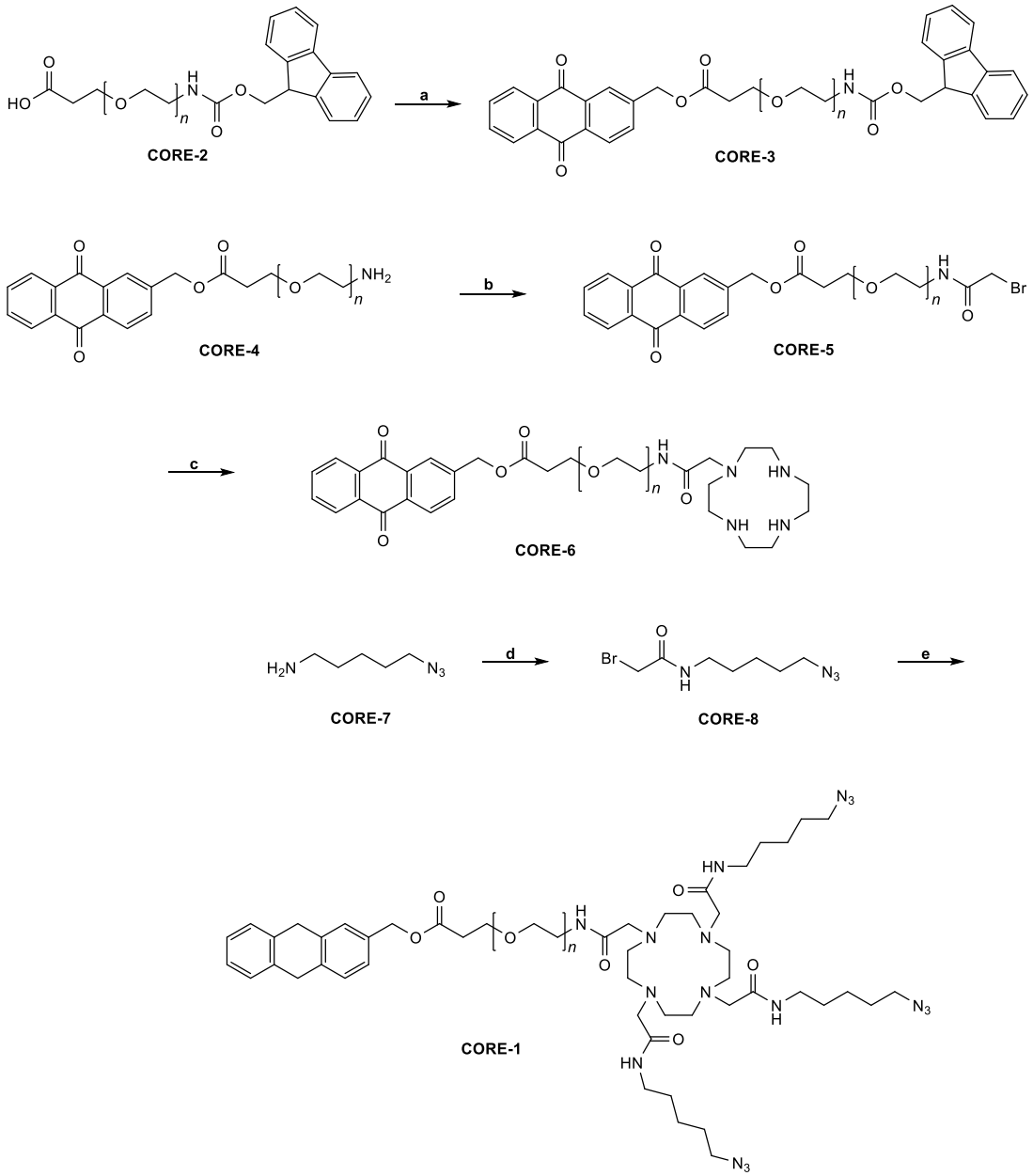

Scheme 7.1. Synthesis of dendrimer core. Reagents and conditions: (a) MOM, $SOCl_2$, DMSO; (b) piperidine, CH_2Cl_2; (c) bromoacetyl bromide, K_2CO_3, CH_2Cl_2, H_2O; (d) bromoacetyl bromide, K_2CO_3, CH_2Cl_2, H_2O; (e) CORE-6, K_2CO_3, MeCN.

will be used following reports that the anthrylmethyl moiety is stable to TFA.[166] This functionalization will be done using thionyl chloride in DMSO which should quickly and efficiently yield the ester through an acid chloride intermediate. If the thionyl chloride coupling conditions are found to affect the functionality of the Fmoc-protected terminal amine, standard coupling conditions such as EDCI or

HOBT/HBTU will be used. Following purification and characterization, the Fmoc-protected amine will be deprotected using piperidine (**CORE-4**) and reacted with bromoacetyl bromide to yield the heterobifunctionalized PEG pendant arm (**CORE-5**). As previously described, this pendant arm will be mono-substituted on cyclen (**CORE-6**). The second arm on the dendrimer core will be an alkyl azide, achieved by reacting the commercially available 5-azidopentan-1-amine (**CORE-7**) with bromoacetyl bromide to yield the completed azide pendant arm (**CORE-8**). Should it be needed, flash chromatography will be used to purify the completed arm. The azide arm will then be mono-substituted onto the mono-substituted cyclen (**CORE-6**) to yield the fully-alkylated DOTA-tetramide core (**CORE-1**). The resulting completed dendrimer core will be purified by size exclusion chromatography (SEC), and characterized using ^{1}H and ^{13}C NMR, and high resolution ESI-MS.

Monomer A (Scheme 7.2)

Completed Monomer A (**A-1**, Scheme 8.2) will be reacted with the synthesized **CORE-1** product (Scheme 8.1) resulting in a G1 dendrimer. Therefore, a pendant arm with a terminal acetylene group is needed on **A-1** to react with the azide functional arms of the dendrimer core (**CORE-1**) using “click” chemistry. This will be achieved by reacting commercially available propargylamine (**A-2**) with bromoacetyl bromide, to substitute the terminal amine with a bromoacetamide group yielding the completed propargylic pendant arm (**A-3**). If needed, flash chromatography will be used to purify the resulting product. The propargyl arm will then be mono-substituted onto cyclen (**A-4**). The other pendant arm will be a heterobifunctional PEG, terminated by α-bromoacetamide on one end and BOC-protected terminal amine on the other (**A-7**). This molecule will be produced by a selective mono-protection of commercially available bis(3-aminopropyl)diethylene glycol (**A-5**) with di-tert-butyl-dicarbonate (BOC_2O). Mono-BOC protection of a terminal amine will prevent a single PEG diamine substituting onto the cyclen ring in later synthetic steps. The product will be purified, if necessary using column chromatography. The mono-BOC-protected product (**A-**

5) will then be functionalized with an α-bromoacetamide group, through treatment with bromoacetyl bromide (**A-7**) and purified with flash chromatography. The purified product will be used to fully alkylate the mono-substituted cyclen (**A-4**) to form the tetra-substituted DOTA-tetramide monomer (**A-1**). The monomer product (**A-1**) will then be purified by SEC. The final product as well as intermediates will be characterized by ^{1}H and ^{13}C NMR and high resolution ESI-MS.

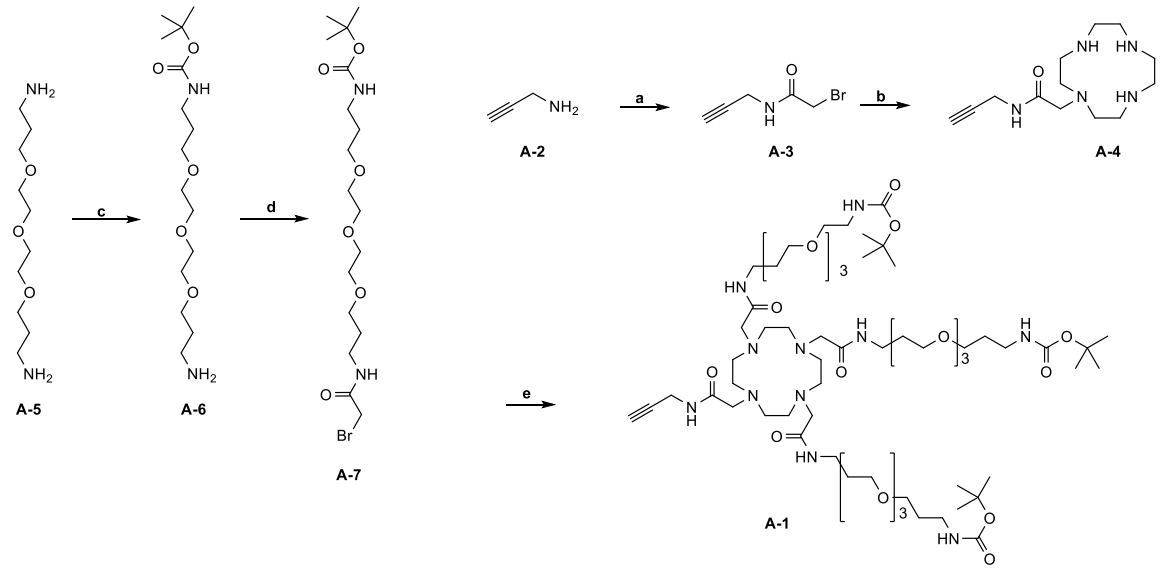

Scheme 7.2. Synthesis of monomer A. Reagents and conditions: (a) bromoacetyl bromide, K_2CO_3, CH_2Cl_2, H_2O, 1 h; (b) Cyclen, Et_3N, $CHCl_3$, 60°C, 18 h; (c) BOC_2O, CH_2Cl_2, 18 h; (d) bromoacetyl bromide, K_2CO_3, CH_2Cl_2, H_2O, 1 h; (e) K_2CO_3, MeCN 60°C, 18h.

Monomer B (Scheme 7.3)

Of the four pendant arms on completed monomer B (**B-1**, Scheme 7.3), only one will react with the three terminal amine pendant arms on monomer A (**A-1**, Scheme 7.2). A carboxylic acid on completed monomer B (**B-1**), will react with the deprotected primary amine on monomer A (**A-1**) to form the amide. This pendant arm will be formed in four synthetic steps. First, the carboxylic acid of 6-(Fmoc-amino) hexanoic acid (**B-2**) will be protected via Fischer esterification (**B-3**). Methoxy methanol (MOM) was chosen as a protective group due to its ease of installation and mild orthogonal deprotection reaction conditions ($MgBr_2$, DMF). Next, the Fmoc-protected amine will be deprotected using piperidine to expose the

terminal amine (**B-4**), which will be subsequently treated with bromoacetylbromide to yield the completed arm (**B-5**). The completed arm will then be mono-substituted onto cyclen (**B-6**). The products and its preceding intermediates will be purified by flash chromatography, where needed. The remaining pendant arm will be the same azide arm synthesized and substituted onto cyclen in the dendrimer core scheme (**CORE-8**). The mono-substituted cyclen (**B-6**) from scheme 8.3 will be alkylated with the azide pendant arm (**CORE-8**), from scheme 1 to form the fully alkylated DOTA-tetraamide monomer B. Following purification by SEC, the final monomer will be characterized by ^{1}H and ^{13}C NMR and high resolution ESI-MS.

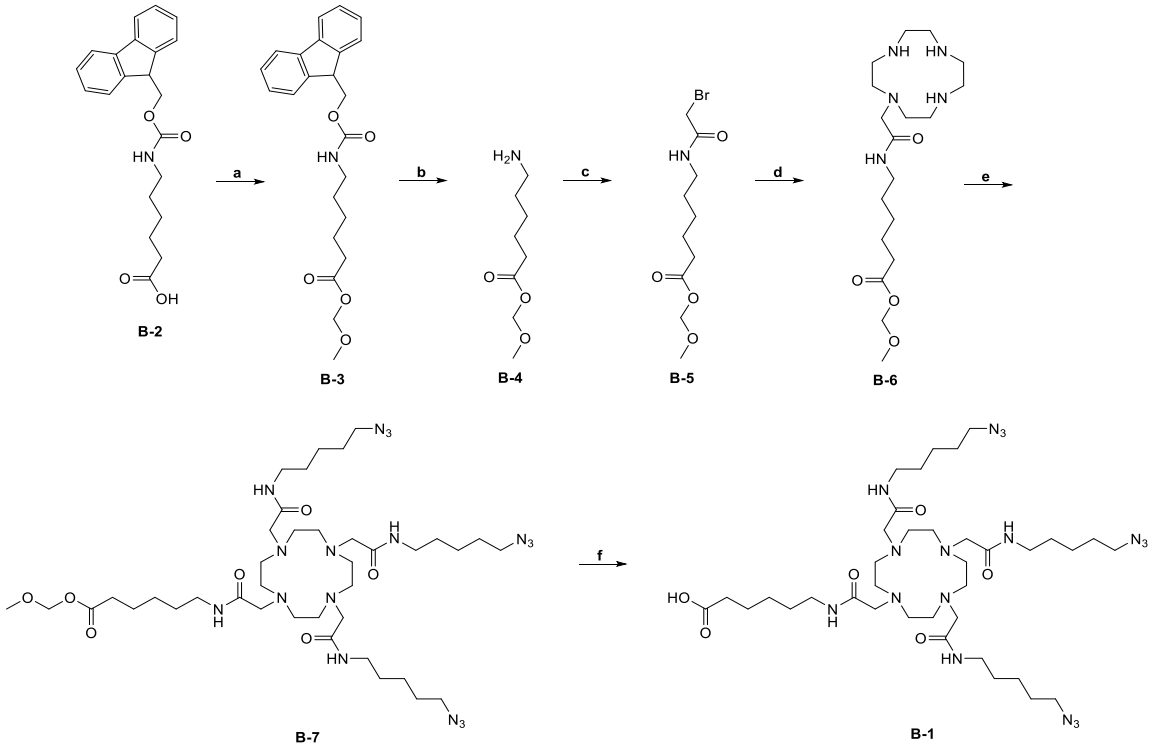

Scheme 7.3. Synthesis of monomer B. Reagents and conditions: (a) MOM, H_2SO_4, H_2O; (b) piperidine, CH_2Cl_2; (c) bromoacetyl bromide, K_2CO_3, CH_2Cl_2, H_2O; (d) Cyclen, Et_3N, $CHCl_3$, 60°C, 18 h; (e) B-6, CORE-9, K_2CO_3, MeCN; (f) $MgBr_2$, DMF.

Final Dendrimer Construction (Scheme 7.4)

Once all three monomers are synthesized, the dendrimer can be assembled. Before beginning assembly, the choice must be made whether to chelate the lanthanides pre- or post-assembly. The ability to add the lanthanide post-assembly is appealing from the ease of application standpoint, where a lanthanide of choice

could be chelated by an empty polymer directly before use in mass cytometry, as is currently done. However, some dendrimer assembly reaction conditions require the use of tetrafluoroacetic acid (TFA), which could work to unseat a lanthanide from any of the DOTA tetraamides. Conversely, as the dendrimer is synthesized, each DOTA moiety becomes progressively more sterically hindered. This could result in difficult metallation, reducing the magnitude of the expected increase in sensitivity obtained by using a high lanthanide-capacity dendrimer. At this time, the more important characteristic to be assessed is the gain in sensitivity obtained when using this dendrimer scaffold. To that end, metalated monomers are preferable.

To assemble the dendrimer, three distinct synthetic steps are performed (Scheme 7.4). First, one equivalent of the dendrimer core (**CORE-1**) and three equivalents of monomer A (**A-1**) will be reacted together in the presence of five equivalents of copper (I) ascorbate at an acidic pH. The resulting product, a G1 dendrimer (**FA-2**) will then be purified by SEC. Following purification, the G1 dendrimer will be subjected to standard TFA deprotection will remove the BOC-protecting groups from the primary amines at the periphery of the molecule (**FA-3**). In the second step, one equivalent of the product from the previous step, a deprotected G1 dendrimer (**FA-3**), will be added to three equivalents of monomer B (**B-1**) in standard amide coupling conditions, linking G1 and G2 (**FA-4**). The G2 dendrimer will be purified using SEC. In the next step, one equivalent of the G2 dendrimer (**FA-4**) formed in the previous step, will be reacted with three equivalents of monomer **A** (**A-1**) in the presence of copper (I)

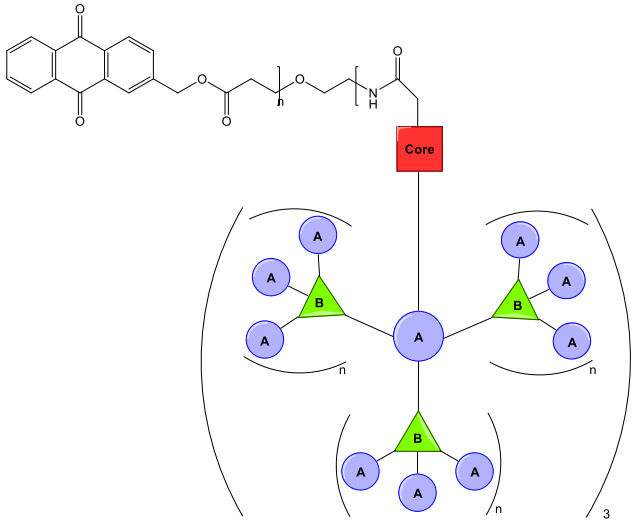

Figure 7.2. Simplified representation of synthesized metallodendrimer. Each shape represents a unique monomer (A or B synthesized in schemes 8.2 or 8.3, respectively) which chelates a single lanthanide ion. Assuming complete metallation of all monomers, the G3 dendrimer shown will chelate 180 lanthanide ions.

ascorbate at an acidic pH. The resulting G3 dendrimer (**FA-5**) will then be purified by SEC. The G3 dendrimer with peripheral BOC-protected primary amines will then be subjected to standard TFA deprotection. The second and third steps are then repeated in order and as described, until the dendrimer is of desired size (Figure 8.2). Following final construction of the dendrimer the UV-active moiety from the exposed, tail end of the 3400 MW PEG will be cleaved to reveal a carboxylic acid available for conjugation to primary amines on an appropriate antibody.

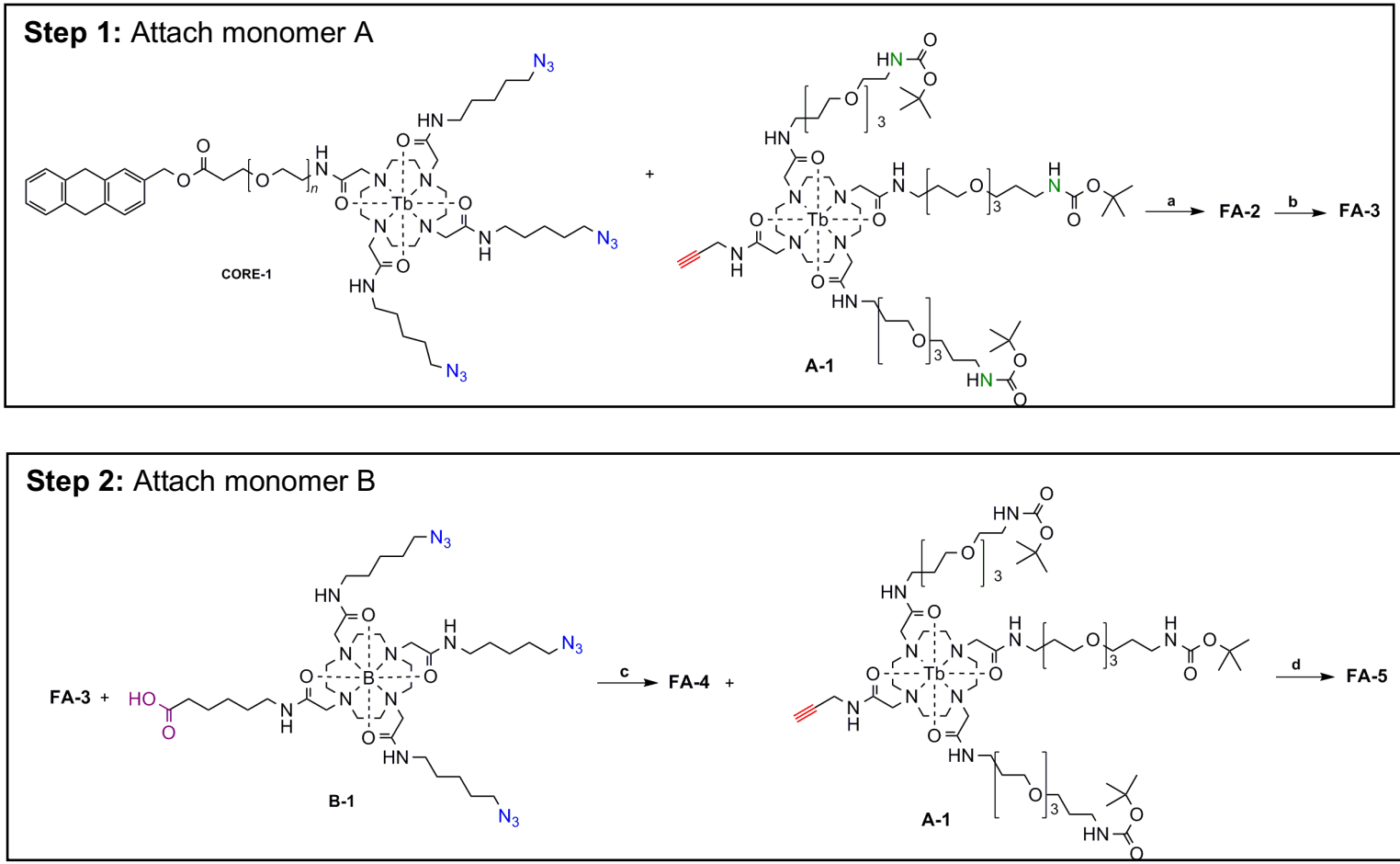

Scheme 7.4. Dendrimer Final Construction. Reagents and conditions: (a) Cu (I) Asc., pH 4.5, RT; (b) TFA, CH_2Cl_2, 0°C to RT; (c) EDCI, HOBt, $(^iPr)_2$, EtN, DMF; (d) Cu (I) Asc., pH 4.5, RT; (e) TFA, CH_2Cl_2, 0°C to RT. Azides on CORE-1 and B-1 will react with alkynes in A-1. Primary Amine revealed in FA-3 will react with carboxylic acids in B-1. A simplified depiction of the final product is shown in Figure 8.2.

Final characterization of the dendrimer will determine the total number of lanthanide ions chelated by each dendrimer. In addition, it will be important to understand how many dendrimers of a particular size can be conjugated to each specificity conferring reagent. The number of chelated lanthanides increases exponentially (Figure 7.3). If similar sensitivity can be achieved by labelling an antibody with a single G6 dendrimer (1,093 chelated lanthanides) or multiple G5 dendrimers (364 chelated lanthanides) synthesis could be simplified.

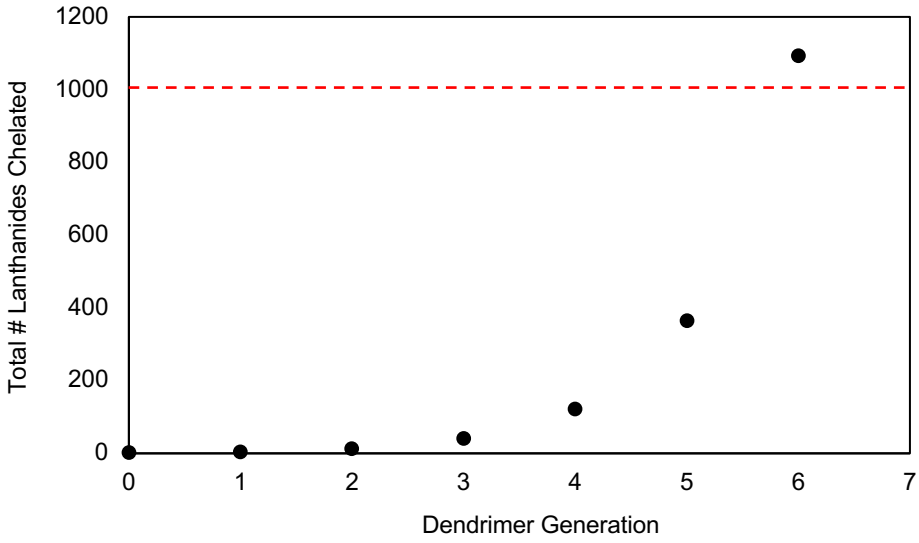

Figure 7.3. Exponential increase in chelated lanthanides with each generation. The synthetic goal was to chelate at least 1,000 lanthanide ions per polymer. In reality, the attachment of multiple, lower generation dendrimer could produce similar technique sensitivity and provide a less complicated synthesis.

Improvements for Synthetic Schemes

The designed dendrimer synthesis spans four schemes that are not synthetically trivial. Initial attempts at the synthesis of monomer A showed the monoprotection of bis(3-aminopropyl)diethylene glycol (Scheme 7.1, **A-6**) using BOC produced product in low yield (15%) with the di-protected species as the dominate product. To circumvent these issues, improvements can be made to the proposed schemes to take advantage of newly commercially available reagents such butyne-DOTA (Macrocyclics, Plano, TX), which would simplify the synthesis of monomer A (Scheme 7.1) through elimination of the mono-substitution of cyclen

(**A-4**) with the synthesized propargyl arm (**A-3**). The availability of carboxylic acids on DOTA also eliminates the need for the mono-functionalization of the bis(3-aminopropyl)diethylene glycol, which we found was difficult to synthesize with high yield. In addition to the improvements to Scheme 7.1 described above, a recent report showed an improved method for covalently linking MCPs to specificity conferring reagents using strain-promoted copper-free azide–alkyne [3+2] cycloaddition chemistry (SPAAC) or tetrazine-strained alkene [4+2] inverse electron demand Diels–Alder cycloaddition to conjugate MCPs to specificity conferring molecules.[167] The authors describe MCPs with a terminal azide or *trans*-cyclooctene moieties, chelating 50 lanthanide ions per MCP. This method could be incorporated to the final dendrimer assembly, providing site-specific control during covalent linking to an antibody or other specificity conferring reagent. The inherent limitation to this approach lack of availability of cyclooctene or tetrazine moietites on most commercially available antibodies.

The successful completion of this synthesis will yield a G6 dendrimer capable of chelating at least 1,093 lanthanide ions per molecule. Used as a mass tag for antibodies specific to low abundance cellular targets will unlock a new dimension biological inquiry probed using mass cytometry. Specifically, it will be possible to reliably measure low abundance transcription factors and post-translational modifications involved in myogenesis and autophagy flux, adding new dimensions to the analyses performed in Chapters 3 and 4. In addition, the use of lanthanide chelating dendrimers could improve the detection of individual organelles through the expansion of detectable targets that are too low in abundance on individual organelles.

7.1.2 Development of Aptamers Against Autophagosomes

Immuno-labelling via antibodies is frequently used to specifically label a cellular target of interest. In autophagy-related research an antibody against microtubule light chain 3 (LC3) is routinely used to specifically identify the presence of autophagy-related organelles, as was done in Chapters 3 through 5. Not only does this protein have at least two isoforms (LC3-I, cytosolic; and LC3-II, lipid

bound; see Chapter 2, Figure 2.17), autophagy proceeds through at least four functionally unique organelle types, all of which contain LC3-II protein. Therefore, immuno-labelling LC3 for individual cell or organelle analysis is insufficient for the elucidation of a fundamental understanding autophagy flux.

In the case where a cellular target (i.e. an organelle) does not have a unique characteristic that can unambiguously identify it, alternate probes are needed. Aptamers are ssDNA or single stranded RNA oligonucleotides that fold in on themselves to form distinctive three-dimensional secondary structures that specifically bind unique surface characteristics of a desired target.[168] Aptamer secondary structure is made up of common motifs, such as: hairpin stems and loops, bulges flanked by helical regions, pseudoknots, and G quartets. Generally, aptamers are 40-80 bp, with longer sequences able to form more complex secondary structures sometimes resulting in higher affinity products.[169] Aptamers have been developed against whole cells without a particular surface target in mind.[170]. The same logic could be applied to the development of an aptamer specific to individual autophagy organelles.

Functionally, antibodies and aptamers are similar in that both interact with specific substrates based on favorable electrostatic, H-bonding, and dipole-dipole interactions. The most favorable interactions occur between a target and ligand that have mirror image surface shapes and compatible charge distributions.[171] A major morphological difference that distinguishes them from one another is the relative rigidity of oligonucleotides as compared to the hypervariable regions of antibodies. Of the functional groups that make up aptamers, only the ribose ring, phosphodiester and glyosidic bonds have any significant torsional mobility, with base pairing further restricting movement within aptamers. Therefore, during aptamer development poor conformational or unfavorable energetic fits to a target cannot be selected, due to rigidity of the structure. In this way, it is unlikely that an aptamer will be developed that has high affinity ($K_d = 10^{-6} – 10^{-9}$)[172] without having high specificity. In contrast, hypervariable regions of antibodies are comprised of a wide variety of amino acids with largely variable side chain moieties, giving both

the backbone and side chains more torsional mobility. A more flexible structure in antibody hypervariable region can result in less selective binding.[171]

Aptamer sequences are selected from a large (10^{14}) pool of ssDNA oligonucleotides via selective evolution of ligands by exponential enrichment (SELEX), first described by Tuerk[173] and Ellington[174] in 1990. In the case of Organelle-SELEX, a random library of about 10^{14} single stranded DNA sequences is first incubated with a suspension of organelles (Figure 7.4). A fractionation step follows where unbound oligonucleotides are removed, and the remaining target-bound aptamers are amplified via a polymerase chain reaction (PCR). The PCR reaction produces many sequences with higher overall affinity for the target than the original DNA library. The SELEX process is iterative in that the new library is used for subsequent rounds of selection. After each round of selection, aptamer

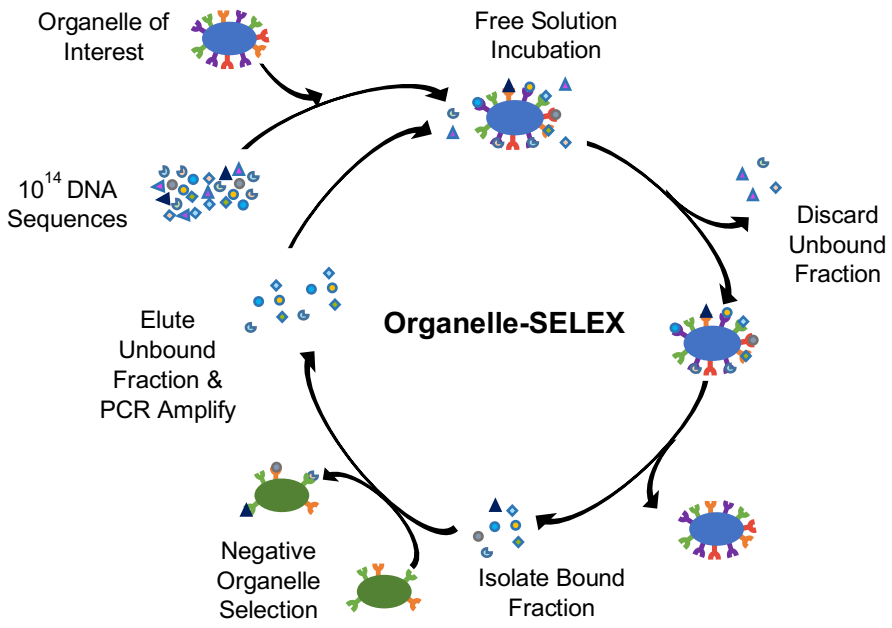

Figure 7.4. Schematic for Organelle-SELEX. An organelle population of interest is incubated with a library of ssDNA sequences, and unbound sequences are discarded. Bound sequences are collected and PCR amplified to produce a new DNA library more specific for the organelle of interest in subsequent rounds of selection. The addition of a negative organelle selection will increase organelle specificity.

affinity for its target is assessed, with the number of rounds necessary for optimal affinity being reached as the dissociation constant (K_d) shows little change from round to round of selection.[175] For organelle aptamer development, a specific outer membrane target does not need to be identified before selection, and in many cases, the ambiguity of the target makes selecting a high affinity aptamer specific to a cell or organelle type easier than a specific protein.[175] However, Organelle-SELEX should include round(s) of negative selection for contaminating organelles. Specifically, after exposing the ssDNA library to an organelle of interest and collecting bound sequences, the sequences should be subjected to a negative control population of organelles (i.e. contaminating).[170] This is a round of selection where sequences that bind to contaminating organelles are discarded, and unbound sequences, specific to the organelle of interest are collected and subjected to PCR, thus in proving the specificity of the selected aptamer.

A particularly challenging aspect of Organelle-SELEX is the preparation of phenotypically pure fractions of organelles. Commonly used methods for sub-cellular fractionation, including differential centrifugation and density gradient centrifugation do not produce phenotypically pure fractions. This limitation can be overcome in two ways, i) increasing the abundance of the organelle of interest in cells before isolation, and ii) the use of individual organelle sorting via fluorescence activated sorting (FACS)[176]. In an attempt to increase the number of autophagosomes present in cells prior to organelle isolation, we subjected C2C12 myoblasts to nutrient depravation conditions for 1 hour to increase cellular autophagosome content. Cells were then subjected to disruption and differential centrifugation to obtain a post-nuclear organelle fraction. The organelle fraction was subjected to a phenotypic purification via adsorption to anti-LC3 antibody coated magnetic beads (or IgG isotype coated magnetic bead control). We collected the organelles adsorbed to the magnetic beads to analyse the efficacy of the purification. Western blot analysis of the resulting fractions show enrichment of LC3-II membranes in vinblastine treated cells, though the cytosolic LC3-I is still

detected in a “pure” organelle fraction (Figure. 7.5). Selection of organelles via FACS after incubation with vinblastine may provide a pure organelle fraction for Organelle-SELEX.

α-LC3 captured	+	-	+
IgG captured	-	+	-
Vinblastine treated	-	-	+

Figure 7.5. Western blot analysis of autophagosome organelle fractions immune-captured on magnetic beads. α-LC3 coated magnetic beads enrich for LC3-I protein over IgG coated magnetic beads. Vinblastine treatment increases the capture of LC3-II^{+} organelles. This method may be useful to increase the number of autophagosomes present in cells prior to collection for Organelle-SELEX (see Figure 7.4).

The successful selection of an aptamer specific to autophagosomes would yield a revolutionary tool in the field of autophagy research, allowing for the specific detection of autophagosomes across many techniques (i.e. CE-LIF, mass cytometry, microscopy, MS-based proteomics, and western blots). The specific detection of autophagosomes would allow for detailed study of organelle dynamics via individual organelle mass cytometry experiments (Chapter 5), providing new insight from organelle progression from phagophore to autolysosome (see Chapter 2, Figure 2.16). In addition, it would enable a detailed profile of autophagy flux measured in Chapters 3 and 4.

7.1.3 Functional Labelling

As described in Chapter 5, individual organelle analysis via mass cytometry is a promising technique to probe inter-organelle interactions. While organelle detection is possible using conventional MCP-labeled antibodies, increasing the sensitivity of the method and eliminating the potential for non-specific binding could be accomplished using small molecule probes. Function-based probe are of particular interest, as they will eliminate complicate compensations for non-specific interactions, as was required in Chapters 3 through 5. Two distinct parameters are required for mass cytometry reagents: the inclusion of a specific probe to a cellular

target of interest, and a metal ion with a mass within the detectable range of the time of flight mass detector. Cellular targets or biological processes for which reliable antibody clones are unavailable present an area for novel small molecule[177-178] or nucleotide-based reagent[179] development (see Chapter 7, Section 7.1.2).

An organelle of interest in monitoring autophagy-related organelle dynamics is mitochondria, which are known to be recycled via mitophagy.[180-181] Thus, a small molecule probe specifically targeted towards mitochondrial identification that afforded increased numbers of lanthanide ions present per organelle would increase the flexibility of individual organelle detection via mass cytometry, both by increasing confidence of identification and reserving more sensitive channels (see Chapter 2, for transmission efficiency) for the quantification of less abundant organelle targets; A common approach to direct small molecules to mitochondria is via conjugation to a lipophilic cation.[182-183] The triphenylphosphonium (TPP) cation is widely used for the delivery of small molecules to the mitochondrial matrix driven by the mitochondrial membrane potential. This accumulation is dictated by the Nernst equation (equation 7.1) which dictates that the uptake of singly charged cations increases 10-fold for every 61.5 mV of membrane potential ($\Delta\Psi_M$) at 37°C.[184]

$$\Delta\Psi_M = -\frac{RT}{ZF} \ln\left(\frac{C_{matrix}}{C_{outside}}\right) \qquad \text{equation 7.1}$$

Where $\Delta\Psi_M$ is the membrane potential, Z is the charge on the ion, R is the ideal gas law constant, T is the absolute temperature, and C_{matrix} and $C_{outside}$ are the concentrations in the mitochondrial matrix and outside, respectively.

We hypothesize that the specific delivery of lanthanide ions to isolated mitochondria can be accomplished through labelling with a TPP-DOTA ligand chelating a lanthanide ion, as was described by Li[185] and Hardy[186] for use in magnetic resonance imaging. In collaboration with Dr. Sylvie Pallioux, we synthesized a TPP-Ho-DOTA reagent (**1**) as shown in Scheme 7.5.

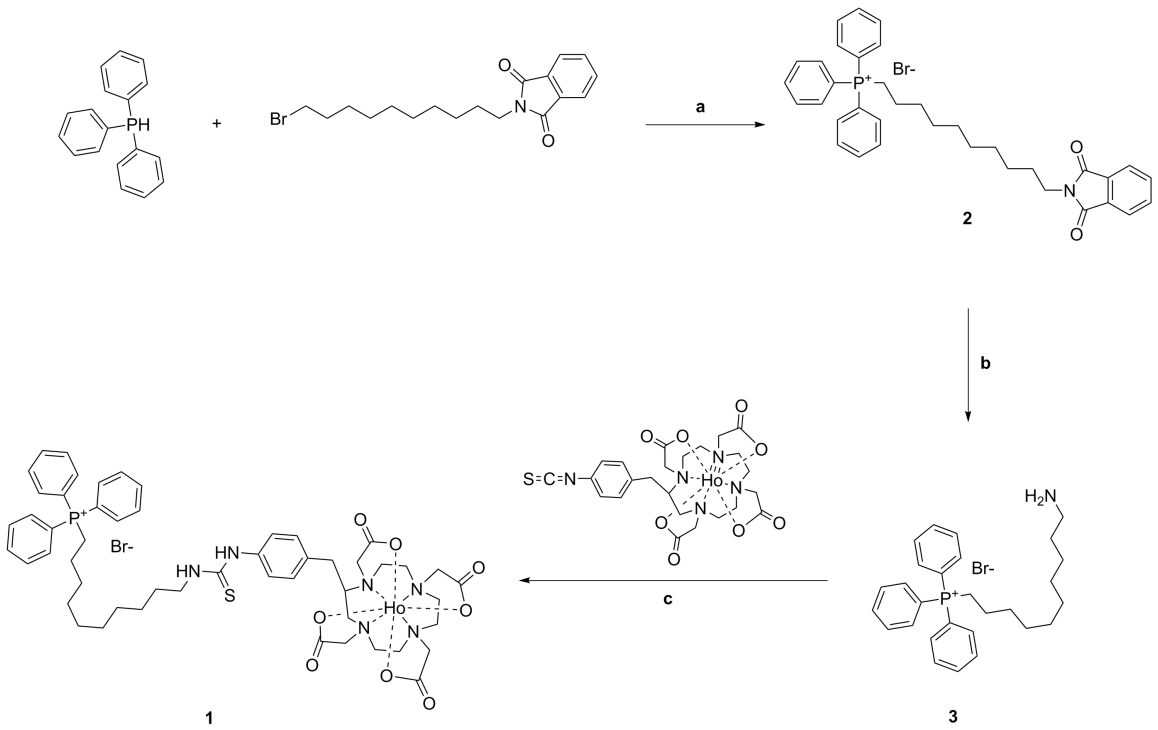

Scheme 7.5. Synthetic Scheme for TPP-Ho-DOTA. Reagents and conditions: (a) CH_3CN, N_2, reflux, 18 hrs. (b) NH2NH2, EtOH, reflux, 15 hrs. (c) TEA, p-SCN-Bn-Ho-DOTA, anhydrous DMSO. See Appendix D for ^{1}H, ^{13}C, and ^{31}P NMR, and ESI-MS characterization.

While this probe has not yet been tested, it is possible that it will not be sequestered inside mitochondria during fixation. While the TPP-Ho-DOTA reagent synthesized above would be sufficient for labelling functional, isolated mitochondria, upon fixation (required for mass cytometry) this label would likely leak out of isolated mitochondria due to a lack of membrane potential. This issue is common to most mitochondria targeting probes containing lipophilic cations but has been overcome by the inclusion of a thiol-reactive chloromethyl moiety to anchor the probe in place.[183] In the event the probe leaks from fixed mitochondria, modification of this synthesized material at either secondary amine with a chloromethyl group would yield a reagent appropriate for functional labelling of mitochondria that would be stable during required sample preparation procedures.

This synthesis yielded TPP-Ho-DOTA, a functional probe for the unambiguous identification of polarized mitochondria via mass cytometry, enabling the measurement of mitochondrial turnover via autophagy (i.e. mitophagy), a

required process during myogenesis. This will benefit analyses of mitophagy flux, such as was done in Chapter 3 through unambiguous identification of functional mitochondria, and a measure of autophagy adaptor protein (i.e. p62) accumulation at less functional mitochondria.

7.1.4 Activity-Based Probes

Incredible detail of biological processes has been elucidated relying solely on quantification of steady state protein abundance using commercially available reagents by mass cytometry. However, protein expression levels do not always directly correlate to their activity as many proteins are regulated by post-translational modifications.[187] Of interest to the field of autophagy research is the post-translational modification known as prenylation. Prenyl modification of select proteins increases their hydrophobicity via covalent binding of a farnesyl (15-carbon) or geranylgeranyl (20-carbon) isoprenoid.[188] This modification anchors proteins to lipid membranes and influencing their function. Known proteins targed for prenylation include the master regulators of vesicle-trafficking, Rab GTPases.[189] The Rab GTPases localize to the hydrophobic membrane of vesicles via their prenyl moiety to exert control over membrane trafficking.[190] Prenylation activity has been shown to be increased in autophagy deficient cell systems.[191] The application of this activity-based probe (ABP) for prenylation in measurements of autophagy flux by mass cytometry will unlock a new dimension of biological information regarding the regulation of autophagy organelle trafficking. This will be useful in autophagy flux measurements similar to those made in Chapters 3 and 4 of this work.

ABPs are advantageous in that they directly report on protein activity though quantification of the specific incorporation of a detectable probe. This approach has been extensively used in proteomics[192] and pharmaceutical development[193], among other fields. ABPs are generally made of three distinct modules: a i) reactive group, ii) selectivity conferring element, and iii) reporter moiety. The reactive group mediates covalent binding of the probe to the target protein via a

specific mechanism. Selective labelling is achieved through the selection of an appropriate selectivity conferring element, and labelling is detected via the reporter. Common labelling moieties include fluorophores and affinity tags.[187] Many variations of ABPs exist to decrease non-specific signal,[194] increase membrane permeability, or increase multiplexing ability.[195]

ABPs for protein prenylation has been reported,[196-199] usually exploiting the C-terminal CAAX motif common to most prenylated proteins. Within this motif, C is a cystine residue, AA are two aliphatic amino acids, and X is any amino acid. The cystine residue specifically serves as the attachment point for the prenyl pyrophosphate via protein prenyltransferase enzymes.[200] The metabolic labelling and detection of prenylation in whole cells via fluorescent reporters has been reported by Palsuledesai[191] (Figure 7.6). This approach utilizes an alkyne isoprenoid analog (C15Alk) which is metabolically incorporated as a prenyl post-translational modification on select proteins. The bio-orthogonal alkyne handle is reacted in situ with a fluorescent azide reporter (5-FAM-PEG-N_3), and resulting fluorescent signal is detected via flow cytometry or confocal microscopy.

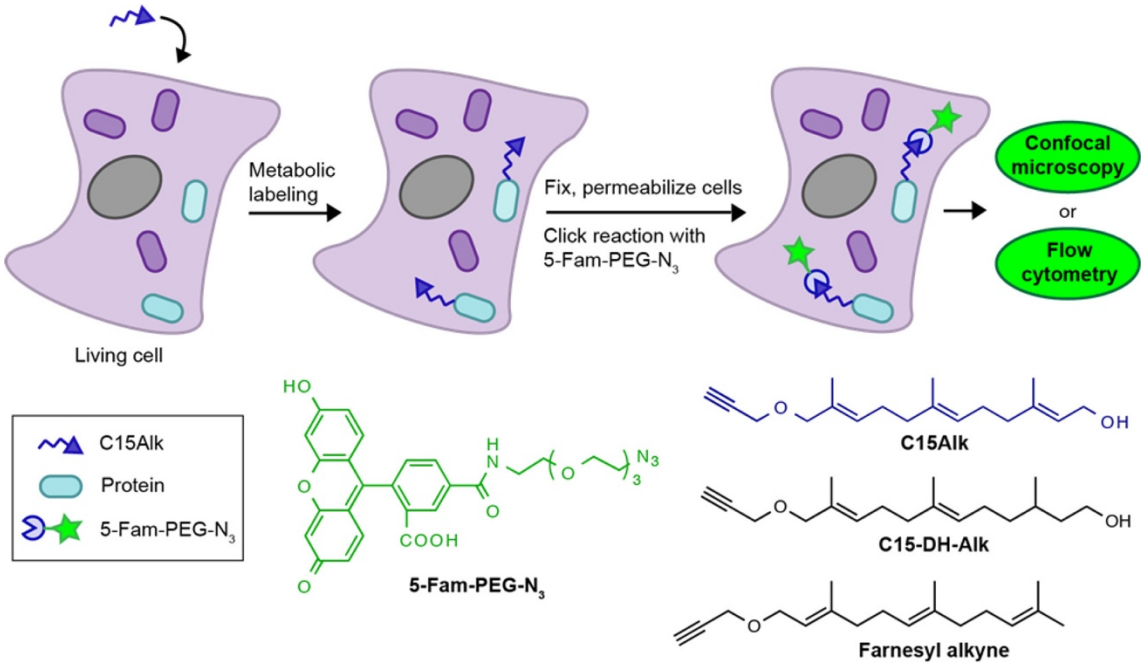

Figure 7.6. Metabolic labelling of prenylated proteins using an alkyne modified isoprenoid analog. Palsuledesai and coworkers report the in situ labelling of protein prenylation via an alkyne isoprenoid analog (C15Alk) which reacts with a fluorescent azide reporter (5-Fam-PEG-N_3), via a Cu-catalyzed alkyne azide cycloaddition (CuAAC). Resulting fluorescence signal is quantified via flow cytometry or confocal microscopy. Modified with permission from Palsuledesai.[191]

In collaboration with Dr. Mark Distefano and Kiall Suazo, we have exploited the same ABP for detection of protein prenylation via mass cytometry. To make the approach compatible with mass cytometry detection, we replaced the fluorophore azide reporter with an azide modified DOTA moiety chelating ^{159}Tb (Tb-azide), similar to the molecule reported by Shaklee[201] (Figure 7.7). In addition, we employed a diphosphate C15 isoprenoid analog (C15AlkOPP) developed by the Distefano lab, rather than the farnesol isoprenoid analog (Figure 7.7). Despite its negative charge, the diphosphate isoprenoid analog has improved incorporation via metabolic labelling than the farnesol analog [Dr. Mark Distefano & Kiall Suazo, personal communication]

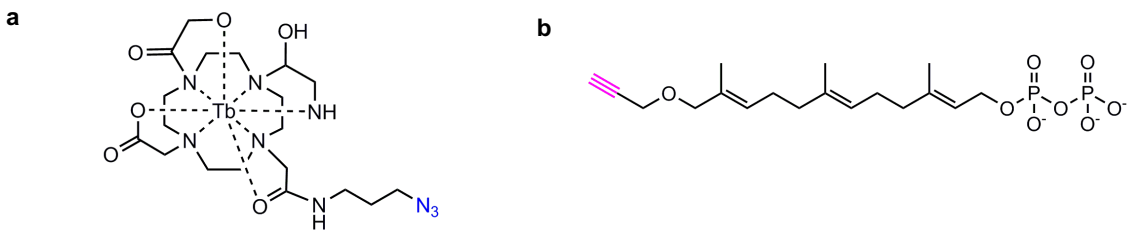

Figure 7.7. Structure of Tb-azide and diphosphate isoprenoid analog (C15AlkOPP) substituted for use in mass cytometry. The Tb-azide (a) reacts with the alkyne moiety of the C15AlkOPP probe (b) via a CuAAC reaction in situ following metabolic labelling of prenylated proteins.

In preliminary experiments, we applied the reported labelling protocol[191] using Tb-azide[201] in L6 myoblasts to profile the off-target interactions of Tb-azide in situ. Optimization of labelling conditions maintained signal while reducing noise (Figure 7.8).

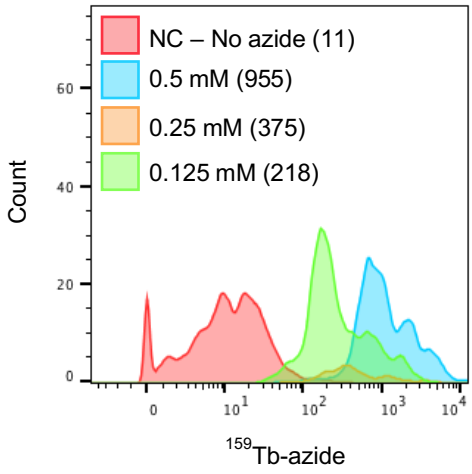

Figure 7.8. Histograms showing Tb-azide signal in individual cells detected via mass cytometry. All cell samples were metabolically labelled with 10 μM C15AlkOPP probe, then treated with 0, 0.13, 0.25 or 0.50 mM Tb-azide. Tb-azide signal increases in a dose dependent manner (median signal in parenthesis) but is sufficiently above background (NC – No azide) at 0.125 mM Tb-azide.

The optimized labelling conditions were used to probe the prenylation profile of autophagy deficient L6 myoblasts via mass cytometry. L6 myoblasts were treated with siRNA targeting ATG7 (or a scrambled negative control oligo) to knock-down Atg7 activity, halting autophagy flux. In contrast to previous experiments, the signal to noise ratio for Tb-azide signal resulting from non-specific interactions of the Tb-azide reporter was relatively high (ten-fold increase, see Figure 7.9). This is likely an artifact of transfection, indicating the need to optimize labelling conditions for each biological model in use. Future experiments will repeat this experiment in the ATG7 deficient L6 myoblasts described in Chapter 3, which have been genetically modified via CRISPR-Cas9. This will eliminate transfection-related artifacts in metabolic incorporation of the C15AlkOPP probe or labelling with Tb-azide. Additional controls will greatly improve the optimization of in situ reaction conditions and should include an azide deficient lanthanide-chelating DOTA molecule, and modulation of probe incorporation via prenyltransferase inhibitors.

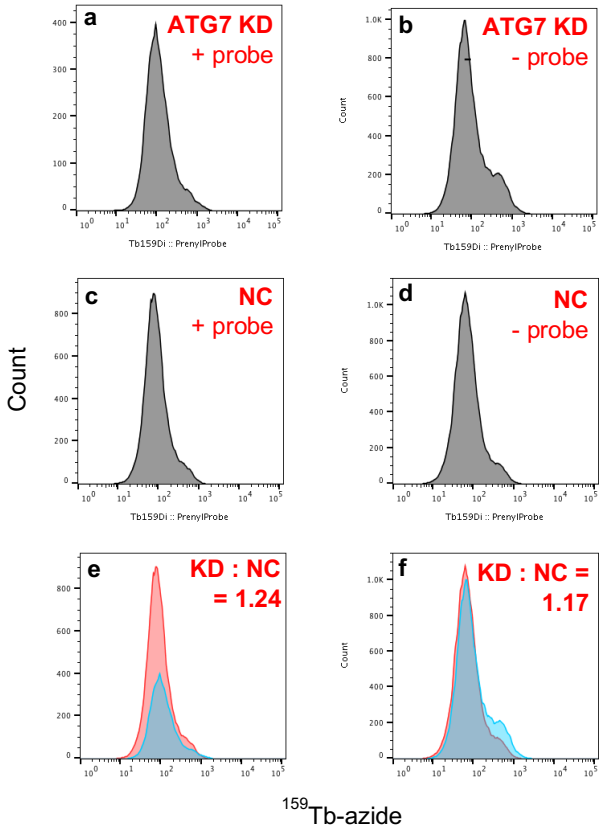

Figure 7.9. Prenylation profile for ATG7 siRNA KD L6 myoblasts. siRNA KD L6 myoblasts (a-b), and associated negative controls (c-d) were treated with Tb-azide (0.5 μM) after metabolic labelling of prenylation (a & c) or vehicle control treatment (c-d). The ratio of median Tb-azide signal between ATG7 KD and negative control were very similar for cells exposed to the C15AlkOPP probe and for those lacking the bio-orthogonal handle (e-f).

Successful use of the prenylation ABP used above will highlight the contribution of protein prenylation autophagy flux. It could be included in analyses such as those carried out in Chapters 3 and 4, to enable the investigation into the requirement of active protein prenylation during autophagy flux.

7.2 Analysis of Autophagy Flux in Individual Muscle Fiber Segments via Mass Cytometry

As described in Chapter 2, skeletal muscle is a highly heterogeneous tissue composed of phenotypically and functionally distinct cell types responsible for maintaining tissue mass and function. Myofibers are a unique multi-nucleated, cylindrical cell type responsible for producing the contractile force necessary for controlled movement.[202] In mature skeletal muscle these multi-nucleated cells show functional and structural heterogeneity and can be sub-categorized (type 1, 2A, 2B, 2X) by their predominate metabolic mechanism of ATP generation.

Muscle mass homeostasis is attained through a balance between protein synthesis and degradation, processes which are regulated by a variety of intra- and extra-cellular signals. Protein synthesis serves to build muscle mass in times of nutrient excess while autophagy functions to degrade cytosolic components to be used for energy production in times of nutrient deprivation. Recent reports show type 2 fibers are relatively more prone to degradation with age than type 1 fibers, though the cellular mechanism(s) responsible for these observations remain unclear.[203-205] These observations may indicate a role for dysfunctional autophagy in aged myofibers as autophagy flux is greater in type 2 fibers than type 1 fibers.[206] Thus, a comprehensive investigation into the role autophagy dysfunction in the development of age-related musculoskeletal diseases requires the development of a method for the analysis of autophagy flux in individual muscle fibers.

As was shown in Chapters 3 and 4, functional measurement of autophagy flux is possible across a phenotypically diverse cell sample collected from murine skeletal tissue. A similar analysis of autophagy flux in murine muscle fibers is

currently limited by the unique morphology of muscle fibers. The large, non-spherical size of muscle fibers hinder their movement through the microfluidic sample delivery system of CyTOF2 resulting in few fibers reaching the ICP torch for analysis in the instrument.

7.2.1 Development of a Methods for Muscle Fiber Segment Phenotyping via Mass Cytometry by MHC Expression

Individual muscles are comprised of bundles of myofibers with similar structural and functional properties, though individual fibers show considerable plasticity in structure in function.[202] Type 1 fibers are contain high numbers of mitochondria and have high oxidative capacity, making them suited to continuous activity (i.e. slow twitch). Type 2 fibers (including subcategories A, B, and X) contain fewer mitochondria and rely primarily on glycolytic generation of ATP for punctuated bursts of activity;[202] though type 2A fibers also contain a compliment of oxidative enzymes.[207]. A common method for the identification of the distinct sub-categories of myofibers is based on the expression of a unique myosin heavy chain (MHC) protein isoform throughout a fiber, though recent single-fiber studies have shown the existence of fibers with hybrid MHC expression.[208-209] The presence of multiple MHC isoforms follows the scheme of fiber type switching shown below (Figure 7.10). Despite the plasticity of MHC expression in individual fibers, it remains the best available scheme for identifying myofiber type to date.[202]

1 ↔ 1/2A ↔ 2A ↔ 2A/2X ↔ 2X ↔ 2X/2B ↔ 2B

Oxidative **Glycolytic**
Slow **Fast**

Figure 7.10. Organization Scheme for Hybrid Muscle Fiber Types. Individual muscle fiber transitions between types generally proceed according to the scheme shown here, though it is not always the case.

To phenotypically identify myofiber segments, we assembled a metal-labelled panel of antibodies to identify MHC isoforms found in type 1, type 2A and types 2B, shown in table 7.2. These particular clones were chosen based on their ability to identify a fiber type of choice, and their IgG structure which is amenable to metal-

labelling with currently available reagents based on maleimide chemistry. Hybridoma cell lines producing each antibody clone were purchased from the Developmental Studies Hybridoma Bank at the University of Iowa, sub-cultured at UMN, and sent to ProMab Biotechnologies (Richmond, CA) for culture scale-up and purification.

Table 7.2. Fiber Type Phenotyping Antibody Panel. The following three antibody clones were metal-labelled and used to phenotypically identify myofiber segments by fiber type.

	Antibody Clone – Metal Label		
Fiber Type	**BAF8 - ^{169}Tm**	**2F7 – ^{152}Sm**	**BF35 – ^{145}Nd**
Type 1	**+**	**-**	**-**
Type 2A	**-**	**+**	**+**
Type 2B	**-**	**-**	**+**

Myofiber segment preparations (see Appendix D, Supplementary Methods) were stained with the metal-labelled anti-MHC antibodies shown in Table 7.2 and analysed via mass cytometry. SPADE analysis of the resulting data indicated some specific antibody binding as indicated by the differential abundance of each isoform on unique clusters of myofiber segments in Figure 7.11. While promising, this analysis also indicated a significant amount of non-specific antibody binding evidenced by consistent detection of all MHC isoforms in the bottom clusters of each SPADE tree (broken box, Figure 7.11).

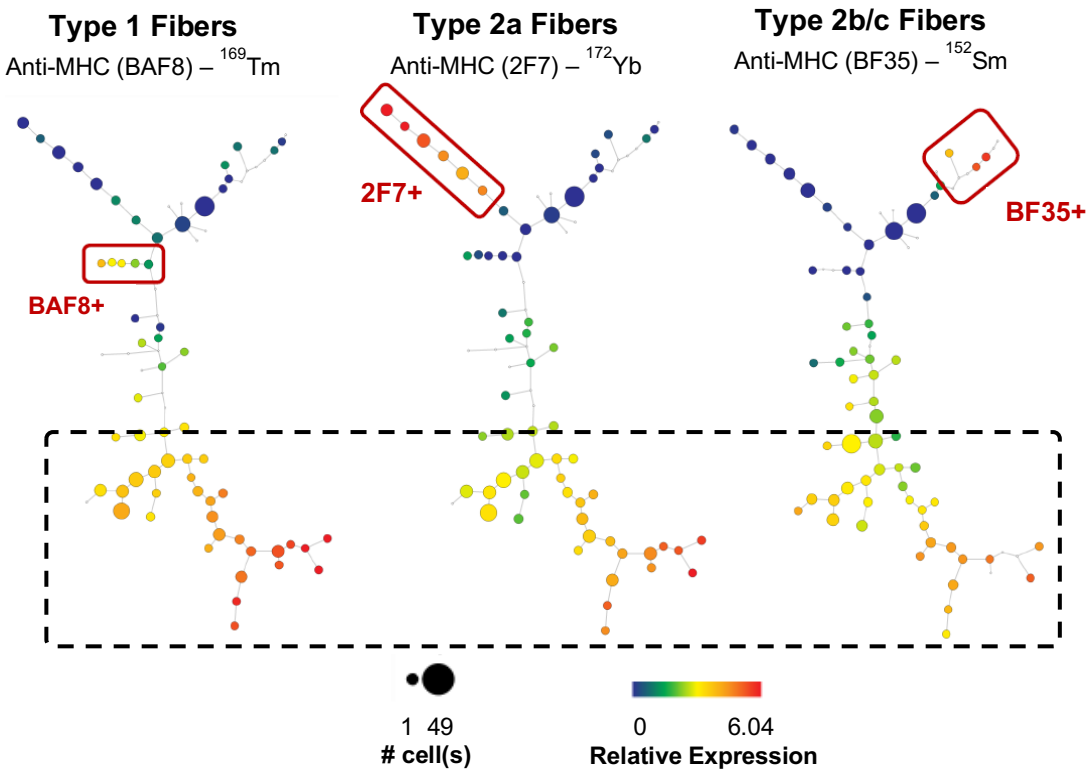

Figure 7.11. SPADE Analysis of Muscle Fiber Segments. Clusters with differential expression of unique MHC isoforms (solid line boxes) can be grouped and identified by fiber type. The SPADE analysis also revealed clusters of fibers in which all three MHC isoforms were detected (broken line box), likely due to non-specific binding of the anti-MHC antibodies.

Subsequent confocal microscopy experiments to confirm the non-specific binding of each anti-MHC antibody revealed very little antibody binding and almost no penetration of staining reagents into the inner body of the fiber (see Appendix D, Figure D8). To improve permeability suspensions of muscle fiber segments were incubated in a glyceration buffer prior to fixation (see Appendix D, Supplemental Methods). Confocal microscopy of glycerated fibers stained with anti-MHC (BF35) and a secondary antibody showed improved permeability of prepared muscle fiber segments (Figure 7.12).

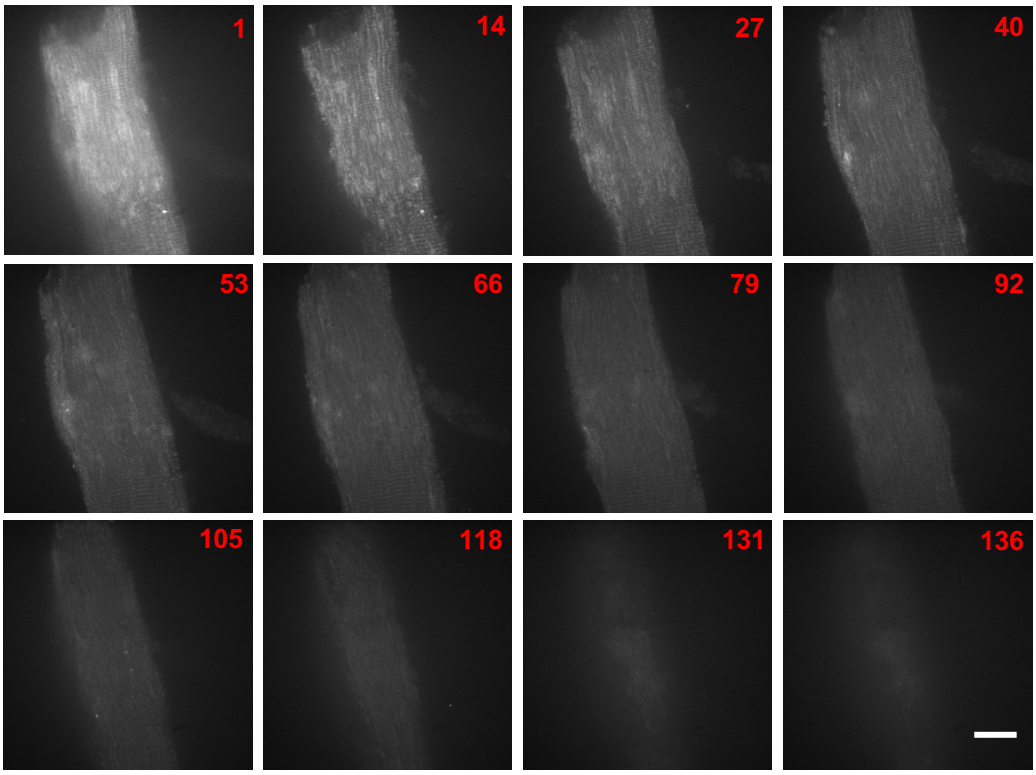

Figure 7.12. Confocal Microscopy Slices of Glycerated Muscle Fiber Segments. Incubation in glyceration buffer effectively permeabilized muscle fiber segments. Glycerated and fixed fibers were stained with anti-MHC (BF35) antibody and a secondary Alexafluor 488 antibody for fluorescence visualization via confocal microscopy. Each sequential panel is an individual z-axis slice through a single muscle fiber. Scale bar represents 20 μm.

Future experiments will test the usefulness of the glyceration permeabilization scheme in the preparation of muscle fiber segments for mass cytometry analysis of fiber type. If successfully tested via mass cytometry for fiber typing, the glyceration permeabilization scheme will also allow for the analysis of autophagy-related cellular targets in individual muscle fiber segments due to the vastly improved accessibility of the inner fiber to antibody cocktails. The successful analysis of autophagy flux in muscle fiber segments and mononuclear cells will provide a comprehensive analysis of autophagy flux in skeletal muscle.

Bibliography

1. Gheller, B. J.; Riddle, E. S.; Lem, M. R.; Thalacker-Mercer, A. E., Understanding Age-Related Changes in Skeletal Muscle Metabolism: Differences Between Females and Males. *Annu Rev Nutr* **2016,** *36*, 129-56.
2. United Nations, Department of Economic and Social Affairs, Population Division **2015**. World Population Ageing 2015 (ST/ESA/SER.A/390).
3. Thompson, D. D., Aging and sarcopenia. *J Musculoskelet Neuronal Interact* **2007,** *7* (4), 344-345.
4. Dikic, I.; Elazar, Z., Mechanism and medical implications of mammalian autophagy. *Nat Rev Mol Cell Biol* **2018,** *19* (6), 349-364.
5. Kaur, J.; Debnath, J., Autophagy at the crossroads of catabolism and anabolism. *Nat Rev Mol Cell Biol* **2015,** *16* (8), 461-72.
6. Rubinsztein, D. C.; Marino, G.; Kroemer, G., Autophagy and aging. *Cell* **2011,** *146* (5), 682-95.
7. Martinez-Lopez, N.; Athonvarangkul, D.; Singh, R., Autophagy and aging. *Advances in experimental medicine and biology* **2015,** *847*, 73-87.
8. Butler, D., Translational Research: Crossing the valley of death. *Nature* **2008**, *453*, 840-842.
9. Wang, Y. X.; Rudnicki, M. A., Satellite cells, the engines of muscle repair. *Nat Rev Mol Cell Biol* **2011,** *13* (2), 127-33.
10. Pannerec, A.; Formicola, L.; Besson, V.; Marazzi, G.; Sassoon, D. A., Defining skeletal muscle resident progenitors and their cell fate potentials. *Development* **2013,** *140* (14), 2879-91.
11. Frontera, W. R.; Ochala, J., Skeletal muscle: a brief review of structure and function. *Calcif Tissue Int* **2015,** *96* (3), 183-95.
12. Anand, R. K.; Chiu, D. T., Analytical tools for characterizing heterogeneity in organelle content. *Current opinion in chemical biology* **2012,** *16* (3-4), 391-9.
13. Chang, A. Y.; Marshall, W. F., Organelles - understanding noise and heterogeneity in cell biology at an intermediate scale. *Journal of cell science* **2017,** *130* (5), 819-826.
14. Fleming, A., On the Antibacterial Action of Cultures of a Penicillium, with Special Reference to their Use in the Isolation of B. influenzæ. *British journal of experimental pathology* **1929,** *10* (3), 226-236.
15. Akira, E.; Yoshio, T.; Masao, K.; Kazuhiko, T., Effects of ML-236B on cholesterol metabolism in mice and rats: Lack of hypocholesterolemic activity in normal animals. *Biochimica et Biophysica Acta (BBA) - Lipids and Lipid Metabolism* **1979,** *575* (2), 266-276.
16. Ernster, L.; Schatz, G., Mitochondria: a historical review. *The Journal of Cell Biology* **1981,** *91* (3), 227s-255s.
17. Simpson, E. H., The Interpretation of Interaction in Contingency Tables. *Journal of the Royal Statistical Society. Series B (Methodological)* **1951,** *13* (2), 238-241.
18. Carlo, D. D.; Lee, L. P., Dynamic Single-Cell Analysis for Quantitative Biology. *Analytical Chemistry* **2006,** *78* (23), 7918-7925.
19. Carlo, D. D.; Wu, L. Y.; Lee, L. P., Dynamic single cell culture array. *Lab on a chip* **2006,** *6* (11), 1445-1449.
20. Faley, S. L.; Copland, M.; Wlodkowic, D.; Kolch, W.; Seale, K. T.; Wikswo, J. P.; Cooper, J. M., Microfluidic single cell arrays to interrogate signalling dynamics of

individual, patient-derived hematopoietic stem cells. *Lab on a chip* **2009,** *9* (18), 2659-2664.
21. Ma, C.; Fan, R.; Ahmad, H.; Shi, Q.; Comin-Anduix, B.; Chodon, T.; Koya, R. C.; Liu, C.-C.; Kwong, G. A.; Radu, C. G.; Ribas, A.; Heath, J. R., A clinical microchip for evaluation of single immune cells reveals high functional heterogeneity in phenotypically similar T cells. *Nature medicine* **2011,** *17* (6), 738-743.
22. Ma, C.; Fan, R.; Elitas, M., Single Cell Functional Proteomics for Assessing Immune Response in Cancer Therapy: Technology, Methods, and Applications. *Frontiers in Oncology* **2013,** *3*, 133.
23. Shin, Young S.; Remacle, F.; Fan, R.; Hwang, K.; Wei, W.; Ahmad, H.; Levine, R. D.; Heath, James R., Protein Signaling Networks from Single Cell Fluctuations and Information Theory Profiling. *Biophysical Journal* **2011,** *100* (10), 2378-2386.
24. Shi, Q.; Qin, L.; Wei, W.; Geng, F.; Fan, R.; Shik Shin, Y.; Guo, D.; Hood, L.; Mischel, P. S.; Heath, J. R., Single-cell proteomic chip for profiling intracellular signaling pathways in single tumor cells. *Proceedings of the National Academy of Sciences* **2012,** *109* (2), 419-424.
25. Ahmad, H.; Sutherland, A.; Shin, Y. S.; Hwang, K.; Qin, L.; Krom, R.-J.; Heath, J. R., A robotics platform for automated batch fabrication of high density, microfluidics-based DNA microarrays, with applications to single cell, multiplex assays of secreted proteins. *The Review of Scientific Instruments* **2011,** *82* (9), 094301.
26. Wang, Y.; Taylor, T. H.; Arriaga, E. A., Analysis of the bioactivity of magnetically immunoisolated peroxisomes. *Analytical and bioanalytical chemistry* **2012,** *402* (1), 41-9.
27. Wolken, G. G.; Arriaga, E. A., Simultaneous Measurement of Individual Mitochondrial Membrane Potential and Electrophoretic Mobility by Capillary Electrophoresis. *Analytical Chemistry* **2014,** *86* (9), 4217-4226.
28. Wolken, G. G.; Kostal, V.; Arriaga, E. A., Capillary Isoelectric Focusing of Individual Mitochondria. *Analytical chemistry* **2011,** *83* (2), 612-618.
29. Satori, C. P.; Arriaga, E. A., Describing autophagy via analysis of individual organelles by capillary electrophoresis with laser induced fluorescence detection. *Analytical chemistry* **2013,** *85* (23), 11391-400.
30. Muratore, K. A.; Grundhofer, H. M.; Arriaga, E. A., Capillary Electrophoresis with Laser-Induced Fluorescent Detection of Immunolabeled Individual Autophagy Organelles Isolated from Liver Tissue. *Analytical chemistry* **2016,** *88* (23), 11691-11698.
31. Duffy, C. F.; MacCraith, B.; Diamond, D.; O'Kennedy, R.; Arriaga, E. A., Fast electrophoretic analysis of individual mitochondria using microchip capillary electrophoresis with laser induced fluorescence detection. *Lab on a chip* **2006,** *6* (8), 1007-11.
32. Fuller Kathryn, M.; Duffy Ciarán, F.; Arriaga Edgar, A., Determination of the cardiolipin content of individual mitochondria by capillary electrophoresis with laser-induced fluorescence detection. *ELECTROPHORESIS* **2002,** *23* (11), 1571-1576.
33. Johnson, R. D.; Navratil, M.; Poe, B. G.; Xiong, G.; Olson, K. J.; Ahmadzadeh, H.; Andreyev, D.; Duffy, C. F.; Arriaga, E. A., Analysis of mitochondria isolated from single cells. *Analytical and bioanalytical chemistry* **2007,** *387* (1), 107-18.
34. Chattopadhyay, P. K.; Hogerkorp, C. M.; Roederer, M., A chromatic explosion: the development and future of multiparameter flow cytometry. *Immunology* **2008,** *125* (4), 441-9.

35. Chattopadhyay, P. K.; Price, D. A.; Harper, T. F.; Betts, M. R.; Yu, J.; Gostick, E.; Perfetto, S. P.; Goepfert, P.; Koup, R. A.; De Rosa, S. C.; Bruchez, M. P.; Roederer, M., Quantum dot semiconductor nanocrystals for immunophenotyping by polychromatic flow cytometry. *Nature medicine* **2006,** *12* (8), 972-7.
36. Razumienko, E.; Ornatsky, O.; Kinach, R.; Milyavsky, M.; Lechman, E.; Baranov, V.; Winnik, M. A.; Tanner, S. D., Element-tagged immunoassay with ICP-MS detection: evaluation and comparison to conventional immunoassays. *Journal of immunological methods* **2008,** *336* (1), 56-63.
37. Ornatsky, O.; Baranov, V. I.; Bandura, D. R.; Tanner, S. D.; Dick, J., Multiple cellular antigen detection by ICP-MS. *Journal of immunological methods* **2006,** *308* (1-2), 68-76.
38. Tanner, S. D.; Ornatsky, O.; Bandura, D. R.; Baranov, V. I., Multiplex bio-assay with inductively coupled plasma mass spectrometry: Towards a massively multivariate single-cell technology. *Spectrochimica Acta Part B: Atomic Spectroscopy* **2007,** *62* (3), 188-195.
39. Tanner, S. D.; Bandura, D. R.; Ornatsky, O.; Baranov, V. I.; Nitz, M.; Winnik, M. A., Flow cytometer with mass spectrometer detection for massively multiplexed single-cell biomarker assay. *Pure and Applied Chemistry* **2008,** *80* (12).
40. Quinn, Z. A. B., V.I.; Tanner, S.D.; Wrana, J.L., Simultaneous determination of proteins using an element-tagged immunoassay coupled with ICP-MS detection. *Journal of Analytical Atomic Spectroscopy* **2002,** *17*, 892-896.
41. Baranov, V. I.; Quinn, Z.; Bandura, D. R.; Tanner, S. D., A Sensitive and Quantitative Element-Tagged Immunoassay with ICPMS Detection. *Analytical Chemistry* **2002,** *74* (7), 1629-1636.
42. Ornatsky, O. I.; Kinach, R.; Bandura, D. R.; Lou, X.; Tanner, S. D.; Baranov, V. I.; Nitz, M.; Winnik, M. A., Development of analytical methods for multiplex bio-assay with inductively coupled plasma mass spectrometry. *Journal of analytical atomic spectrometry* **2008,** *23* (4), 463-469.
43. Bandura, D., Baranov, V., Ornatsky, O., Antonov, A., Kinach, R., Lou, X., Pavlov, S., Dick, J., Tanner, S., Mass Cytometry: Techniques for Real Time Single Cell Multitarget Immunoassay Based on Inductively Coupled Plasma Time-of-Flight Mass Spectrometry. *Analytical chemistry* **2009,** *81* (16), 6813-6822.
44. Tanner, S. D.; Baranov, V. I.; Ornatsky, O. I.; Bandura, D. R.; George, T. C., An introduction to mass cytometry: fundamentals and applications. *Cancer immunology, immunotherapy : CII* **2013,** *62* (5), 955-65.
45. Tricot, S.; Meyrand, M.; Sammicheli, C.; Elhmouzi-Younes, J.; Corneau, A.; Bertholet, S.; Malissen, M.; Le Grand, R.; Nuti, S.; Luche, H.; Cosma, A., Evaluating the efficiency of isotope transmission for improved panel design and a comparison of the detection sensitivities of mass cytometer instruments. *Cytometry. Part A : the journal of the International Society for Analytical Cytology* **2015,** *87* (4), 357-68.
46. Bendall, S. C.; Simonds, E. F.; Qiu, P.; Amir el, A. D.; Krutzik, P. O.; Finck, R.; Bruggner, R. V.; Melamed, R.; Trejo, A.; Ornatsky, O. I.; Balderas, R. S.; Plevritis, S. K.; Sachs, K.; Pe'er, D.; Tanner, S. D.; Nolan, G. P., Single-cell mass cytometry of differential immune and drug responses across a human hematopoietic continuum. *Science* **2011,** *332* (6030), 687-96.
47. Seamer, L.; Bagwell, C.; Barden, L.; Redelman, D.; Salzman, G.; Wood, J.; Murphy, R., Proposed new data file standard for flow cytometry, version FCS 3. 0. *Cytometry* **1997,** *28*.

48. Finck, R.; Simonds, E. F.; Jager, A.; Krishnaswamy, S.; Sachs, K.; Fantl, W.; Pe'er, D.; Nolan, G. P.; Bendall, S. C., Normalization of mass cytometry data with bead standards. *Cytometry. Part A : the journal of the International Society for Analytical Cytology* **2013,** *83* (5), 483-94.
49. Leipold, M. D.; Maecker, H. T., Mass Cytometry: Protocol for Daily Tuning and Running Cell Samples on a CyTOF Mass Cytometer. **2012,** (69), e4398.
50. Xudong Lou, G. Z., and Isaac Herrera, Polymer-Based Elemental Tags for Sensitive Bioassays. *Angewandte Chemie* **2007,** *46* (32), 6111-6114.
51. Daniel Majonis, I. H., Olga Ornatsky, Maren Schulze, Xudong Lou, Mohsen Soleimani,; Mark Nitz, a. M. A. W., Synthesis of a Functional Metal-Chelating Polymer and Steps toward Quantitative Mass Cytometry Bioassays. *Analytical chemistry* **2010,** *82*, 8961-8969.
52. Illy, N.; Majonis, D.; Herrera, I.; Ornatsky, O.; Winnik, M. A., Metal-chelating polymers by anionic ring-opening polymerization and their use in quantitative mass cytometry. *Biomacromolecules* **2012,** *13* (8), 2359-69.
53. Parker, D.; Dickins, R. S.; Puschmann, H.; Crossland, C.; Howard, J. A. K., Being Excited by Lanthanide Coordination Complexes: Aqua Species, Chirality, Excited-State Chemistry, and Exchange Dynamics. *Chemical reviews* **2002,** *102* (6), 1977-2010.
54. Majonis, D.; Ornatsky, O.; Weinrich, D.; Winnik, M. A., Dual-purpose polymer labels for fluorescent and mass cytometric affinity bioassays. *Biomacromolecules* **2013,** *14* (5), 1503-13.
55. Baumgart, S.; Schulz, A. R.; Peddinghaus, A.; Stanislawiak, S.; Gillert, S.; Hirseland, H.; Krauthauser, S.; Dose, C.; Mei, H. E.; Grutzkau, A., Dual-labelled antibodies for flow and mass cytometry: A new tool for cross-platform comparison and enrichment of target cells for mass cytometry. *Eur J Immunol* **2017,** *47* (8), 1377-1385.
56. Buckle, T.; van der Wal, S.; van Malderen, S. J.; Muller, L.; Kuil, J.; van Unen, V.; Peters, R. J.; van Bemmel, M. E.; McDonnell, L. A.; Velders, A. H.; Koning, F.; Vanhaeke, F.; van Leeuwen, F. W., Hybrid Imaging Labels: Providing the Link Between Mass Spectrometry-Based Molecular Pathology and Theranostics. *Theranostics* **2017,** *7* (3), 624-633.
57. Schäfer, S.; Sheldrick, W. S., Coligand tuning of the DNA binding properties of half-sandwich organometallic intercalators: Influence of polypyridyl (pp) and monodentate ligands (L = Cl, (NH2)2CS, (NMe2)2CS) on the intercalation of (η5-pentamethylcyclopentadienyl)-iridium(III)- dipyridoquinoxaline and -dipyridophenazine complexes. *Journal of Organometallic Chemistry* **2007,** *692* (6), 1300-1309.
58. Pyle, A. M.; Long, E. C.; Barton, J. K., Shape-selective targeting of DNA by phenanthrenequinone diiminerhodium(III) photocleaving agents. *Journal of the American Chemical Society* **1989,** *111* (12), 4520-4522.
59. Long, E. C.; Barton, J. K., On demonstrating DNA intercalation. *Accounts of Chemical Research* **1990,** *23* (9), 271-273.
60. Pyle, A. M.; Chiang, M. Y.; Barton, J. K., Synthesis and characterization of physical, electronic, and photochemical aspects of 9,10-phenanthrenequinonediimine complexes of ruthenium(II) and rhodium(III). *Inorganic Chemistry* **1990,** *29* (22), 4487-4495.
61. Fienberg, H. G.; Simonds, E. F.; Fantl, W. J.; Nolan, G. P.; Bodenmiller, B., A platinum-based covalent viability reagent for single-cell mass cytometry. *Cytometry.*

Part A : the journal of the International Society for Analytical Cytology **2012,** *81* (6), 467-75.
62. Wang, D.; Lippard, S. J., Cellular processing of platinum anticancer drugs. *Nat Rev Drug Discov* **2005,** *4* (4), 307-320.
63. Siddik, Z. H., Cisplatin: mode of cytotoxic action and molecular basis of resistance. *Oncogene* **2003,** *22* (47), 7265-7279.
64. Newell, E. W.; Sigal, N.; Bendall, S. C.; Nolan, G. P.; Davis, M. M., Cytometry by Time-of-Flight Shows Combinatorial Cytokine Expression and Virus-Specific Cell Niches within a Continuum of CD8(+) T Cell Phenotypes. *Immunity* **2012,** *36* (1), 142-152.
65. Chen, T. J.; Kotecha, N., Cytobank: providing an analytics platform for community cytometry data analysis and collaboration. *Current topics in microbiology and immunology* **2014,** *377*, 127-57.
66. Amir el, A. D.; Davis, K. L.; Tadmor, M. D.; Simonds, E. F.; Levine, J. H.; Bendall, S. C.; Shenfeld, D. K.; Krishnaswamy, S.; Nolan, G. P.; Pe'er, D., viSNE enables visualization of high dimensional single-cell data and reveals phenotypic heterogeneity of leukemia. *Nature biotechnology* **2013,** *31* (6), 545-52.
67. Qiu, P.; Simonds, E. F.; Bendall, S. C.; Gibbs, K. D., Jr.; Bruggner, R. V.; Linderman, M. D.; Sachs, K.; Nolan, G. P.; Plevritis, S. K., Extracting a cellular hierarchy from high-dimensional cytometry data with SPADE. *Nature biotechnology* **2011,** *29* (10), 886-91.
68. Aghaeepour, N.; Finak, G.; Flow, C. A. P. C.; Consortium, D.; Hoos, H.; Mosmann, T. R.; Brinkman, R.; Gottardo, R.; Scheuermann, R. H., Critical assessment of automated flow cytometry data analysis techniques. *Nat Methods* **2013,** *10* (3), 228-38.
69. Samusik, N.; Good, Z.; Spitzer, M. H.; Davis, K. L.; Nolan, G. P., Automated mapping of phenotype space with single-cell data. *Nat Methods* **2016,** *13* (6), 493-6.
70. Levine, Jacob H.; Simonds, Erin F.; Bendall, Sean C.; Davis, Kara L.; Amir, E.-ad D.; Tadmor, Michelle D.; Litvin, O.; Fienberg, Harris G.; Jager, A.; Zunder, Eli R.; Finck, R.; Gedman, Amanda L.; Radtke, I.; Downing, James R.; Pe'er, D.; Nolan, Garry P., Data-Driven Phenotypic Dissection of AML Reveals Progenitor-like Cells that Correlate with Prognosis. *Cell* **2015,** *162* (1), 184-197.
71. Bendall, S. C.; Davis, K. L.; Amir el, A. D.; Tadmor, M. D.; Simonds, E. F.; Chen, T. J.; Shenfeld, D. K.; Nolan, G. P.; Pe'er, D., Single-cell trajectory detection uncovers progression and regulatory coordination in human B cell development. *Cell* **2014,** *157* (3), 714-25.
72. Setty, M.; Tadmor, M. D.; Reich-Zeliger, S.; Angel, O.; Salame, T. M.; Kathail, P.; Choi, K.; Bendall, S.; Friedman, N.; Pe'er, D., Wishbone identifies bifurcating developmental trajectories from single-cell data. *Nature biotechnology* **2016,** *34* (6), 637-45.
73. Moon, K. R.; van Dijk, D.; Wang, Z.; Chen, W.; Hirn, M. J.; Coifman, R. R.; Ivanova, N. B.; Wolf, G.; Krishnaswamy, S., PHATE: A Dimensionality Reduction Method for Visualizing Trajectory Structures in High-Dimensional Biological Data. *bioRxiv* **2017**.
74. Masiero, E.; Agatea, L.; Mammucari, C.; Blaauw, B.; Loro, E.; Komatsu, M.; Metzger, D.; Reggiani, C.; Schiaffino, S.; Sandri, M., Autophagy is required to maintain muscle mass. *Cell metabolism* **2009,** *10* (6), 507-15.

75. Mammucari, C.; Milan, G.; Romanello, V.; Masiero, E.; Rudolf, R.; Del Piccolo, P.; Burden, S. J.; Di Lisi, R.; Sandri, C.; Zhao, J.; Goldberg, A. L.; Schiaffino, S.; Sandri, M., FoxO3 controls autophagy in skeletal muscle in vivo. *Cell metabolism* **2007,** *6* (6), 458-71.
76. Sakuma, K.; Aoi, W.; Yamaguchi, A., Current understanding of sarcopenia: possible candidates modulating muscle mass. *Pflugers Arch* **2015,** *467* (2), 213-29.
77. Fry, C. S.; Drummond, M. J.; Glynn, E. L.; Dickinson, J. M.; Gundermann, D. M.; Timmerman, K. L.; Walker, D. K.; Volpi, E.; Rasmussen, B. B., Skeletal muscle autophagy and protein breakdown following resistance exercise are similar in younger and older adults. *J Gerontol A Biol Sci Med Sci* **2013,** *68* (5), 599-607.
78. Sandri, M., Autophagy in skeletal muscle. *FEBS letters* **2010,** *584* (7), 1411-6.
79. Peterson, C. M.; Johannsen, D. L.; Ravussin, E., Skeletal muscle mitochondria and aging: a review. *J Aging Res* **2012,** *2012*, 194821.
80. Ceafalan, L. C.; Popescu, B. O.; Hinescu, M. E., Cellular players in skeletal muscle regeneration. *Biomed Res Int* **2014,** *2014*, 957014.
81. Zierath, J. R.; Hawley, J. A., Skeletal muscle fiber type: influence on contractile and metabolic properties. *PLoS Biol* **2004,** *2* (10), e348.
82. Rigamonti, E.; Zordan, P.; Sciorati, C.; Rovere-Querini, P.; Brunelli, S., Macrophage plasticity in skeletal muscle repair. *Biomed Res Int* **2014,** *2014*, 560629.
83. Garcia-Prat, L.; Martinez-Vicente, M.; Perdiguero, E.; Ortet, L.; Rodriguez-Ubreva, J.; Rebollo, E.; Ruiz-Bonilla, V.; Gutarra, S.; Ballestar, E.; Serrano, A. L.; Sandri, M.; Munoz-Canoves, P., Autophagy maintains stemness by preventing senescence. *Nature* **2016,** *529* (7584), 37-42.
84. Kogot-Levin, A.; Saada, A.; Leibowitz, G.; Soiferman, D.; Douiev, L.; Raz, I.; Weksler-Zangen, S., Upregulation of Mitochondrial Content in Cytochrome c Oxidase Deficient Fibroblasts. *PloS one* **2016,** *11* (10), e0165417.
85. Parzych, K. R.; Klionsky, D. J., An overview of autophagy: morphology, mechanism, and regulation. *Antioxidants & redox signaling* **2014,** *20* (3), 460-73.
86. Lazarou, M.; Sliter, D. A.; Kane, L. A.; Sarraf, S. A.; Wang, C.; Burman, J. L.; Sideris, D. P.; Fogel, A. I.; Youle, R. J., The ubiquitin kinase PINK1 recruits autophagy receptors to induce mitophagy. *Nature* **2015,** *524* (7565), 309-14.
87. Yin, H.; Price, F.; Rudnicki, M. A., Satellite cells and the muscle stem cell niche. *Physiological reviews* **2013,** *93* (1), 23-67.
88. Bentzinger, C. F.; Wang, Y. X.; Rudnicki, M. A., Building muscle: molecular regulation of myogenesis. *Cold Spring Harbor perspectives in biology* **2012,** *4* (2).
89. Sin, J.; Andres, A. M.; Taylor, D. J.; Weston, T.; Hiraumi, Y.; Stotland, A.; Kim, B. J.; Huang, C.; Doran, K. S.; Gottlieb, R. A., Mitophagy is required for mitochondrial biogenesis and myogenic differentiation of C2C12 myoblasts. *Autophagy* **2016,** *12* (2), 369-80.
90. Pichavant, C.; Pavlath, G. K., Incidence and severity of myofiber branching with regeneration and aging. *Skeletal Muscle* **2014,** *4* (1), 9.
91. Bua, E. A.; McKiernan, S. H.; Wanagat, J.; McKenzie, D.; Aiken, J. M., Mitochondrial abnormalities are more frequent in muscles undergoing sarcopenia. *Journal of Applied Physiology* **2002,** *92* (6), 2617-2624.
92. Wanagat, J.; Cao, Z.; Pathare, P.; Aiken, J. M., Mitochondrial DNA deletion mutations colocalize with segmental electron transport system abnormalities, muscle fiber atrophy, fiber splitting, and oxidative damage in sarcopenia. *The FASEB Journal* **2001,** *15* (2), 322-332.

93. Raben, N.; Hill, V.; Shea, L.; Takikita, S.; Baum, R.; Mizushima, N.; Ralston, E.; Plotz, P., Suppression of autophagy in skeletal muscle uncovers the accumulation of ubiquitinated proteins and their potential role in muscle damage in Pompe disease. *Human molecular genetics* **2008,** *17* (24), 3897-908.
94. Tothova, Z.; Gilliland, D. G., FoxO Transcription Factors and Stem Cell Homeostasis: Insights from the Hematopoietic System. *Cell Stem Cell* **2007,** *1* (2), 140-152.
95. Blanpain, C.; Fuchs, E., Epidermal homeostasis: a balancing act of stem cells in the skin. *Nature Reviews Molecular Cell Biology* **2009,** *10*, 207.
96. Discher, D. E.; Mooney, D. J.; Zandstra, P. W., Growth Factors, Matrices, and Forces Combine and Control Stem Cells. *Science* **2009,** *324* (5935), 1673.
97. Gurumurthy, S.; Xie, S. Z.; Alagesan, B.; Kim, J.; Yusuf, R. Z.; Saez, B.; Tzatsos, A.; Ozsolak, F.; Milos, P.; Ferrari, F.; Park, P. J.; Shirihai, O. S.; Scadden, D. T.; Bardeesy, N., The Lkb1 metabolic sensor maintains haematopoietic stem cell survival. *Nature* **2010,** *468* (7324), 659-663.
98. Bosurgi, L.; Manfredi, A. A.; Rovere-Querini, P., Macrophages in injured skeletal muscle: a perpetuum mobile causing and limiting fibrosis, prompting or restricting resolution and regeneration. *Front Immunol* **2011,** *2*, 62.
99. Oishi, Y.; Manabe, I., Macrophages in age-related chronic inflammatory diseases. *NPJ Aging Mech Dis* **2016,** *2*, 16018.
100. Franceschi, C.; BonafÈ, M.; Valensin, S.; Olivieri, F.; De Luca, M.; Ottaviani, E.; De Benedictis, G., Inflamm-aging: An Evolutionary Perspective on Immunosenescence. *Annals of the New York Academy of Sciences* **2006,** *908* (1), 244-254.
101. Salminen, A.; Kaarniranta, K.; Kauppinen, A., Inflammaging: disturbed interplay between autophagy and inflammasomes. *Aging* **2012,** *4* (3), 166-175.
102. Franceschi, C.; Garagnani, P.; Vitale, G.; Capri, M.; Salvioli, S., Inflammaging and 'Garb-aging'. *Trends in endocrinology and metabolism: TEM* **2017,** *28* (3), 199-212.
103. Yoshida, N.; Yoshida, S.; Koishi, K.; Masuda, K.; Nabeshima, Y., Cell heterogeneity upon myogenic differentiation: down-regulation of MyoD and Myf-5 generates 'reserve cells'. *Journal of cell science* **1998,** *111* (6), 769.
104. Flamini, V.; Ghadiali, R. S.; Antczak, P.; Rothwell, A.; Turnbull, J. E.; Pisconti, A., The Satellite Cell Niche Regulates the Balance between Myoblast Differentiation and Self-Renewal via p53. *Stem Cell Reports* **2018,** *10* (3), 970-983.
105. Kadandale, P.; Kiger, A. A., Role of selective autophagy in cellular remodeling. *Autophagy* **2014,** *6* (8), 1194-1195.
106. Mizushima, N.; Levine, B., Autophagy in mammalian development and differentiation. *Nature cell biology* **2010,** *12* (9), 823-30.
107. Guerin, C. M.; Kramer, S. G., Cytoskeletal remodeling during myotube assembly and guidance: Coordinating the actin and microtubule networks. *Communicative & Integrative Biology* **2009,** *2* (5), 452-457.
108. Call, J. A.; Wilson, R. J.; Laker, R. C.; Zhang, M.; Kundu, M.; Yan, Z., Ulk1-mediated autophagy plays an essential role in mitochondrial remodeling and functional regeneration of skeletal muscle. *American Journal of Physiology-Cell Physiology* **2017,** *312* (6), C724-C732.
109. Porpiglia, E.; Samusik, N.; Van Ho, A. T.; Cosgrove, B. D.; Mai, T.; Davis, K. L.; Jager, A.; Nolan, G. P.; Bendall, S. C.; Fantl, W. J.; Blau, H. M., High-resolution myogenic lineage mapping by single-cell mass cytometry. *Nature cell biology* **2017,** *19* (5), 558-567.

110. Prinz, F.; Schlange, T.; Asadullah, K., Believe it or not: how much can we rely on published data on potential drug targets? *Nat Rev Drug Discov* **2011,** *10* (9), 712.
111. Kaufman, E. N.; Jain, R. K., Effect of Bivalent Interaction upon Apparent Antibody Affinity: Experimental Confirmation of Theory Using Fluorescence Photobleaching and Implications for Antibody Binding Assays. *Cancer Research* **1992,** *52* (15), 4157.
112. Afshin, et al., Health Effects of Overweight and Obesity in 195 Countries over 25 Years. *N Engl J Med* **2017,** *377* (1), 13-27.
113. Zammit, P. S., Function of the myogenic regulatory factors Myf5, MyoD, Myogenin and MRF4 in skeletal muscle, satellite cells and regenerative myogenesis. *Seminars in cell & developmental biology* **2017,** *72*, 19-32.
114. Tapscott, S. J., The circuitry of a master switch: Myod and the regulation of skeletal muscle gene transcription. *Development* **2005,** *132* (12), 2685.
115. Torgan, C. E.; Daniels, M. P., Regulation of Myosin Heavy Chain Expression during Rat Skeletal Muscle Development In Vitro. *Molecular biology of the cell* **2001,** *12* (5), 1499-1508.
116. Stuelsatz, P.; Pouzoulet, F.; Lamarre, Y.; Dargelos, E.; Poussard, S.; Leibovitch, S.; Cottin, P.; Veschambre, P., Down-regulation of MyoD by Calpain 3 Promotes Generation of Reserve Cells in C2C12 Myoblasts. *Journal of Biological Chemistry* **2010,** *285* (17), 12670-12683.
117. Michiorri, S.; Gelmetti, V.; Giarda, E.; Lombardi, F.; Romano, F.; Marongiu, R.; Nerini-Molteni, S.; Sale, P.; Vago, R.; Arena, G.; Torosantucci, L.; Cassina, L.; Russo, M. A.; Dallapiccola, B.; Valente, E. M.; Casari, G., The Parkinson-associated protein PINK1 interacts with Beclin1 and promotes autophagy. *Cell Death Differ* **2010,** *17* (6), 962-74.
118. Fu, X.; Wang, H.; Hu, P., Stem cell activation in skeletal muscle regeneration. *Cellular and Molecular Life Sciences* **2015,** *72* (9), 1663-1677.
119. Martinez Fernando, O., Regulators of macrophage activation. *European Journal of Immunology* **2011,** *41* (6), 1531-1534.
120. Costamagna, D.; Costelli, P.; Sampaolesi, M.; Penna, F., Role of Inflammation in Muscle Homeostasis and Myogenesis. *Mediators Inflamm* **2015,** *2015*, 805172.
121. Sousa-Victor, P.; Garcia-Prat, L.; Serrano, A. L.; Perdiguero, E.; Munoz-Canoves, P., Muscle stem cell aging: regulation and rejuvenation. *Trends in endocrinology and metabolism: TEM* **2015,** *26* (6), 287-96.
122. Blau, H. M.; Cosgrove, B. D.; Ho, A. T., The central role of muscle stem cells in regenerative failure with aging. *Nature medicine* **2015,** *21* (8), 854-62.
123. Sousa-Victor, P.; Gutarra, S.; García-Prat, L.; Rodriguez-Ubreva, J.; Ortet, L.; Ruiz-Bonilla, V.; Jardí, M.; Ballestar, E.; González, S.; Serrano, A. L.; Perdiguero, E.; Muñoz-Cánoves, P., Geriatric muscle stem cells switch reversible quiescence into senescence. *Nature* **2014,** *506*, 316.
124. Brack, A. S.; Conboy, M. J.; Roy, S.; Lee, M.; Kuo, C. J.; Keller, C.; Rando, T. A., Increased Wnt Signaling During Aging Alters Muscle Stem Cell Fate and Increases Fibrosis. *Science* **2007,** *317* (5839), 807.
125. Shefer, G.; Van de Mark, D. P.; Richardson, J. B.; Yablonka-Reuveni, Z., Satellite-cell pool size does matter: defining the myogenic potency of aging skeletal muscle. *Dev Biol* **2006,** *294* (1), 50-66.
126. Hawke, T. J.; Garry, D. J., Myogenic satellite cells: physiology to molecular biology. *Journal of Applied Physiology* **2001,** *91* (2), 534-551.

127. Lepper, C.; Partridge, T. A.; Fan, C. M., An absolute requirement for Pax7-positive satellite cells in acute injury-induced skeletal muscle regeneration. *Development* **2011,** *138* (17), 3639-46.
128. Sambasivan, R.; Yao, R.; Kissenpfennig, A.; Van Wittenberghe, L.; Paldi, A.; Gayraud-Morel, B.; Guenou, H.; Malissen, B.; Tajbakhsh, S.; Galy, A., Pax7-expressing satellite cells are indispensable for adult skeletal muscle regeneration. *Development* **2011,** *138* (17), 3647-56.
129. Saini, J.; McPhee, J. S.; Al-Dabbagh, S.; Stewart, C. E.; Al-Shanti, N., Regenerative function of immune system: Modulation of muscle stem cells. *Ageing Res Rev* **2016,** *27*, 67-76.
130. Summan, M.; Warren, G. L.; Mercer, R. R.; Chapman, R.; Hulderman, T.; Van Rooijen, N.; Simeonova, P. P., Macrophages and skeletal muscle regeneration: a clodronate-containing liposome depletion study. *Am J Physiol Regul Integr Comp Physiol* **2006,** *290* (6), R1488-95.
131. Uezumi, A.; Ikemoto-Uezumi, M.; Tsuchida, K., Roles of nonmyogenic mesenchymal progenitors in pathogenesis and regeneration of skeletal muscle. *Front Physiol* **2014,** *5*, 68.
132. Draganidis, D.; Karagounis, L. G.; Athanailidis, I.; Chatzinikolaou, A.; Jamurtas, A. Z.; Fatouros, I. G., Inflammaging and Skeletal Muscle: Can Protein Intake Make a Difference? *The Journal of Nutrition* **2016,** *146* (10), 1940-1952.
133. Farup, J.; Madaro, L.; Puri, P. L.; Mikkelsen, U. R., Interactions between muscle stem cells, mesenchymal-derived cells and immune cells in muscle homeostasis, regeneration and disease. *Cell Death & Disease* **2015,** *6* (7), e1830.
134. Lamark, T.; Svenning, S.; Johansen, T., Regulation of selective autophagy: the p62/SQSTM1 paradigm. *Essays In Biochemistry* **2017,** *61* (6), 609.
135. Katsuragi, Y.; Ichimura, Y.; Komatsu, M., p62/SQSTM1 functions as a signaling hub and an autophagy adaptor. *The FEBS journal* **2015,** *282* (24), 4672-4678.
136. Mitchell, K. J.; Pannerec, A.; Cadot, B.; Parlakian, A.; Besson, V.; Gomes, E. R.; Marazzi, G.; Sassoon, D. A., Identification and characterization of a non-satellite cell muscle resident progenitor during postnatal development. *Nature cell biology* **2010,** *12* (3), 257-66.
137. Sancricca, C.; Mirabella, M.; Gliubizzi, C.; Broccolini, A.; Gidaro, T.; Morosetti, R., Vessel-associated stem cells from skeletal muscle: From biology to future uses in cell therapy. *World J Stem Cells* **2010,** *2* (3), 39-49.
138. Valm, A. M.; Cohen, S.; Legant, W. R.; Melunis, J.; Hershberg, U.; Wait, E.; Cohen, A. R.; Davidson, M. W.; Betzig, E.; Lippincott-Schwartz, J., Applying systems-level spectral imaging and analysis to reveal the organelle interactome. *Nature* **2017,** *546* (7656), 162-167.
139. Cuervo, A. M.; Bergamini, E.; Brunk, U. T.; Dröge, W.; Ffrench, M.; Terman, A., Autophagy and Aging: The Importance of Maintaining "Clean" Cells. *Autophagy* **2014,** *1* (3), 131-140.
140. Seglen, E.-L. E. F. R. M. B. A. L. K. P. O., Seeing is believing: The impact of electron microscopy on autophagy research. *Autophagy* **2011,** *7* (9), 935-956.
141. Rajotte, D.; Stearns, C. D.; Kabcenell, A. K., Isolation of mast cell secretory lysosomes using flow cytometry. *Cytometry. Part A : the journal of the International Society for Analytical Cytology* **2003,** *55* (2), 94-101.
142. Daniele, J. R.; Heydari, K.; Arriaga, E. A.; Dillin, A., Identification and Characterization of Mitochondrial Subtypes in Caenorhabditis elegans via Analysis

of Individual Mitochondria by Flow Cytometry. *Analytical chemistry* **2016,** *88* (12), 6309-16.
143. Leipold, M. D.; Ornatsky, O.; Baranov, V.; Whitfield, C.; Nitz, M., Development of mass cytometry methods for bacterial discrimination. *Analytical biochemistry* **2011,** *419* (1), 1-8.
144. Chinopoulos, C.; Zhang, S. F.; Thomas, B.; Ten, V.; Starkov, A. A., Isolation and functional assessment of mitochondria from small amounts of mouse brain tissue. *Methods in molecular biology* **2011,** *793*, 311-24.
145. Frezza, C.; Cipolat, S.; Scorrano, L., Organelle isolation: functional mitochondria from mouse liver, muscle and cultured fibroblasts. *Nature protocols* **2007,** *2* (2), 287-95.
146. Kielar, F.; Tei, L.; Terreno, E.; Botta, M., Large Relaxivity Enhancement of Paramagnetic Lipid Nanoparticles by Restricting the Local Motions of the GdIII Chelates. *Journal of the American Chemical Society* **2010,** *132* (23), 7836-7837.
147. Ju, W. K.; Kim, K. Y.; Noh, Y. H.; Hoshijima, M.; Lukas, T. J.; Ellisman, M. H.; Weinreb, R. N.; Perkins, G. A., Increased mitochondrial fission and volume density by blocking glutamate excitotoxicity protect glaucomatous optic nerve head astrocytes. *Glia* **2015,** *63* (5), 736-53.
148. Koike, M.; Shibata, M.; Waguri, S.; Yoshimura, K.; Tanida, I.; Kominami, E.; Gotow, T.; Peters, C.; von Figura, K.; Mizushima, N.; Saftig, P.; Uchiyama, Y., Participation of Autophagy in Storage of Lysosomes in Neurons from Mouse Models of Neuronal Ceroid-Lipofuscinoses (Batten Disease). *The American Journal of Pathology* **2005,** *167* (6), 1713-1728.
149. Delettre, C.; Lenaers, G.; Griffoin, J.-M.; Gigarel, N.; Lorenzo, C.; Belenguer, P.; Pelloquin, L.; Grosgeorge, J.; Turc-Carel, C.; Perret, E.; Astarie-Dequeker, C.; Lasquellec, L.; Arnaud, B.; Ducommun, B.; Kaplan, J.; Hamel, C. P., Nuclear gene OPA1, encoding a mitochondrial dynamin-related protein, is mutated in dominant optic atrophy. *Nature Genetics* **2000,** *26*, 207.
150. Chen, H.; Chomyn, A.; Chan, D. C., Disruption of fusion results in mitochondrial heterogeneity and dysfunction. *The Journal of biological chemistry* **2005,** *280* (28), 26185-92.
151. Zuchner, S.; Mersiyanova, I. V.; Muglia, M.; Bissar-Tadmouri, N.; Rochelle, J.; Dadali, E. L.; Zappia, M.; Nelis, E.; Patitucci, A.; Senderek, J.; Parman, Y.; Evgrafov, O.; Jonghe, P. D.; Takahashi, Y.; Tsuji, S.; Pericak-Vance, M. A.; Quattrone, A.; Battaloglu, E.; Polyakov, A. V.; Timmerman, V.; Schroder, J. M.; Vance, J. M., Mutations in the mitochondrial GTPase mitofusin 2 cause Charcot-Marie-Tooth neuropathy type 2A. *Nat Genet* **2004,** *36* (5), 449-51.
152. van der Matten, L. H., Geoffrey, Visualizing Data using t-SNE. *Journal of Machine Learning Research* **2008,** *9*, 2579-2605.
153. Ornatsky, O.; Bandura, D.; Baranov, V.; Nitz, M.; Winnik, M. A.; Tanner, S., Highly multiparametric analysis by mass cytometry. *Journal of immunological methods* **2010,** *361* (1-2), 1-20.
154. Mizushima, N.; Yoshimori, T.; Ohsumi, Y., The role of Atg proteins in autophagosome formation. *Annual review of cell and developmental biology* **2011,** *27*, 107-32.
155. Zola, H., High-Sensitivity Immunofluorescence/Flow Cytometry: Detection of Cytokine Receptors and Other Low-Abundance Membrane Molecules. *Current Protocols in Cytometry* **2004,** *30* (1), 6.3.1-6.3.13.

156. Liu, R.; Wu, P.; Yang, L.; Hou, X.; Lv, Y., Inductively coupled plasma mass spectrometry-based immunoassay: A review. *Mass spectrometry reviews* **2014,** *33* (5), 373-93.
157. Lin, W.; Hou, Y.; Lu, Y.; Abdelrahman, A. I.; Cao, P.; Zhao, G.; Tong, L.; Qian, J.; Baranov, V.; Nitz, M.; Winnik, M. A., A high-sensitivity lanthanide nanoparticle reporter for mass cytometry: tests on microgels as a proxy for cells. *Langmuir : the ACS journal of surfaces and colloids* **2014,** *30* (11), 3142-53.
158. Tong, L.; Lu, E.; Pichaandi, J.; Zhao, G.; Winnik, M. A., Synthesis of Uniform NaLnF4(Ln: Sm to Ho) Nanoparticles for Mass Cytometry. *The Journal of Physical Chemistry C* **2016,** *120* (11), 6269-6280.
159. Tomalia, D. A. C., J.B.; Boas, U., *Dendrimers, Dendrons, and Dendritic Polymers: Discovery, Applications, and the Future*. Cambridge University Press: 2012.
160. Lee, C. C.; MacKay, J. A.; Frechet, J. M.; Szoka, F. C., Designing dendrimers for biological applications. *Nature biotechnology* **2005,** *23* (12), 1517-26.
161. Balzani, V. C., S.; Denti, G.; Juris, A.; Serroni, S.; Venturi, M., Designing Dendrimers Based on Transition-Metal Complexes, Light-Harvesting Properties and Predetermined Redox Patterns. *Accounts of Chemical Research* **1998,** *31*, 26-34.
162. Caminade, A.-M.; Laurent, R.; Ouali, A.; Majoral, J.-P., Poly(phosphorhydrazone) metallodendrimers. A review. *Inorganica Chimica Acta* **2014,** *409*, 68-88.
163. Vsevolod V. Rostovtsev, L. G. G.; Valery V. Fokin, a. K. B. S., A Stepwise Huisgen Cycloaddition Process: Copper (I)-Catalyzed Regioselective "Ligation" of Azides and Terminal Alkynes. *Angew Chem Int Ed* **2002,** *41* (14), 2596-2599.
164. Franc, G.; Kakkar, A. K., "Click" methodologies: efficient, simple and greener routes to design dendrimers. *Chemical Society reviews* **2010,** *39* (5), 1536-44.
165. Massue, J.; Plush, S. E.; Bonnet, C. S.; Moore, D. A.; Gunnlaugsson, T., Selective mono N-alkylations of cyclen in one step syntheses. *Tetrahedron Letters* **2007,** *48* (45), 8052-8055.
166. Wuts, P. G. M. G., T.W., *Greene's PRotective Groups in Organic Synthesis*. 4th ed.; Wiley & Sons: 2007.
167. Allo, B.; Lou, X.; Bouzekri, A.; Ornatsky, O., Clickable and High-Sensitivity Metal-Containing Tags for Mass Cytometry. *Bioconjug Chem* **2018,** *29* (6), 2028-2038.
168. *The Aptamer Handbook*. Wiley-VCH: 2006.
169. Carothers, J. M. O., S.C.; Davis, J.H.; Szostak, J.W., Informational Complexity and Functional Acitivity of RNA Structures. *Journal of the American Chemical Society* **2004,** *126*, 5130-5137.
170. Shangguan, D.; Li, Y.; Tang, Z.; Cao, Z. C.; Chen, H. W.; Mallikaratchy, P.; Sefah, K.; Yang, C. J.; Tan, W., Aptamers evolved from live cells as effective molecular probes for cancer study. *Proceedings of the National Academy of Sciences of the United States of America* **2006,** *103* (32), 11838-43.
171. BRUCE E EATON, L. G. A. D. A. Z., Let's Get Specifc: The Relationship Between Specificity and Affinity. *Chemistry & Biology* **1995,** *2*, 633-638.
172. Nunez, C. E.; Rodrigues, V. S.; Gomes, F. S.; Moura, R. F.; Victorio, S. C.; Bombassaro, B.; Chaim, E. A.; Pareja, J. C.; Geloneze, B.; Velloso, L. A.; Araujo, E. P., Defective regulation of adipose tissue autophagy in obesity. *International journal of obesity* **2013,** *37* (11), 1473-80.
173. Gold, C. T. L., Systematic enrichment of ligands by exponential enrichment: RNA ligands to bacteriophage T4 DNA polymerase. *Science* **1990,** *3* (249), 505-510.

174. Ellington, A. S., J.W., In vitro selection of RNA molecules that bind specific ligands. *Nature* **1990,** *346*, 818-822.
175. Sefah, K.; Shangguan, D.; Xiong, X.; O'Donoghue, M. B.; Tan, W., Development of DNA aptamers using Cell-SELEX. *Nature protocols* **2010,** *5* (6), 1169-85.
176. Degtyarev, M.; Reichelt, M.; Lin, K., Novel quantitative autophagy analysis by organelle flow cytometry after cell sonication. *PloS one* **2014,** *9* (1), e87707.
177. Edgar, L. J.; Vellanki, R. N.; Halupa, A.; Hedley, D.; Wouters, B. G.; Nitz, M., Identification of hypoxic cells using an organotellurium tag compatible with mass cytometry. *Angewandte Chemie* **2014,** *53* (43), 11473-7.
178. Lumba, M. A.; Willis, L. M.; Santra, S.; Rana, R.; Schito, L.; Rey, S.; Wouters, B. G.; Nitz, M., A beta-galactosidase probe for the detection of cellular senescence by mass cytometry. *Org Biomol Chem* **2017,** *15* (30), 6388-6392.
179. Frei, A. P.; Bava, F. A.; Zunder, E. R.; Hsieh, E. W.; Chen, S. Y.; Nolan, G. P.; Gherardini, P. F., Highly multiplexed simultaneous detection of RNAs and proteins in single cells. *Nat Methods* **2016,** *13* (3), 269-75.
180. Youle, R. J.; Narendra, D. P., Mechanisms of mitophagy. *Nat Rev Mol Cell Biol* **2011,** *12* (1), 9-14.
181. Klionsky, D. J.; et al., Guidelines for the use and interpretation of assays for monitoring autophagy (3rd edition). *Autophagy* **2016,** *12* (1), 1-222.
182. Smith Robin, A. J.; Porteous Carolyn, M.; Coulter Carolyn, V.; Murphy Michael, P., Selective targeting of an antioxidant to mitochondria. *European Journal of Biochemistry* **2001,** *263* (3), 709-716.
183. Zielonka, J.; Joseph, J.; Sikora, A.; Hardy, M.; Ouari, O.; Vasquez-Vivar, J.; Cheng, G.; Lopez, M.; Kalyanaraman, B., Mitochondria-Targeted Triphenylphosphonium-Based Compounds: Syntheses, Mechanisms of Action, and Therapeutic and Diagnostic Applications. *Chemical reviews* **2017,** *117* (15), 10043-10120.
184. Ehrenberg, B.; Montana, V.; Wei, M. D.; Wuskell, J. P.; Loew, L. M., Membrane potential can be determined in individual cells from the nernstian distribution of cationic dyes. *Biophysical Journal* **1988,** *53* (5), 785-794.
185. Li, Z.; Lopez, M.; Hardy, M.; McAllister, D. M.; Kalyanaraman, B.; Zhao, M., A (99m)Tc-Labeled Triphenylphosphonium Derivative for the Early Detection of Breast Tumors. *Cancer Biotherapy & Radiopharmaceuticals* **2009,** *24* (5), 579-587.
186. Kalyanaraman, B.; Joseph, J.; Schmainda, K.M.; Prah, D.E.; Lopez, M.; Hardy, M.J., In vivo mitochondrial labeling using positively-charged nitoxide enhanced and gadolinium chelate enhanced magnetic resonance imaging. US8388936B2, March 5th, 2013.
187. Willems, L. I.; Overkleeft, H. S.; van Kasteren, S. I., Current developments in activity-based protein profiling. *Bioconjug Chem* **2014,** *25* (7), 1181-91.
188. Wang, M.; Casey, P. J., Protein prenylation: unique fats make their mark on biology. *Nat Rev Mol Cell Biol* **2016,** *17* (2), 110-22.
189. Hutagalung, A. H.; Novick, P. J., Role of Rab GTPases in membrane traffic and cell physiology. *Physiological reviews* **2011,** *91* (1), 119-49.
190. Lee, M. T.; Mishra, A.; Lambright, D. G., Structural mechanisms for regulation of membrane traffic by rab GTPases. *Traffic* **2009,** *10* (10), 1377-89.
191. Palsuledesai, C. C.; Ochocki, J. D.; Kuhns, M. M.; Wang, Y. C.; Warmka, J. K.; Chernick, D. S.; Wattenberg, E. V.; Li, L.; Arriaga, E. A.; Distefano, M. D., Metabolic Labeling with an Alkyne-modified Isoprenoid Analog Facilitates Imaging and Quantification of the Prenylome in Cells. *ACS chemical biology* **2016,** *11* (10), 2820-2828.

192. Fonovic, M.; Bogyo, M., Activity-based probes as a tool for functional proteomic analysis of proteases. *Expert Rev Proteomics* **2008,** *5* (5), 721-30.
193. Heal, W. P.; Dang, T. H.; Tate, E. W., Activity-based probes: discovering new biology and new drug targets. *Chemical Society reviews* **2011,** *40* (1), 246-57.
194. Blum, G.; Mullins, S. R.; Keren, K.; Fonovic, M.; Jedeszko, C.; Rice, M. J.; Sloane, B. F.; Bogyo, M., Dynamic imaging of protease activity with fluorescently quenched activity-based probes. *Nat Chem Biol* **2005,** *1* (4), 203-9.
195. Speers, A. E.; Adam, G. C.; Cravatt, B. F., Activity-Based Protein Profiling in Vivo Using a Copper(I)-Catalyzed Azide-Alkyne [3 + 2] Cycloaddition. *Journal of the American Chemical Society* **2003,** *125* (16), 4686-4687.
196. Charron, G.; Tsou, L. K.; Maguire, W.; Yount, J. S.; Hang, H. C., Alkynyl-farnesol reporters for detection ofproteinS-prenylation in cells. *Mol. BioSyst.* **2011,** *7* (1), 67-73.
197. Duckworth, B. P.; Zhang, Z.; Hosokawa, A.; Distefano, M. D., Selective labeling of proteins by using protein farnesyltransferase. *Chembiochem* **2007,** *8* (1), 98-105.
198. Hosokawa, A.; Wollack, J. W.; Zhang, Z.; Chen, L.; Barany, G.; Distefano, M. D., Evaluation of an Alkyne-containing Analogue of Farnesyl Diphosphate as a Dual Substrate for Protein-prenyltransferases. *International Journal of Peptide Research and Therapeutics* **2007,** *13* (1-2), 345-354.
199. Krzysiak, A. J.; Rawat, D. S.; Scott, S. A.; Pais, J. E.; Handley, M.; Harrison, M. L.; Fierke, C. A.; Gibbs, R. A., Combinatorial Modulation of Protein Prenylation. *ACS chemical biology* **2007,** *2* (6), 385-389.
200. Zhang, F. L.; Casey, P. J., Protein Prenylation: Molecular Mechanisms and Functional Consequences. *Annual Review of Biochemistry* **1996,** *65* (1), 241-269.
201. Shaklee, J.; Srivastava, K.; Brown, H.; Arriaga, E. A.; Pierre, V. C.; van Berlo, J. H., Development of a Click-Chemistry Reagent Compatible with Mass Cytometry. *Sci Rep* **2018,** *8* (1), 6657.
202. Schiaffino, S.; Reggiani, C., Fiber Types in Mammalian Skeletal Muscles. *Physiological reviews* **2011,** *91* (4), 1447-1531.
203. Paolini, A.; Omairi, S.; Mitchell, R.; Vaughan, D.; Matsakas, A.; Vaiyapuri, S.; Ricketts, T.; Rubinsztein, D. C.; Patel, K., Attenuation of autophagy impacts on muscle fibre development, starvation induced stress and fibre regeneration following acute injury. *Sci Rep* **2018,** *8* (1), 9062.
204. Wang, Y.; Pessin, J. E., Mechanisms for fiber-type specificity of skeletal muscle atrophy. *Curr Opin Clin Nutr Metab Care* **2013,** *16* (3), 243-50.
205. Yamada, E.; Bastie, C. C.; Koga, H.; Wang, Y.; Cuervo, A. M.; Pessin, J. E., Mouse skeletal muscle fiber-type-specific macroautophagy and muscle wasting are regulated by a Fyn/STAT3/Vps34 signaling pathway. *Cell reports* **2012,** *1* (5), 557-69.
206. Mofarrahi, M.; Guo, Y.; Haspel, J. A.; Choi, A. M.; Davis, E. C.; Gouspillou, G.; Hepple, R. T.; Godin, R.; Burelle, Y.; Hussain, S. N., Autophagic flux and oxidative capacity of skeletal muscles during acute starvation. *Autophagy* **2013,** *9* (10), 1604-20.
207. Santos-Zas, I.; Cid-Diaz, T.; Gonzalez-Sanchez, J.; Gurriaran-Rodriguez, U.; Seoane-Mosteiro, C.; Porteiro, B.; Nogueiras, R.; Casabiell, X.; Relova, J. L.; Gallego, R.; Mouly, V.; Pazos, Y.; Camina, J. P., Obestatin controls skeletal muscle fiber-type determination. *Sci Rep* **2017,** *7* (1), 2137.

208. Pette, D. S., R.S., Cellular and molecular diversities of mammalian skeletal muscle fibers. In *Reviews of Physiology, Biochemistry and Pharmacology*, Springer: Berlin, Heidelberg, 1990; Vol. 116.
209. Bottinelli, R. B., R.; Schiaffino, S.; Reggiani, C., Maximum shortening velocity and coexistence of myosin heavy chain isoforms in single skinned fast fibres of rat skeletal muscle. *J Muscle Res. Cell Motil.* **1994,** *15* (4), 413-9.

Appendix A

Supporting Information for Chapter 3

A.1 **Antibody Panel Characterization**

Table A1. Metal-Labeled Antibody Panel Characterization. The following antibodies were metal labeled and characterized to quantify the average number of lanthanide ions chelated by each polymer-antibody conjugate.

Target	Metal Isotope	Isotype	Vendor & p/n	Average Lanthanide Ions / Antibody
Mouse IgG #1	^{141}Pr	-----	Invitrogen, 026502	42.5
LC3	^{142}Nd	rabbit	Novus, NB100-2220	59.2
BF35	^{145}Nd	mouse	DSHB / promab, custom	56.6
CC3	^{147}Sm	Rabbit	R&D Systems, MAB835	68.3
Atg5	^{149}Sm	mouse	Novus, NB110-53818	31.3
MyoD	^{153}Eu	mouse	BD Pharmingen, 554130	48.0
Goat IgG	^{155}Gd	-----	Invitrogen, 02-9602	66.9
Mfn1	^{156}Gd	mouse	Abcam, ab57602	174.9
Mouse IgG #2	^{160}Gd	------	Thermo Scientific, 10400C	48.8
Bec1 / Atg6	^{161}Dy	mouse	R&D Systems, MAB 5295	92.1
Mouse IgG #3	^{163}Dy	-----	Thermo Fisher, 31903	46.6
Lrrk2	^{165}Ho	goat	R&D Systems, AF6674	14.2
p62	^{166}Er	mouse	Abnova, H00008878-M01	51.1
Rat IgG	^{168}Er	-----	R & D Systems, MAB005	69.8
Rabbit IgG	^{171}Yb	-----	Invitrogen, 026102	61.9
GAPDH	^{172}Yb	rabbit	Rockland, 600-401-A33	98.8
Yb1	^{174}Yb	rabbit	Abcam, ab12148	95.7
MyoG	^{175}Lu	mouse	affymetrix, 14-5643	84.2
Atg4a	^{176}Yb	rabbit	Novus, NBP1-68462	74.9

A.2 Quality Control of Corrected and Normalized Mass Cytometry Data

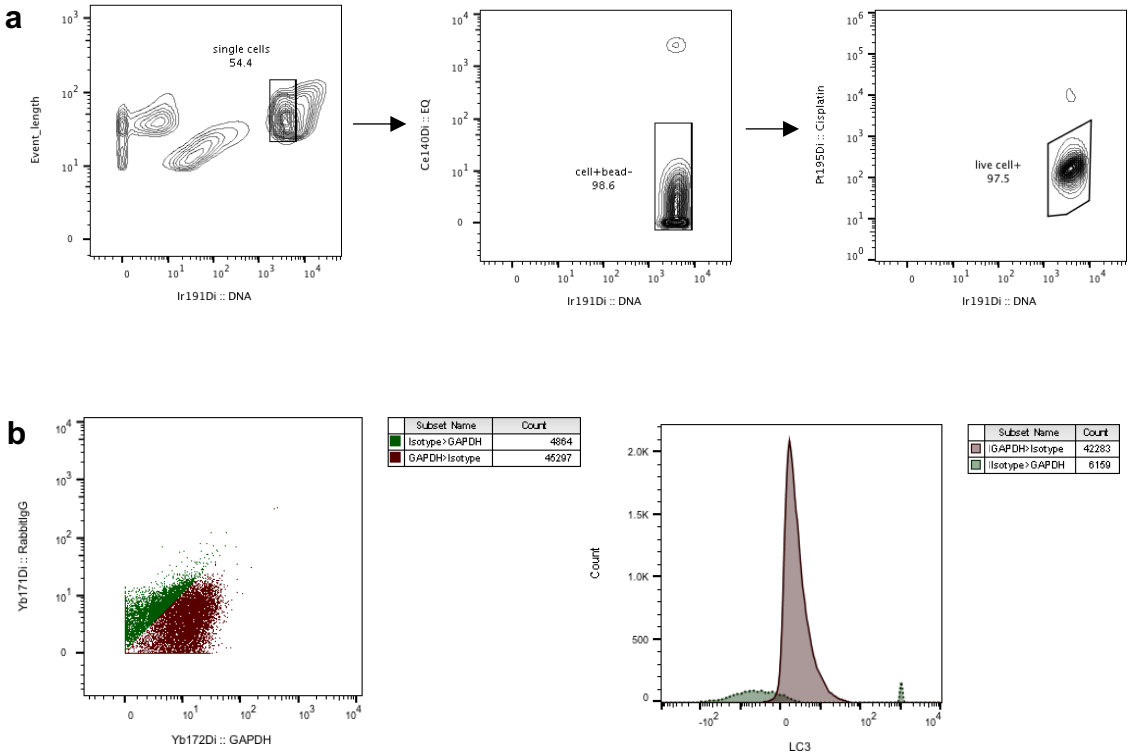

Figure A1. Quality assessment of mass cytometry data after correction and normalization. (a) general gating scheme performed on EQ bead normalized files. Contours represent 2% increases in population density, and percent from parent gate are indicated under gate name. (b) representative biaxial dot plot showing a fraction of population with a lower GAPDH signal than corresponding isotype. Histogram showing negative values for normalized anti-LC3 signal where the isotype is greater than GAPDH. The population where GAPDH is lower than its corresponding isotype were removed from subsequent analyses.

	sample description	total # cell events	# cell events removed	% removed
WT and ATG7 KO L6 Myoblasts	WT_0.25 µg/mL	23033	6692	29
	WT_0.50 µg/mL	21408	5783	27
	WT_1.00 µg/mL	27417	7428	27
	WT_2.00 µg/mL	18277	4534	25
	WT_4.00 µg/mL	33098	7917	24
	ATG7 KO_0.25 µg/mL	28255	8409	30
	ATG7 KO_0.50 µg/mL	22135	6328	29
	ATG7 KO_1.00 µg/mL	14260	4101	29
	ATG7 KO_2.00 µg/mL	19248	4395	23
	ATG7 KO_4.00 µg/mL	12203	2692	22
Drug-Treated C2C12 Myoblasts	NC_0.25 µg/mL	26618	4373	16
	NC_0.50 µg/mL	25410	3700	15
	NC_1.00 µg/mL	31262	4971	16
	NC_2.00 µg/mL	34471	3828	11
	NC_4.00 µg/mL	22336	3105	14
	Treated_0.25 µg/mL	30189	4353	14
	Treated_0.50 µg/mL	26096	3420	13
	Treated_1.00 µg/mL	49321	5837	12
	Treated_2.00 µg/mL	35315	4317	12
	Treated_4.00 µg/mL	39760	4569	11

Table A2. Percentage of cells from each sample removed from analysis. As shown in Figure A2, a bimodal distribution can be observed in normalized and corrected data and is attributable to a larger number of isotype antibodies bound per cell than specific antibodies. We removed these cells from subsequent analyses. The percentage of cells removed from each cell sample are shown below. Similar percentages of cells were removed from biological replicates (data not shown).

A.3 **ATG7 KO L6 Myoblast Cell Line Characterization**

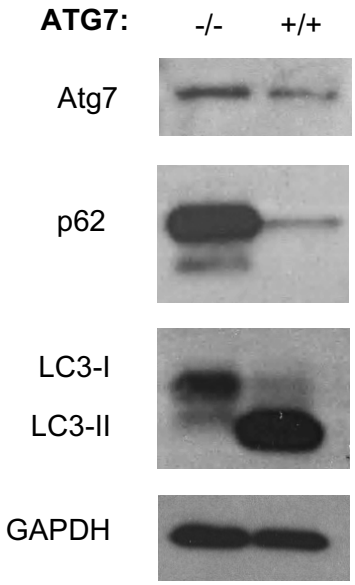

Figure A2. Western blot Autophagy Markers in ATG7 KO L6 Myoblast Cell Line. The ATG7 knock-out cell line was produced using CRISPR-Cas-9 technology by the Genetic Engineering Resource Center at the University of Minnesota and characterized using TIDE sequencing. This clone has a biallelic single base pair deletion in exon 1 (data not shown). Atg7 protein expression is increased in the ATG7 KO clone over WT despite the introduced genetic modification. However, the Atg7 protein seems to be inactive as evidenced by the accumulation of p62 and the lack of lipid-conjugated LC3 (LC3-II).

A.4 Representative Individual Autophagy Marker Histograms

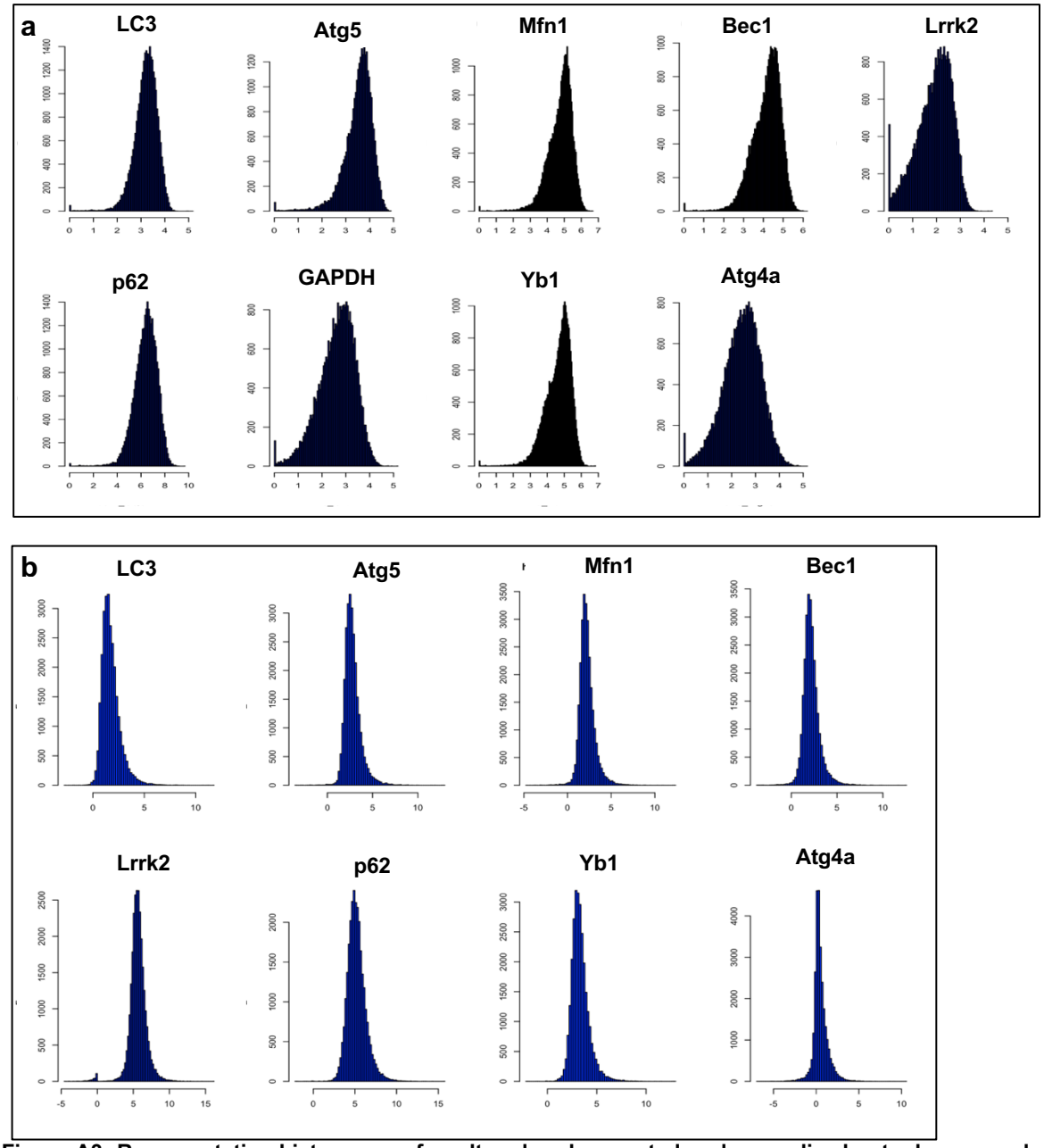

Figure A3. Representative histograms of unaltered and corrected and normalized autophagy panel antibody probes in WT L6 myoblasts. (a) representative histograms showing cell population distributions before correction and normalization. (b) representative histograms of the same data shown in (a), after correction and normalization.

A.5 Normalized ATG7 KO L6 Myoblast Titration Curves

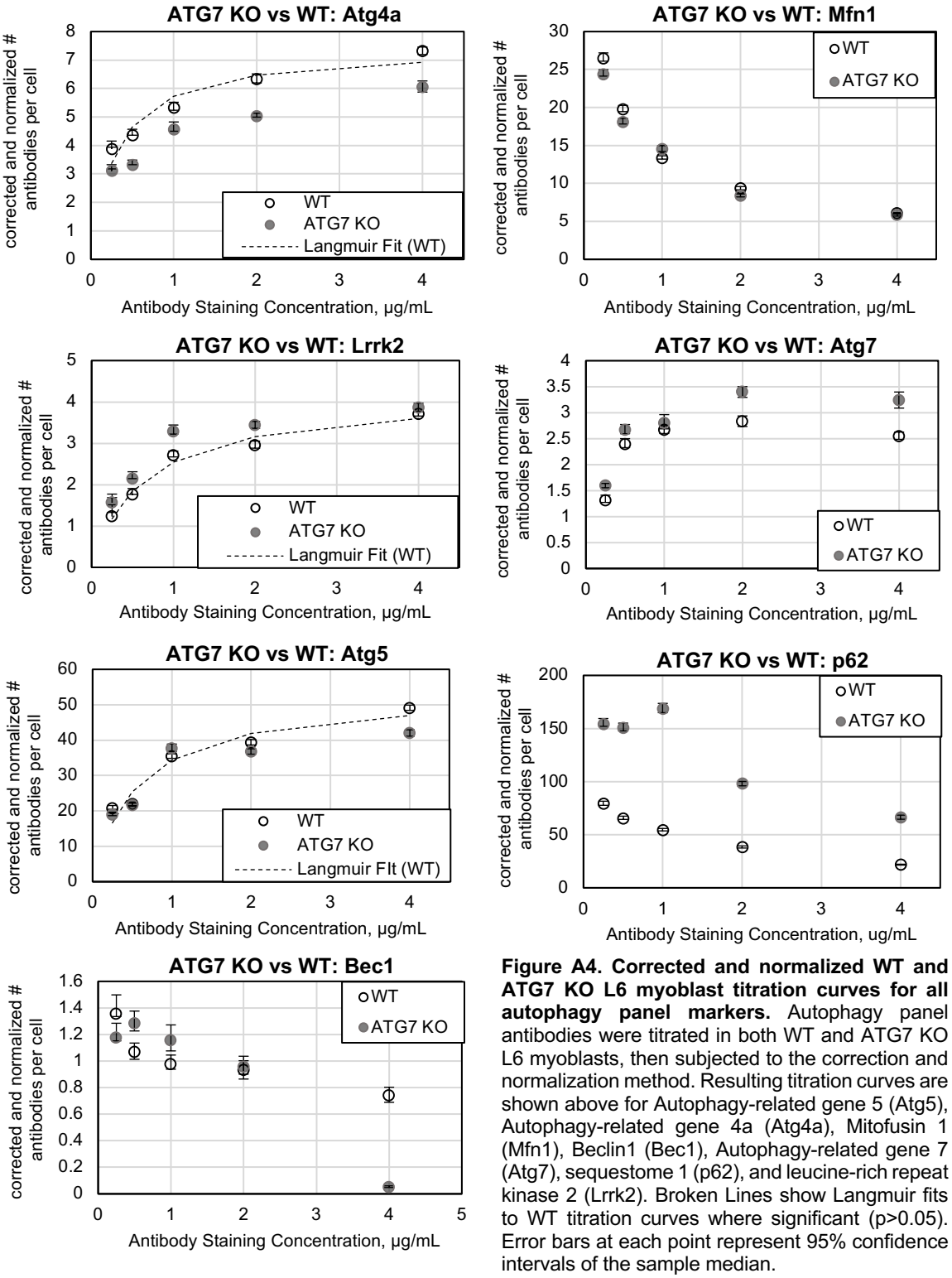

Figure A4. Corrected and normalized WT and ATG7 KO L6 myoblast titration curves for all autophagy panel markers. Autophagy panel antibodies were titrated in both WT and ATG7 KO L6 myoblasts, then subjected to the correction and normalization method. Resulting titration curves are shown above for Autophagy-related gene 5 (Atg5), Autophagy-related gene 4a (Atg4a), Mitofusin 1 (Mfn1), Beclin1 (Bec1), Autophagy-related gene 7 (Atg7), sequestome 1 (p62), and leucine-rich repeat kinase 2 (Lrrk2). Broken Lines show Langmuir fits to WT titration curves where significant ($p>0.05$). Error bars at each point represent 95% confidence intervals of the sample median.

A.6 Non-normalized ATG7 KO L6 Myoblast Titration Curves

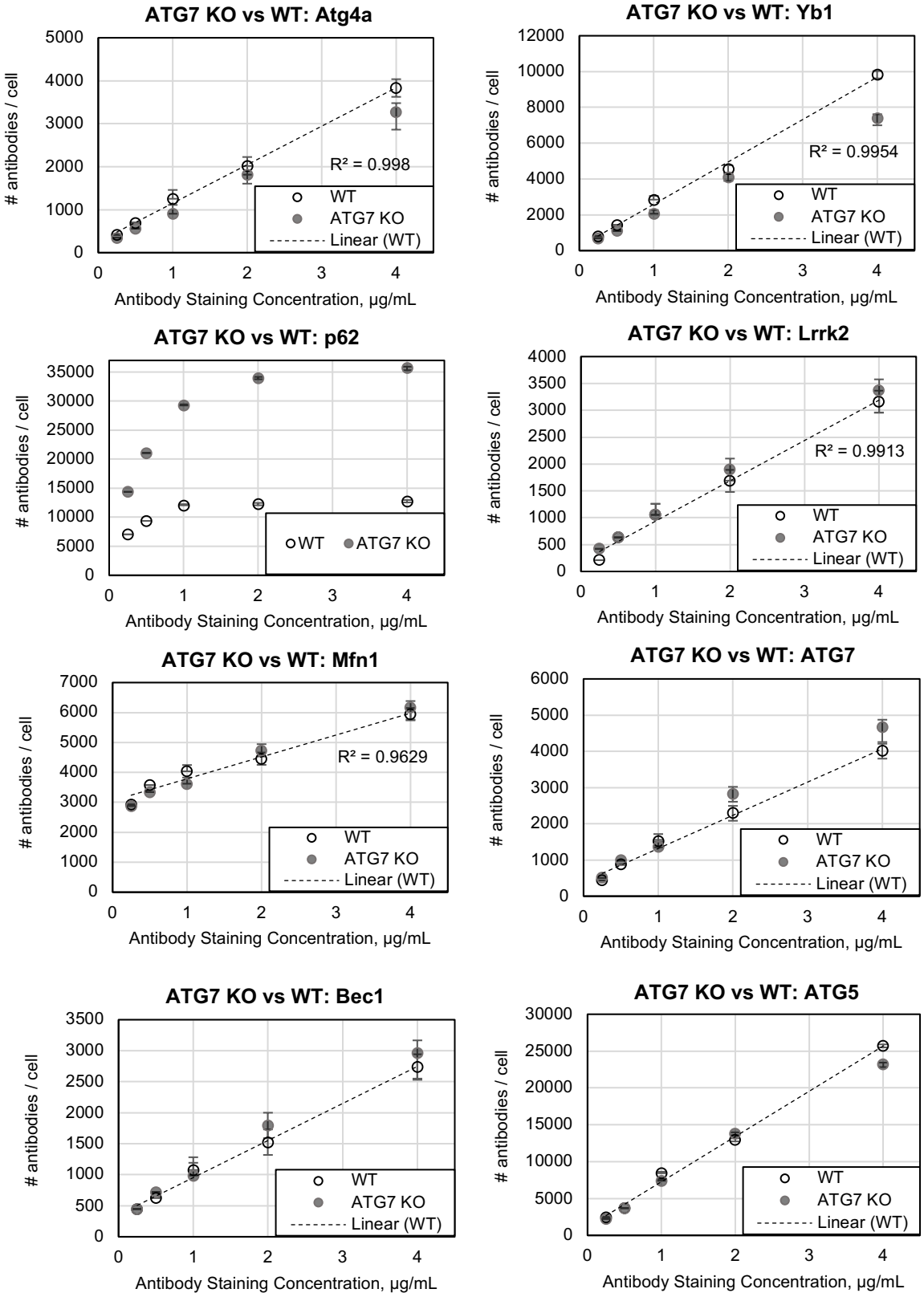

Figure A5. Unaltered WT and ATG7 KO L6 myoblast titration curves for all autophagy panel markers. Autophagy panel antibodies were titrated in both WT and ATG7 KO L6 myoblasts. Resulting titration curves are shown above for Autophagy-related gene 5 (Atg5), Autophagy-related gene 4a (Atg4a), Mitofusin 1 (Mfn1), Beclin 1 (Bec1), Autophagy-related gene 7 (Atg7), sequestome 1 (p62), and leucine rich repeat kinase 2 (Lrrk2). Broken Lines show linear regression fits to WT titration curves with R^2 values where significant ($p>0.05$). Error bars at each point represent 95% confidence intervals of the sample median.

A.7 Corrected and Normalized Titration Curves for Rapamycin / Bafilomycin A1 Treated C2C12 Myoblasts

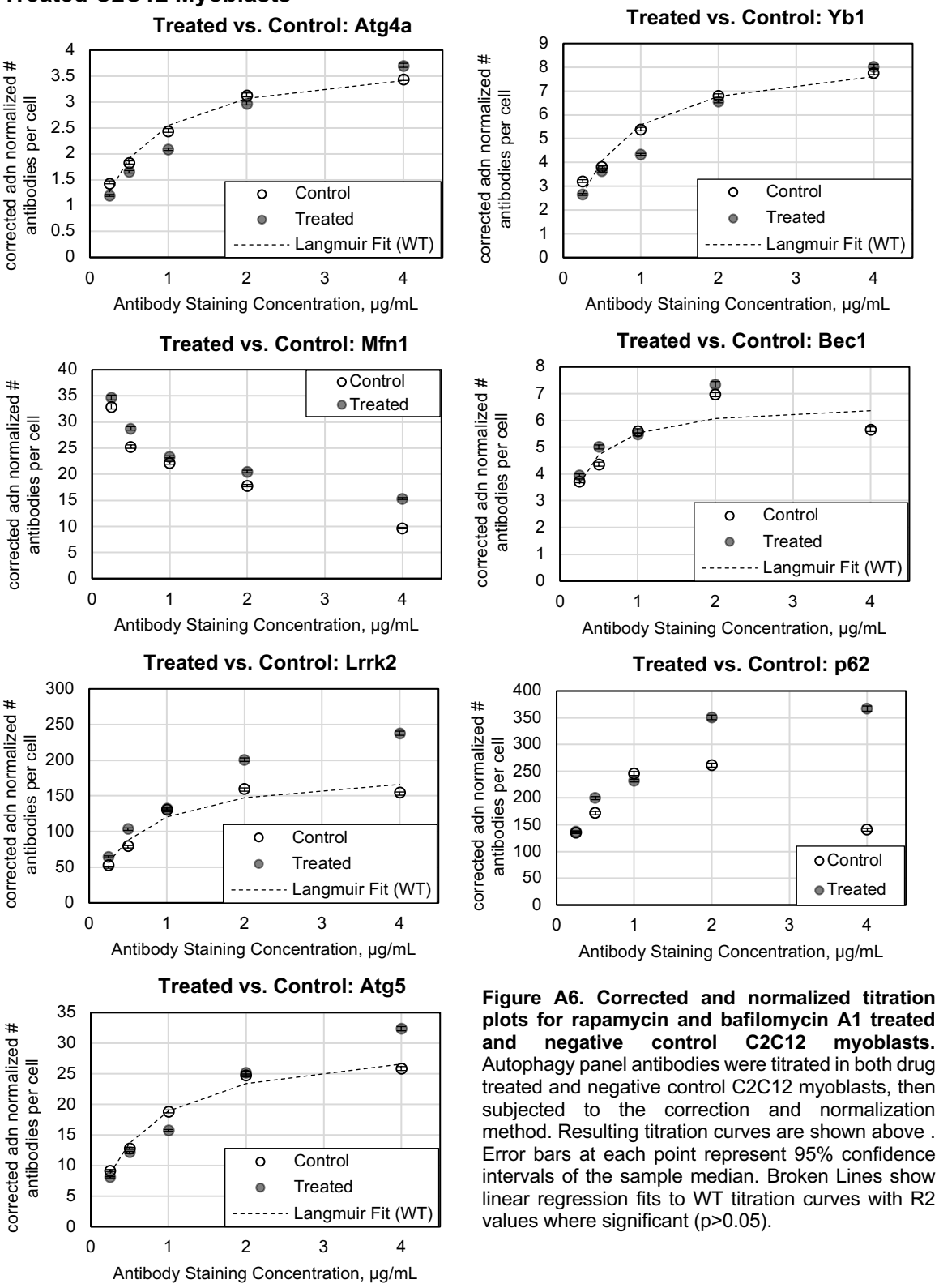

Figure A6. Corrected and normalized titration plots for rapamycin and bafilomycin A1 treated and negative control C2C12 myoblasts. Autophagy panel antibodies were titrated in both drug treated and negative control C2C12 myoblasts, then subjected to the correction and normalization method. Resulting titration curves are shown above . Error bars at each point represent 95% confidence intervals of the sample median. Broken Lines show linear regression fits to WT titration curves with R2 values where significant (p>0.05).

A.8 Non-corrected or Normalized Titration Plots for Rapamycin / Bafilomycin A1 Treated C2C12 Myoblasts

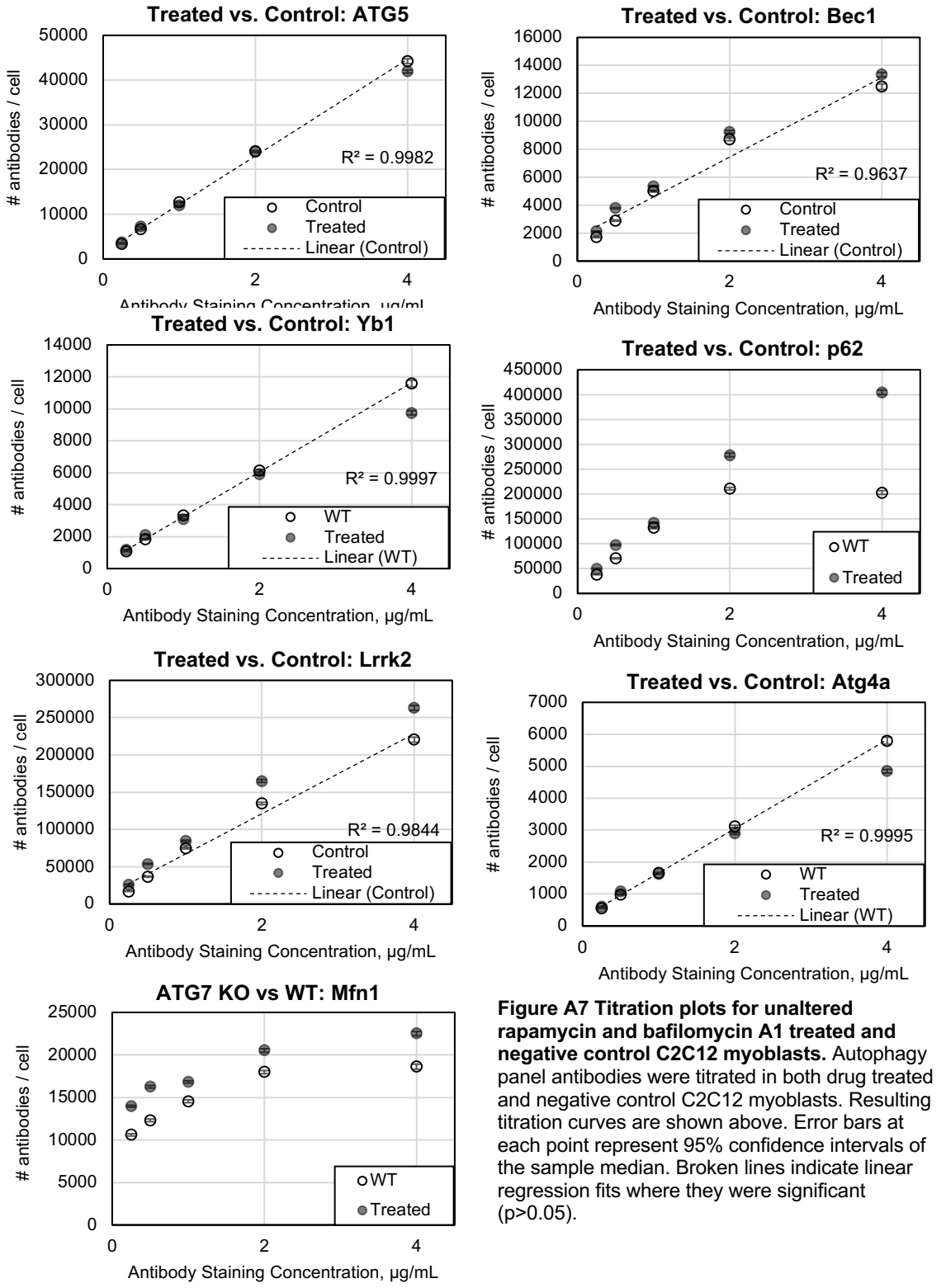

Figure A7 Titration plots for unaltered rapamycin and bafilomycin A1 treated and negative control C2C12 myoblasts. Autophagy panel antibodies were titrated in both drug treated and negative control C2C12 myoblasts. Resulting titration curves are shown above. Error bars at each point represent 95% confidence intervals of the sample median. Broken lines indicate linear regression fits where they were significant ($p>0.05$).

A.9 Correction and Normalization Return Consistent Results Across Isotype Antibody Clones and Separate Day Biological Replicates

To establish the reproducibility of the correction and normalization method, two areas of potential variability were investigated, including: i) the variability in isotype antibody affinity and avidity between separate commercially available isotype antibody clones, and ii) the ability of the correction and normalization method to normalize inter-day staining and instrument variation.

We tested the robustness of this method to changes in isotype antibody formulation. Isotype control antibodies have been used extensively in flow cytometry experiments to estimate non-specific antibody binding, though finding a “true” control with equal affinity, avidity, fluorescence / protein ratio, concentration, host species and type is often difficult. We adopted the concept for mass cytometry, where we have controlled for isotype control antibody type, host species, concentration, and metal atom per antibody content. However, we cannot control for differences in the affinity or avidity of an isotype control antibody clone. We investigated the effect of using different isotype control antibody clones on quantifying non-specific binding. Three separate clones (see Table A1) were purchased, metal-labeled and simultaneously titrated along with the corresponding specific antibodies. At each antibody staining concentration, the number of bound specific antibodies is the same regardless of the isotype antibody clone (Figure A8), as shown by overlapping 95% confidence intervals for each point in the titration curve.

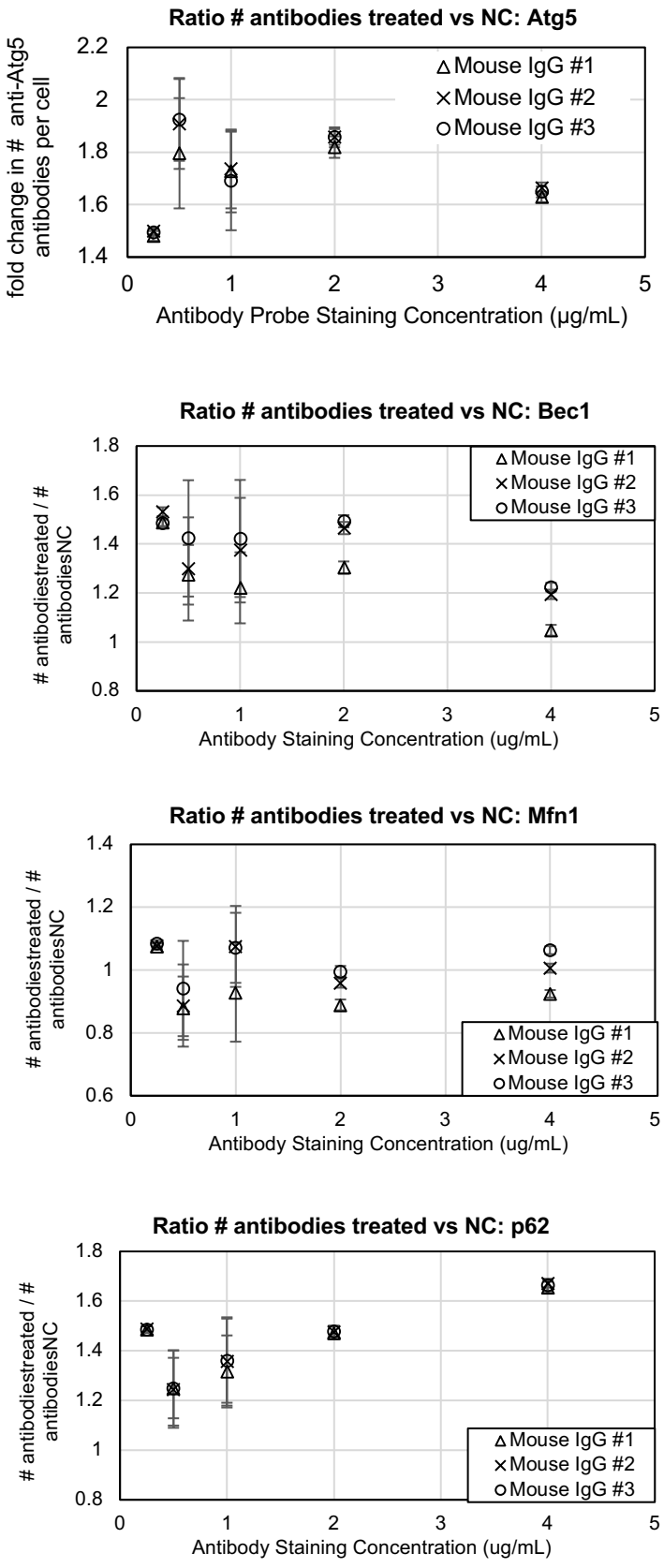

Figure A8. Isotype clone does not affect correction and normalization titration data. To characterize the utility of this method, we needed to ensure the clonality of the isotype antibodies used did not return significantly different results. This plot shows the fold change between rapamycin and bafilomycin A1 treated vs negative control cells at each point in a titration curve. Each series represents correction and normalization done using a separate mouse isotype clone. The overlap of the 95% confidence intervals for each clone at every concentration indicates no significant change with isotype clone. Error bars represent a 95% confidence interval about a median.

To investigate the ability of the correction and normalization method to normalize between cell samples prepared and analyzed on separate days, C2C12 myoblasts were titrated following the same procedure roughly one month apart. Titration plots showing the non-corrected and normalized data show linear trends with different sensitivities (Figure A9). After correction and normalization, the titration plots follow the expected trajectory and show a plateau at the same antibody staining concentration (2 µg/mL antibody, Figure A9). These data indicate that the correction and normalization method are resistant to inter-day variation arising from sample preparation or instrument variability.

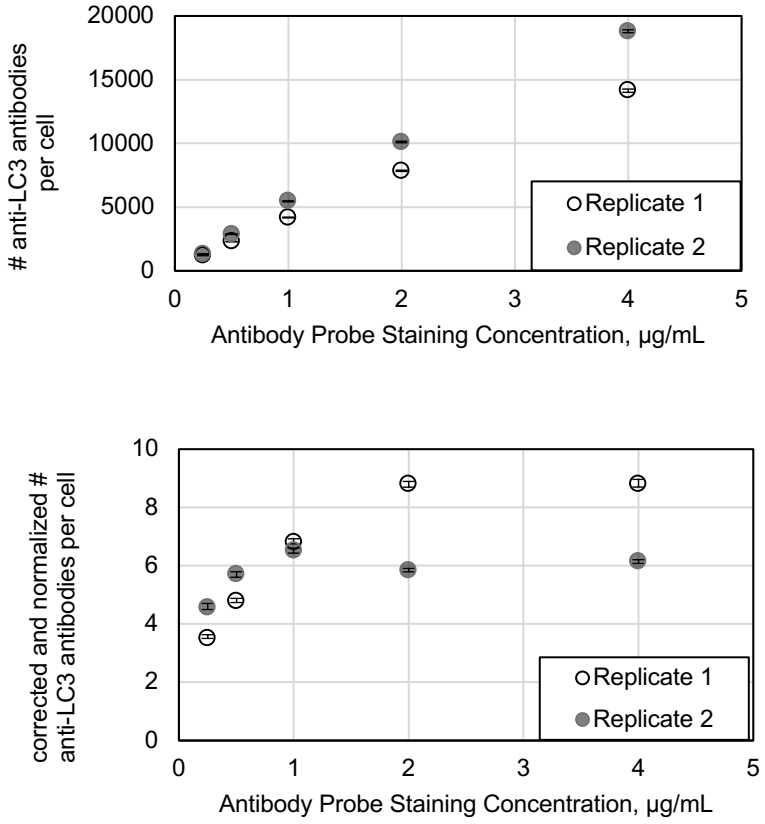

Figure A9. Correction and normalization corrects for day to day sample preparation and instrument variation. (a) unaltered titration plot of anti-LC3 antibody probe shows a linear trend on two separate days. (b) correction and normalization of titration data in (a) show titration curves with expected trajectories, through elimination of non-specific signal. Error bars represent a 95% confidence interval around a population median.

A.10 **BF Microscopy Images of Trypsinized Myotubes**

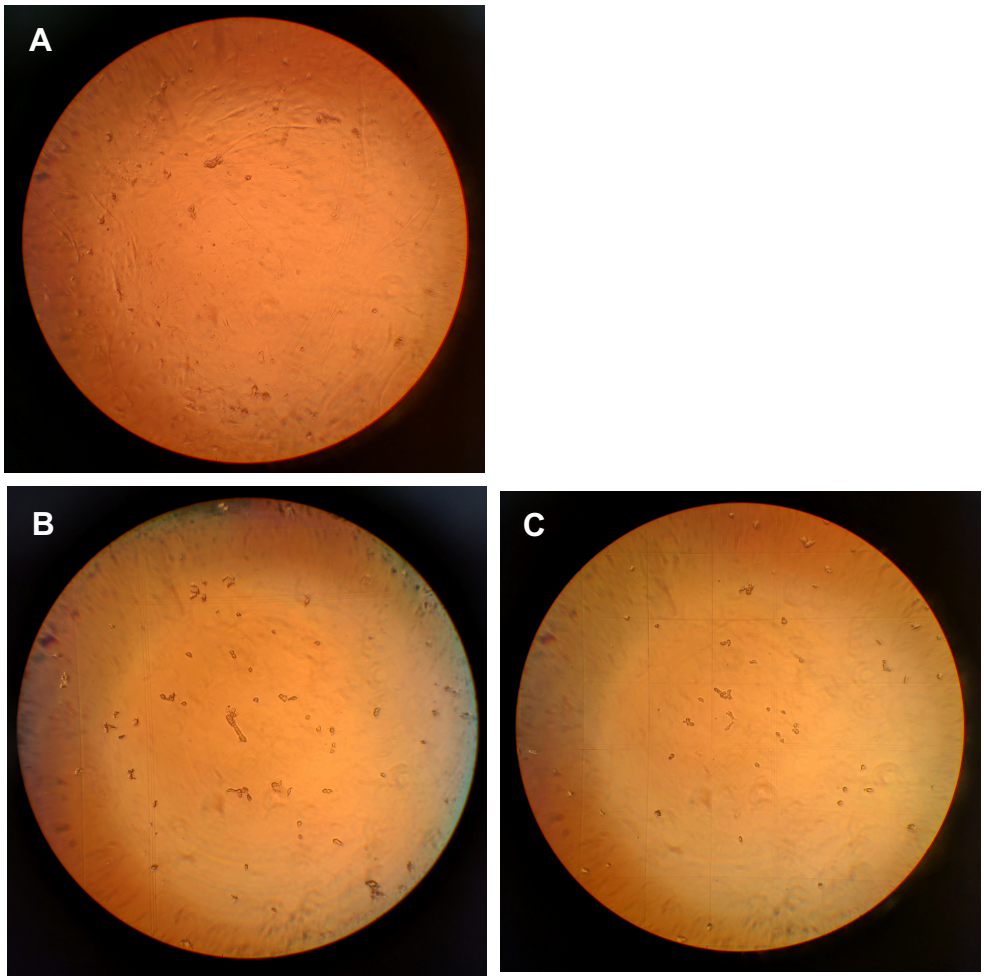

Figure 10. Representitative images of trypsinized culture of 120 h differentiated C2C12 cells. We sought to understand the morphological characteristics of differentiating myoblasts and myotubes subjected to protease treatment required to lift cells from the growth flask surface. (A) Culture of differentiating myoblasts and myotubes. (B-C) Cells in suspension. Most are spherical in shape, with some longer cylindrical myotubes visible.

A.11 Gating Strategy for Differentiating Myoblasts

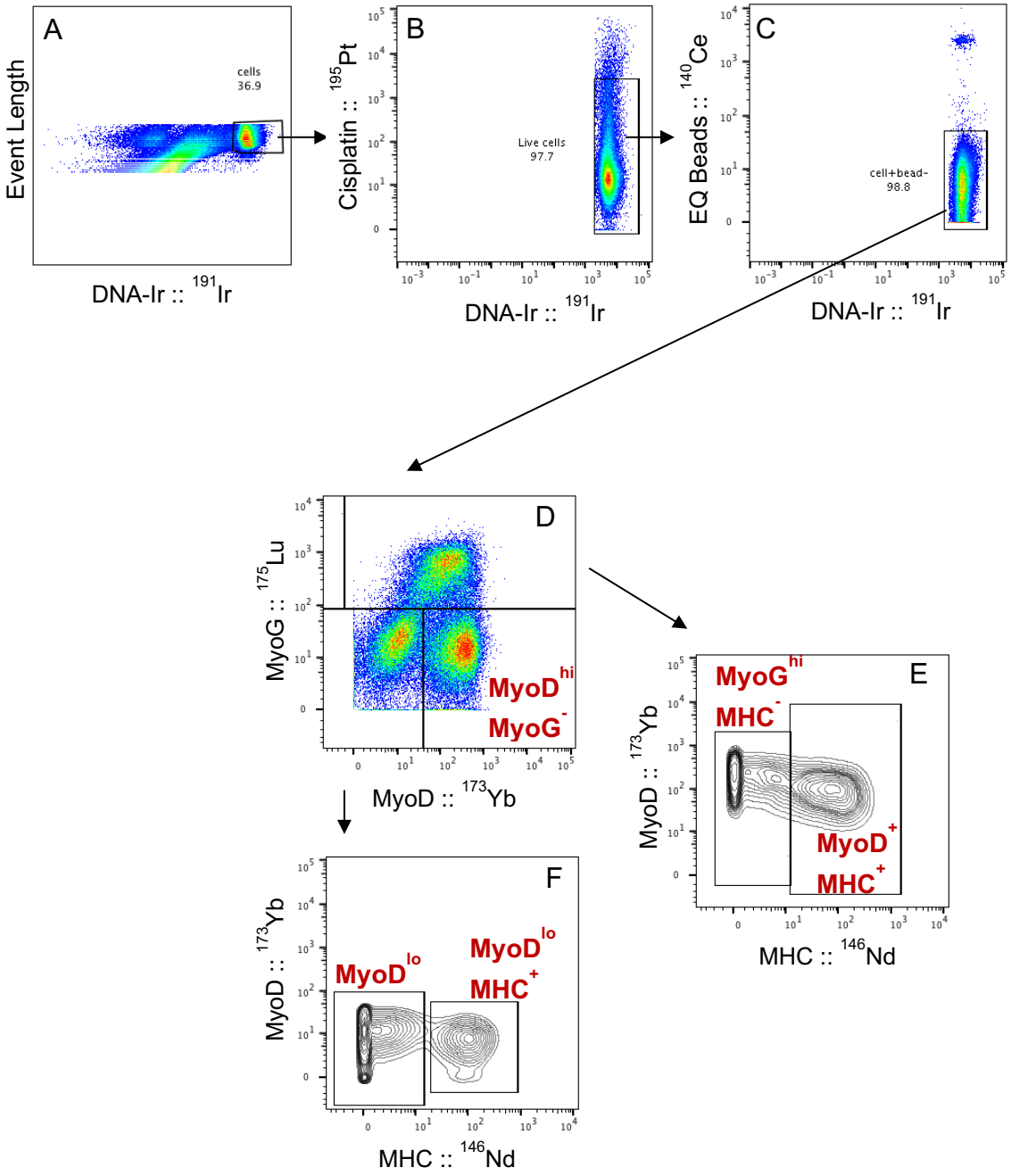

Figure A11. Manual single cell gating strategy. (A) Identification of whole cells. (B) Identification of live cells. (C) Removal of bead-cell conjugates. (D) Identification of MyoD^{hi}, MyoD^{lo}, and MyoG^{+} populations. (E) Identification of MyoG^{+}, MyoD^{+}, MHC^{-} and MyoG^{+}, MyoD^{+}, MHC^{-} populations representative of cells in mid-late differentiation time points. (F) Identification of MyoD^{lo}, MHC^{-} myoblasts vs MyoD^{lo}, MHC^{+} terminally differentiated myotubes.

Appendix B

Supporting Information for Chapter 4

B.1 **Antibody Panel Characterization**

Table B1. Metal-Labeled Antibody Panel Characterization. The following antibodies were metal labeled and characterized (where indicated) to quantify the average number of lanthanide ions chelated by each polymer-antibody conjugate.

Target	Metal Isotope	Isotype	Vendor & p/n	Average Lanthanide Ions per Antibody	Labeled at UMN?
LC3	^{142}Nd	rabbit	Novus, NB100-2220	59.2	Y
BF35	^{145}Nd	mouse	DSHB / promab, custom	56.6	Y
CC3	^{147}Sm	rabbit	R&D Systems, MAB835	68.3	Y
Atg5	^{149}Sm	mouse	Novus, NB110-53818	31.3	Y
MyoD	^{153}Eu	mouse	BD Pharmingen, 554130	48.0	Y
Goat IgG	^{155}Gd	-----	Invitrogen, 02-9602	66.9	Y
Mfn1	^{156}Gd	mouse	Abcam, ab57602	174.9	Y
Mouse IgG	^{160}Gd	------	Thermo Scientific, 10400C	48.8	Y
Bec1 / Atg6	^{161}Dy	mouse	R&D Systems, MAB 5295	92.1	Y
Lrrk2	^{165}Ho	goat	R&D Systems, AF6674	14.2	Y
p62	^{166}Er	mouse	Abnova, H00008878-M01	51.1	Y
Rat IgG	^{168}Er	-----	R & D Systems, MAB005	69.8	Y
Rabbit IgG	^{171}Yb	-----	Invitrogen, 026102	61.9	Y
GAPDH	^{172}Yb	rabbit	Rockland, 600-401-A33	98.8	Y
Yb1	^{174}Yb	rabbit	Abcam, ab12148	95.7	Y
MyoG	^{175}Lu	mouse	affymetrix, 14-5643	84.2	Y
Atg4a	^{176}Yb	rabbit	Novus, NBP1-68462	74.9	Y
CD31	^{144}Nd	rat	BD Pharmingen, 553708	33.1	Y
F4/80	^{146}Nd	rat	Fluidigm, 3146008B	-----	N
CD45	^{147}Sm	rat	Fludiigm, 3147003B	-----	N
α-7-integrin	^{148}Nd	rat	Ablab, 21-0010-05	49.9	Y
VCAM1	^{151}Eu	rat	BD Pharmingen, 553330	46.7	Y
CD11b	^{154}Sm	rat	Fluidigm, 3154006B	-----	N
Sca1	^{169}Tm	rat	Fluidigm, 3169015B	-----	N
PDGFRα	^{158}Gd	rat	BD Pharmingen, 562171	123.8	Y
Pax7	^{150}Nd	mouse	R & D Systems, MAB1675	42.1	Y

B.2 Individual Cell Phenotypic Gating Strategy

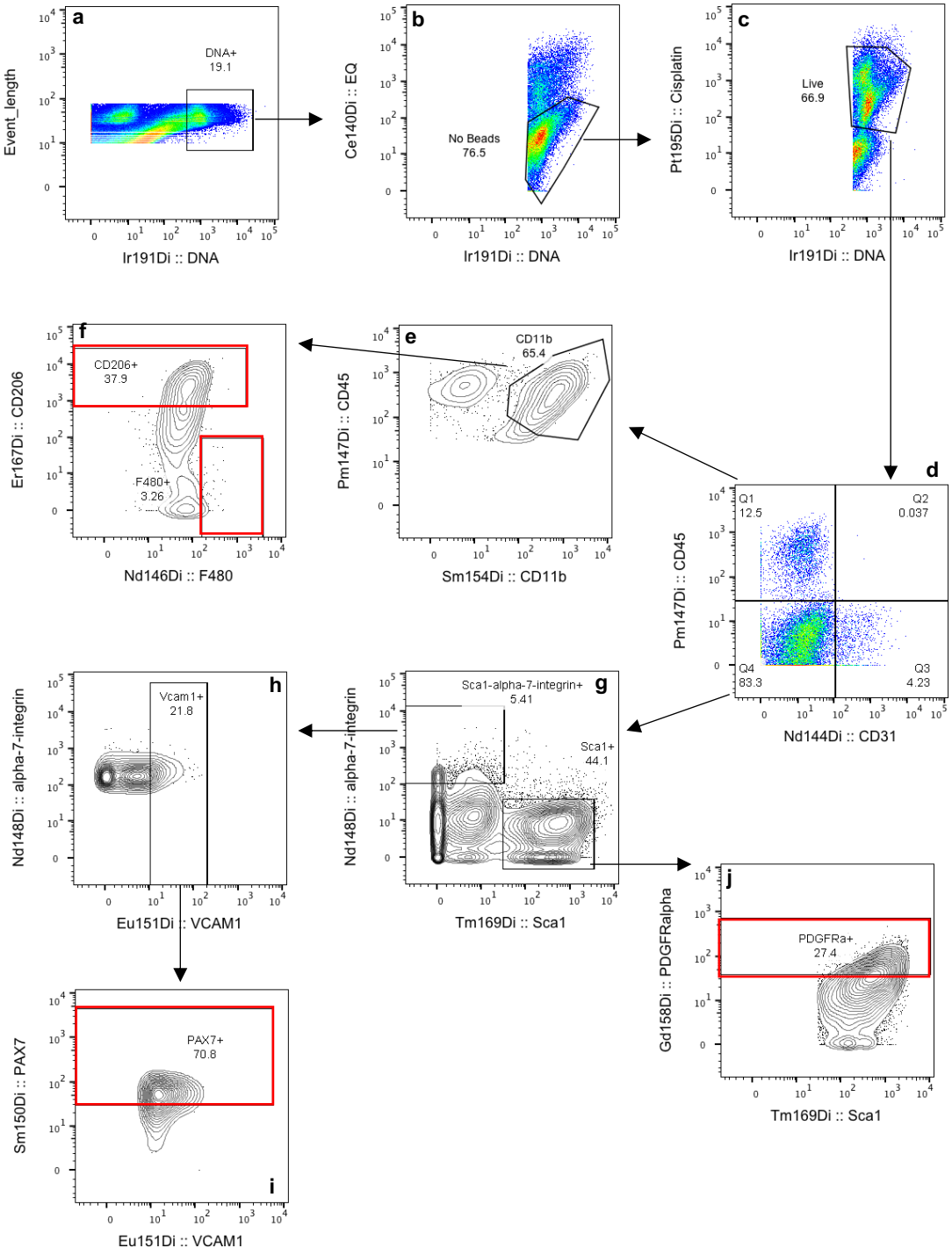

Figure B2. Manual single cell gating strategy. (a) Identification of whole cells. (b) Removal of bead-cell conjugates (c) . Identification of live cells. (d) splits endothelial ($CD31^{+,}$ Q3), immune ($CD45^{+}$, Q1) cell subsets from everything else (Q4). (d-f) M1 and M2 macrophages are identified as $CD11b^{+}$, and either $F4/80^{+}$ or $CD206^{+}$, respectively. (d-i) Satellite cells are identified as α-7-$integrin^{+}$/$Sca1^{-}$, $VCAM1^{+}$, and $Pax7^{+}$. (g,j) FAP cells are identified as $Sca1^{+}$/ α-7-$integrin^{-}$ and $PDGFR\alpha^{+}$. All gates are labeled by the positive marker and the % of parent gate.

B.3 Enumeration of unique cell subsets

Table B2. Total number phenotypically identified cell populations of interest. The absolute number of cells detected for each population in each sample is listed in columns. The total number of intact cells detected per sample is listed in the last column.

	M1 Macrophages	M2 Macrophages	Satellite Cells	FAP cells	Total Cells
Young - 1	35	2037	61	1054	76087
Young - 2	14	561	11	686	28000
Young - 3	113	757	4	93	32286
Geriatric - 1	50	581	131	1888	18519
Geriatric - 2	15	384	34	210	13636
Geriatric - 3	5	331	465	3158	35714
Geriatric - 4	5	367	184	1097	22727

Appendix C

Supporting Information for Chapter 5

C.1 Antibody Panel Characterization

Table C1. Metal-labeled antibody panel. Characteristics of the assembled metal-labeled antibody panel used to phenotype individual organelles via mass cytometry.

Target	*Metal Isotope*	*Host Isotype*	*Clone*	*# Metal Ions per Antibody*	*Antibody Vendor & P/N*
TOMM22	^{154}Sm	Mouse, IgG2a κ	4G4	56	Sigma, WHO0056993M1
LAMP2	^{162}Dy	Rabbit, IgG	poly	78	Sigma, L0668
LC3	^{142}Nd	Rabbit, IgG	poly	76	Novus, NB100-2220
Rabbit Isotype	^{171}Yb	Rabbit, IgG	poly	62	Invitrogen, 026102
Mouse Isotype	^{141}Pr	Mouse, IgG	poly	58	Invitrogen, 026502

C.2 Sample and Instrument Stability

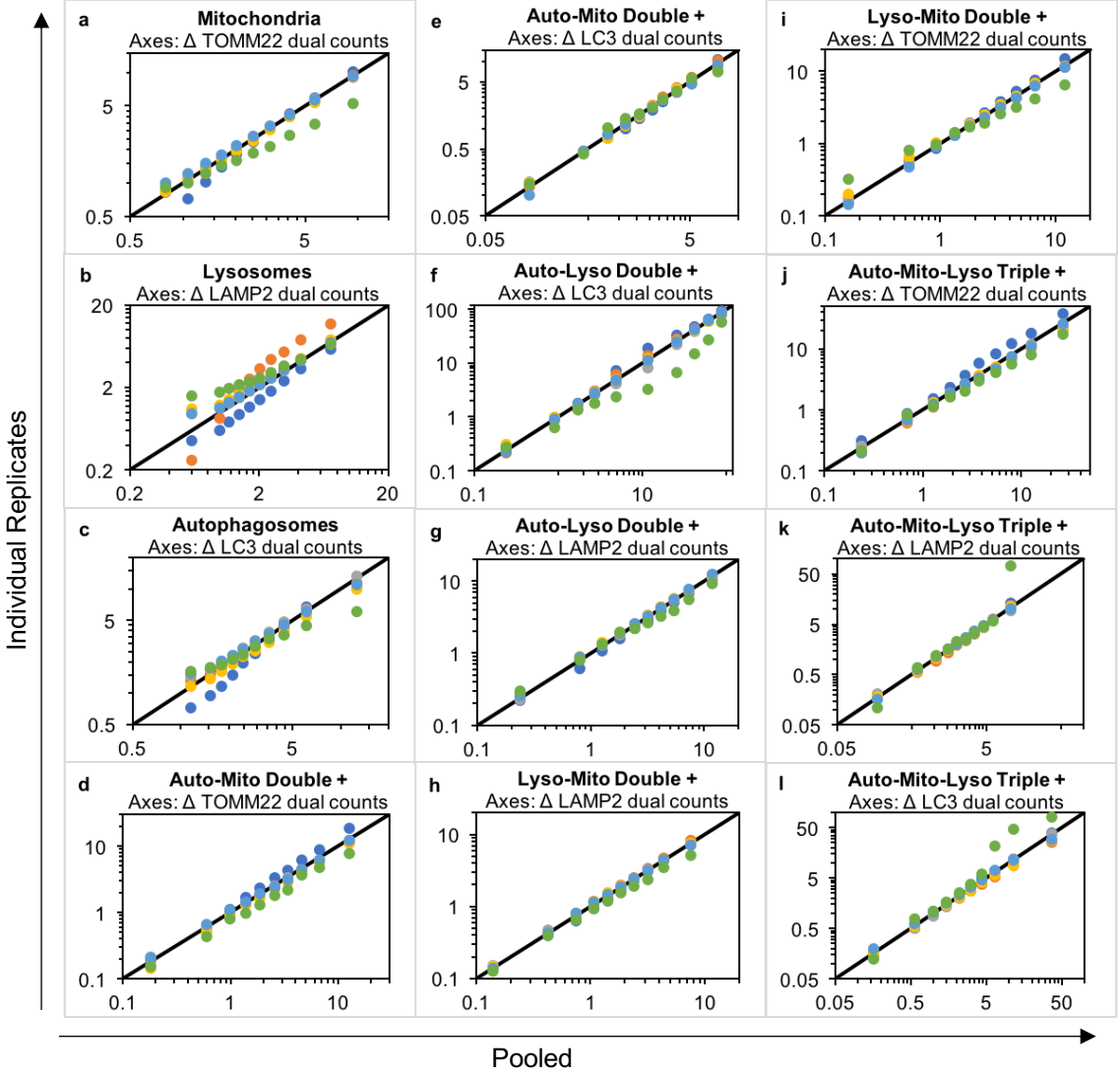

Figure C1. Intra-assay precision assessed via technical replicates. Intra-assay precision was assessed via acquisition of six technical replicates spaced over thirteen hours of data acquisition. Phenotypically unique organelle distributions from each replicate were binned into deciles and plotted on a quantile-quantile plot. If the replicate distribution is similar to the pooled distribution, the plot will approach the x=y line. Scales vary in each panel based on the marker represented. Replicates (shown as different colored series) show minimal deviation from x=y, indicating that all replicate distributions are similar enough to originate from the same pooled distribution. Where deviations do occur (i.e. panels a, b, c f, i-l) series that deviate were data collected at the end of 13 hours, indicating a potential limit in sample or instrument stability. These observations apply to all phenotypically unique organelle populations, including: a) mitochondria (TOMM22+), b) lysosomes (LAMP2+), c) LC3+ autophagy organelles (LC3+), d-e) LC3+ autophagy organelles – mitochondria (LC3+TOMM22+), f-g) LC3+ autophagy organelles – lysosomes (LC3+LAMP2+), h-i) lysosomes – mitochondria (LAMP2+TOMM22+), and j-l) LC3+ autophagy organelles – mitochondria – lysosome (TOMM22+LAMP2+LC3+). The number of organelles in each technical replicate were as follows: replicate 1, n = 20,440; replicate 2, n = 19,995; replicate 3, n = 22,195; replicate 4, n = 9,208; replicate 5, n = 22,410; replicate 6, n = 1,632.

C.3 Setting Individual Organelle Signal Thresholds and Application to Gating Strategies

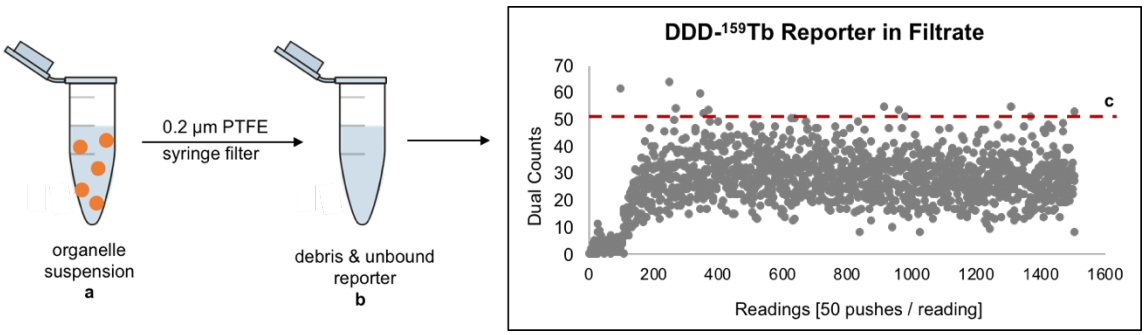

Figure C2. Calculation of Individual Organelle Signal Thresholds. To set a low threshold for each monitored m/z channel, an aliquot of organelle suspension (a) was filtered and the filtrate containing debris & unbound reporter (b) analyzed in solution mode on the CyTOF2. The low signal threshold (c) is calculated as the mean dual count signal in a given channel plus three times the standard deviation of the mean. This low signal threshold value was calculated over a stable range, typically 400-1400 readings.

Table C2. Calculated Low Signal Threshold Value. A threshold value was calculated for each m/z value in each organelle sample. B = brain, L = liver, M = skeletal muscle, R1 = biological replicate 1, R2 = biological replicate 2.

Tissue - Replicate	Calculated low signal threshold value (DC signal)			
	^{142}Nd-LC3	^{154}Sm-TOMM22	DDD-^{159}Tb	^{162}Dy-LAMP2
B-R1	0.5264	0.4218	8.2087	0.3114
B-R2	0.9078	0.6404	9.9606	0.6100
L-R1	0.4400	0.7324	26.3693	0.8331
L-R2	0.7978	0.6900	15.9290	1.4507
M-R1	0.7324	0.7189	8.9970	0.4163
M-R2	1.0010	0.7720	12.9580	0.7039

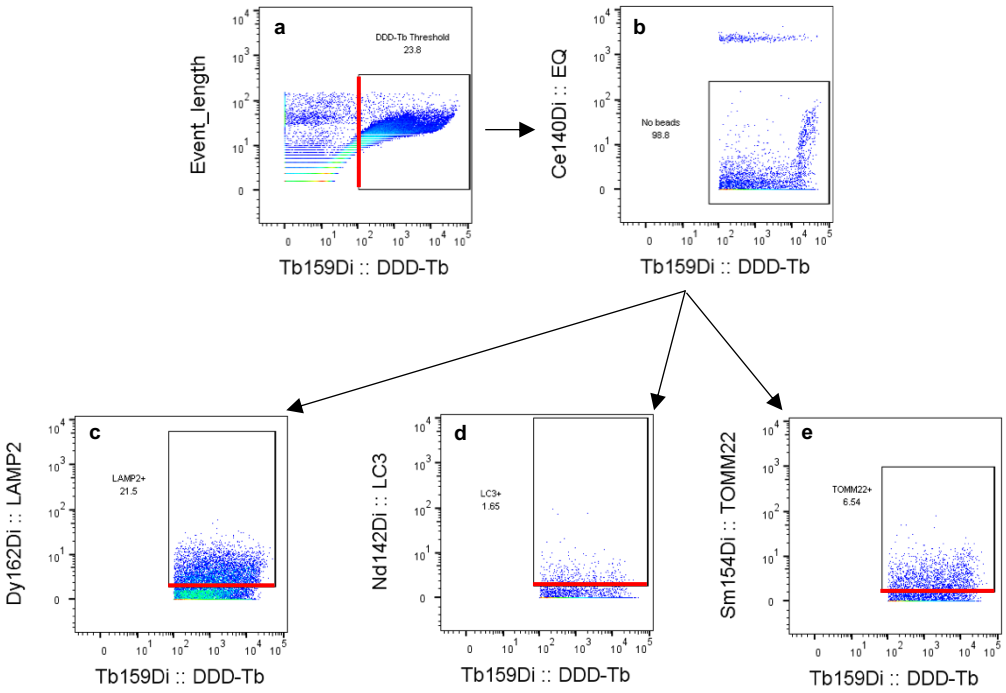

Figure C3. Gating Strategy for Phenotypically Unique Autophagy Organelles. Calculated low signal threshold values used as lower bounds for phenotypic identification. The first two panels (a-b) show sequential gates: (a) application of DDD-Tb low signal threshold, (b) removal of EQ normalization bead – organelle aggregate events. The lower three panels show the application of the calculated lower signal threshold to phenotypically identify organelle events: d) LAMP2 (lysosome), e) LC3 (LC3+ organelles), f) TOMM22 (mitochondria).

C.4 Population level analyses of phenotyped organelles from liver and skeletal muscle tissue

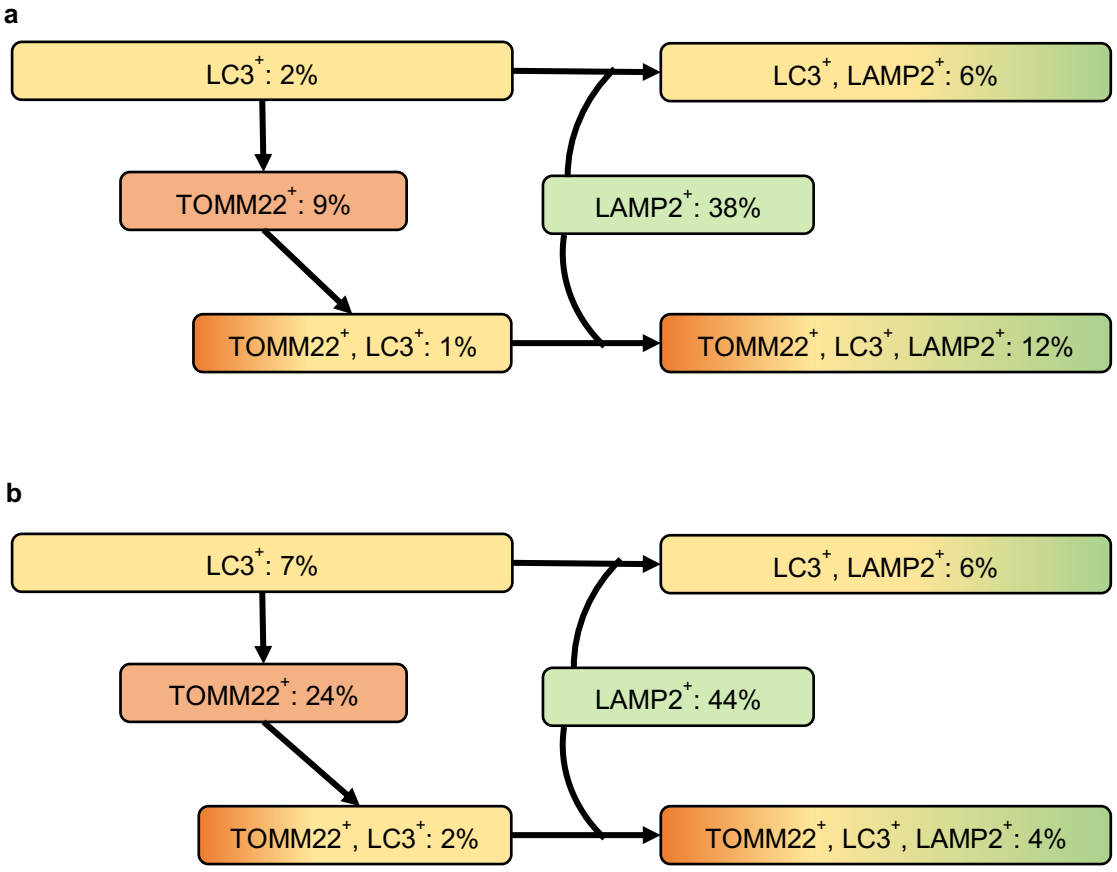

Figure C4. Percent identification of individual organelles from liver and skeletal muscle tissue. The percent contribution from each phenotypically unique organelle type to the total number of identified organelles was calculated for liver (a) and skeletal muscle (b) tissues. Tissue-specific differences in organelle content are expected due to differences cellular function of the organelle types in each tissue.

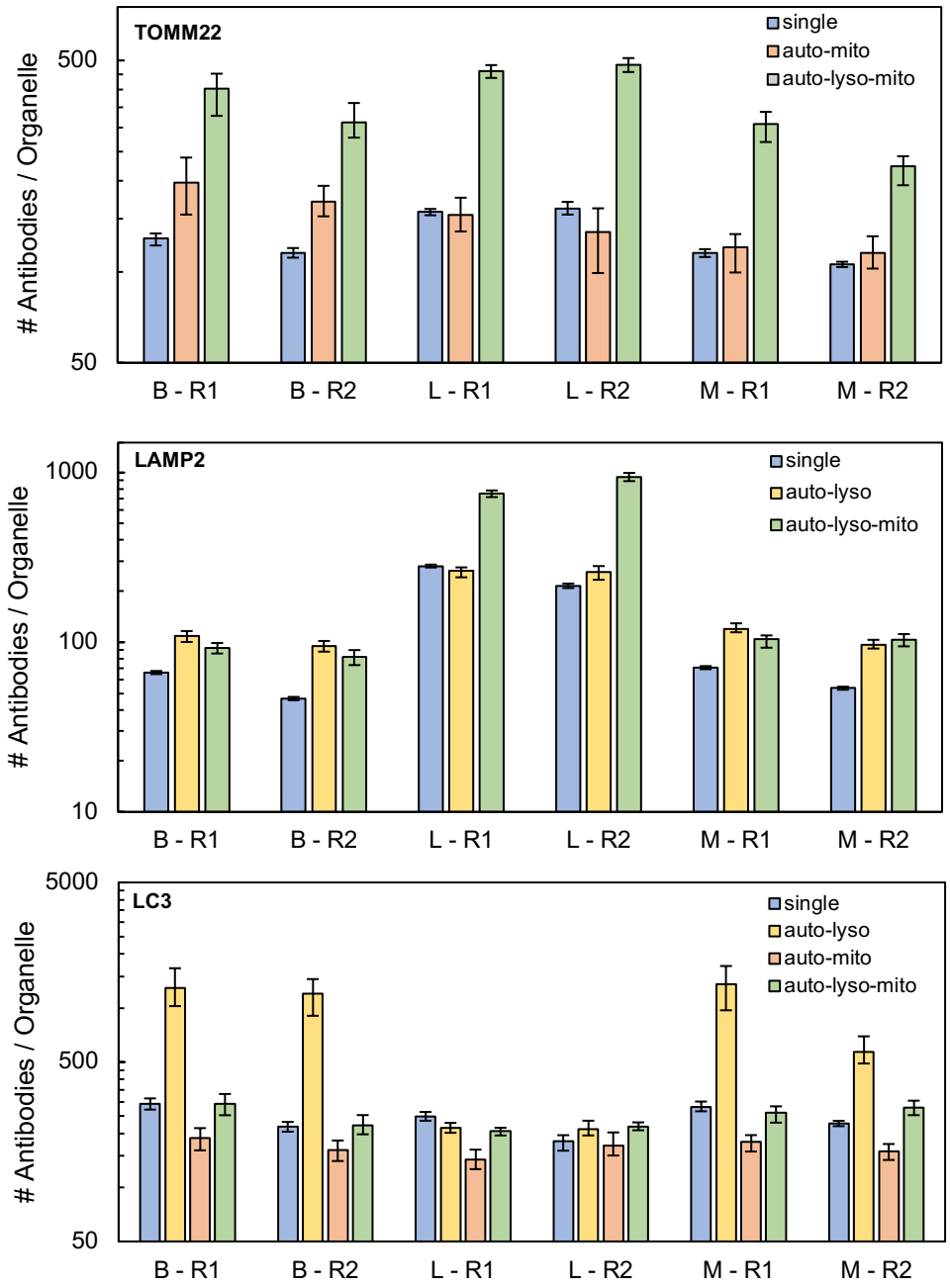

Figure C5. Comparison of the number of specific marker antibodies bound to each organelle type. The calculated number of specific marker antibodies detected per organelle generally increases with progression to late autophagic organelles. The increase in markers is generally accompanied by an increase in the number of DDD-Tb molecules per detected organelle indicated an increase in total membrane volume. The number of specific marker antibodies per organelle was normalized to the DDD-Tb dual count signal, and the resulting plots are shown in Figure 2a-c. Error represented as 95% confidence intervals of the median. B = brain, L = liver, M = skeletal muscle, R1 = biological replicate 1, R2 = biological replicate 2.

C.5 **Multi-dimensional t-SNE analysis of organelles from liver and skeletal muscle tissues**

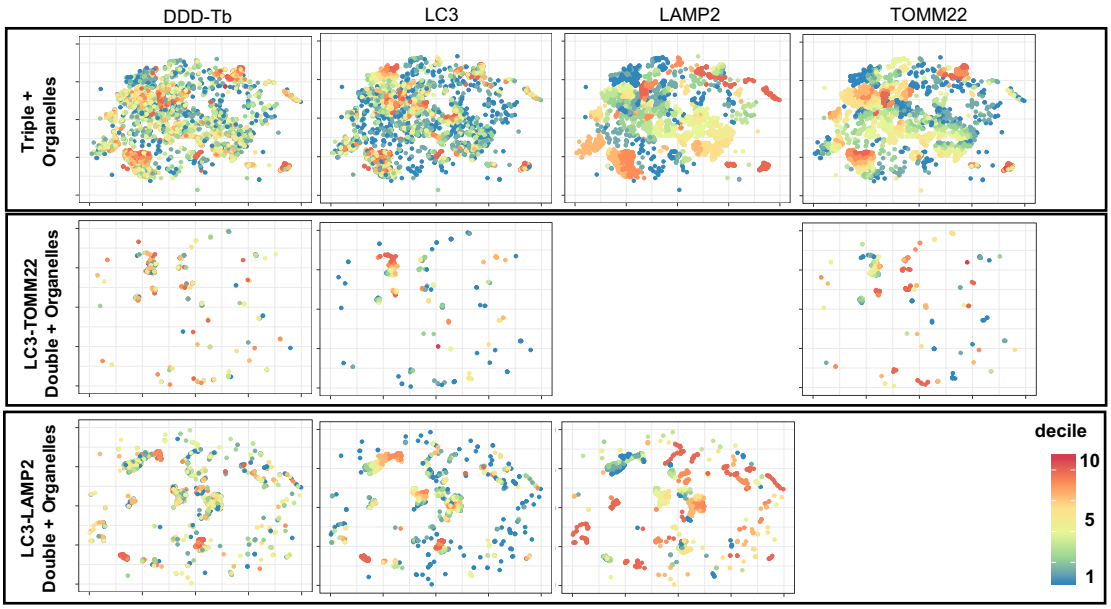

Figure C6. Multi-dimensional t-SNE analysis of organelles from liver. t-SNE plots from murine liver tissue show phenotypically identified populations of organelles. Distributions of specific markers on individual organelles were binned into deciles and color-coded according to their assigned decile. Wide variation in color across specific markers in t-SNE plots indicate heterogenous sub-populations, which may have significantly different function. Triple + organelles represent autolysosomes associated with mitochondria, while LC3-TOMM22 double + organelles represent autophagosomes associated with mitochondria, and LC3-LAMP2 double + organelles represent autolysosomes.

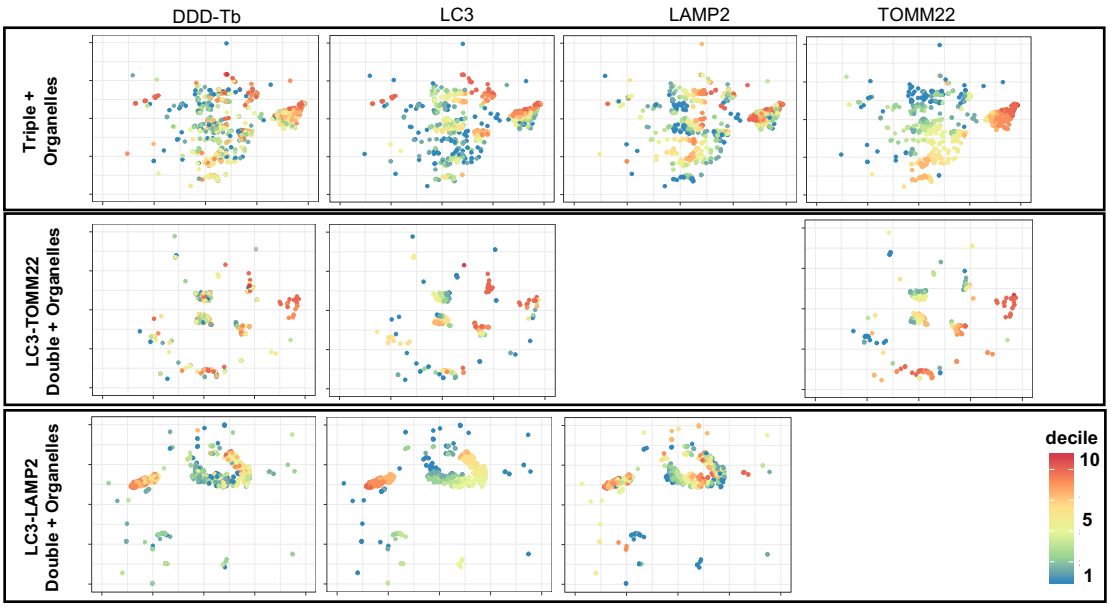

Figure C7. Multi-dimensional t-SNE analysis of organelles from skeletal muscle. t-SNE plots from murine skeletal muscle tissue show phenotypically identified populations of organelles. Distributions of specific markers on individual organelles were binned into deciles and color-coded according to their assigned decile. Wide variation in color across specific markers in t-SNE plots indicate heterogenous sub-populations, which may have significantly different function. Triple + organelles represent autolysosomes associated with mitochondria, while LC3-TOMM22 double + organelles represent autophagosomes associated with mitochondria, and LC3-LAMP2 double + organelles represent autolysosomes

Appendix D

Supporting Information for Chapter 7

D.1 Synthesis of New Mitochondria-Targeting Functional Reagent for Mass Cytometry

General Considerations

^{1}H NMR spectra were recorded on a Bruker AX 400 at 400 MHz at the Le Claire-Dow Characterization Facility of the Department of Chemistry of the University of Minnesota; the solvent residual peak was used as an internal reference. ^{1}H NMR data are reported as follows: chemical shift (δ, ppm), multiplicity (s, singlet; d, doublet; t, triplet; m, multiplet), integration, coupling constant (Hz). Mass spectra (ESI MS = electrospray ionization - mass spectrometry) were recorded on a Bruker BioTOF II at the Waters Center for Innovation for Mass Spectrometry Facility at the Department of Chemistry at the University of Minnesota, Twin-Cities. Analytical HPLC was performed on a Variant pro star instrument (Agilent, Santa Clara, CA) equipped with a diode array detector a thermostat set at 25 °C, and a Zorbax Eclipse XDB-C18 column (9.4 × 250 mm, 5 µm, Agilent, Santa Clara, CA). The mobile phase of a binary gradient (2 min 15 % B, 20 min 15 to 100 % B, 3 min, 100 % B, 4 min 100 to 15% B, 1 min 15% B) where A is water (0.1 % TFA) and B acetonitrile (0.1 % TFA at a flow rate of 1 mL/min was used for analytical and preparative HPLC.

Unless otherwise noted, starting materials were obtained from commercial suppliers and used without further purification. The synthesis of TPP-Ho-DOTA (**1**) was completed in three steps. The synthesis of (10-aminodecyl) triphenylphosphonium bromide (**2**) was carried out following the procedure described by Zhixin Li.[185] The condensation of bromododecyl phtalimide and triphenylphosphine was carried out in reflux of acetonitrile overnight. The phtalimide protective group was removed after an overnight reaction of hydrazine reflux in ethanol. The coupling between the amine (**3**) and the succinimide was adapted from the procedure described in X[186] and allowed the formation of TPP-Ho-DOTA.

Synthesis of (10-phtalimidyl) triphenylphosphonium bromide (**2**)

Bromodecyl phtalimide (7g, 0.019 mol) and triphenylphosphine (5g, 0.019 mol) were dissolved under N_2 in acetonitrile (60 mL) and refluxed overnight. The solvent

was removed under reduced pressure. The crude product was purified using a combiflash system with silica gel and a gradient of EtOH in DCM (compound come out at 15% of EtOH) afforded a white solid (**2**) (6 g, 49%). ESI+ (m/z) calculated for $[C_{36}H_{39}NO_2P]^+$: 548.3; found: 548.3.

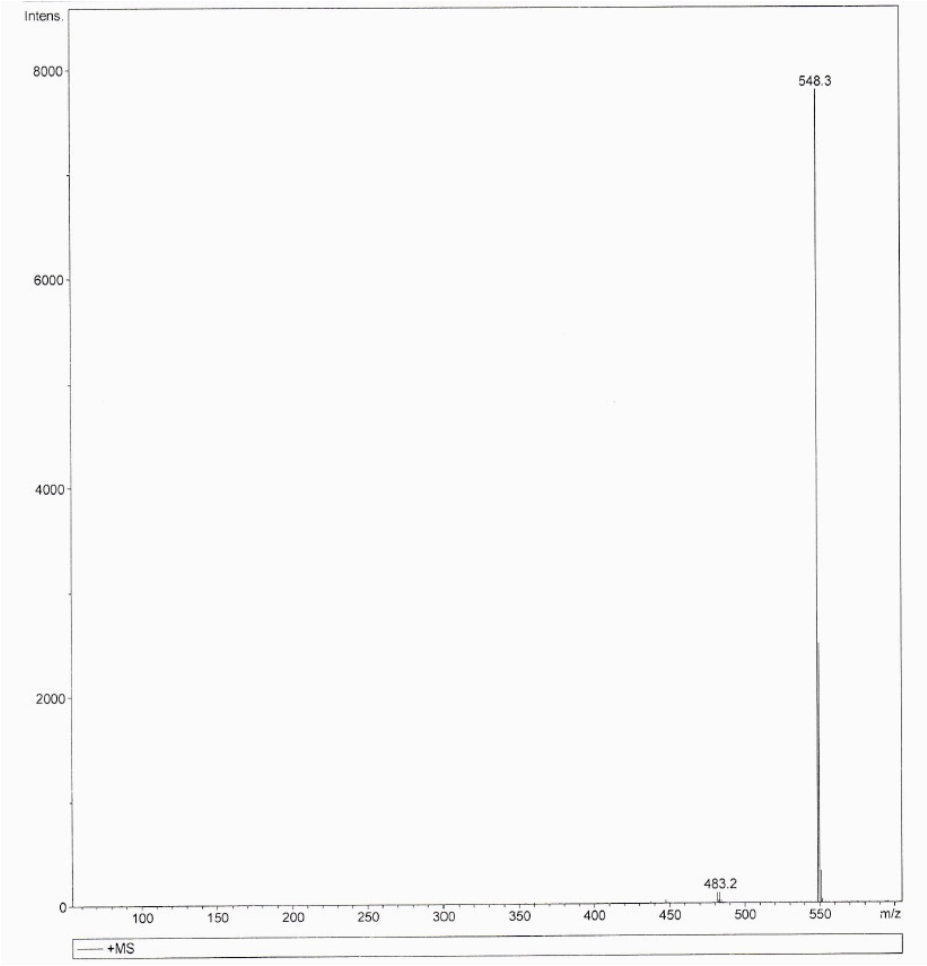

Figure D1. ESI (+) of (10-phtalimidyl) triphenylphosphonium bromide (2).

*Synthesis of (10-aminodecyl) triphenylphosphonium bromide (**3**)*

To a solution of 1 (6 g, 9.2 mmol) in EtOH (70 mL) hydrazine was added (0.46 mL, 9.2 mmol). The mixture was refluxed for 15 hours. The solvent was removed under reduced pressure. The product was purified using a combiflash system with on silica gel and a gradient of EtOH in DCM (compound eluted at 20 % EtOH) afforded a white solid (**3**) (3.4g, 73%).

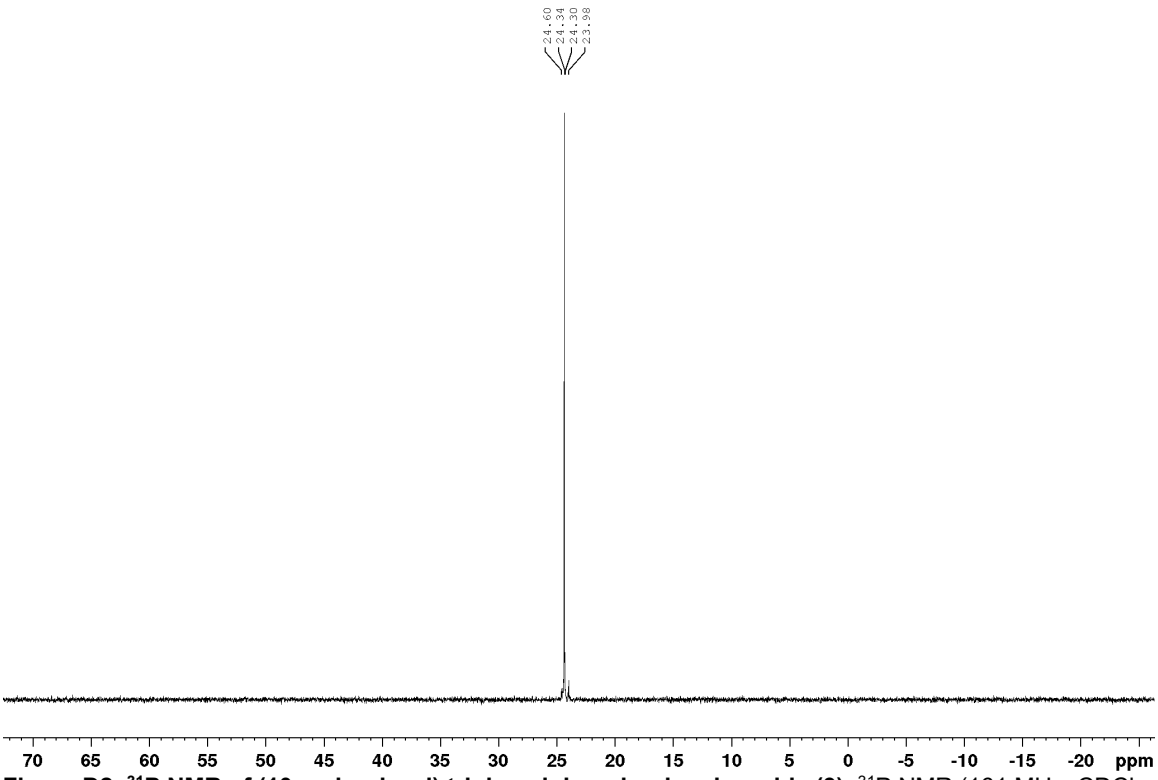

Figure D2. ^{31}P NMR of (10-aminodecyl) triphenylphosphonium bromide (3). ^{31}P NMR (161 MHz, $CDCl_3$, δ, ppm): 24.3.

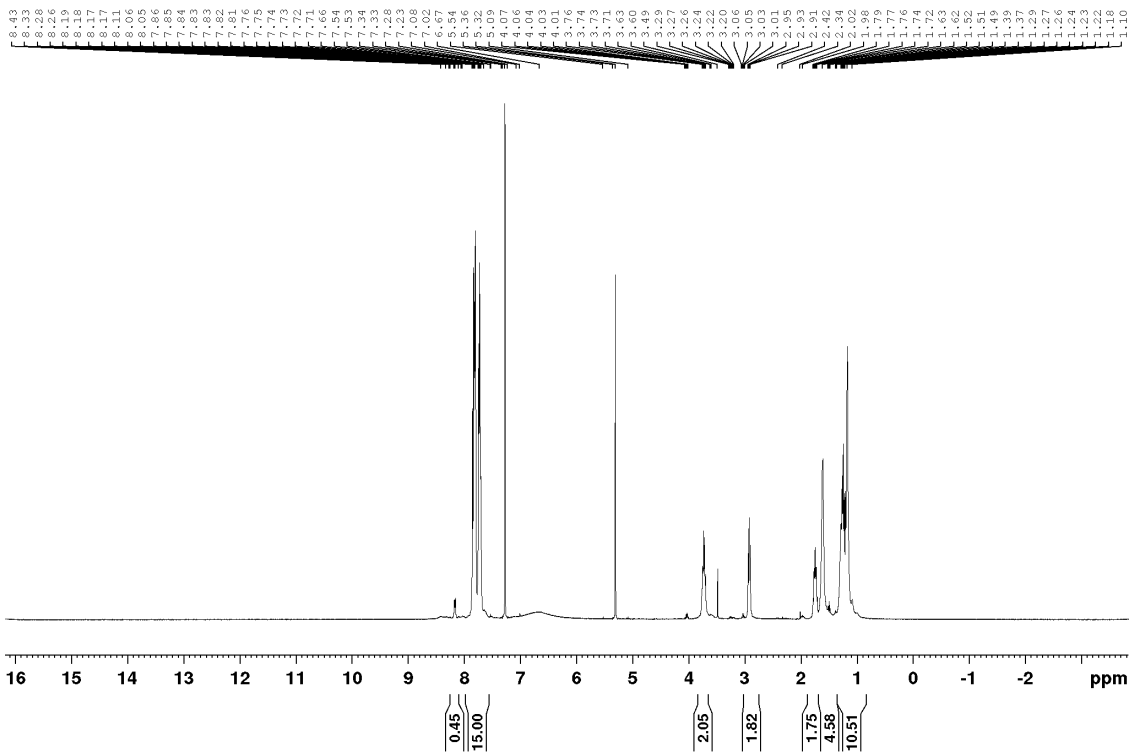

Figure D3. ^{1}H NMR of (10-aminodecyl) triphenylphosphonium bromide (3). ^{1}H NMR (400 MHz, $CDCl_3$, δ, ppm): 7.86–7.75 (15H, m), 3.73–3.60 (2H, m), 2.03–2.2.91 (2H, m), 1.79-1.74 (2H, m), 1.63-1.52 (4H, m) 1.39–1.10 (10H, m).

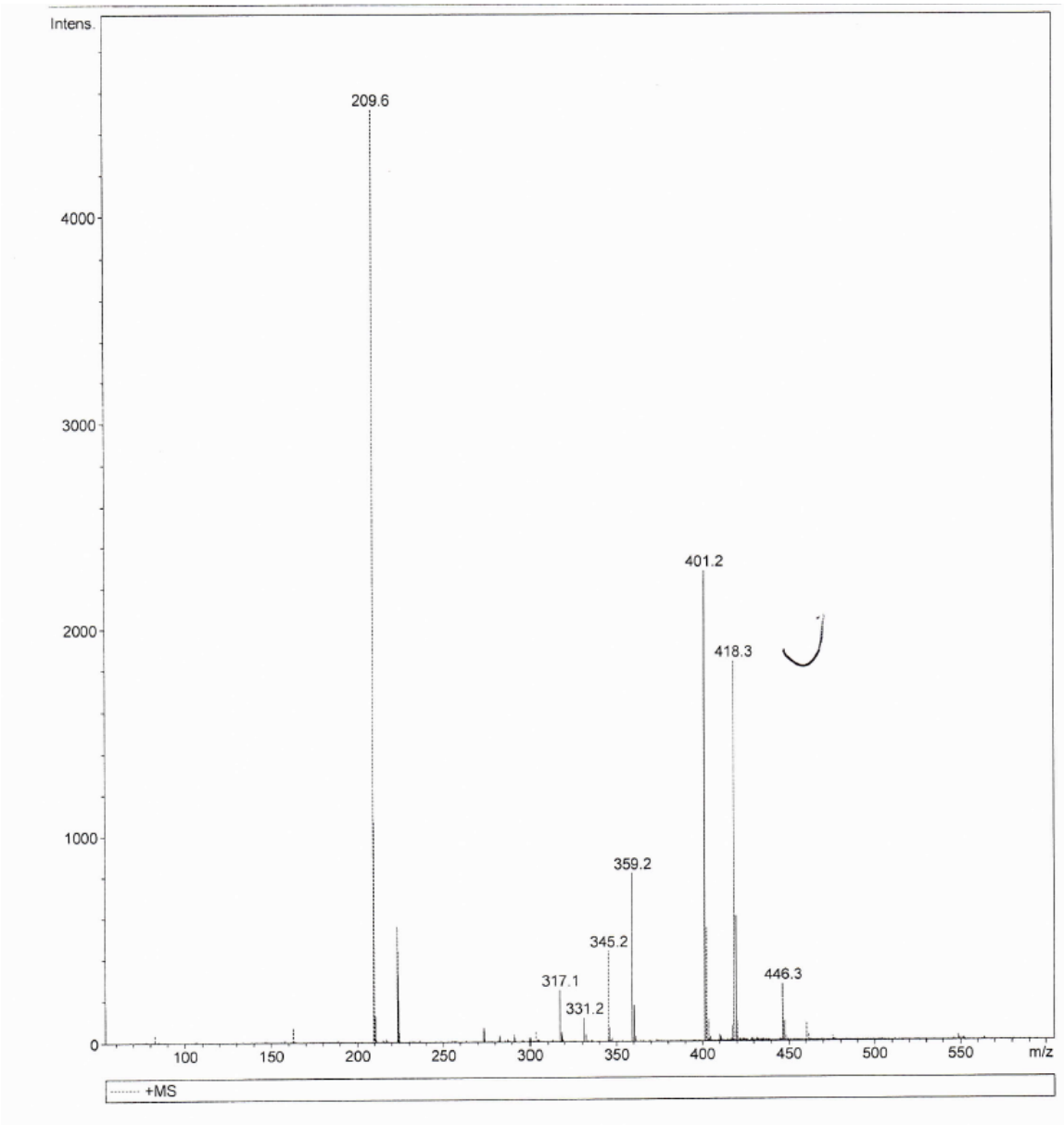

Figure D4. ESI (+) of (10-aminodecyl) triphenylphosphonium bromide (3). ESI^+ (m/z) calculated for $[C_{28}H_{37}NP]^+$: 418.2; found: 418.3.

Mito-Ho-DOTA

TEA (17.1 mg, 9.3 mmol) was added to a nitrogen purged solution of p-SCN-Bn-Ho-DOTA (37.3 mg, 52.6 mmol) and **3** (30.9 mg 63.4 mmol) in dry DMSO (10 mL). The reaction mixture was stirred at room temperature overnight. The solvent was removed under reduced pressure and the residue was purified using combiflash system and reverse phase C18 with water and acetonitrile gradient both phases containing 0.1 % TFA (Mito-Ho-DOTA eluted at 40% of CH_3CN) to afford a pinkish solid **1** (40 mg, 63%).

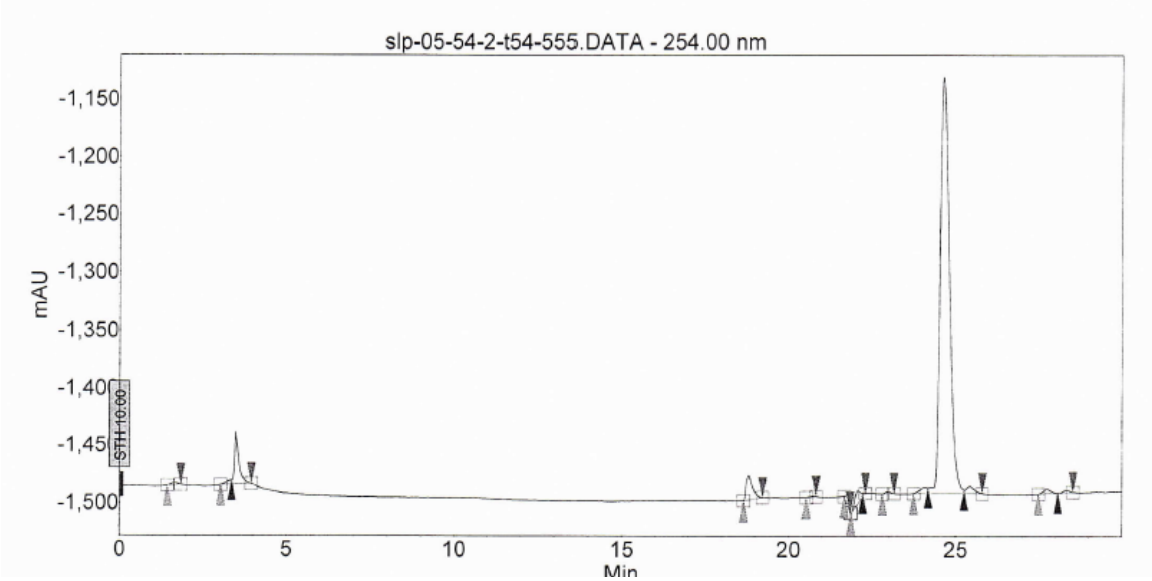

Figure D5. HPLC trace at 250nm of TPP-Ho-DOTA (1). Elution time: 24.6 min

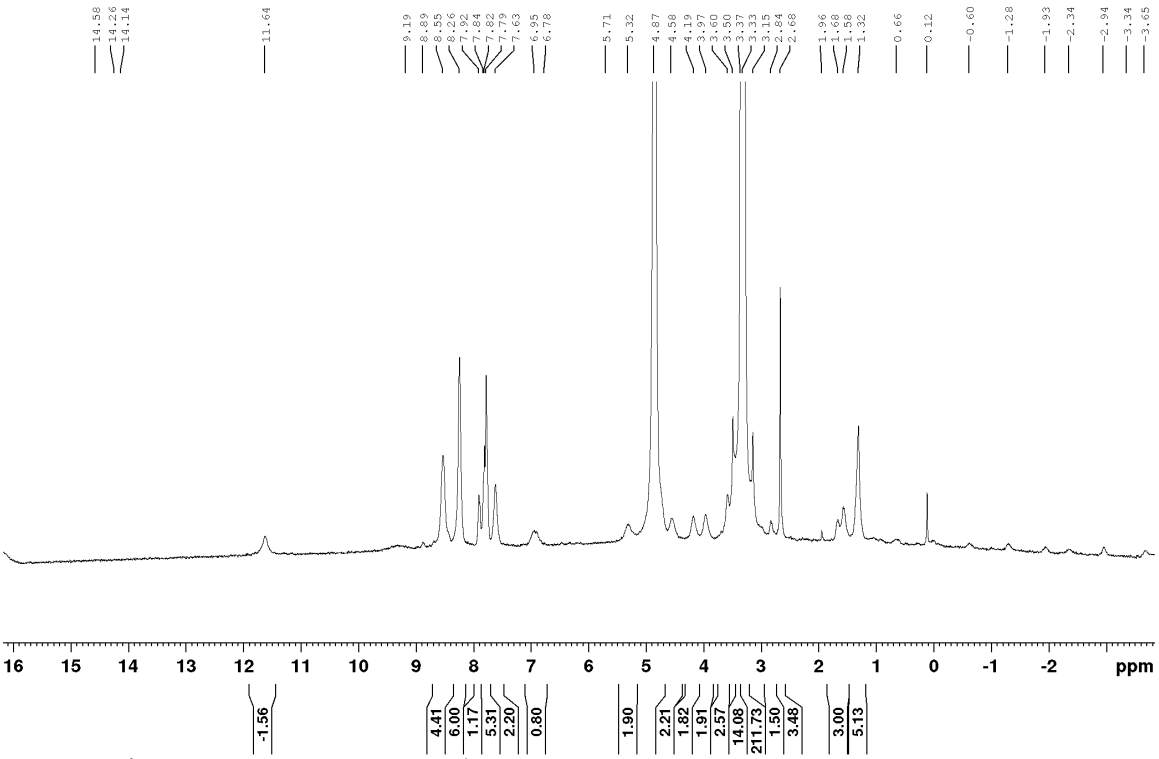

Figure D6. ^{1}H NMR of TPP-Ho-DOTA (1). ^{1}H NMR (400 MHz, MeOH, δ, ppm):8.55 (4H, brs), 8.26 (6H, brs), 7.92 (2H, brs), 7.82 (5H, brs), 7.63 (2H, brs), 6.95 (1H, NH), 5.32 (2H, brs), 4.56 (2H, brs), 4.19 (2H, brs), 3.97 (2H, brs), 3.60 (2H, brs), 3.37 (14H, brs), 2.84 (2H, brs), 2.68 (4H, brs),1.68 (3H, brs), 1.32 (5H, brs). (8 H under the solvent peak at 3.37 ppm)

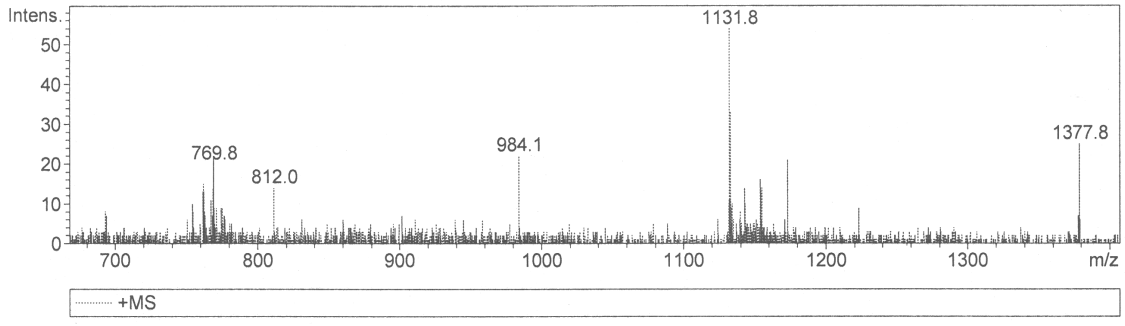

Figure D7. ESI (+) of TPP-Ho-DOTA (1). ESI$^+$ (m/z) calculated $[C_{52}H_{66}HoN_6O_8PS]^+$ 1130.4, found: 1131.8.